

University of Strathclyde
Department of Naval Architecture, Ocean &
Marine Engineering



**Analysis of diesel combustion in four-stroke marine engines:
an integrated CFD and reduced chemical kinetics approach**

by

Aristeidis Kiourtzis

A thesis presented in fulfilment of the requirements for the degree
of Doctor of Philosophy
Glasgow, UK

2021

This thesis is the result of the author's original research. It has been composed by the author and has not been previously submitted for examination which has led to the award of a degree.

The copyright of this thesis belongs to the author under the terms of the United Kingdom Copyright Acts as qualified by University of Strathclyde Regulation 3.50. Due acknowledgement must always be made of the use of any material contained in, or derived from, this thesis.

Signed: Aristeidis Kiourtzis

Date: 29/09/2021

Table of Contents

Abstract	i
Acknowledgements	ii
List of Figures	iii
List of Tables	xi
Nomenclature	xii
1. Introduction	1
1.1 Marine Engines	2
1.2 Marine Engine Emissions and Regulations	5
1.3 Literature Review of Marine Engine Aerothermochemistry	7
1.3.1 Experimental Studies	7
1.3.1.1 Combustion Chambers and Research Engines.....	7
1.3.1.2 Engines.....	9
1.3.2 CFD Studies	10
1.4 Research Gap, Aim and Research Objectives.....	14
2. CFD modelling.....	16
2.1 Fundamentals – Governing Equations	16
2.2 Physical processes and models for fuel spray breakup	20
2.2.1 Taylor Analogy Breakup model (TAB).....	22
2.2.2 Enhanced Taylor Analogy Breakup model (ETAB).....	24
2.2.3 Cascade Atomisation and droplet Breakup model (CAB).....	26
2.3 Collision model.....	28
2.4 Evaporation model	30
2.5 Ignition model	33
2.6 Combustion modelling.....	35
2.6.1 One-step approach.....	36
2.6.2 Realistic chemistry	38
2.7 Pollutant emission models	40
2.7.1 NO _x Model	40
2.7.2 Soot Model.....	42
2.8. CFD code ‘KIVA-3vr2’	43
3. CFD spray studies in a constant volume chamber	44
3.1 Problem definition and resolution tests.....	44
3.1.1 Computational Grid.....	45

3.1.2 Resolution tests	46
3.2 Adaptation of ETAB and CAB models.....	53
3.3 Non-reactive spray flow: analysis of CFD results	55
3.4 Chapter conclusions	63
4. CFD studies of diesel combustion in an experimental dual fuel engine.....	64
4.1 Problem definition.....	64
4.2 Analysis of CFD results	67
4.2.1 Carbon-based emissions.....	86
4.2.2 NO _x emissions.....	108
4.3 Chapter conclusions	113
5. CFD studies of diesel combustion in a marine dual fuel engine.....	115
5.1 Problem definition.....	115
5.2 Analysis of CFD results	116
5.2.1 Carbon-based emissions.....	135
5.2.2 NO _x emissions.....	156
5.3 Chapter conclusions	161
6. Novelty and contribution	162
6.1 Methodology aspects.....	162
6.2 New findings	164
6.3 Journal publications under preparation	164
7. Concluding remarks	165
8. Recommendations for future work	166
References.....	167
Appendix A.....	176

Abstract

The present thesis aims at characterising and understanding flow and combustion processes in four-stroke marine engines by means of detailed Computational Fluid Dynamics (CFD) modelling. In particular, two dual-fuel engines operating in the diesel mode are considered: Lister LV1 and Wärtilä 50DF. A systematic approach is followed, consisting in: (a) Characterising the spray dynamics in a constant volume chamber, and adapting the Cascade Atomisation Breakup (CAB) spray model, for conditions relevant to operation of the engines considered in the present study. (b) Adapting a tool developed by means of coupling the chemical kinetics CHEMKIN-II code with the KIVA-3vr2 CFD code, thus enabling CFD simulations with reliable chemistry. (c) Performing CFD simulations of flow and combustion in the two engines for operation in the 80% load for Lister LV1, and in the full load range for Wärtilä 50DF, and comparing results against one-step chemistry simulations, as well as against respective experimental data. Thus, to author's knowledge, the present thesis reports the first CFD studies in marine engines operating in the diesel mode, including realistic combustion chemistry.

The computational results demonstrate that the spray breakup corresponds to the catastrophic regime. Adaptation of the CAB model has yielded values of model constants in a range that does not considerably deviate from relevant literature studies. Two validated reduced-order chemical kinetic mechanisms of n-heptane combustion have been implemented in the course of the present CFD studies: (i) Patel et al. (2004), with 29 species and 52 elementary reactions, and (ii) Ra and Reitz (2008), with 45 species and 142 elementary reactions. The two mechanisms have been supplemented with a NO_x sub-mechanism. The main findings of the present study can be summarised as follows:

- Ignition delay times are in good agreement with chemical kinetics simulations using realistic chemistry.
- For simulations with reduced order chemistry, fuel disintegration nearly terminates at the end of injection, in contrast to results of the one-step approach. On the other hand, similarities in Rate of Heat Release Rates are attained for the two approaches.
- The evolution of important species can differ considerably between the two reduced mechanisms.
- The distribution of main pollutants bears similarities between the two reduced mechanisms, and may differ significantly from the one-step approach.

While the present study demonstrates that using reduced order chemistry is essential for characterising engine aerothermochemistry albeit at a significant increase in computational cost, the one-step approach is shown to still be valid as an engineering tool, providing a basic characterisation of flow and combustion, which can be useful in the frame of marine engine development.

Acknowledgements

In this paragraph, I have the opportunity to express my gratitude towards my parents, Gavriil and Eirini, my sister Maria, as well as, my sister's husband, Konstantinos, my niece, Eirini, and the little baby, who continuously supported and encouraged my efforts all these years to conclude the present Ph.D. thesis. Without their tremendous understanding and encouragement in the past few years, it would have been impossible for me to complete my study.

I would also like to express my sincere gratitude to my supervisor, Prof. G. Theotokatos, as well as to Prof. L. Kaiktsis of the National Technical University of Athens (NTUA), for their continuous support and valuable contribution. Their thoughtful comments and recommendations were vital to the completion of this dissertation.

In addition, I would like to thank the rest of the research team for their collaborative effort during my Ph.D. studies. Thus, special thanks are also expressed to Mr. D. Kazangas, researcher at NTUA, as well as Dr. P. Kontoulis, for their continuous support and valuable contribution during my PhD studies. Moreover, I am grateful to Mr. X. Vouvakos Dr. K. Aivalis, researchers at NTUA, for their support and many helpful discussions. Our meetings and conversations were vital, and have provided me with a comprehensive and objective critique from multiple perspectives, which inspired me to think outside the box.

I would also like to acknowledge the Department Naval Architecture, Ocean and Marine Engineering of University of Strathclyde, for its participation and engagement in the study.

Finally, many thanks to all participants that took part in the study and contributed to a positive outcome of this research.

List of Figures

Figure 1.1 Speed-power range of main families of two-stroke marine Diesel engines manufactured by MAN (Marine Engines and Systems, MAN, 2017).....	3
Figure 1.2: Speed-power range of main families of two-stroke marine Diesel engines manufactured by Wärtilä (now: Winterthu Gas and Diesel – WinGD) (Spahni and Kyratos, 2014).....	3
Figure 1.3: Map of existing and possible future ECAs (Det Norske Veritas (DNV). 2018. Maritime Forecast to 2050).....	5
Figure 1.4: Fuel sulphur content limits (www.imo.org).	6
Figure 1.5: Adaptive multi-grid in a 2D mesh (Shi et al., 2009).	13
Figure 2.1: Sketch of spray flow structure, depicting the three areas of different liquid phase density (Stiesch, 2003).	20
Figure 2.2: Illustration of cavitation bubbles and distribution of static pressure inside an injector nozzle (Stiesch, 2003).	21
Figure 2.3: Schematic of the five different breakup regimes and corresponding drop Weber number limits (Reitz, 2012).	22
Figure 2.4: Analogy between fuel drop deformation and forced mass-spring oscillation system with damping, used in the TAB model (Baumgarten, 2006).	23
Figure 2.5: Sketch of collision parameters for collision of two drops (Baumgarten, 2006).....	29
Figure 2.6: Droplet collision regimes (left) and the corresponding mechanisms (right) (Baumgarten, 2006).	29
Figure 2.7: Procession of drop vaporization (Baumgarten, 2006).....	30
Figure 2.8: Sketch of heat fluxes to a droplet from the ambient gas (Baumgarten, 2006).	30
Figure 2.9: Sketch of the simplified system of ignition characteristic times, accounting for the overall ignition characteristic time (Weisser et al.,1998).	33
Figure 2.10: Sketch of typical Rate of Heat Release curve in a Diesel engine, in which the different phases of combustion are depicted (Heywood, 1988).	36
Figure 2.11: Coupled code KIVA-CHEMKIN flowchart (Kakaee et al., 2015).	39
Figure 3.1: Schematic of the high-pressure and temperature constant volume cell (Schneider, 2003).	44
Figure 3.2 : Sketch of a finite volume cell (Amsden, 1989).....	45
Figure 3.3: Portion of a momentum cell (i;j;k) lying within a regular cell (i,j,k) (Amsden, 1989)...	46
Figure 3.4: Top and bottom views of the computational grids used in spatial resolution tests.	47
Figure 3.5: Injection rate versus time for Case 1 (Schneider, 2003).	48

Figure 3.6: Case 1: calculated penetration length versus time for the three computational grids considered, using the ETAB model and a time step value of $\Delta t=2 \cdot 10^{-6}$ s. The corresponding experimental curve (Scheider, 2003) is also included.	49
Figure 3.7: Case 1: colour-coded contours of gas velocity, droplet Sauter Mean Diameter - SMD (in microns) and spray droplet velocity using the ETAB model, at the vertical plane including the injector.	50
Figure 3.8: Case 1: calculated penetration length versus time for the three computational grids considered, using the CAB model and a time step value of $\Delta t=2 \cdot 10^{-6}$ s. The corresponding experimental curve (Scheider, 2003) is also included.	51
Figure 3.9: Case 1: colour-coded contours of gas velocity, droplet Sauter Mean Diameter - SMD (in microns) and spray droplet velocity using the CAB model, at the vertical plane including the injector.	52
Figure 3.10: Case 1: Computed penetration length versus time for CAB and the ETAB model using the “fine” computational grid. The experimental curve of Scheider (2003) is also included.	55
Figure 3.11: Case 1: colour-coded contours of gas velocity for the CAB and ETAB models, at a vertical plane including the injector, at representative time instants	56
Figure 3.12: Case 1: colour-coded contours of droplet SMD (in microns) for the CAB and ETAB models, at a vertical plane including the injector, at representative time instants.	57
Figure 3.13: Case 1: colour-coded contours of spray droplet velocity for the CAB and ETAB models, at a vertical plane including the injector, at representative time instants.	58
Figure 3.14: Cases 1, 2: colour-coded contours of gas velocity for the CAB and ETAB models, at a vertical plane including the injector, at representative time instants.	60
Figure 3.15: Cases 1, 2: colour-coded contours of droplet SMD (in microns) for the CAB and ETAB models, at a vertical plane including the injector, at representative time instants.	61
Figure 3.16: Cases 1, 2: colour-coded contours of spray droplet velocity for the CAB and ETAB models, at a vertical plane including the injector, at representative time instants.	62
Figure 4.1: Top and front views of the polar and cartesian grid used in the simulations of the Lister LV1 engine.	67
Figure 4.2: Definition of injection direction in terms of angles α and β	68
Figure 4.3: Injection profile of the Lister LV1 engine for operation at a load of 80%.	69
Figure 4.4: Proportionality constant K_{bu} versus Weber number for the ETAB and CAB models. ...	70
Figure 4.5: Computed traces of cylinder pressure using one-step chemistry and the two reduced order chemical kinetics mechanisms (Mech.29 and Mech.45), at an engine load of 80%. The corresponding experimental curve (Papagiannakis and Hountalas, 2003) is also included.	71

Figure 4.6: Computed traces of normalized Rate of Heat Release using one-step chemistry and the two reduced order chemical kinetics mechanisms (Mech.29 and Mech.45), at an engine load of 80%. The corresponding experimental curve (Papagiannakis and Hountalas, 2003) is also included.	71
Figure 4.7: Computed traces of mean cylinder temperature using one-step chemistry and the two reduced order chemical kinetics mechanisms (Mech.29 and Mech.45), at an engine load of 80%. .	72
Figure 4.8: Horizontal and vertical planes used in visualisation of the computed fields.	72
Figure 4.9: Colour-coded contours of temperature for one-step chemistry and reduced order chemistry using mechanisms Mech.29 and Mech.45. A horizontal plane very close to the injector is considered, at selected time instants.....	75
Figure 4.10: Colour-coded contours of temperature for one-step chemistry and reduced order chemistry using mechanisms Mech.29 and Mech.45. A vertical plane including the injector is considered, at selected time instants.	77
Figure 4.11: Colour-coded contours of equivalence ratio for one-step chemistry and reduced order chemistry using mechanisms Mech.29 and Mech.45. A horizontal plane very close to the injector is considered, at selected time instants.	79
Figure 4.12: Calculated ignition delay times versus temperature for: (a) present CFD simulations using one-step chemistry and realistic chemistry with the reduced mechanisms Mech.29 and Mech.45 in the Lister LV1 engine (colour dots); (b) CFD simulations in a constant volume combustion chamber using two marine fuels with CCAI value in the upper and low limit of marine HFOs, as reported in Kontoulis, 2019; (c) chemical kinetics calculations of n-heptane (C_7H_{16}) combustion at $P=90$ bar and $\phi=1$, as reported in Weisser, 2001.	80
Figure 4.13: Computed traces of mean fuel decomposition rate using one-step chemistry and the two reduced order chemical kinetics mechanisms (Mech.29 and Mech.45), at an engine load of 80%. .	81
Figure 4.14: Colour-coded contours of fuel decomposition rate for one-step chemistry and reduced order chemistry using mechanisms Mech.29 and Mech.45. A horizontal plane very close to the injector is considered, at selected time instants.	83
Figure 4.15: Colour-coded contours of fuel decomposition rate for one-step chemistry and reduced order chemistry using mechanisms Mech.29 and Mech.45. A vertical plane including the injector is considered, at selected time instants.	85
Figure 4.16: Reaction pathways for methane consumption. The dashed lines correspond to paths active only under specific conditions (Hashemi et al., 2016).	86
Figure 4.17: Computed traces of mean OH (Hydroxyl radical) concentration using one-step chemistry and the two reduced order chemical kinetics mechanisms (Mech.29 and Mech.45), at an engine load of 80%.	87
Figure 4.18: Colour-coded contours of OH concentration for one-step chemistry and reduced order	

chemistry using mechanisms Mech.29 and Mech.45. A horizontal plane very close to the injector is considered, at selected time instants.	89
Figure 4.19: Computed traces of mean O (Oxygen radical) concentration using one-step chemistry and the two reduced order chemical kinetics mechanisms (Mech.29 and Mech.45), at an engine load of 80%.....	90
Figure 4.20: Computed traces of mean H (Hydrogen radical) concentration using one-step chemistry and the two reduced order chemical kinetics mechanisms (Mech.29 and Mech.45), at an engine load of 80%.....	90
Figure 4.21: Computed traces of mean CH ₄ (Methane) concentration using the two reduced order chemical kinetics mechanisms (Mech.29 and Mech.45), at an engine load of 80%.	91
Figure 4.22: Colour-coded contours of CH ₄ concentration for reduced order chemistry using mechanisms Mech.29 and Mech.45. A horizontal plane very close to the injector is considered, at selected time instants.	93
Figure 4.23: Computed traces of mean CH ₃ (methyl radical) concentration using the two reduced order chemical kinetics mechanisms (Mech.29 and Mech.45), at an engine load of 80%.	94
Figure 4.24: Computed traces of mean CH ₂ O (formaldehyde) concentration using the two reduced order chemical kinetics mechanisms (Mech.29 and Mech.45), at an engine load of 80%.	95
Figure 4.25: Colour-coded contours of CH ₂ O concentration for reduced order chemistry using mechanisms Mech.29 and Mech.45. A horizontal plane very close to the injector is considered, at selected time instants.	97
Figure 4.26: Computed traces of mean HCO (formyl radical) concentration using the two reduced order chemical kinetics mechanisms (Mech.29 and Mech.45), at an engine load of 80%.	98
Figure 4.27: Computed traces of mean CO (Carbon monoxide) concentration using the one-step chemistry and the two reduced order chemical kinetics mechanisms (Mech.29 and Mech.45), at an engine load of 80%.	99
Figure 4.28: Colour-coded contours of CO concentration for reduced order chemistry using mechanisms Mech.29 and Mech.45. A horizontal plane very close to the injector is considered, at selected time instants.	101
Figure 4.29: Computed traces of mean CO ₂ (Carbon dioxide) concentration using the one-step chemistry and the two reduced order chemical kinetics mechanisms (Mech.29 and Mech.45), at an engine load of 80%.	102
Figure 4.30: Colour-coded contours of CO ₂ concentration for one-step chemistry and reduced order chemistry using mechanisms Mech.29 and Mech.45. A horizontal plane very close to the injector is considered, at selected time instants.	104
Figure 4.31: Computed traces of total soot mass using the one-step chemistry, at an engine load of	

80%	105
Figure 4.32: Colour-coded contours of soot density for one-step chemistry. A horizontal plane close to the injector and a vertical plane including the injector are considered, at selected time instants.	107
Figure 4.33: Computed traces of mean NO _x (Nitrogen Oxides) concentration using the one-step chemistry and the two reduced order chemical kinetics mechanisms (Mech.29 and Mech.45), at an engine load of 80%. A measured value of final NO _x concentration is also included (Papagiannakis and Hountalas, 2003).	108
Figure 4.34: Colour-coded contours of NO _x concentration for one-step chemistry and reduced order chemistry using mechanisms Mech.29 and Mech.45. A horizontal plane very close to the injector is considered, at selected time instants.	110
Figure 4.35: Colour-coded contours of NO _x concentration for one-step chemistry and reduced order chemistry using mechanisms Mech.29 and Mech.45. A vertical plane very close to the injector is considered, at selected time instants.	112
Figure 5.1: Top and front views of the polar and cartesian grid used in the simulations of the Wärtilä 50DF engine.	116
Figure 5.2: Definition of injection direction in terms of angles α and β	117
Figure 5.3: Injection profile of the Wärtilä 50 DF for operation at a load of 100%.	118
Figure 5.4: Proportionality constant K_{bu} versus Weber number for the ETAB and CAB models. .	118
Figure 5.5: P-V diagrams calculated using one-step chemistry and the two reduced order chemical kinetics mechanisms (Mech.29 and Mech.45), at an engine load of 100%.	119
Figure 5.6: Computed traces of cylinder pressure using one-step chemistry and the two reduced order chemical kinetics mechanisms (Mech.29 and Mech.45), at an engine load of 100%. The corresponding trace from the 0-D simulation (Stoumpos et al., 2018)), as well as the maximum experimental value of pressure for an undetermined crank angle, are also included.	120
Figure 5.7: Computed traces of normalized Rate of Heat Release using one-step chemistry and the two reduced order chemical kinetics mechanisms (Mech.29 and Mech.45), at an engine load of 100%.	121
Figure 5.8: Computed traces of mean cylinder temperature using one-step chemistry and the two reduced order chemical kinetics mechanisms (Mech.29 and Mech.45), at an engine load of 100%. The corresponding burned zone trace from the 0-D simulation (Stoumpos et al., 2018) is also included.	121
Figure 5.9: Horizontal and vertical planes used in visualisation of the computed fields.	122
Figure 5.10: Colour-coded contours of temperature for one-step chemistry and reduced order	

chemistry using mechanisms Mech.29 and Mech.45. A horizontal plane very close to the injector is considered, at selected time instants.	124
Figure 5.11: Colour-coded contours of temperature for one-step chemistry and reduced order chemistry using mechanisms Mech.29 and Mech.45. A vertical plane including the injector is considered, at selected time instants.	126
Figure 5.12: Colour-coded contours of equivalence ratio for one-step chemistry and reduced order chemistry using mechanisms Mech.29 and Mech.45. A horizontal plane very close to the injector is considered, at selected time instants.	128
Figure 5.13: Calculated ignition delay times versus temperature for: (a) present CFD simulations using one-step chemistry and realistic chemistry with the reduced mechanisms Mech.29 and Mech.45 in the Wärtilä 50DF engine (colour dots); (b) CFD simulations in a constant volume combustion chamber using two marine fuels with CCAI value in the upper and low limit of marine HFOs, as reported in Kontoulis, 2019; (c) chemical kinetics calculations of n-heptane (C ₇ H ₁₆) combustion at P=90 bar and φ=1, as reported in Weisser, 2001.	129
Figure 5.14: Computed traces of mean fuel decomposition rate using one-step chemistry and the two reduced order chemical kinetics mechanisms (Mech.29 and Mech.45), at an engine load of 100%.	130
Figure 5.15: Colour-coded contours of fuel decomposition rate for one-step chemistry and reduced order chemistry using mechanisms Mech.29 and Mech.45. A horizontal plane very close to the injector is considered, at selected time instants.	132
Figure 5.16: Colour-coded contours of fuel decomposition rate for one-step chemistry and reduced order chemistry using mechanisms Mech.29 and Mech.45. A vertical plane including the injector is considered, at selected time instants.	134
Figure 5.17: Computed traces of mean OH (Hydroxyl radical) concentration using one-step chemistry and the two reduced order chemical kinetics mechanisms (Mech.29 and Mech.45), at an engine load of 100%.	135
Figure 5.18: Colour-coded contours of OH concentration for one-step chemistry and reduced order chemistry using mechanisms Mech.29 and Mech.45. A horizontal plane very close to the injector is considered, at selected time instants.	137
Figure 5.19: Computed traces of mean O (Oxygen radical) concentration using one-step chemistry and the two reduced order chemical kinetics mechanisms (Mech.29 and Mech.45), at an engine load of 100%.	138
Figure 5.20: Computed traces of mean H (Hydrogen radical) concentration using one-step chemistry and the two reduced order chemical kinetics mechanisms (Mech.29 and Mech.45), at an engine load of 100%.	138

Figure 5.21: Computed traces of mean CH ₄ (Methane) concentration using the two reduced order chemical kinetics mechanisms (Mech.29 and Mech.45), at an engine load of 100%.	139
Figure 5.22: Colour-coded contours of CH ₄ concentration for reduced order chemistry using mechanisms Mech.29 and Mech.45. A horizontal plane very close to the injector is considered, at selected time instants.	141
Figure 5.23: Computed traces of mean CH ₃ (methyl radical) concentration using the two reduced order chemical kinetics mechanisms (Mech.29 and Mech.45), at an engine load of 100%.	142
Figure 5.24: Computed traces of mean CH ₂ O (formaldehyde) concentration using the two reduced order chemical kinetics mechanisms (Mech.29 and Mech.45), at an engine load of 100%.	143
Figure 5.25: Colour-coded contours of CH ₂ O concentration for reduced order chemistry using mechanisms Mech.29 and Mech.45. A horizontal plane very close to the injector is considered, at selected time instants.	145
Figure 5.26: Computed traces of mean HCO (formyl radical) concentration using the two reduced order chemical kinetics mechanisms (Mech.29 and Mech.45), at an engine load of 100%.	146
Figure 5.27: Computed traces of mean CO (Carbon monoxide) concentration using one-step chemistry and the two reduced order chemical kinetics mechanisms (Mech.29 and Mech.45), at an engine load of 100%.	147
Figure 5.28: Colour-coded contours of CO concentration for one-step chemistry and reduced order chemistry using mechanisms Mech.29 and Mech.45. A horizontal plane very close to the injector is considered, at selected time instants.	149
Figure 5.29: Computed traces of mean CO ₂ (Carbon dioxide) concentration using one-step chemistry and the two reduced order chemical kinetics mechanisms (Mech.29 and Mech.45), at an engine load of 100%.	150
Figure 5.30: Colour-coded contours of CO ₂ concentration for one-step chemistry and reduced order chemistry using mechanisms Mech.29 and Mech.45. A horizontal plane very close to the injector is considered, at selected time instants.	152
Figure 5.31: Computed traces of mean soot mass using the one-step chemistry, at an engine load of 100%.	153
Figure 5.32: Colour-coded contours of soot density for one-step chemistry. A horizontal plane close to the injector and a vertical plane including the injector are considered, at selected time instants.	155
Figure 5.33: Computed traces of mean NO _x (Nitrogen Oxides) concentration using the one-step chemistry and the two reduced order chemical kinetics mechanisms (Mech.29 and Mech.45), at an engine load of 100%. A measured value of final NO _x concentration is also included (G. Theotokatos, private communication).	156

Figure 5.34: Colour-coded contours of NO _x concentration for one-step chemistry and reduced order chemistry using mechanisms Mech.29 and Mech.45. A horizontal plane very close to the injector is considered, at selected time instants.	158
Figure 5.35: Colour-coded contours of NO _x concentration for one-step chemistry and reduced order chemistry using mechanisms Mech.29 and Mech.45. A vertical plane very close to the injector is considered, at selected time instants.	160
Figure 6.1: Sketch of modelling approach of the present study.....	163
Figure A-1: Colour-coded contours of temperature using one-step chemistry with polar mesh for three different values of SN (Swirl Number). A horizontal plane very close to the injector is considered, at selected time instants.	178
Figure A-2: Colour-coded contours of temperature using the reduced order chemistry mechanisms Mech.45 with cartesian mesh for three different values of SN (Swirl Number). A horizontal plane very close to the injector is considered, at selected time instants.	180

List of Tables

Table 1: Regulations for NO _x emissions for slow speed marine engines ($n \leq 130$ r/min), as prescribed by Annex VI of the MARPOL convention (IMO, 2008).....	6
Table 2: Parameter values of the ignition model for n-heptane (C ₇ H ₁₆) (Weisser et al., 1998).	34
Table 3: Reactions and constants of specific rate of NO _x mechanism (Weisser, 2001).	41
Table 4: Values of soot model constants (Douladiris, 2010).	42
Table 5: Simulations in constant volume chamber: conditions of the two test cases.	45
Table 6: Features of the computational grids used in spatial resolution tests.	47
Table 7: Optimal values of the ETAB model constants, obtained for conditions corresponding to Case 1.	53
Table 8: Optimal values of the CAB model constants, obtained for conditions corresponding to Case 1 and Case 2.	54
Table 9: Main characteristics of the Lister LV1 engine.	65
Table 10: Chemical kinetics mechanisms of s n-heptane combustion.	66
Table 11: Parameters pertinent to operation and injection characteristics of the Lister LV1 engine.	68
Table 12: Main characteristics of the Wärtilä 50DF engine.	115
Table 13: Parameters pertinent to operation and injection characteristics of the Wärtilä 50DF engine.	117
Table 14: Calculated values of power for the closed part of the cycle using one-step chemistry and the two reduced order chemical kinetics mechanisms (Mech.29 and Mech.45), at an engine load of 100%. The value of Nominal Power (provided by the engine manufacturer) is also included.	119

Nomenclature

List of Abbreviations

ALE	Arbitrary Lagrangian-Eulerian (method)
AMC	Adaptive Multi-grid Chemistry
ATDC	After Top Dead Centre
BFO	Bunker Fuel Oil
CA	Crank Angle
CAB	Cascade Atomisation and drop Breakup model
CFD	Computational Fluid Dynamics
CPU	Central Processing Unit
DF	Dual Fuel
ECA	Emission Control Area
EGR	Exhaust Gas Recirculation
ERC	Engine Research Centre
ETAB	Enhanced Taylor Analogy Breakup (model)
EVC	Exhaust Valve Closing
EVO	Exhaust Valve Opening
GO	Gas Oil
HCCI	Homogeneous Charge Compression Ignition
HCT	Hydrodynamics, Chemistry and Transport
IDSD	Initial Droplet Size Distribution
IMO	International Maritime Organization
LANL	Los Alamos National Laboratory
LFO	Light Fuel Oil
NO _x	Nitric Oxides
NTUA	National University of Athens
PaSR	Partially Stirred Reactor
PCCI	Premixed Charged Compression Ignition
PGS	Pressure Gradient Scaling method
PPCI	Partially Premixed Compression Ignition
PSR	Perfectly Stirred Reactor
RNG	Re-Normalization Group (technique)
ROHR	Rate of Heat Release
SCC	Spray Combustion Chamber

SFOC	Specific Fuel Oil Consumption
SMD	Sauter Mean Diameter
SOI	Start Of Injection
SO _x	Sulphur Oxides
SN	Swirl Number
TAB	Taylor Analogy Breakup (model)
TDC	Top Dead Centre
0-D	Zero-Dimensional (model)
3-D	Three-Dimensional (model)

Main symbols

Symbol	Description
--------	-------------

Lower case latin symbols

α	Parameter of the Pressure Gradient Scaling method (PGS)
a	Convection heat transfer coefficient
a_{mr}	Stoichiometric coefficient of species m on the side of the reactants
a_i	Parameters of kinetic model in the Arrhenius relation
b_i	Temperature exponent in the Arrhenius relation
b_{mr}	stoichiometric coefficients of species m on the side of the products
$c_{p,l}$	Specific heat capacity of liquid fuel
$c_{p,vap}$	Specific heat capacity of fuel vapour
$c_{p,g}$	Specific heat capacity of the surrounding gas
c_μ	Empirical constant
d	Damping coefficient
d	Droplet diameter
d_0	Nozzle diameter
d_1	Larger diameter
d_2	Smaller diameter
d_{drop}	Drop diameter
f	Weight factor
g	Acceleration of gravity
$h_i(\Phi)$	Function of the local fuel/air equivalence ratio
k	Turbulent kinetic energy
k	Spring coefficient
k	Specific constant of the reaction
k_{fr}	Specific constants of forward reactions
k_{br}	Specific constants of the reverse reactions
k_1	Constant of breakup model (bag breakup)
k_2	Constant of breakup model (stripping breakup)
k_3	Constant of breakup model (catastrophic breakup)
m	Species
m	Droplet mass
m_{evap}	Fuel mass evaporating

m_s	Soot mass
$m_{s,f}$	Mass of soot produced
$m_{s,ox}$	Mass of oxidised soot
m_{drop}	Liquid droplet mass
$m_{f,v}$	Mass of fuel vapor
\dot{m}_{evap}	Evaporation mass flow rate
n	Constant of the model
p	Pressure of the fluid
p	Pressure
r	Ratio of the amount of products to that of total reactive species
r	Radius of the droplets
r	Droplet radius
r_d	Fuel droplet radius
r_0	Radius of the injector hole
t	Time
t_{bu}	Drop breakup time
u	Velocity of the surrounding gas
u	Vector of the velocity of the gas phase
u_o	Diffusion constant
u_0	Jet exit velocity
u_{rel}	Relative velocity between droplet and surrounding gas
v_{rel}	Relative velocity between droplet and surrounding gas
ν	kinematic viscosity
x	Displacement
y	Droplet deformation

Capital case latin symbols

A_{br}	Pre-exponential factors (backward) in the Arrhenius relation
A_f	Constant of the soot production correlation
A_{fr}	Pre-exponential factors (forward) in the Arrhenius relation
A_i	Pre-exponential factor in the Arrhenius relation
A_o	Constant
A_{ox}	Constant in the soot oxidation correlation
A_1, A_2	Constant values
B	Impact parameter

B_i	Activation temperature in the Arrhenius relation
C_α	Constant depending on nozzle design
C_{ig}	Ignition progress variable
C_λ	Model constant
C_2	Factor accounting for the mixing characteristics
D	Mass diffusion coefficient
E	Activation energy
E_{br}	Activation temperatures (backward) in the Arrhenius relation
E_{fr}	Activation temperatures (forward) in the Arrhenius relation
$E_{s,f}$	Activation energy in the soot production correlation
$E_{s,ox}$	Activation energy in the soot oxidation correlation
F	Excitation force
F^s	Rate of momentum delivery from the liquid phase to the gas phase
I	Identity matrix
I	Specific internal energy of the fluid
J	Vector of heat flow
K_{bu}	Proportionality constant
N	Engine revolution speed
$N_{(t)}$	Droplet population
Nu	Nusselt number
Pr	Prandtl number
Q_{chem}	Total chemical energy of the injected fuel
\dot{Q}^c	Source term due to chemistry
\dot{Q}^s	Source term due to liquid phase evaporation
\dot{Q}_{drop}	Total heat flux from hot gas to the liquid droplet
$\dot{Q}_{heating}$	The thermal power for the heat-up of the liquid droplet
\dot{Q}_{evap}	Thermal power for evaporation of the fuel mass flux
R	Specific gas constant
Re	Reynolds number
Re_{coll}	Collision Reynolds number
Sc	Schmidt number
T	Inverse matrix of the velocity gradient ($\nabla \mathbf{u}$)
T	Local temperature

T	Regional temperature
T_{drop}	Liquid droplet temperature
T_g	Temperature of surrounding gas
T_R	Temperature of liquid droplet
W_m	Molecular weight of the species m
We	Weber number
$We_{b,s}$	Weber transition number between bag and stripping regions
We_{coll}	Collision Weber number
We_{crit}	Critical Weber number
$We_{s,c}$	Weber transition number between stripping and catastrophic regimes
We_t	Weber transition number
X	Projection of the distance between the droplet centres
X_m	Mole of species m
$Y_{f,\infty}$	Fuel vapor mass fraction in the far field
$Y_{f,R}$	Fuel vapor mass fraction at droplet surface
Y_i	Instantaneous concentration
Y_i^{eq}	Equilibrium concentration
Y_m	Mass fraction of species m

Lower case greek symbols

δ_{m1}	Dirac function
ε	Dissipation rate
ζ_{fr}	Temperature exponents (forward) in the Arrhenius relation
ζ_{br}	Temperature exponents (backward) in the Arrhenius relation
θ	Initial spray cone angle
λ	Second viscosity coefficient of the fluid
λ_g	Thermal conductivity of gas phase
μ	Dynamic viscosity of the fluid
μ_{air}	Viscosity of air
μ_g	Dynamic viscosity of the surrounding gas
μ_l	Fuel dynamic viscosity
ρ	Density of the mixture
ρ	Density of the surrounding gas
ρ_g	Density of surrounding gas

ρ_l	Fuel density
ρ_m	Density of the species m
$\dot{\rho}_m^c$	Source term due to chemical reactions
$\dot{\rho}^s$	Source term due to spray evaporation
σ	Stress tensor
σ	Fuel surface tension
τ	Overall ignition characteristic time
τ_c	Characteristic time scale of combustion
τ_{lam}	Chemical time scale
τ_{turb}	Turbulent time scale
τ_1	Low temperature regime of ignition
τ_2	Medium temperature regime of ignition
τ_3	High temperature regime of ignition
ω	Drop oscillation frequency
ω_{swirl}	Angular velocity of air flow
ω_{engine}	Angular velocity of engine revolution
$\dot{\omega}_m$	Molecular rates of production of each species, m
$\dot{\omega}_r$	Reaction rate
ζ	Dimensionless correction factor
$\hat{\alpha}$	Horizontal angle
$\hat{\beta}$	Vertical angle

Capital case greek symbols

Δ	Droplet diameter ratio
Δh_{evap}	Enthalpy of evaporation
$(\Delta h_f^0)_m$	Enthalpy of formation of the species m
Φ	Fuel/air equivalence ratio

1.Introduction

The study of flow and combustion of marine engines has been substantially supported in the last decades by Computational Fluid Dynamics (CFD). The accurate representation of marine engine aerothermochemistry is a complex task, requiring modelling of different physical processes, namely: (a) turbulence of the gas phase flow, (b) primary and secondary decomposition of the fuel spray, (c) combustion (involving chemical kinetics and turbulence - chemistry interaction), (d) heat transfer. Given the progress in computational power, incorporation of realistic chemistry in engine CFD studies (essential for a more accurate characterisation of combustion) now appears a realistic goal, and attracts the attention of the international engine research community.

Common practice in engine CFD has been the use of a global reaction approach (one-step reaction of fuel with oxygen), which is computationally efficient, associated with reduced CPU time. Evidently, the approach cannot account for the essentials in the evolution of combustion chemistry, and the associated formation and destruction of important species, such as the carbon monoxide (CO) and important radicals. Further, this may affect the temporal evolution of important global parameters, as the Rate of Heat Release and pressure. Using realistic chemistry is thus essential; nonetheless detailed kinetics mechanisms can still not be incorporated in engine CFD simulations, due to the excessive increase in computational cost. Accurate reduced kinetic mechanisms are therefore needed.

1.1 Marine Engines

Diesel engines consist the most common type of propulsion system of merchant ships. The term 'Diesel engine' refers to the self-igniting combustion piston engine, invented by Rudolf Diesel in 1892. Its main feature is the fuel self-ignition, due to the high temperature achieved by the compression of air in the combustion chamber (Heywood, 1988). Diesel engines have dominated marine applications over steam turbines and gas turbines, due to their high efficiency, as well as their ability to burn very poor quality fuels.

Both two- and four-stroke Diesel engines are used as ship prime movers, and their main differences can be summarised as follows:

- Two-stroke marine engines operate at low rotational speed (in the range of $60 \div 200$ rpm), have relatively lower fuel consumption (≈ 170 g/kWh), and are connected directly to the engine shaft (without the presence of a gearbox). In comparison to four-stroke engines, they have more weight (and volume), and are characterised by significantly lower maintenance costs. They extend to a very high power range, and are generally connected to Fixed Pitch Propellers. They mainly serve as prime movers of large commercial seagoing vessels, such as bulk carriers, tankers and container ships.
- Four-stroke marine engines operate at medium rotational speeds ($300 \div 1000$ rpm), have a fuel consumption of about 185 g/kWh or higher, and are capable of operating with the same (low quality) marine fuel as the (low speed) two-stroke engines. Four-stroke marine engines are connected to the shaft via a gearbox and clutch, and are in many cases coupled to Controllable Pitch Propellers. They commonly operate in a power range lower to the one of two-stroke marine engines.

At present, few manufacturers produce marine Diesel engines for seagoing ships. Figures 1.1 and 1.2 present the main families of low-speed Diesel engines manufactured by MAN and Wärtilä (now: Winterthur Gas and Diesel – WinGD), in a speed – power domain.

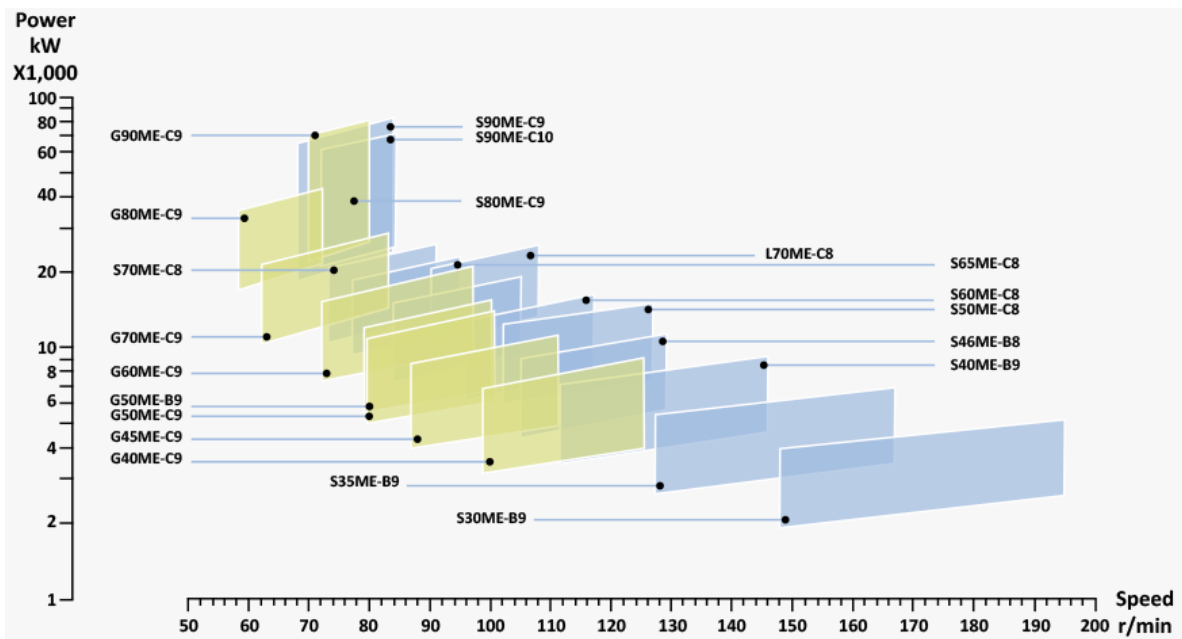


Figure 1.1 Speed-power range of main families of two-stroke marine Diesel engines manufactured by MAN (Marine Engines and Systems, MAN, 2017).

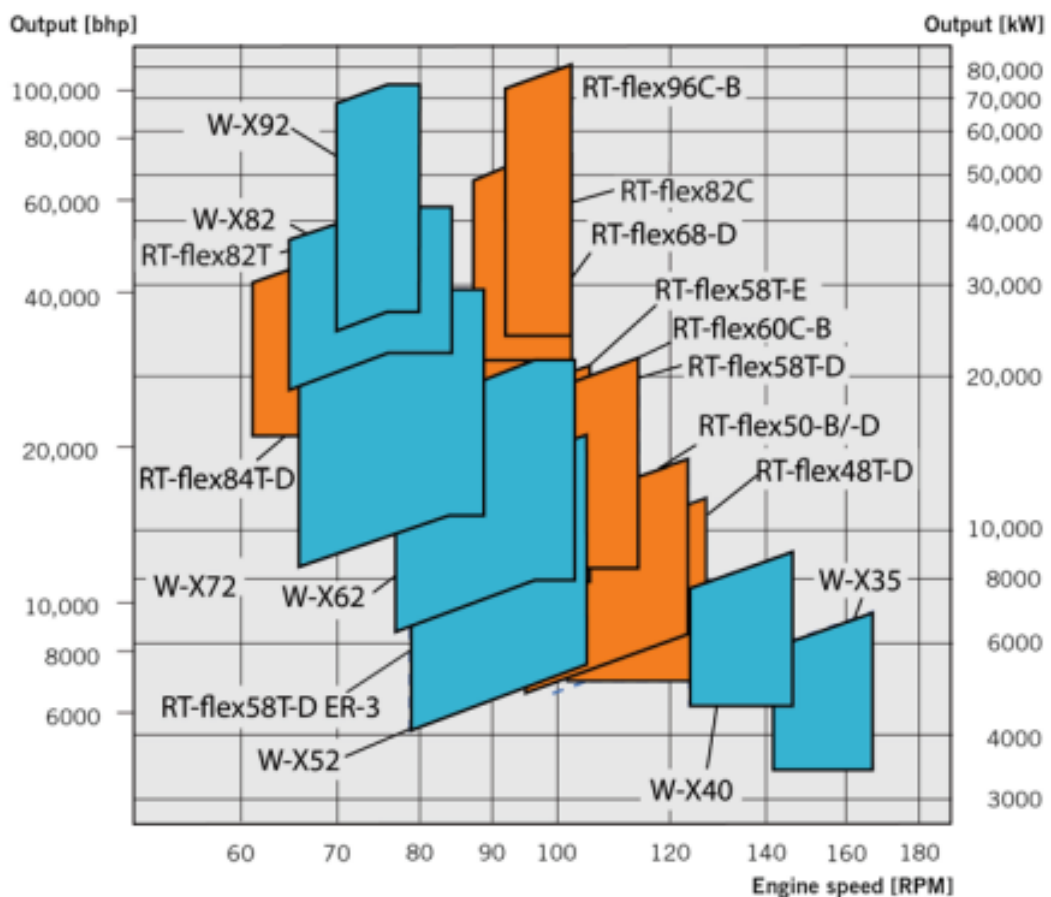


Figure 1.2: Speed-power range of main families of two-stroke marine Diesel engines manufactured by Wärtilä (now: Winterthur Gas and Diesel – WinGD) (Spahni and Kyratos, 2014).

Dual-fuel marine engines can operate both in the Diesel mode and in the gas mode; they have an increasing penetration in the maritime sector for more than a decade, mainly using LNG for gas mode operation. Depending on the stage in which LNG is introduced in the combustion chamber, dual-fuel

engines are categorised as: (a) low-pressure gas admission engines, operating under the Otto cycle, (b) high-pressure gas admission engines, operating under the Diesel cycle. The use of LNG results in a potential reduction of CO₂ emissions of 25%. Low-pressure gas admission engines are characterised by the presence of a premixed flame, which contributes to a substantial reduction of NO_x emissions; nonetheless, a narrow window in air-fuel ratio (λ) constrains stable operation, due to presence of knock (low range of λ) and misfire (high range of λ) (Weisser, 2013, Wärtilä, 2009).

1.2 Marine Engine Emissions and Regulations

Emission regulations have been a main driving force of marine engine development in the past two decades. The International Maritime Organization (IMO) and several national institutions have imposed strict standards for pollutant emissions from ships. A set of regulations pertinent to nitric oxides (NO_x) and sulphur oxides (SO_x) emitted from ships was adopted in 1997, and is outlined in Annex VI of the MARPOL Convention. These emission regulations came into force in 2005, and were modified in 2008 (IMO, 2008). The limits in NO_x emissions are set for marine engines as a function of their operating speed. NO_x standards Tier I and Tier II have set global limits, while Tier III standards apply only within specific areas (Emission Control Areas - ECAs). Figure 1.2 presents the existing ECAs, as well as possible future ones.

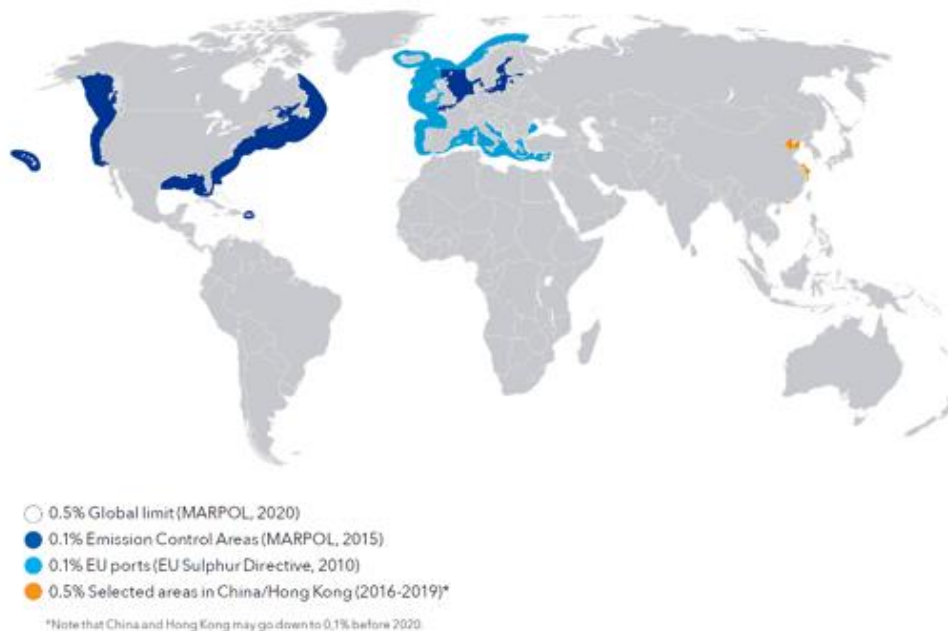


Figure 1.3: Map of existing and possible future ECAs (Det Norske Veritas (DNV). 2018. Maritime Forecast to 2050).

In more detail, the limits in NO_x emissions for slow-speed marine engines ($n \leq 130$ rpm) are 14.4 g/kWh globally (Tier II) and 3.4 g/kWh within the ECAs (Tier III). The drastic reduction in NO_x from Tier II to Tier III has resulted in drastic changes in marine engine design, which include Exhaust Gas Recirculation (EGR) and emissions aftertreatment. As indicated in Table 1, the reduction introduced by Tier III (effective since January 2016, for NO_x ECAs) is about 75% with respect to Tier III.

Table 1: Regulations for NO_x emissions for slow speed marine engines ($n \leq 130$ r/min), as prescribed by Annex VI of the MARPOL convention (IMO, 2008).

Tier	Engine construction date (on or after)	Total weighted cycle emission limit (g/kWh) n=engine rated speed (rpm)
		n < 130
I	January 2000	17.0
II	January 2011	14.4
III	January 2016	3.4

Regarding SO_x emission standards, it is noted that they are set indirectly, by specifying the fuel sulphur mass content; a global limit of 3.5% in sulphur content held until Dec. 31 2020, and was reduced to 0.5% subsequently. A limit of 0.1% has been imposed within the ECAs since 2015. No regulations for soot particles have yet been imposed. With respect to the fuel sulphur content, the prescribed limits, both global and ECA ones, are presented in Figure 1.3 (IMO, 2008).

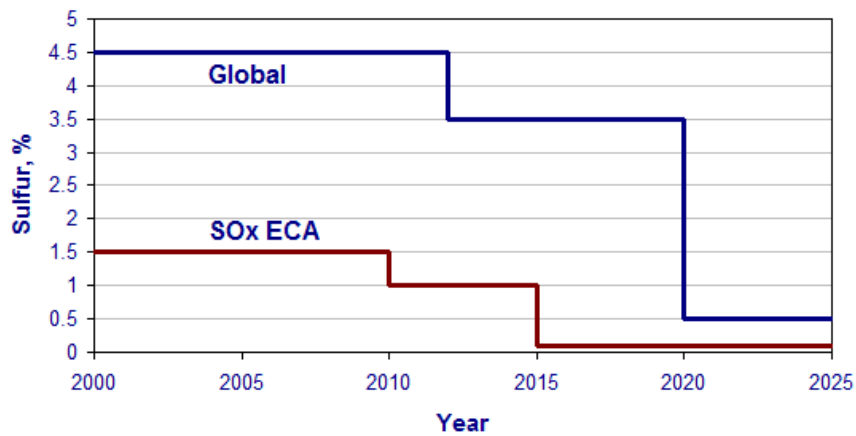


Figure 1.4: Fuel sulphur content limits (www.imo.org).

1.3 Literature Review of Marine Engine Aerothermochemistry

This section contains a literature review of research on the spray breakup, ignition and combustion pertinent to constant volume combustion chambers, research engines, as well as marine engines.

1.3.1 Experimental Studies

1.3.1.1 Combustion Chambers and Research Engines

Many years of past and ongoing experimental investigations contribute to our understanding of diesel spray breakup processes. A selection of important representative works is highlighted next.

Hult and Mayer (2013) and Hult et al. (2014) implemented constant volume combustion chamber experiments of sprays, for conditions relevant to large marine engines. Optical access to the combustion chamber has utilised 24 optical ports with clear diameters of 40 mm. Fuel injection was visualised based on laser Mie scattering imaging of fuel spray structures, giving quantitative information regarding the liquid penetration and spray cone angle.

Taylor and Walsham (1969) studied the fuel-spray formation and penetration based on a constant volume chamber, with the goal of understanding and improving combustion of medium-speed Diesel engines. The experiments of Fink et al. (2008), performed in a constant volume combustion chamber, for conditions relevant to medium speed marine engines, have shown that, changing of the fuel type (from diesel fuel to heavy fuel oil (HFO) or fuel-water emulsion), affects the spray structure and dynamics, as well as the reactive flow emissions.

Prescher et al. (1999) performed spray experiments in a high-pressure chamber, in order to study the effects of fuel type, as well as its temperature and injection pressure. The results have verified a higher penetration for HFO, associated with longer and taller (decreased spray cone angle) sprays; the findings were mainly attributed to the higher kinematic viscosity of HFO, resulting in increased droplet diameters. Further, the role of low evaporation rates, caused by the low proportion of light components in the fuel, resulting in a lower vapor volume in comparison to diesel fuel sprays, was highlighted.

Experimental investigations into smaller engines with similar operating conditions include the study of Lacoste et al. (2003) in a single-cylinder two-stroke engine, using the Phase Doppler Anemometry (PDA). They verified that the increase in cylinder pressure decreased droplet velocities, whereas increasing the injection and cylinder pressures enhanced spray atomisation.

Schneider (2003) performed experiments in a constant volume spray chamber under evaporating and non-evaporating conditions, in a wide range of operating parameters, including injection pressure, gas density and temperature, orifice diameter and orifice diameter-to-length ratio, using a shadowgraph imaging technique and PDA. Spray penetration and spray angles were quantified from the analysis of shadowgraph spray images. PDA was also used to characterise droplet velocities and diameters; results were processed to improve an empirical spray tip penetration model. This work was complemented by experiments by Schneider et al. (2020) for reactive spray flow.

Naber and Siebers (1996) analysed their experimental results in a constant volume combustion chamber, focusing on the effects of ambient gas density on fuel vaporization, as well as on spray penetration and fuel dispersion. This study demonstrated that the ambient gas density has a pronounced effect on spray penetration, and a smaller one on fuel dispersion. Vaporization resulted in reduced penetration and dispersion, in comparison to non-vaporizing sprays, while the influence of vaporization declined with rising gas density.

Developing spray models from experimental spray results has been an active research field for several decades. Among the early works, Dent (1971) analysed experimental results in spray chambers operating at low or high temperature, in order to derive a formula for spray penetration, and to demonstrate the differences between the different temperature regimes. Hiroyasu and Arai (1990) analysed the experimental results of high-speed injection into a high-pressure chamber, in order to characterise and explain the spray breakup mechanism and internal spray structure, and to quantify spray penetration, spray angle and Sauter Mean Diameter. A spray propagation model was contributed by Najar et al. (2014), applicable to large and medium sized engines, which accounts for hydraulic effects within the nozzle. The model has the benefit of reflecting the dynamic hydraulic effects, especially during the opening and closing of injection valve, including the effects of pressure waves on the instantaneous injection rate.

Experiments pertinent to large two-stroke marine engine applications include the ones of Schmid et al. (2014) in a large-scale optically accessible 'Spray Combustion Chamber' (SCC) test facility, using different fuel qualities. Further, von Rotz et al. (2015) performed non-reactive spray experiments in the same facility, to characterise spray structure, as well as mixture formation. For different fuel qualities, they reported results for different injection pressures, chamber pressures, nozzle diameters, including spray-swirl interaction. Subsequently, Rotz et al. (2016) complemented the above study with reactive flow experiments. The results of the two studies present important information regarding the effects of fuel quality (distillate fuel – LFO or residual fuel oil - HFO) on spray morphology, droplet size, tip penetration, evaporation rate and ignition delay, including the effects of air swirl intensity.

1.3.1.2 Engines

Spray research pertinent to engine applications is extensive. However, few studies have addressed marine engines, especially with respect to using HFO or other residual fuels. Takasaki et al. (1999) have presented a comparison between reactive spray flow for using Gas Oil (GO) and Bunker Fuel Oil (BFO). Based on experimental results in a four-stroke Diesel engine, including spray visualisation, they found that use of BFO contributes to a larger liquid core and longer ignition delay, as well as to a significant increase of particulate emissions. Further, BFO sprays were characterised by a less homogeneous fuel distribution, in comparison to GO sprays.

Imhof and Takasaki (2012) performed reactive flow experiments in an optically accessible Rapid Compression Machine (RCM) (of a size representative of marine engine dimensions) using Light Fuel Oil (LFO). Their results show that, by implementing proper injection strategies, problems of LFO associated with increased ignition delay and resulting near-wall combustion can be resolved.

Experimental studies of direct relevance to the present thesis include the ones of Papagiannakis and Hountalas (2003, 2004), performed in a single-cylinder four-stroke dual fuel engine (Lister LV1). Their results include operation in both the diesel mode and the gas mode; in the latter case, natural gas is used as fuel, with a pilot amount of diesel fuel used as an ignition source. Experimental results are accompanied by computational results, based on thermodynamic modelling. This engine is used as a basis for the CFD studies of Chapter 4 of the present thesis.

Thermodynamic modelling of dual fuel engine operation includes Liu and Karim (1997), who developed a multi-zone model with a double Wiebe function, accounting for the combustion of pilot and gas fuel. A detailed thermodynamic model for a large four-stroke marine dual fuel engine was presented by Stoumpos et al. (2018), utilising a single- or a multi-Wiebe function for operation in the diesel mode and gas mode, respectively, and a Woschni heat transfer model.

A novel optically accessible engine test facility (Flex-OeCoS) was used by Wüthrich et al. (2020) and Humair et al. (2020) to investigate dual fuel for multi-mode combustion process. Their results refer to ignition delay and location, heat release, soot emissions, as well as combustion stability.

1.3.2 CFD Studies

The present section considers published Computational Fluid Dynamics (CFD) results relevant for marine engine operation. First studies include Nakagawa et al. (1990), for a constant volume combustion chamber. Rodatz et al. (2000) performed CFD studies in a two-stroke common rail marine Diesel engine operating with HFO, using a KIVA-3 code, calculating pressure and heat release traces, as well as NO_x emissions, and referred their results to experimental data. Kontoulis et al. (2014, 2018, 2019) developed a detailed general model of HFO thermophysical properties, and validated it against experiments of non-reactive and reactive spray flow in a large 'Spray Constant Volume Combustion Chamber' (von Rotz, 2015); first simulations in a two-stroke marine engine operating with HFO were also presented in Kontoulis et al. (2019). These CFD studies have used an adapted version of the Cascade Atomisation and droplet Breakup (CAB) spray breakup model (Tanner, 2004). For the same experimental apparatus, particular effects related to the impact of nozzle diameter were addressed in the CFD study of Bolla et al. (2014), in which results of lift-off length and flame evolution are reported. Earlier work regarding the same chamber includes Hensel et al. (2012).

Spray modelling studies of relevance to the present thesis date back to the work of Tanner (1997), who introduced the Enhanced Taylor Analogy Breakup (ETAB) model. ETAB adopts the droplet deformation dynamics introduced in the standard TAB model (O'Rourke and Amsden, 1987), and proposes an improved description of the generation of new droplets after a drop breakup. Tanner (1997) tested ETAB for non-evaporating solid-cone fuel sprays in a constant volume chamber under Diesel engine conditions. Further, Tanner and Weisser (1998) modified this model to account for a proper drop size distribution in the near-nozzle region. Furthermore, Tanner (2004) extended the model in terms of drop size distribution in the catastrophic breakup regime, both for non-evaporating, evaporating and reactive sprays; the resulting model (Cascade Atomisation and drop Breakup – CAB) is thus more prominent in comparison to ETAB. Spray simulations for a constant volume chamber using ETAB are reported in Pizza et al. (2007), where model constants are calibrated in terms of the experimental results of Nakagawa et al. (1990) and Scheider (2003).

Modelling of ignition in the frame of CFD studies has followed different approaches. An interesting one, adopted in the present thesis for one-step chemistry calculations, has been introduced by Weisser et al. (1998), in terms of solving a transport equation for an ignition progress variable. This variable is defined in terms of the concentration of an intermediate species normalized by a critical value, and signals ignition when exceeding a threshold value. The model has been validated against a detailed n-heptane mechanism (Weisser, 2001).

In one-step chemistry calculations, combustion modelling, yielding the local (and global)

instantaneous heat release rate, is essential. A widely accepted model, adopted in the present thesis, is the one of Kong et al. (1995). The model considers a characteristic time of combustion, considering the superposition of a laminar (chemical) time scale and turbulent time scale accounting for turbulent mixing.

CFD studies in marine engines using one-step chemistry, of relevance to the present study, include Andreadis et al. (2011) and Stratsianis et al. (2016). Both refer to two-stroke marine Diesel engines, and address the problem of optimising engine performance and emissions by means of split injection. In both studies, the above mentioned physical models have been used, i.e., ETAB for spray breakup, ignition progress variable for ignition modelling, and characteristic time model for combustion modelling. The same modelling framework was used in Pananakis et al. (2013), to optimise operation of a two-stroke marine engine by means of twin-needle injectors and split injection, thus implementing Partially Premixed Compression Ignition (PPCI).

Similar to the progress of engine CFD codes, the detailed chemistry coupling with CFD has evolved in the same fashion progressing from simplified, single-zone, zero-dimensional models to more realistic physical and chemical sub-models in three dimensions. Nevertheless, the numerical study of the detailed chemical kinetics with CFD is computationally expensive due to the extended size of the reaction mechanism.

Engine CFD literature studies using more detailed chemistry concern small (automotive) engines, and mainly focus on Homogeneous Charge Compression Ignition (HCCI) engines. Aceves et al. (2000, 2001) implemented the detailed chemistry solver HCT (Hydrodynamics, Chemistry and Transport) to the CFD code KIVA-3V, and applied the computational tool developed to investigate combustion in the HCCI automotive Volvo TD 100 Diesel engine. These studies have considered 10 zones, to account for combustion chemistry, described in terms of a scheme including 179 chemical species and 1125 elementary reactions for natural gas and propane (Aceves et al., 2000, 2001), and 859 species and 3606 chemical reactions for iso-octane (Aceves et al., 2001). A more detailed CFD approach, accounting for detailed chemistry in all computational cells, was followed by the Wisconsin research team in Kong and Reitz (2002) and Kong et al. (2001), using a computational tool developed by coupling the KIVA-3V CFD code with the CHEMKIN-II kinetics code (Kee et al., 1989). In these studies, a Perfectly Stirred Reactor (PSR) modelling accounts for chemistry in each computational cell, corrected using a turbulent timescale to account for micro-mixing, along the lines of the characteristic time combustion model. The approach was applied to a single-cylinder engine, Caterpillar Scote, operating in the HCCI mode with different levels of Exhaust Gas Recirculation (EGR), using an n-heptane mechanism consisting of 40 species and 165 reactions. Kong and Reitz (2003) applied a similar modelling approach to simulate HCCI combustion in the single-cylinder

Cummins C engine, using an iso-octane reaction mechanism.

Other engine CFD studies with realistic chemistry include Mazi (2009), who used a combined KIVA-4 – CHEMKIN tool to investigate combustion in an automotive HCCI engine; chemistry was accounted for in terms of an n-heptane mechanism, with 29 species and 52 elementary reactions (Patel et al. 2004). For an RCCI operation mode, Kakaee, et al. (2015) used a coupled KIVA-3V - CHEMKIN tool, representing combustion chemistry by means of an n-heptane mechanism consisting of 45 species and 142 reactions, extended for NO_x chemistry (Ra and Reitz, 2008). Using a coupled KIVA-3V – CHEMKIN code, Maghbouli et al. (2013) studied combustion in a medium duty dual fuel engine, in both the diesel and gas mode, using an assembled reduced n-heptane – methane mechanism. Pang et al. (2016) used the STAR-CCM+ CFD code to simulate the two-stroke marine Diesel engine MAN Diesel & Turbo 4T50ME-X, using an n-heptane kinetics mechanism with 30 species and 68 reactions, extended for soot chemistry. This work was extended in Pang et al. (2017) to account for the chemistry of sulphur oxides (SO_x) formation, in terms of a small number of elementary reactions. Similar approaches include Hong et al. (2008), as well as the work of Golovitchev and co-workers (Golovitchev et al., 2000, Golovitchev and Nordin, 2001), which consider a Partially-Stirred Reactor (PaSR) in each computational cell.

In summary, the vast majority of works implementing realistic chemistry has considered small automotive engines, and accounted for chemistry by means of relatively small kinetic schemes. The extension of the approach to marine engines is not straight-forward, and the present thesis is among the first efforts undertaken.

Attempts to increase the computational efficiency of CFD engines studies with realistic chemistry include Perini et al. (2014), who integrated a KIVA-based code with a sparse analytical Jacobian chemistry solver (SpeedCHEM) in a parallel code, applied it to different engine combustion modes with multi-component fuels. Shi et al. (2009) built on the model of Babajimopoulos et al. (2005) and implemented an Adaptive Multi-grid Chemistry (AMC) model (semi-tabulated chemistry approach), to simulate HCCI and Diesel engine combustion with realistic chemistry (see Figure 1.5). The approach uses an integrated KIVA-CHEMKIN tool, and, for HCCI engines, yields an increase in computational efficiency, with respect to ‘standard’ CFD simulations with realistic chemistry, by a factor of 10. Other attempts to increase computational efficiency include the work of Liang et al. (2007), who improved a non-interaction semi-implicit method, and applied it to the simulation of the Caterpillar 3401E single-cylinder engine, for operation in the diesel mode.

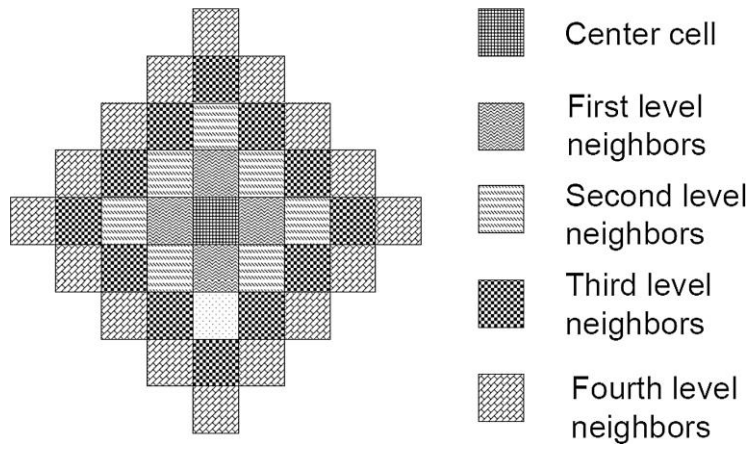


Figure 1. 5: Adaptive multi-grid in a 2D mesh (Shi et al., 2009).

1.4 Research Gap, Aim and Research Objectives of the present thesis

As illustrated in section 1.3, the studies reported in the open literature regarding spray and mixture formation and ignition/combustion in marine engines are not extensive. Moreover, there is very limited information regarding combustion chemistry in marine engines. The present thesis thus aims to substantially improve the description and understanding of combustion chemistry in four-stroke marine engine applications. Here, a main contribution consists in implementing detailed chemistry to the study of four-stroke marine engine combustion, for the first time to the author's knowledge, with the goal of providing an improved understanding of combustion. To this end, the Computational Fluid Dynamics code KIVA-3vr2 is coupled with the chemical kinetics code CHEMKIN-II.

To achieve the main objective of characterising and understanding marine engine combustion, a systematic approach is followed, consisting in: (a) Characterising spray dynamics in a constant volume chamber. (b) Adapting a tool developed by means of coupling the chemical kinetics CHEMKIN-II code with the KIVA-3vr2 CFD code, thus enabling CFD simulations with reliable chemistry. (c) Performing CFD simulations of flow and combustion with detailed chemistry in two four-stroke engines, and comparing results against one-step chemistry simulations, as well as against experimental data. Thus, to the author's knowledge, the present thesis reports the first CFD studies in marine engines operating in the diesel mode, including realistic combustion chemistry.

In the present study, two versions of the KIVA-3vr2 CFD code (Amsden, 1999), in Fortran77, have been used and further developed: (i) An one-step chemistry code, in which the following physical models were implemented: (a) the CAB spray model (Tanner, 2004), (b) the Weisser et al. ignition model (Weisser et al., 1998), (c) the Kong et al. characteristic time combustion model (Kong et al. (1995)). (ii) A coupled KIVA-CHEMKIN code. It builds on initial development by Reitz et al. (<https://erc.wisc.edu/>) tested for HCCI engine applications, and further development by the NTUA research group of Prof. L. Kaiktsis, and tested for two-stroke marine Diesel engine applications (Galetakis, 2019). The adaptations in the course of the present thesis consist in: (1) developing grids and identifying grid quality that is appropriate for the coupled code and the present applications, and (2) implementing the two reduced chemical kinetics mechanisms used in the present study (Patel et al. 2004, and Ra and Reitz, 2008).

To achieve the main objective of characterising and understanding marine engine combustion, a systematic approach is followed, consisting in: (a) Characterising spray dynamics in a constant volume chamber, and in adapting the Cascade Atomisation Breakup (CAB) spray model, for conditions relevant to operation of the engines considered in the present study. (b) Adapting a tool developed by means of coupling the chemical kinetics CHEMKIN-II code with the KIVA-3vr2 CFD

code, thus enabling CFD simulations with reliable chemistry. (c) Performing CFD simulations of flow and combustion in the two engines, for operation at 80% load for Lister LV1, and in the full load range for Wärtilä 50DF, and comparing results against one-step chemistry simulations, as well as against experimental data. Thus, to the author's knowledge, the present thesis reports the first CFD studies in four-stroke marine engines operating in the diesel mode with realistic combustion chemistry. Finally, it is noted that that the CPU requirements differ for the two approaches considered, and are in all cases higher for the Wärtilä 50DF calculations. For this engine, indicative CPU times on a desktop processor are about 6 hours for one-step chemistry, one week for calculations using realistic chemistry in terms of the 29 species mechanism, and four weeks for the 45 species mechanism.

2. CFD modelling

The present thesis studies the flow and combustion phenomena taking place in four-stroke engines by means of CFD. The accurate representation of marine engine aerothermochemistry is a challenging task, as it involves physical modelling of different processes: (a) turbulence in the gas phase, (b) fuel spray (two-phase) flow (primary and secondary breakup, evaporation, collisions), (c) combustion chemistry, and (d) turbulence-chemistry interactions. This Chapter presents the governing equations and physical models used in this thesis.

2.1 Fundamentals – Governing Equations

The conservation equations in differential form are the following (Stiesch, 2003, Amsden et al., 1989):

Conservation equation of mass of each chemical species, m:

$$\frac{\partial \rho_m}{\partial t} + \nabla \cdot (\rho_m \cdot u) = \nabla \cdot \left[\rho D \nabla \left(\frac{\rho_m}{\rho} \right) \right] + \dot{\rho}_m^c + \dot{\rho}^s \delta_{m1} \quad (2.1)$$

where, ρ_m is the density of species m , ρ is the density of the mixture, and u is the velocity vector of the gas phase. The mass diffusion coefficient, D , is defined in equation (2.10), while the calculation of the source term $\dot{\rho}_m^c$ due to chemical reactions is explained in a following section (see section 2.6.1). The source term $\dot{\rho}^s$ account for spray evaporation (Amsden et al., 1989). Species 1 accounts for the fuel; thus, the term δ_{m1} is a Dirac function, taking a value of 1 for $m=1$, and a value of 0 for all other chemical species.

Based on formula (2.1) the equation of continuity is obtained:

$$\frac{\partial \rho}{\partial t} + \nabla \cdot (\rho u) = \dot{\rho}^s \quad (2.2)$$

Momentum conservation equation:

$$\frac{\partial (\rho u)}{\partial t} + \nabla \cdot (\rho u u) = -\frac{1}{a^2} \nabla p - A_o \nabla \left(\frac{2}{3} \rho k \right) + \nabla \cdot \sigma + F^s + \rho g \quad (2.3)$$

where, p is the pressure of the fluid. The dimensionless value a is a parameter of the Pressure Gradient Scaling method (PGS), commonly taking a value of 1 for engine applications (Amsden et al., 1989). The constant A_o takes the value 0 for laminar flow and 1 for turbulent flow. For turbulence modelling, the KIVA code uses the k- ϵ model (Amsden, 1989) or the RNG k- ϵ model (Amsden, 1997); the latter

has been selected in the present study. The value of F^s correspond to the rate of momentum delivery from the liquid phase (spray) to the gas phase (Amsden et al., 1989). The acceleration of gravity is considered constant, and is denoted by g .

Finally, σ accounts for the stress tensor.

$$\sigma = \begin{pmatrix} \sigma_{xx} & \tau_{xy} & \tau_{xz} \\ \tau_{yx} & \sigma_{yy} & \tau_{yz} \\ \tau_{zx} & \tau_{zy} & \sigma_{zz} \end{pmatrix} \quad (2.4)$$

which is calculated by the following equation:

$$\sigma = \mu[\nabla \mathbf{u} + (\nabla \mathbf{u})^T] + \lambda \nabla \cdot \mathbf{u} \mathbf{I} \quad (2.5)$$

The identity matrix is symbolized by \mathbf{I} , while the T operator denotes the inverse matrix of the velocity gradient ($\nabla \mathbf{u}$).

By expressing the shear stresses in terms of the velocity gradients and substituting in relation (2.4), the stress tensor σ is obtained in the following form:

$$\sigma = \mu \cdot \begin{pmatrix} 2 \frac{\partial u}{\partial x} & \frac{\partial u}{\partial y} + \frac{\partial v}{\partial x} & \frac{\partial u}{\partial z} + \frac{\partial w}{\partial x} \\ \frac{\partial u}{\partial y} + \frac{\partial v}{\partial x} & 2 \frac{\partial v}{\partial y} & \frac{\partial v}{\partial z} + \frac{\partial w}{\partial y} \\ \frac{\partial u}{\partial z} + \frac{\partial w}{\partial x} & \frac{\partial v}{\partial z} + \frac{\partial w}{\partial y} & 2 \frac{\partial w}{\partial z} \end{pmatrix} + \lambda \cdot \begin{pmatrix} \frac{\partial u}{\partial x} + \frac{\partial v}{\partial y} + \frac{\partial w}{\partial z} & 0 & 0 \\ 0 & \frac{\partial u}{\partial x} + \frac{\partial v}{\partial y} + \frac{\partial w}{\partial z} & 0 \\ 0 & 0 & \frac{\partial u}{\partial x} + \frac{\partial v}{\partial y} + \frac{\partial w}{\partial z} \end{pmatrix} \quad (2.6)$$

Where, μ denotes the dynamic viscosity of the fluid, calculated based on the following relation, which accounts for both laminar and turbulent flow:

$$\mu = (1 - A_o) \cdot \rho u_o + \mu_{air} + A_o \cdot c_\mu \frac{k^2}{\varepsilon} \quad (2.7)$$

The second viscosity coefficient λ of the fluid is related to the dynamic viscosity through the following relation (Stokes assumption):

$$\lambda = -\frac{2}{3} \cdot \mu \text{ (turbulent flow)} \quad (2.8)$$

The diffusion constant u_o is an input CFD parameter, while the empirical constant c_μ takes the value 0.09.

The viscosity of air μ_{air} is given by the equation:

$$\mu_{air} = \frac{A_1 \cdot T^{\frac{3}{2}}}{T + A_2} \quad (2.9)$$

where A_1 and A_2 are constants.

The mass diffusion constant D is given by the equation:

$$D = \frac{\mu}{\rho \cdot Sc} \quad (2.10)$$

The dimensionless Schmidt number is an input parameter of the KIVA code and defined as the ratio of the kinematic viscosity to the mass diffusion coefficient:

$$Sc = \frac{\nu}{D} \quad (2.11)$$

Energy conservation equation:

$$\frac{\partial(\rho I)}{\partial t} + \nabla \cdot (\rho u I) = -p \nabla \cdot u + (1 - A_o) \sigma: \nabla \cdot u - \nabla \cdot J + A_o \rho \varepsilon + \dot{Q}^c + \dot{Q}^s \quad (2.12)$$

where, I denotes the specific internal energy of the fluid, without taking into account the contribution of heat from each single reaction. The vector of heat flow J results as the sum of heat transfer due to conduction and the heat transfer due to the mass diffusion of the chemical compounds (each species m has enthalpy h_m).

The source term \dot{Q}^s accounts for the contribution of liquid phase (spray) evaporation, while the source term \dot{Q}^c quantifies the contribution of chemistry (Amsden et al., 1989).

The k- ε RNG turbulence model comprises two partial differential equations for the turbulent kinetic energy (per unit mass) and its dissipation rate.

Source terms \dot{Q}^c and $\dot{\rho}_m^c$ due to chemical reactions

A chemical reaction can be written in the following generalised form:



where, X_m denotes one mole of species m and a_{mr} and b_{mr} denote the stoichiometric coefficients of species m on the side of the reactants and products, respectively, for reaction r .

The reaction rate, $\dot{\omega}_r$, is calculated as follows:

$$\dot{\omega}_r = k_{fr} \prod_m \left(\frac{\rho_m}{W_m} \right)^{a_{mr}} - k_{br} \prod_m \left(\frac{\rho_m}{W_m} \right)^{b_{mr}} \quad (2.14)$$

where, W_m is the molecular weight of the species m . The reaction constants k_{fr} (specific constants of forward reactions) and k_{br} (specific constants of the reverse reactions) are calculated from the Arrhenius formula, in terms of the absolute local temperature, T :

$$k_{fr} = A_{fr} T^{\zeta_{fr}} \exp\left(-\frac{E_{fr}}{T}\right) \quad (2.15)$$

$$k_{br} = A_{br} T^{\zeta_{br}} \exp\left(-\frac{E_{br}}{T}\right) \quad (2.16)$$

where,

A_{fr}, A_{br} are the pre-exponential factors

ζ_{fr}, ζ_{br} are the temperature exponents

E_{fr}, E_{br} are the activation temperatures

Having determined the reaction rate, $\dot{\omega}_r$, for all elementary reactions, the source terms in the mass conservation equation (2.14) and energy conservation (2.12), $\dot{\rho}_m^c$ and \dot{Q}^c , are calculated as follows:

$$\dot{\rho}_m^c = W_m \sum_r (b_{mr} - a_{mr}) \dot{\omega}_r \quad (2.17)$$

$$\dot{Q}^c = \sum_r Q_r \dot{\omega}_r \quad (2.18)$$

where, Q_r is the negative heat of the reaction.

$$Q_r = \sum_m (a_{mr} - b_{mr}) (\Delta h_f^0)_m \quad (2.19)$$

and $(\Delta h_f^0)_m$ is the enthalpy of formation of the species m .

Heat Release Rate

In the present work, results of global heat release rate are presented in non-dimensional form, as follows:

$$ROHR = \frac{d(Q_{chem})}{d(CA)} \cdot \frac{100}{Q_{chem,tot}} \quad (2.20)$$

Here, the quantity Q_{chem} is the total chemical energy of the injected fuel, i.e., the product of fuel mass times the fuel lower calorific value. An indicative value of the lower calorific value for heptane is LHV = 44566 kJ/kg, which is used in the present work.

2.2 Physical processes and models for fuel spray breakup

Spray breakup substantially affects fuel combustion and pollutant formation. The main goal related to the fuel spray is the strong disintegration of the liquid fuel into small droplets, thus increasing the overall surface to volume ratio. In turn, this increases the heat transfer rate from the gas phase to the liquid phase, and thus the liquid fuel evaporation rate. Consequently, enhanced mixing between the evaporated fuel and air is attained, resulting in an efficient combustion, with reduced pollutants. Further, the spray kinetic energy represents the main turbulence addition to the combustion chamber, and thus governs the microscale turbulent air-fuel mixing, while it also affects the turbulent flame speed, in the case of the presence of a premixed combustion phase.

A typical fuel spray flow is shown in Figure 2.1 (Stiesch, 2003). When the intact core of the liquid fuel leaves the nozzle hole, it breaks into individual liquid nuclei (churning flow), and subsequently into droplets. This area of the spray is referred to as the “thick” region, characterised by high values of liquid volume fraction. Downstream this dense area, as a result of further breakup and evaporation of drops, a dispersed (“thin”) structure is attained, becoming “very thin” farther downstream (Figure 2.1).

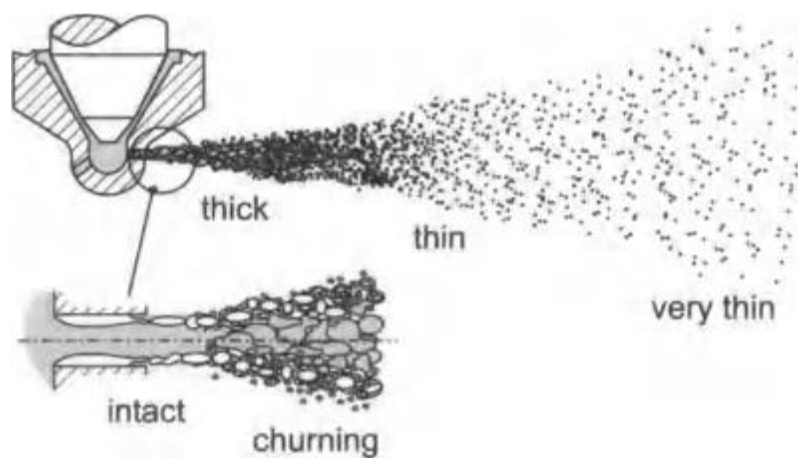


Figure 2.1: Sketch of spray flow structure, depicting the three areas of different liquid phase density (Stiesch, 2003).

In high pressure injectors, the decomposition of the liquid fuel jet into large blobs and droplets is initiated very close to the nozzle exit. This decomposition is referred to as the “primary breakup”. The drops generated further break into smaller droplets, a process referred to as the “secondary breakup”. The latter process thus concerns the regime downstream the dense spray region.

Primary Breakup

The primary breakup of liquid jet at the nozzle exit is caused from the combination of three factors

(Arcoumanis et al., 1997):

- Turbulent flow inside the nozzle [$Re \gg 2300$ (laminar flow limit for circular cross-section pipes)].
- Presence of cavitation bubbles.
- Effects of aerodynamic forces at the surface of liquid fuel.

Because of the pressure drop along the nozzle and the high contraction of the geometry, the liquid fuel is accelerated within the injection orifice, resulting in high Reynolds number turbulent flow. Thus, the creation of high levels of turbulence within the orifice acts as a destabilisation factor to the injected liquid jet. In highly contracting regions, fuel acceleration leads to a decrease in static pressure, which can become lower than the vapor pressure. Thus, cavitation bubbles form within the injector (Figure 2.2), which act as an additional factor of the jet destabilisation. Finally, the high relative velocity between the jet structure and the surrounding jet leads to the formation of strong aerodynamic forces from the gas to the liquid phase, forming the main factor for destabilizing the spray jet. Jet and droplet breakup is resisted by surface tension forces.

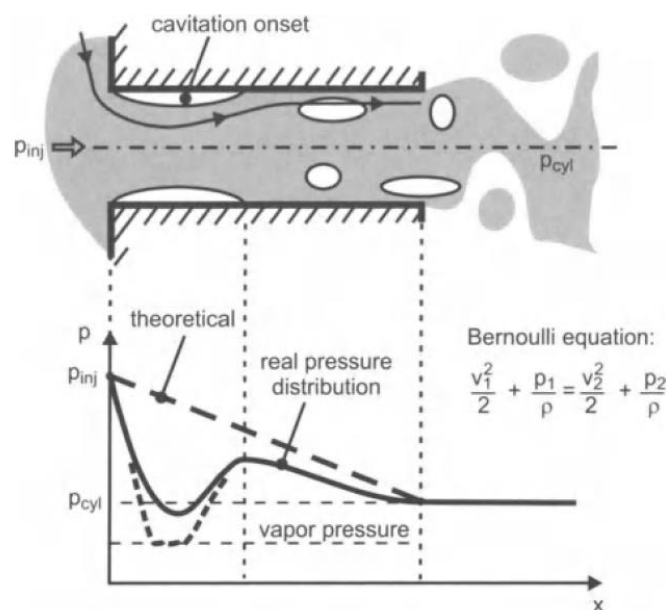


Figure 2.2: Illustration of cavitation bubbles and distribution of static pressure inside an injector nozzle (Stiesch, 2003).

Secondary Breakup

The secondary breakup consists in the disintegration of liquid fuel drops into even smaller droplets due to the action of aerodynamics forces from the surrounding gas phase. These forces distort the initial droplets, promoting their breakup, which also depends on the resistance due to surface tension. The ratio of dynamic pressure to surface tension is the dimensionless droplet Weber number,

characterising the dynamics of droplet breakup.

$$We = \frac{\rho_g \cdot r_d \cdot v_{rel}^2}{\sigma} \quad (2.21)$$

where,

ρ_g is the density of the surrounding gas

r_d is the fuel droplet radius

v_{rel} is the relative velocity between droplet and surrounding gas

σ is the fuel surface tension

Several secondary breakup mechanisms have been developed, also considering experimental studies; the limits between the corresponding five regions depend mainly on the drop Weber number (Figure 2.3). Diesel engine spray break commonly falls into the “catastrophic” and “stretching and thinning” regimes, especially in the region close to the nozzle, where the Weber number attains maximum values. Next, secondary breakup models pertinent to this study are briefly presented.

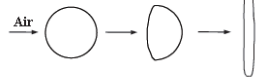
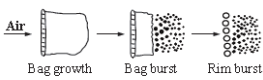

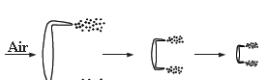
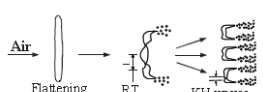
Breakup stages	Deformation or breakup regimes	Breakup process	Weber number
First breakup stage	(1) Deformation and flattening		$We < 12$
Second breakup stage	(b) Bag breakup		$12 \leq We \leq 100$ (including the Bag-and-Stamen breakup)
	(c) Shear breakup		$We < 80$
	(d) Stretching and thinning breakup		$100 \leq We \leq 350$
	(e) Catastrophic breakup		$350 \leq We$

Figure 2.3: Schematic of the five different breakup regimes and corresponding drop Weber number limits (Reitz, 2012).

2.2.1 Taylor Analogy Breakup model (TAB)

The original KIVA-3vr2 code uses the TAB (Taylor Analogy Breakup) model to model fuel spray breakup (O’Rourke and Amsden, 1987). This model is widely used to describe account for secondary breakup. The model makes an analogy between an oscillating drop penetrating a gas environment and a forced mass-spring oscillation system with damping, as illustrated in the Figure 2.4.

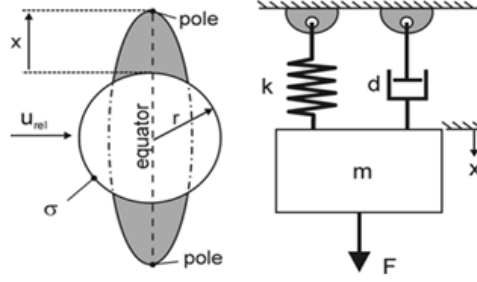


Figure 2.4: Analogy between fuel drop deformation and forced mass-spring oscillation system with damping, used in the TAB model (Baumgarten, 2006).

The ordinary differential equation governing the forced mass-spring oscillation system with damping is:

$$\ddot{x} + \frac{d}{m} \cdot \dot{x} + \frac{k}{m} \cdot x = \frac{F}{m} \quad (2.22)$$

where,

x is the displacement of the droplet's equator from its equilibrium state

m is the droplet mass

d is the damping coefficient

k is the spring coefficient

F is the excitation force

In the case of the oscillating drop, the above formula applies correspondingly; in this case the force term results from the aerodynamic interaction of the fuel drop with the ambient gas, the damping term is due to the cohesiveness of the liquid fuel and the restoring force is due to surface tension. The deformation of the drop is described by the non-dimensional displacement $y = 2x/r$, where x denotes the deformation of the drop with respect to its equilibrium position, and r denotes the drop radius. A necessary condition for drop breakup in TAB is that the non-dimensional displacement becomes higher than unity ($y > 1$). The damping coefficient depends on the viscous forces within the droplet, whereas the spring coefficient depends on surface tension forces. The excitation force is due to aerodynamic forces, which are proportional to the surrounding gas density.

The drop deformation is thus governed by the following equation:

$$\ddot{y} + \frac{5\mu_l}{\rho_l r^2} \dot{y} + \frac{8\sigma}{\rho_l r^3} y = \frac{2\rho_g v_{rel}^2}{3\rho_l r^2} \quad (2.23)$$

$$\text{Damping term: } \frac{d}{m} = \frac{5 \cdot \mu_l}{\rho_l \cdot r^2} \quad (2.24)$$

$$\text{Spring term: } \frac{k}{m} = \frac{8 \cdot \sigma}{\rho_l \cdot r^3} \quad (2.25)$$

$$\text{Excitation term: } \frac{F}{m} = \frac{2 \cdot \rho_g \cdot u_{rel}^2}{3 \cdot \rho_l \cdot r^2} \quad (2.26)$$

where,

ρ_l denotes the fuel density

μ_l denotes the fuel dynamic viscosity

σ is the fuel surface tension

v_{rel} is the relative velocity between the drop and the gas

ρ_g is the density of the surrounding gas

2.2.2 Enhanced Taylor Analogy Breakup model (ETAB)

In engine applications, the TAB model was shown to overpredict evaporation rates, as an outcome of a predicted intense breakup. Thus, the model was improved by Tanner (1997), in terms of the ETAB model. ETAB has introduced an Initial Droplet Size Distribution (IDSD) function for the radius of injected droplets, thereby also accounting for the jet stripping in the near-nozzle regime (Tanner and Weisser, 1998). Further, to properly capture the lifespan of the initial drops of the spray (avoiding excessive breakup), the drops injected may have a proper negative initial deformation. The ETAB model can thus predict a more accurate overall spray structure.

In particular, the ETAB model introduces the following IDSD function (Tanner and Weisser, 1998):

$$f(r) = \frac{n+1}{r_0} \cdot \left(\frac{r}{r_0}\right)^n \quad (2.27)$$

where,

r is the radius of the droplets

r_0 is the radius of the injector hole

n is a constant of the model, with a suggested value of 0.5

Drops can be also injected as parcels, leading to the following expression for the IDSD:

$$g(r) = \frac{n+4}{r_0} \cdot \left(\frac{r}{r_0}\right)^{n+3} \quad (2.28)$$

The model adopts a prediction of primary breakup length, as follows (Tanner, 1997):

$$L_b = u_0 \cdot t_{bu} = C_\lambda \cdot d_0 \cdot \sqrt{\frac{\rho_l}{\rho_g}} \quad (2.29)$$

where,

u_0 is the jet exit velocity

t_{bu} is the drop breakup time

C_λ is a model constant, depending on nozzle geometry

d_0 is the nozzle diameter

ρ_l is the liquid fuel density

ρ_g is the density of the surrounding gas

The initial spray cone angle, θ , can be determined by the following formula (Tanner and Weisser, 1998):

$$\tan\left(\frac{\theta}{2}\right) = C_\alpha \cdot \sqrt{\frac{\rho_g}{\rho_l}} \quad (2.30)$$

where,

C_α is a constant depending on nozzle design

The constant C_α can be calculated via the constant C_λ as follows:

$$C_\alpha = \frac{1}{\sqrt{\frac{\left(16 \cdot C_\lambda^{2/3}\right) + \left(\frac{3}{C_\lambda^2}\right) + 8}{16}}} \quad (2.31)$$

The constants C_α and C_λ depend on nozzle as well as the properties of the injection system, and are thus adjustable parameters of the ETAB model.

The condition to activate drop breakup is $We > We_{crit}$, where $We_{crit} = 6$, while breakup affects the droplet population, N , as follows (Tanner, 1997):

$$\frac{dN(t)}{dt} = 3 \cdot K_{bu} \cdot N(t) \quad (2.32)$$

The proportionality constant K_{bu} depends on the breakup regime (ETAB accounts for two regions,

namely bag and stripping breakup), and can be estimated (Tanner, 1997):

$$K_{bu} = \begin{cases} k_1 \cdot \omega, & \text{if } We_{crit} < We \leq We_t \text{ (bag breakup)} \\ k_2 \cdot \omega \cdot \sqrt{We}, & \text{if } We > We_t \text{ (stripping breakup)} \end{cases} \quad (2.33)$$

where,

k_1 and k_2 are constants of the model from experimental measurements

ω is the frequency of droplet oscillation

We is the Weber number of the drop before breakup

We_{crit} is the critical Weber number

We_t is the Weber transition number between bag and stripping breakup, with a suggested value of 80

Finally, the drop oscillation frequency is given by the following relation (O'Rourke and Amsden, 1987):

$$\omega^2 = \frac{8 \cdot \sigma}{\rho_l \cdot r^3} - \frac{25 \cdot \mu_l^2}{4 \cdot \rho_l^2 \cdot r^4} \quad (2.34)$$

where,

σ is the fuel surface tension

ρ_l is the fuel density

μ_l is the fuel dynamic viscosity

r is the droplet radius

2.2.3 Cascade Atomisation and droplet Breakup model (CAB)

Tanner (2004) recommended a further development of the ETAB model, extending in it to the catastrophic drop breakup regime. In the new model (Cascade Atomisation and droplet Breakup model - CAB), the proportionality constant K_{bu} accounts for all three breakup regimes, bag, stripping and catastrophic, and is calculated as follows:

$$K_{bu} = \begin{cases} k_1 \cdot \omega, & \text{if } We_{crit} < We \leq We_{b,s} \text{ (bag breakup)} \\ k_2 \cdot \omega \cdot \sqrt{We}, & \text{if } We_{b,s} < We < We_{s,c} \text{ (stripping breakup)} \\ k_3 \cdot \omega \cdot We^{3/4}, & \text{if } We > We_{s,c} \text{ (catastrophic breakup)} \end{cases} \quad (2.35)$$

where,

k_1, k_2 and k_3 are model constants

ω is the frequency of droplet oscillation

We is the Weber number of a drop before breakup

We_{crit} is the critical Weber number

$We_{b,s}$ is the Weber transition number between the bag and stripping regions, with a suggested value of 80 (Liu and Reitz, 1993)

$We_{s,c}$ is the Weber transition number between the stripping and catastrophic regimes, with a suggested value of 350 (Liu and Reitz, 1993)

Constants k_1 , k_2 and k_3 can be determined utilising experimental data, and the transition from one breakup region to another is considered continuous. To determine the boundaries of the three regions, only the value of the constant k_1 is required (Tanner, 2004).

It is noted that, in a high-pressure diesel fuel spray, the droplets are characterised by a wide range of speed values, hence Weber numbers. Therefore, all of the above secondary breakup mechanisms are expected to occur.

2.3 Collision model

The effects of collisions between droplets are significant, especially in the dense spray region, i.e., close to the nozzle tip. Collisions can result in coalescence or further droplet breakup (Baumgarten, 2006). The parameters affecting droplet collisions are the relative velocity of the droplets, u_{rel} , the sizes of the droplets, d_1 and d_2 , the orientation of droplets (Figure 2.5, Ashgriz, 2011), the density, ρ_l , and the dynamic viscosity, μ_l , of the liquid, and the surface tension, σ . The associated non-dimensional parameters are: Reynolds number, Weber number, the drop diameter ratio and the impact parameter, B (Baumgarten, 2006). These parameters are calculated by the following equations:

Collision Reynolds number

$$Re_{coll} = \frac{\rho_l \cdot u_{rel}^2 \cdot d_1}{\mu_l} \quad (2.36)$$

Collision Weber number

$$We_{coll} = \frac{\rho_l \cdot u_{rel}^2 \cdot d_2}{\sigma} \quad (2.37)$$

Droplet diameter ratio

$$\Delta = \frac{d_2}{d_1} \quad (2.38)$$

Impact parameter

$$B = \frac{2 \cdot X}{d_1 + d_2} \quad (2.39)$$

where,

ρ_l is the density of fuel

μ_l is the dynamic viscosity of fuel

σ_l is the fuel surface tension

u_{rel} is the relative velocity of droplets

d_1 is the larger diameter

d_2 is the smaller diameter

X is the projection of the distance between the droplet centers, in the direction normal to that of relative velocity of droplets (Figure 2.5)

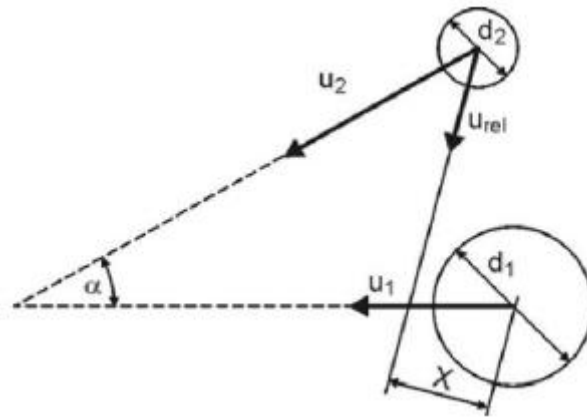


Figure 2.5: Sketch of collision parameters for collision of two drops (Baumgarten, 2006).

The surface tension and the kinetic energy of the droplets have the main contribution to the collision intensity. Depending on the collision Weber number and impact parameter, the different types of collision can be classified in terms of five regimes, bouncing, coalescence, reflexive separation, stretching separation and shattering, sketched in Figure 2.6 (Baumgarten, 2006). The collision model implemented in the KIVA code accounts for coalescence and grazing collision (stretching).

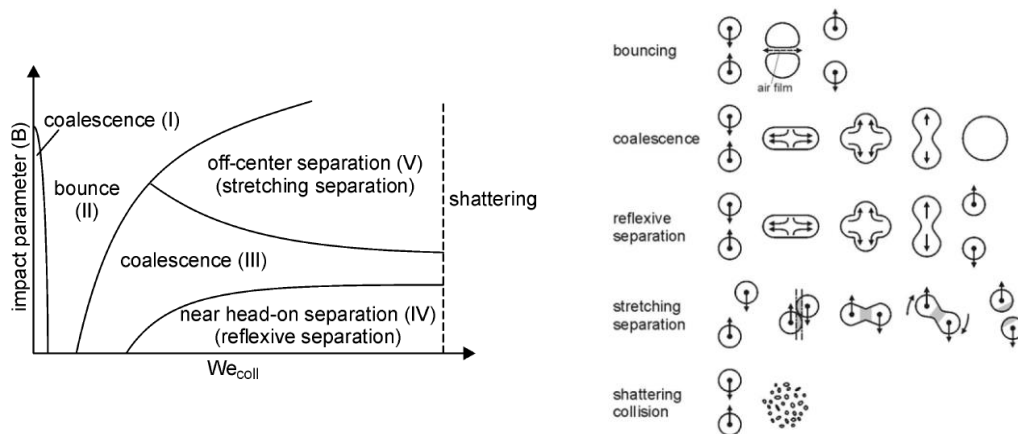


Figure 2.6: Droplet collision regimes (left) and the corresponding mechanisms (right) (Baumgarten, 2006).

2.4 Evaporation model

In the present study, the evaporation model utilises a single-component fuel model. The evaporation process of liquid droplets combines heat and mass transfer. Heat transfer from the gas phase to the droplet surface is due to conduction, convection and radiation, and results in droplet heat-up as well as evaporation; see Figure 2.7 and Figure 2.8 (Baumgarten, 2006).

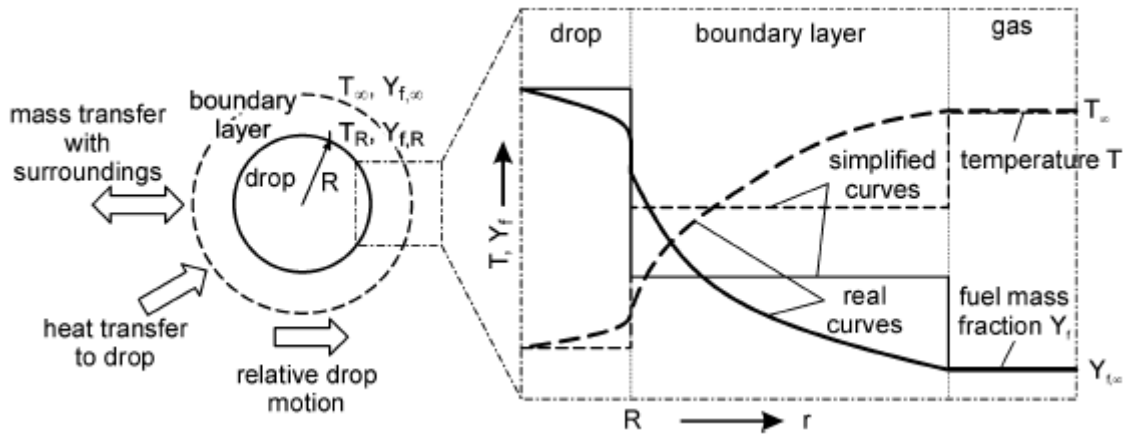


Figure 2.7: Procession of drop vaporization (Baumgarten, 2006).

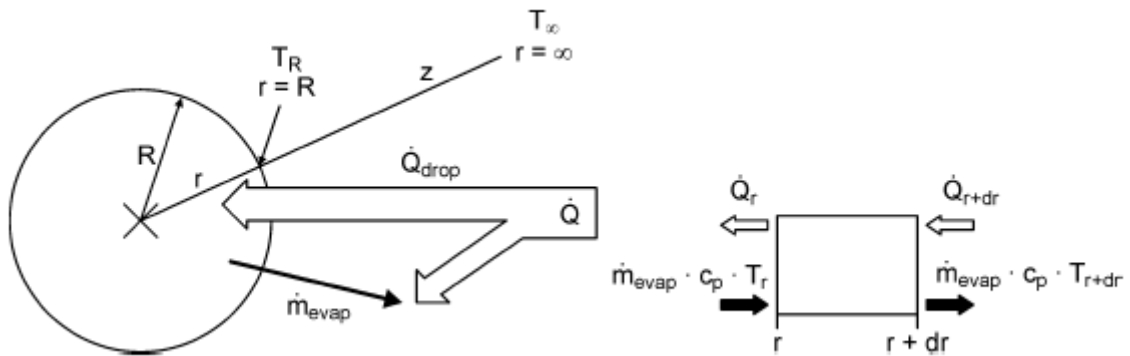


Figure 2.8: Sketch of heat fluxes to a droplet from the ambient gas (Baumgarten, 2006).

The energy balance of a single liquid droplet is given by the following equation (Baumgarten, 2006; Borman and Johnson, 1962):

$$\dot{Q}_{drop} = \dot{Q}_{heating} + \dot{Q}_{evap} \quad (2.40)$$

$$\dot{Q}_{heating} = m_{drop} \cdot c_{p,l} \cdot \frac{dT_{drop}}{dt} \quad (2.41)$$

$$\dot{Q}_{evap} = \Delta h_{evap} \cdot \frac{dm_{evap}}{dt} \quad (2.42)$$

where,

\dot{Q}_{drop} is the total heat flux from hot gas to the liquid droplet

$\dot{Q}_{heating}$ is the thermal power for the heat-up of the liquid droplet

\dot{Q}_{evap} is the thermal power for evaporation of the fuel mass flux

m_{drop} is the liquid droplet mass

T_{drop} is the liquid droplet temperature

$c_{p,l}$ is the specific heat capacity of liquid fuel

Δh_{evap} is the enthalpy of evaporation

m_{evap} is the fuel mass evaporating in the time interval dt

The above equations yield the following relation for the time derivative of fuel drop temperature, which can be integrated in time to give the new temperature value at the next time step:

$$\frac{dT_{drop}}{dt} = \frac{1}{m_{drop} \cdot c_{p,l}} \cdot \left(\frac{dQ_{drop}}{dt} - \Delta h_{evap} \cdot \frac{dm_{evap}}{dt} \right) \quad (2.43)$$

The values $\frac{dQ_{drop}}{dt}$ and $\frac{dm_{evap}}{dt}$ should thus be determined, to calculate $\frac{dT_{drop}}{dt}$. From convection analysis, the total heat flux to the drop, \dot{Q}_{drop} , can be expressed as follows:

$$\dot{Q}_{drop} = \lambda_g \cdot \pi \cdot d_{drop} \cdot (T_g - T_R) \cdot \frac{\zeta}{e^{\zeta} - 1} \cdot Nu \quad (2.44)$$

$$Nu = \frac{a \cdot d_{drop}}{\lambda_g} \quad (2.45)$$

$$\zeta = \frac{\dot{m}_{evap} \cdot c_{p,vap}}{Nu \cdot \lambda_g \cdot \pi \cdot d_{drop}} \quad (2.46)$$

where,

λ_g is the thermal conductivity of gas phase

d_{drop} is the drop diameter

T_g is the temperature of the surrounding gas

T_R is the temperature of liquid droplet

ζ is a dimensionless correction factor, accounting for the decrease of heat transfer due to the concurrent mass transfer from the liquid drop into the gas atmosphere

Nu is the Nusselt number

a is the convection heat transfer coefficient

\dot{m}_{evap} the evaporation mass flow rate

$c_{p,vap}$ is the specific heat capacity of fuel vapour

The Nusselt number, as a function of Reynolds number, Re , and Prandtl number, Pr , can be taken from the formula of Ranz and Marshall (1952):

$$Nu = 2.0 + 0.6 \cdot Re^{1/2} \cdot Pr^{1/3} \quad (2.47)$$

$$Re = \frac{\rho_g \cdot u_{rel} \cdot d_{drop}}{\mu_g} \quad (2.48)$$

$$Pr = \frac{\mu_g \cdot c_{p,g}}{\lambda_g} \quad (2.49)$$

where,

ρ_g is the density of surrounding gas

u_{rel} is the relative velocity between droplet and surrounding gas

μ_g is the dynamic viscosity of the surrounding gas

$c_{p,g}$ is the specific heat capacity of the surrounding gas

d_{drop} is the drop diameter

The evaporating mass flow rate, $\frac{dm_{evap}}{dt}$, can be calculated as follows (Turns, 1996):

$$\dot{m}_{evap} = d_{drop} \cdot \pi \cdot \rho \cdot D \cdot \ln\left(\frac{1-Y_{f,\infty}}{1-Y_{f,R}}\right) \cdot Sh \quad (2.50)$$

$$Sh = 2.0 + 0.6 \cdot Re^{1/2} \cdot Sc^{1/3} \quad (2.51)$$

$$Sc = \frac{\mu_g}{\rho_g \cdot D} \quad (2.52)$$

where,

d_{drop} is the drop diameter

ρ is the density of liquid fuel droplet

D is the diffusivity of fuel vapor in air

$Y_{f,\infty}$ is the fuel vapor mass fraction in the far field

$Y_{f,R}$ is the fuel vapor mass fraction at droplet surface

Sh is the Sherwood number

Re is the Reynolds number

Sc is the gas Schmidt number

μ_g is the dynamic viscosity of the surrounding gas

ρ_g is the density of the surrounding gas

2.5 Ignition model

Ignition modelling in the present reactive flow simulations using one-step chemistry is based on the model Weisser et al. (1998); they have considered an ignition progress variable, governing the ignition delay through a conservation equation, and serving as the ignition criterion. The ignition progress variable, C_{ig} , is a non-dimensional quantity, defined as the concentration of an intermediate species (here: the OH radical) divided by a critical value. When a value of C_{ig} greater than unity is calculated, the combustion model is activated.

The C_{ig} conservation equation has the following form (Weisser, 2001):

$$\frac{\partial(\rho_g C_{ig})}{\partial t} + (\nabla \cdot \mathbf{u}) \rho_g C_{ig} = \nabla \cdot (\rho_g D \nabla C_{ig}) + \frac{\rho_g}{\tau_{ig}}, \quad (2.53)$$

where, ρ_g , \mathbf{u} , D are the density, velocity and effective diffusivity of the surrounding gas, respectively. The overall ignition characteristic time, τ , is calculated from a simplified system of characteristic times, as follows (see also Figure 2.9):

$$\frac{1}{\tau} = \frac{1}{\tau_1 + \tau_2} + \frac{1}{\tau_3} \quad (2.54)$$

where the individual timescales τ_1 , τ_2 and τ_3 represent the low-, medium- and high-temperature regimes of ignition, respectively. These individual timescales are evaluated from Arrhenius-type correlations, considering the pressure, p , and temperature, T , of the surrounding gas, and the local equivalence ratio, Φ :

$$\tau_i = A_i \cdot h_i(\Phi) \cdot \left(\frac{p}{p_{ref}}\right)^{a_i} \cdot T^{b_i} \cdot \exp\left[\frac{B_i}{T}\right], \quad i = 1, 2, 3 \quad (2.55)$$

with A_i , a_i , b_i and B_i being model constants. Values of the model constants have been obtained from the analysis of detailed ignition calculations of homogeneous n-heptane – air mixtures, and are presented in Table 2 (Weisser et al., 1998).

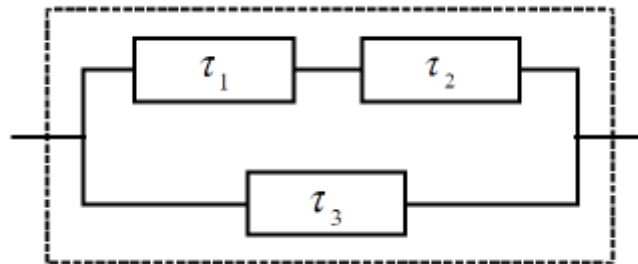


Figure 2.9: Sketch of the simplified system of ignition characteristic times, accounting for the overall ignition characteristic time (Weisser et al., 1998).

Table 2: Parameter values of the ignition model for n-heptane (C₇H₁₆) (Weisser et al., 1998).

Process	A_i	a_i	b_i	B_i	$h_i(\Phi)$
1	2.39E-11	-0.1	0	14000	1
2	1.33E+05	-2.125	0	-10000	Φ^{-1}
3	2.50E-08	-1	0	14000	1

2.6 Combustion modelling

The development of combustion for diesel mode operation is illustrated by the evolution of the Rate of Heat Release (ROHR), sketched in Figure 2.10 for a typical case (Heywood, 1988). Four characteristic phases are thereby identified.

1st Phase (Ignition Delay Period)

It corresponds to the engine operation phase “a” – “b”, where at point “a” the fuel injection initiates, and point “b” is the ignition point. During this period, the fuel is heated by the compressed air, evaporates, and mixes with the surrounding air. If the duration of this phase is long, a large amount of fuel accumulates in the cylinder, which near the Top Dead Centre (TDC), where the temperature is high, will ignite abruptly, resulting in a sudden increase in pressure, noise generation and excessive strain of the engine components. Thus, in general, it is desirable that the duration of this phase should be as short as possible.

2nd Phase (Premixed Combustion)

It corresponds to engine operation phase “b” - “c”, where, after ignition, a premixed flame forms and propagates. Thus, in this phase, burning of the already injected fuel takes place. This phase can be characterised by uncontrolled combustion and associated pressure rise (“combustion knock”).

3rd Phase (Diffusion Combustion)

It corresponds to the engine operation phase “c” - “d”, and is characterised by long duration depending on the engine load. Combustion takes place in a diffusion flame mode, in a controlled manner, and is associated with the ongoing mass injection.

4th Phase (Late Combustion)

It corresponds to the engine operation phase, after point “d”, where injection has been completed, while combustion of unburned fuel continues. This phase is undesirable, as it contributes to overheating of the exhaust valves and the piston head.

Modelling of Diesel engine combustion can adopt simple approaches, as the one-step approach, or complicated ones, accounting for realistic chemistry; they are briefly elaborated next.

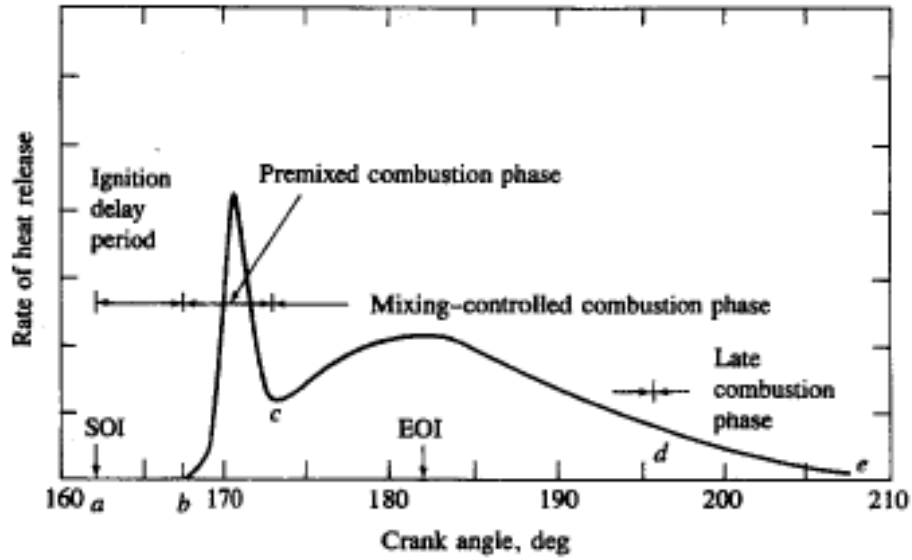


Figure 2.10: Sketch of typical Rate of Heat Release curve in a Diesel engine, in which the different phases of combustion are depicted (Heywood, 1988).

2.6.1 One-step approach

The present one-step chemistry simulations adopt the characteristic time model of Kong et al. (1995). The model considers seven species, fuel, O_2 , N_2 , CO_2 , H_2 , H_2O and CO , and calculates the rate of change of their concentration in terms of a characteristic time scale of combustion, τ_c , d as follows:

$$\frac{dY_i}{dt} = -\frac{Y_i - Y_i^{eq}}{\tau_c} \quad (2.56)$$

where Y_i and Y_i^{eq} are the instantaneous and equilibrium concentration, respectively, of species i . The combustion characteristic time is calculated from the weighted sum of a “laminar” (chemical) time scale, and a turbulent one, which accounts for the local mixing of evaporated fuel and air:

$$\tau_c = \tau_{lam} + f \cdot \tau_{turb} \quad (2.57)$$

The chemical time scale, τ_{lam} , is calculated from an Arrhenius relation, based on ignition experiments:

$$\tau_{lam} = A^{-1} \cdot [C_{14}H_{30}]^{0.75} \cdot [O_2]^{-1.5} \cdot \exp\left[\frac{E}{RT}\right] \quad (2.58)$$

where,

A is the pre-exponential constant

E is the activation energy, in kJ/kg

R is the specific gas constant, in $kJ/kg \cdot K$

T is the local temperature, in K

The turbulent time scale, τ_{turb} , is calculated from the local values of k and ε :

$$\tau_{turb} = C_2 \cdot \frac{k}{\varepsilon} \quad (2.59)$$

where,

C_2 is a factor accounting for the mixing characteristics

k is the turbulent kinetic energy, in kJ/kg

ε is the dissipation rate, in $kJ/kg \cdot s$

The weight factor f is calculated as follows:

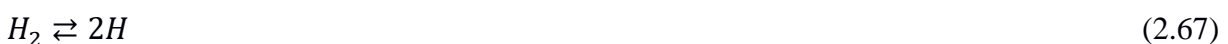
$$f = \frac{1-e^{-r}}{0.632} \quad (2.60)$$

where, r is the ratio of the amount of products to that of total reactive species (except N_2):

$$r = \frac{Y_{CO_2} + Y_{H_2O} + Y_{CO} + Y_{H_2}}{1 - Y_{N_2}} \quad (2.61)$$

The parameter r varies from zero (unburned mixture) to unity (fully burned mixture). As a result, f also varies between zero and unity, depending on local composition.

Finally, it is noted that, in the KIVA-3vr2 code, equilibrium calculations are based on the following system of reactions:



2.6.2 Realistic chemistry

In the realistic chemistry approach, the source terms $\dot{\rho}_m^c$ and \dot{Q}^c , contained in the equations of continuity and energy, respectively, are calculated as follows (Kakaee et. al, 2015):

$$\dot{\rho}_m^c = \rho \frac{dY_m}{dt} \quad (2.68)$$

$$\dot{Q}^c = - \sum_{m=1}^M \frac{dY_m}{dt} \frac{(\Delta h_f^0)_m}{W_m} \quad (2.69)$$

$$\frac{dY_m}{dt} = \frac{\dot{\omega}_m W_m}{\rho} \quad (2.70)$$

where,

$(\Delta h_f^0)_m$ is the molar heat of formation of species m

W_m is the molecular weight of species m

Y_m is the mass fraction of species m

The calculation of the source terms requires the calculation of the molecular rates of production of each species, m ($\dot{\omega}_m$), by kinetics calculations. In the present study, this is enabled by means of a coupled KIVA-3vr2 - CHEMKIN-II code. The CFD code provides the local flow quantities, including pressure and temperature, and the kinetics code returns the source terms of the mass and energy conservation equations, $\dot{\rho}_m^c$ and \dot{Q}^c . Next, the CFD code calculates the fuel density and temperature fields, at the new time step.

In the present coupled KIVA-CHEMKIN code, the chemical kinetics mechanism is introduced via the *ckinterp.f* CHEMKIN subroutine. Specifically, this subroutine reads the input provided in files *chem.inp* and *therm.dat*, returning its output in binary format in the *chem.bin* file. This binary file contains important information of each species entailed in the chemical kinetics mechanism, such as the thermochemical properties (i.e., specific heat capacity, enthalpy and entropy) as a function of temperature, and is an additional input file to the KIVA-CHEMKIN coupled code. In total, all the important information required by the chemical kinetics subroutines of CHEMKIN code is extracted from the *chem.bin* file. The coupling between the two codes is sketched in Figure 2.11.

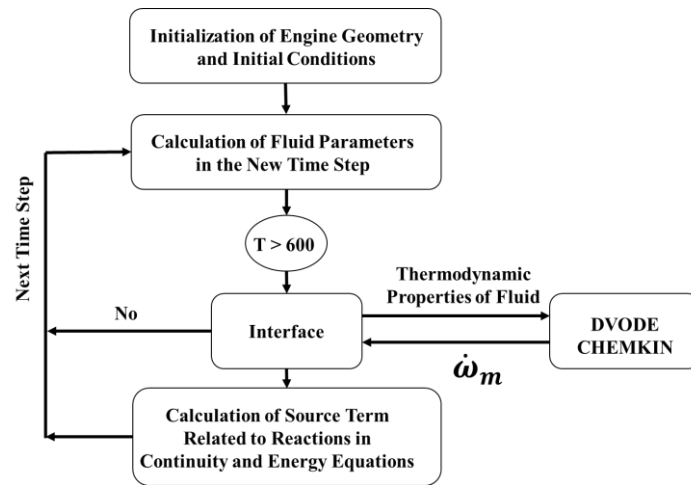


Figure 2.11: Coupled code KIVA-CHEMKIN flowchart (Kakaee et al., 2015).

2.7 Pollutant emission models

In marine engines, the main emissions include nitrogen oxides (NO_x), soot particles (soot), sulphur oxides (SO_x), and unburned hydrocarbons (HC). Here, in the frame of one-step chemistry CFD simulations, calculation of pollutants has considered NO_x formation in terms of a mechanism building on the extended Zeldovich mechanism (Weisser, 2001), and a phenomenological soot model based on the Hiroyasu model (Hiroyasu et al., 1983). In the realistic chemistry approach, NO_x sub-mechanisms are implemented (Kakaee et al., 2015).

2.7.1 NO_x Model

The chemical mechanism accounting for NO_x production is presented in Table 3. The model considers thermal NO formation, building on the extended Zeldovich mechanism presented below (Lavoie et al. 1970), and also accounting for the formation of N_2O (Malte and Pratt 1974). The model also includes the NO_2 formation.



Table 3: Reactions and constants of specific rate of NO_x mechanism (Weisser, 2001).

Reaction	A_{NO_x}	b_{NO_x}	T_{A,NO_x} [K]
$N + NO \rightarrow N_2 + O$	3.30e+12	0.3	0
$N_2 + O \rightarrow N + NO$	6.68e+12	0.4	37707.29
$N + O_2 \rightarrow NO + O$	6.40e+09	1.0	3160.54
$NO + O \rightarrow N + O_2$	5.62e+08	1.1	19086.52
$N + OH \rightarrow NO + H$	3.80e+13	0	0
$NO + H \rightarrow N + OH$	1.29e+15	-0.3	24574.68
$NO + HO_2 \rightarrow NO_2 + OH$	2.10e+12	0	-241.07
$NO_2 + OH \rightarrow NO + HO_2$	8.45e+12	0.02	2971.32
$NO_2 + H \rightarrow NO + OH$	3.50e+14	0	754.91
$NO + OH \rightarrow NO_2 + H$	9.46e+09	0.81	15089.38
$N_2O + H \rightarrow N_2 + OH$	7.60e+13	0	7649.72
$N_2 + OH \rightarrow N_2O + H$	5.73e+07	1.31	38531.49
$N_2O + M \rightarrow N_2 + O + M$	1.60e+14	0	25968.8
$N_2 + O + M \rightarrow N_2O + M$	5.21e+07	1.34	5227.24
$N_2O + O \rightarrow N_2 + O_2$	1.0e+14	0	14192.25
$N_2 + O_2 \rightarrow N_2O + O$	2.91e+10	0.91	53722.71
$N_2O + O \rightarrow 2NO$	1.0e+14	0	14192.25
$2NO \rightarrow N_2O + O$	1.26e+09	0.92	31941.4
$N_2O + OH \rightarrow N_2 + HO_2$	2.0e+12	0	5032.71
$N_2 + HO_2 \rightarrow N_2O + OH$	1.39e+10	0.48	18367.62

2.7.2 Soot Model

Soot is an important pollutant associated with Diesel engine operation. Soot formation depends on local conditions of pressure, temperature and stoichiometry. The production of soot is a very complex process, including particle inception, surface growth and coagulation; a high percentage of the soot formed is oxidised (Haynes and Wagner 1981). In the present study, the phenomenological model of Hiroyasu et al. (1983), as adapted in Douladiris (2010), is used for soot modelling. The model is expressed by the following relations:

$$\frac{dm_s}{dt} = \frac{dm_{s,f}}{dt} - \frac{dm_{s,ox}}{dt} \quad (2.74)$$

$$\frac{dm_{s,f}}{dt} = A_f \cdot m_{f,v} \cdot p^{0.5} \cdot \exp\left(-\frac{E_{s,f}}{R \cdot T}\right) \quad (2.75)$$

$$\frac{dm_{s,ox}}{dt} = A_{ox} \cdot m_s \cdot \frac{p_{O_2}}{p} \cdot p^{1.8} \cdot \exp\left(-\frac{E_{s,ox}}{R \cdot T}\right) \quad (2.76)$$

where,

m_s is the soot mass, in kg

$m_{s,f}$ is the mass of soot produced, in kg

$m_{s,ox}$ is the mass of oxidised soot, in kg

A_f is the constant of the soot production correlation

$m_{f,v}$ is the mass of fuel vapor, in kg

$E_{s,f}$ is the activation energy in the soot production correlation, in $\frac{J}{mole}$

A_{ox} is the constant in the soot oxidation correlation

$E_{s,ox}$ is the activation energy in the soot oxidation correlation, in $\frac{J}{mole}$

R is the universal gas constant

T is the local temperature, in K

Here, the soot model is implemented for each computational cell, considering the local flow field values. The values of soot model constants (for pressures in MPa) are listed in Table 4 (Douladiris, 2010).

Table 4: Values of soot model constants (Douladiris, 2010).

A_f	$E_{s,f} \left[\frac{J}{mole} \right]$	A_{ox}	$E_{s,ox} \left[\frac{J}{mole} \right]$
3162	52335	$2.79e^{+06}$	58615

2.8. CFD code ‘KIVA-3vr2’

The Computational Fluid Dynamics code KIVA-3vr2 (Amsden, 1999), written in FORTRAN, is an advanced version of the KIVA code developed in 1989 by the Los Alamos National Laboratory (LANL), as a widely approved design and research tool for the numerical calculation of transient two- and three-dimensional complex chemically reactive fluid flows with fuel sprays. In addition, the KIVA 3vr-2 code computes reactive flow in complex geometries by utilising block-structured meshes. Specifically, the complex geometries are divided into several blocks with regular simple geometry for generating the mesh, which are then put together to form the mesh for the whole geometry (Amsden, 1992). Moreover, the version of the code used enables the simulation of full engine cycle, as it includes the capability of moving valves (Amsden, 1999). The success of the family of KIVA codes can be largely attributed to their open-source structure, which allows the user to improve the physical sub-models. The code solves numerically the conservation equations of the turbulent engine flow in space and time. In addition, through individual physical models, processes such as spray breakup, droplet evaporation, combustion and heat transfer are taken into account.

3. CFD spray studies in a constant volume chamber

This Chapter presents a validation and adaptation of the ETAB and CAB spray models. Further, it assesses on their applicability to simulating two-phase flow in the two four-stroke engines considered in the present thesis. The present model validation is performed using experimental data in a constant volume Spray Combustion Chamber facility of LAV ETH Zurich, which enables a detailed visualisation of spray, and thus a quantification of spray penetration, spray cone angle and droplet size.

3.1 Problem definition and resolution tests

The problem considered is that of a high-pressure and temperature constant volume cell (Schneider, 2003) of LAV ETH Zürich. Its geometry is characterised by a cylindrical symmetry around its axis, which coincides with the injection direction. The chamber has a size of $\text{Ø}110 \times 40 \text{mm}$, and a single hole of injector is located on top, injecting along the symmetry axis. The chamber quartz glass windows enable optical access by means of Phase Doppler Anemometry (PDA). A schematic of the spray chamber is presented in Figure 3.1.

Non-reactive flow is studied, and thus the surrounding gas is nitrogen. In the present validation studies, relatively low gas temperatures are considered, i.e., the spray is also non-evaporating. The ambient gas is still. Simulations consider n-tetradecane ($\text{C}_{14}\text{H}_{30}$) as fuel, and computational results are compared against the experiments of Pizza et al. (2007). Two test cases are simulated, and the corresponding conditions are presented in Table 5. Estimates of Weber number for large drops close to the orifice yield values of about 25000 and 33000 for Case 1 and Case 2, respectively, illustrating catastrophic droplet breakup.

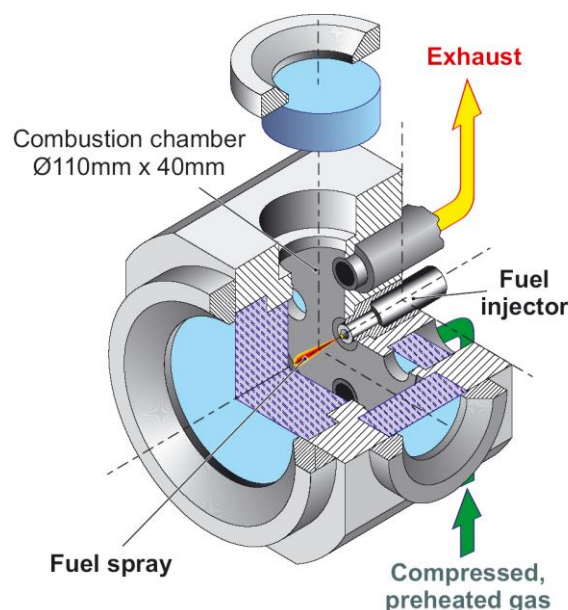


Figure 3.1: Schematic of the high-pressure and temperature constant volume cell (Schneider, 2003).

Table 5: Simulations in constant volume chamber: conditions of the two test cases.

Non-evaporating & non-reactive flow	Case 1	Case 2
Diameter of nozzle hole [mm]	0.15	0.20
Gas temperature [K]	400	
Gas pressure [bar]	40	
Injection pressure [bar]	500	
Gas density [kg/m ³]	33.7	
C ₁₄ H ₃₀ temperature [K]	323	

3.1.1 Computational Grid

The computation of flow in complex geometries can be performed by using block-structured grids. A complex geometry is thereby split into several blocks of regular geometry. Grids are then generated for each block, and are combined together to obtain the mesh for the entire geometry (Amsden, 1992). In the present study, the objective of grid generation is to resolve the spray regime with a sufficiently fine mesh, while also maintaining a proper (albeit coarser) resolution in the remaining parts of the computational domain. It is noted here that, in the case of flows with moving boundaries, as in piston engines, a “snapper” technique can be implemented, properly adding or removing cell layers (Reitz and Rutland, 1993). Further, the capability of treating moving valves can be incorporated, which was indeed implemented in the KIVA-3V code, enabling the simulation of full engine cycles (Amsden, 1997).

KIVA is based on the Arbitrary Lagrangian-Eulerian (ALE) method, which constitutes a mixture of Lagrangian and Eulerian approaches. Spatial discretization is based on finite volumes. Figure 3.2 presents a typical finite volume cell.

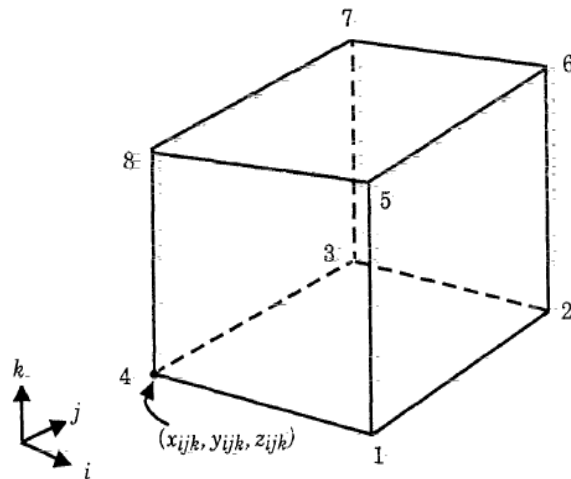


Figure 3.2 : Sketch of a finite volume cell (Amsden, 1989).

The KIVA mesh generator generates file 'otape17', to be read by the main program; it contains all grid coordinates (polar or cartesian), six neighbour connectivity arrays, three cell-face boundary condition arrays, and a region identifier array. Momentum balances are performed for cells staggered with respect to regular cells (see Figure 3.3); they are referred to as 'momentum cells' (Amsden, 1989). The numerical solution of the conservation equations is concluded by generating an adapted mesh (for the next time step), taking into account the moving boundary of the piston.

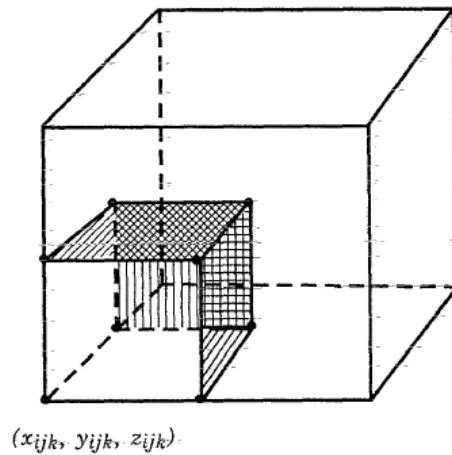


Figure 3.3: Portion of a momentum cell (i;j;k) lying within a regular cell (i,j,k) (Amsden, 1989).

The pre-processor module K3PREP, used for grid generation, accompanies KIVA codes; it does not provide a graphical interface, thus requiring manual geometry input, in the terms of either functions or sets of discretized points of the surfaces or curves. In the present study, both K3PRER and the commercial grid generator ICEM-CFD (ANSYS ICEM CFD version 18.0) have been used. ICEM-CFD provides a graphical interface, while the grid output file can be in KIVA format.

3.1.2 Resolution tests

Spray simulations are characterised by strong dependence on grid density (Aneia and Abraham, 1998, Nordin, 2000, Schmidt and Rutland, 2004); thus, they should be accompanied by careful spatial resolution tests. Here, block-structured grids have been generated using the ICEM-CFD software. In the near-nozzle region, cells of a size comparable to the nozzle diameter were generated. In particular, depending on the overall grid density, near-nozzle cells had typical sizes of 1.0x0.5 mm, 0.5x0.5 mm and 0.4x0.4 mm, in the x (radial) and z (vertical) direction, respectively. Information regarding the three grids generated is provided in Table 6, while a visualisation of grids is presented in Figure 3.4.

Table 6: Features of the computational grids used in spatial resolution tests.

Mesh (Ø110x40 mm)	Number of cells	Spray regime resolution
Coarse	184,109	1.0x0.5 mm
Fine	369,709	0.5x0.5 mm
Very fine	608,108	0.4x0.4 mm

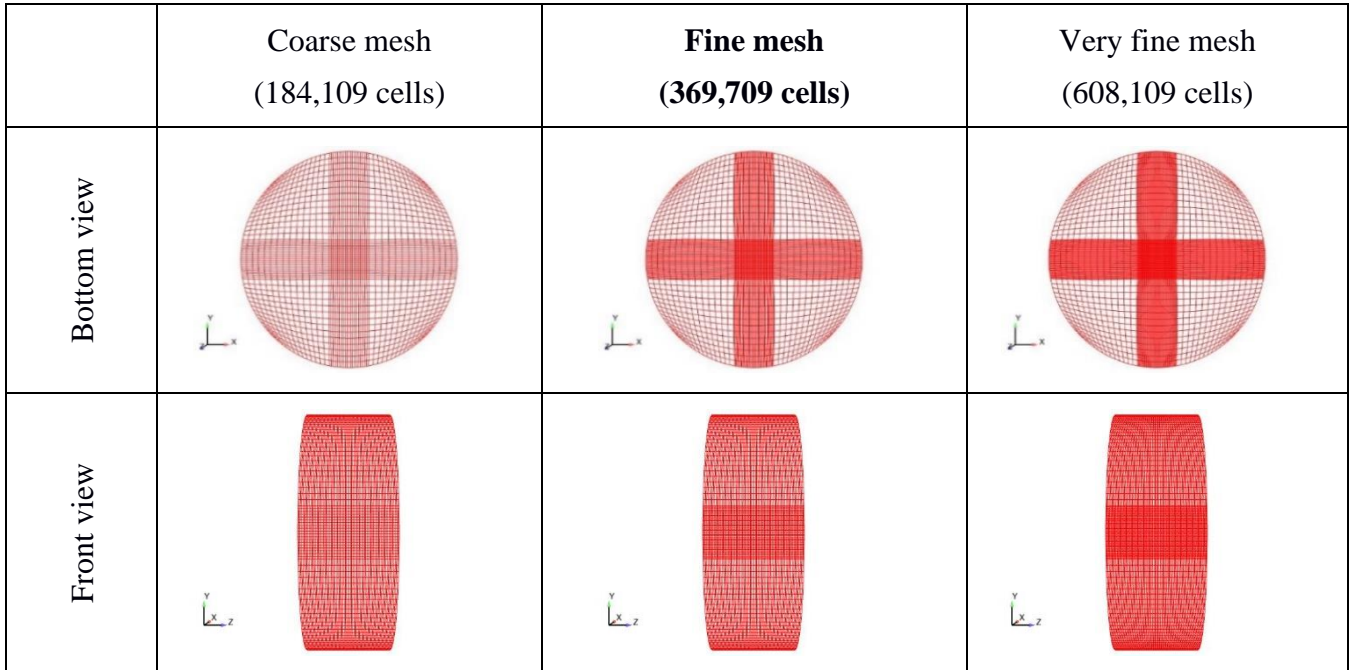


Figure 3.4: Top and bottom views of the computational grids used in spatial resolution tests.

Figure 3.5 presents the injection rate used for Case 1, based on the experiments (Schneider, 2003). Both spatial and temporal resolution tests have been performed using the ETAB and CAB models, in order to investigate the dependence of computational results on discretization parameters. First, spatial resolution tests were performed for Case 1, using the three grids of Table 6. Figures 3.6 and 3.8 illustrate the calculated time history of the spray penetration length for all three grids using the ETAB and the CAB model, respectively, also including the experimental data of Schneider (2003). Both Figures demonstrate that the computational results with the “fine resolution” grid are close to the experimental values. Thus, this grid is selected to calculate the proper values of model constants, for both ETAB and CAB.

For the three grids generated, Figures 3.7 and 3.9 show, for the ETAB and CAB model, respectively, the instantaneous snapshots of gas flow velocity, droplet Sauter Mean Diameter - SMD (in microns)

($SMD = \frac{\sum_{i=1}^n d_i^3}{\sum_{i=1}^n d_i^2}$, d_i accounting from droplet diameter) and spray droplet velocity for Case 1, at a

vertical plane including the injector, at a representative time instant of 0.5 ms after Start of Injection (SOI). The visualisations illustrate that both the “fine” and “very fine” grids enable the computation of a proper spray flow structure; this is not the case for the “coarse” grid. Overall, the “fine” grid produces computational results in good agreement with experiments, while also maintaining a reasonable computational cost. Thus, it is selected for all simulations associated with adapting the values of constants, for both ETAB and CAB.

Temporal resolution tests have been also performed; based on the spatial resolution tests, the “fine” mesh has been used in all cases. Time step values ranging from 10^{-6} to 10^{-5} s were used, and the results have demonstrated independence for values of Δt close to the low limit, i.e., 10^{-6} s or slightly higher. Thus, a value $\Delta t=2 \cdot 10^{-6}$ s was selected, and subsequently used for the model adaptation. Time step values of this order are maintained in all one-step chemistry engine simulations of the present thesis.

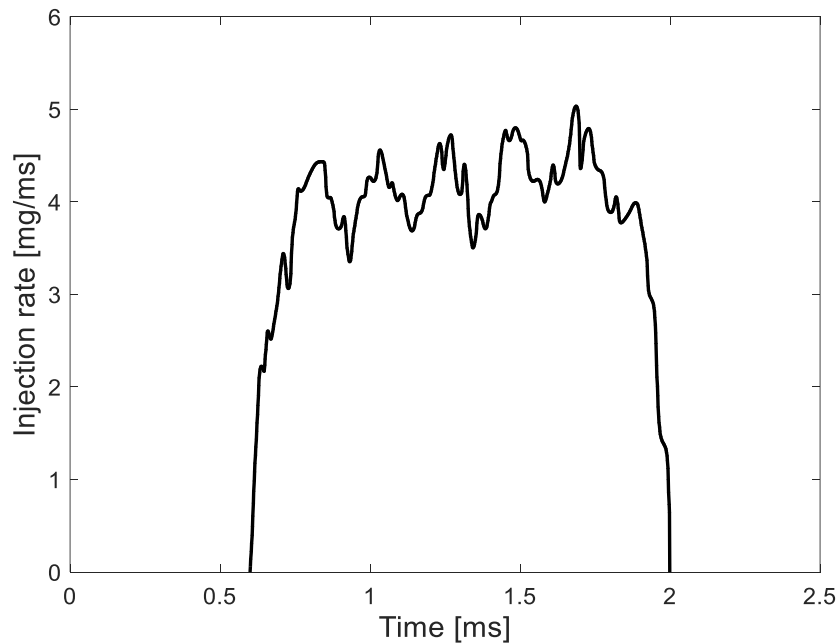


Figure 3.5: Injection rate versus time for Case 1 (Schneider, 2003).

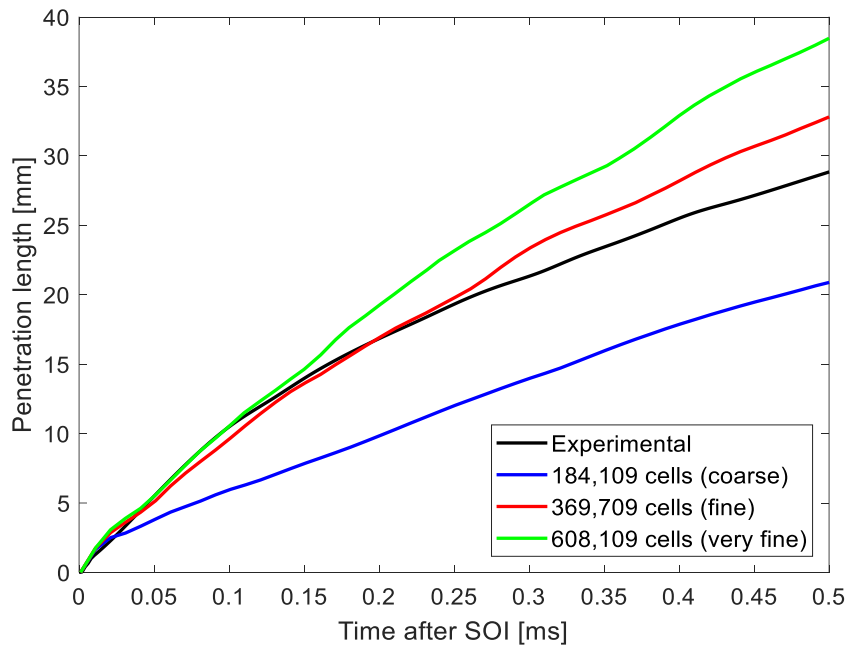


Figure 3.6: Case 1: calculated penetration length versus time for the three computational grids considered, using the ETAB model and a time step value of $\Delta t=2 \cdot 10^{-6}$ s. The corresponding experimental curve (Scheider, 2003) is also included.

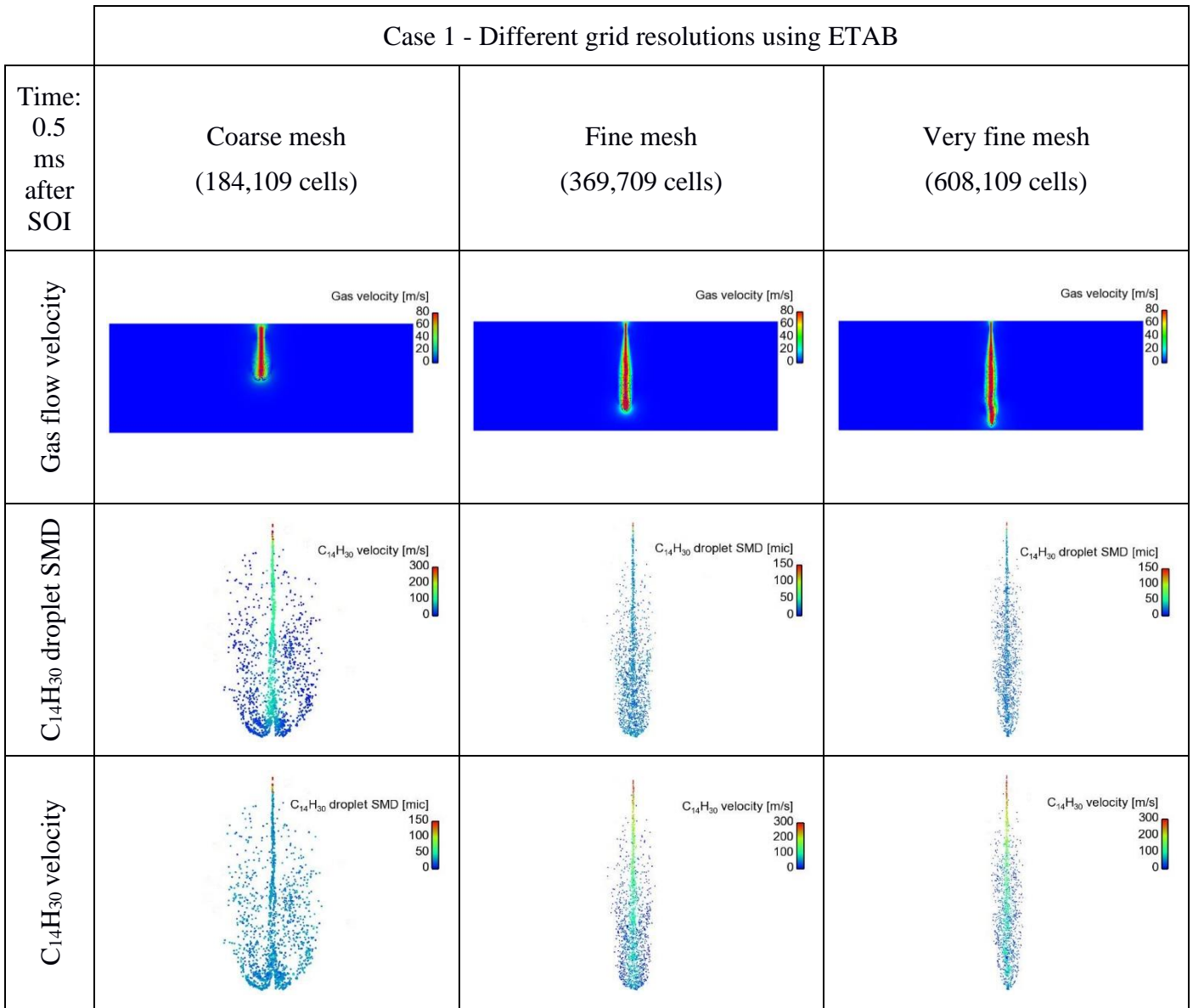


Figure 3.7: Case 1: colour-coded contours of gas velocity, droplet Sauter Mean Diameter - SMD (in microns) and spray droplet velocity using the ETAB model, at the vertical plane including the injector.

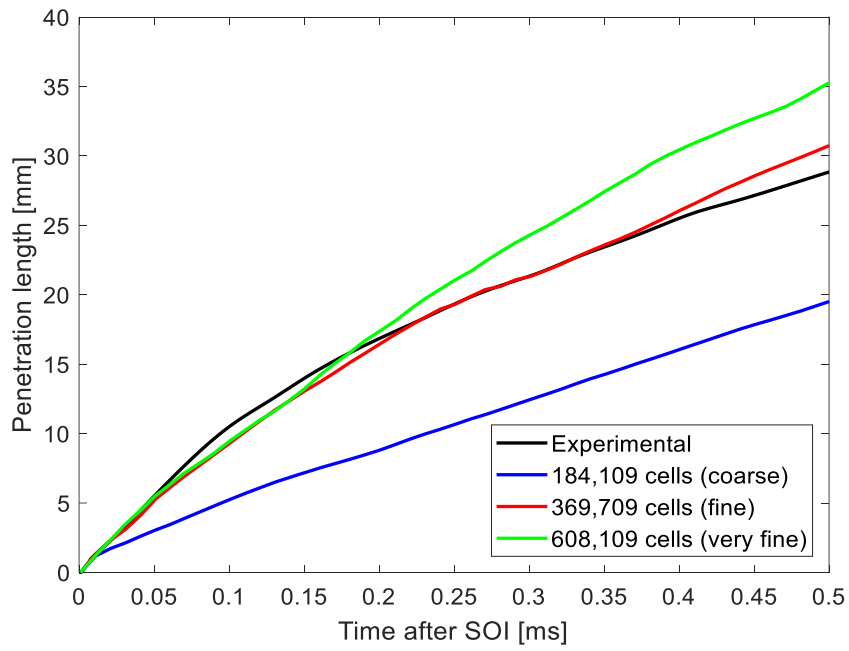


Figure 3.8: Case 1: calculated penetration length versus time for the three computational grids considered, using the CAB model and a time step value of $\Delta t=2 \cdot 10^{-6}$ s. The corresponding experimental curve (Scheider, 2003) is also included.

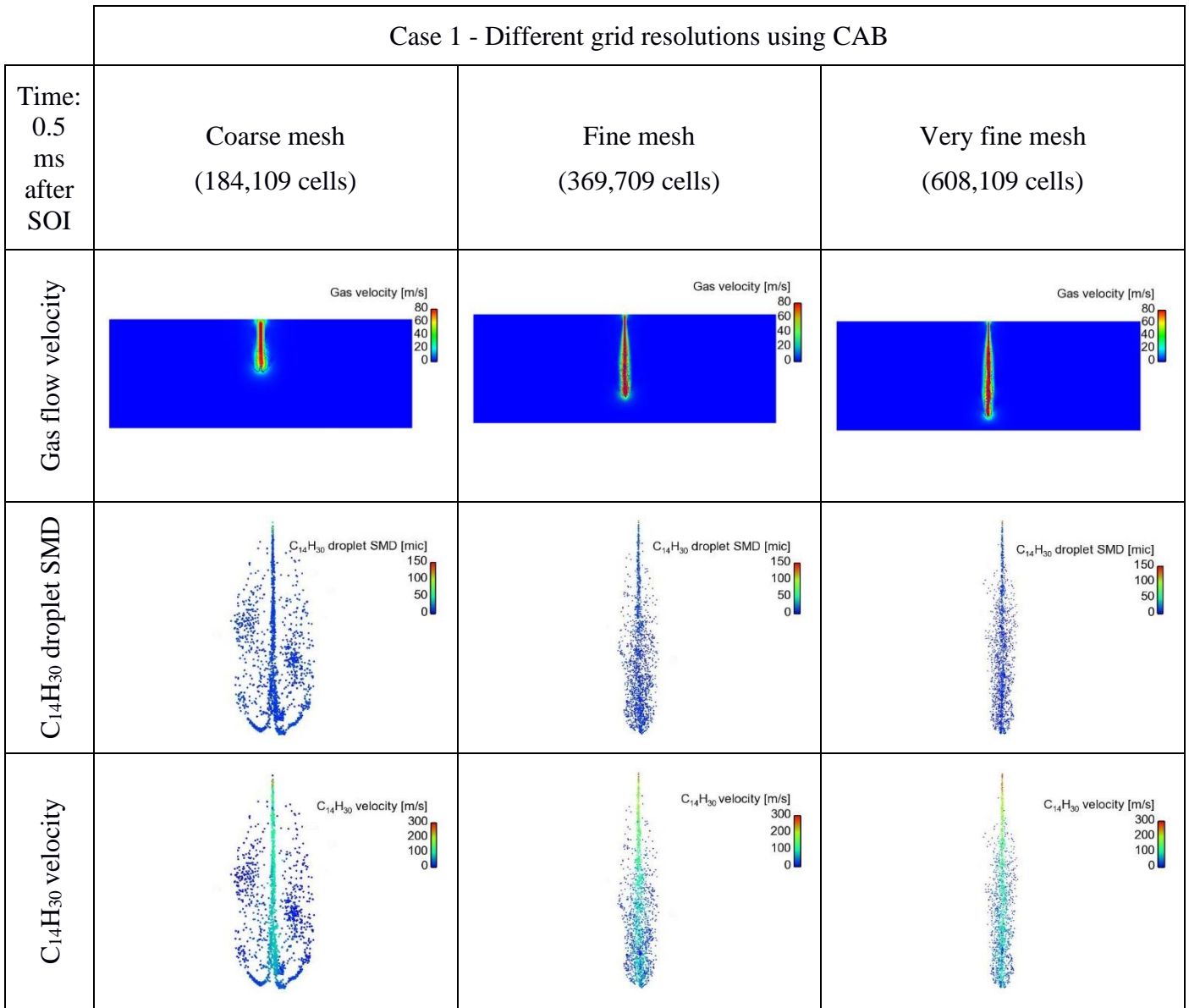


Figure 3.9: Case 1: colour-coded contours of gas velocity, droplet Sauter Mean Diameter - SMD (in microns) and spray droplet velocity using the CAB model, at the vertical plane including the injector.

3.2 Adaptation of ETAB and CAB models

Adaptation of the ETAB and CAB spray models was performed for operating conditions corresponding to: (i) ETAB model: Case 1, (ii) CAB model: Case 1 and Case 2 (Table 5), using the “fine” mesh (Table 6). In the present analysis, proper adaptation of the model constants considers a wide range of possible values; the agreement between the computed and measured time history of penetration length is used as the main criterion for adapting spray models. It is noted that the value of the initial spray cone angle is prescribed as an input to the problem, and is based on the experimental measurements (Schneider, 2003). The optimal constant values obtained are presented in Table 7 and Table 8, for ETAB and CAB, respectively. Maintaining the optimal values of model constants, computations of Case 1 and Case 2 are performed, and discussed in section 3.3.

Table 7: Optimal values of the ETAB model constants, obtained for conditions corresponding to Case 1.

Constant	Description	Default (Pizza et al., 2007)	Default (Tanner and Weisser, 1998)	Outcome	
				Case 1	Case 2
C_λ	Jet breakup length (Nozzle dependent constant)	1.5	5.5	Case 1	Case 2
				1.5	3.5
k_1	Time scale parameter for ‘bag breakup’	0.035	0.2222	0.2222	
k_2	Time scale parameter for ‘stripping breakup’	0.17	0.2222	0.2222	
n	Exponent in IDSD	0.5	0.5	0.5	
θ	Initial spray cone angle [deg.]	Variable (9 - 12)	7.5	Case 1	Case 2
				9	12

Table 8: Optimal values of the CAB model constants, obtained for conditions corresponding to Case 1 and Case 2.

Constant	Description	Default (Tanner, 2003)	Range tested	Outcome	
C_{λ}	Jet breakup length (Nozzle dependent constant)	5.5	0.5 – 7.5	Case 1	Case 2
				1.5	3.5
k_1	Time scale parameter for 'bag breakup'	0.05	0.01 – 0.25	0.05	
k_2	Time scale parameter for 'stripping breakup'	Calculated based on k_1	Calculated based on k_1	Calculated based on k_1	
k_3	Time scale parameter for 'catastrophic breakup'	Calculated based on k_1	Calculated based on k_1	Calculated based on k_1	
n	Exponent in IDSD	0.5	0.2 – 1.5	0.5	
θ	Initial spray cone angle [deg.]	Variable (20 - 25)		Case 1	Case 2
				9	12

3.3 Non-reactive spray flow: analysis of CFD results

In the previous section, resolution tests were performed and used in model adaptation studies, which have yielded optimal values of model constants for ETAB and CAB. In the present section, the performance of the two (adapted) models is compared for Case 1, in terms of spray penetration history and flow visualisations. In all cases, the “fine” grid is used, while the numerical time step is $2 \cdot 10^{-6}$ s. Figure 3.10 shows the computed history of spray penetration length, for the ETAB and the CAB model, and also includes the experimental results of Schneider (2003). While the performance of both models is good, the CAB curve is very close to the experimental one, demonstrating a better overall performance in comparison to ETAB. This is in accordance with the nature of droplet breakup for the present constant volume sprays (catastrophic breakup), which is accounted for by the CAB model.

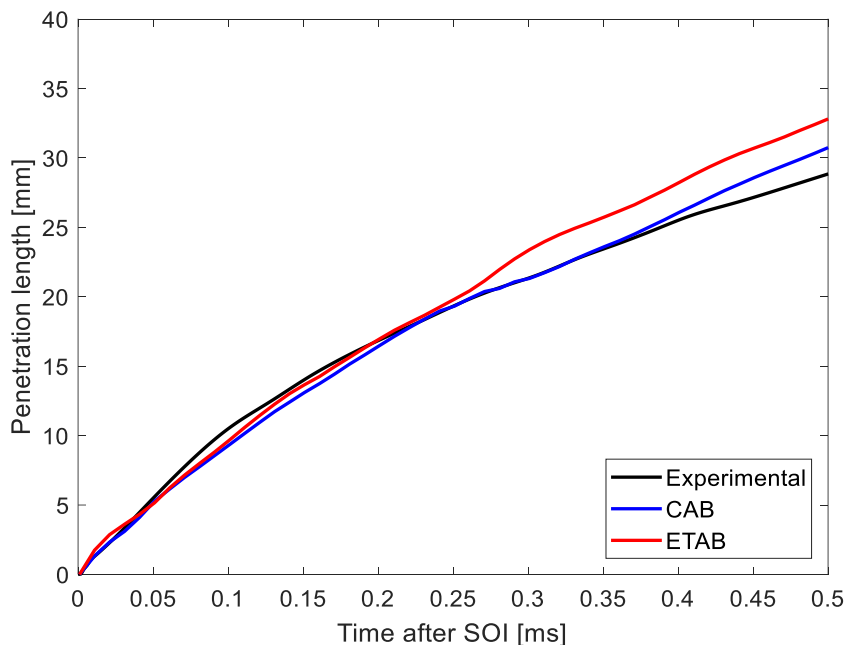


Figure 3.10: Case 1: Computed penetration length versus time for CAB and the ETAB model using the “fine” computational grid. The experimental curve of Schneider (2003) is also included.

For Case 1, Figures 3.11, 3.12 and 3.13 present visualisations of gas velocity, SMD, and spray droplet velocity, for a vertical plane including the geometry axis, at representative times, for both CAB and ETAB. A proper spray structure is predicted for both models. Considering the superiority of CAB in terms of predicting the penetration length, it is concluded that the CAB model, as adapted in the present study, is appropriate for spray simulations under similar conditions. As the sprays of the two engines of the present study are characterised by Weber number values within the catastrophic regime, the CAB model is also implemented in the engine simulations of the subsequent Chapters.

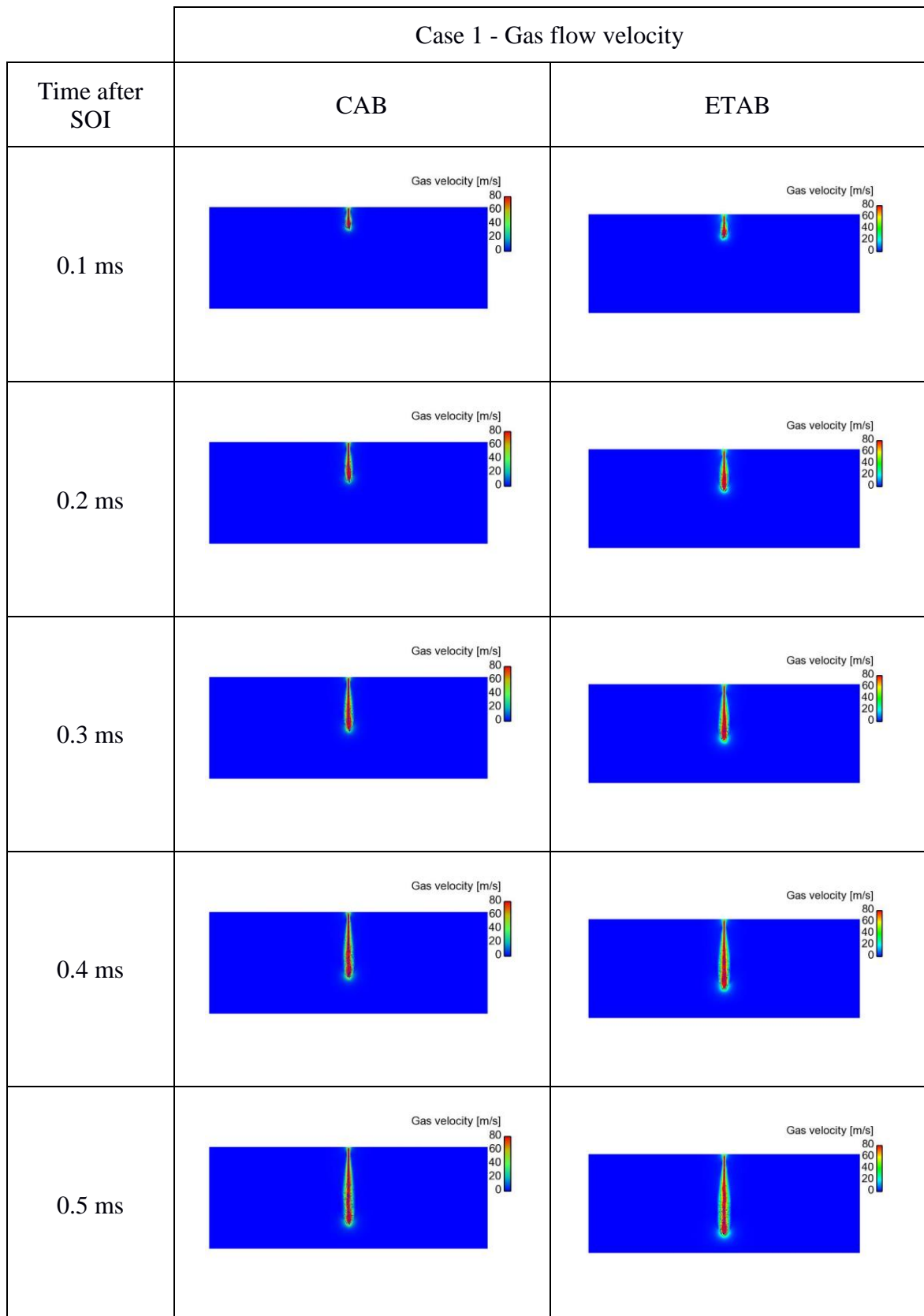


Figure 3.11: Case 1: colour-coded contours of gas velocity for the CAB and ETAB models, at a vertical plane including the injector, at representative time instants

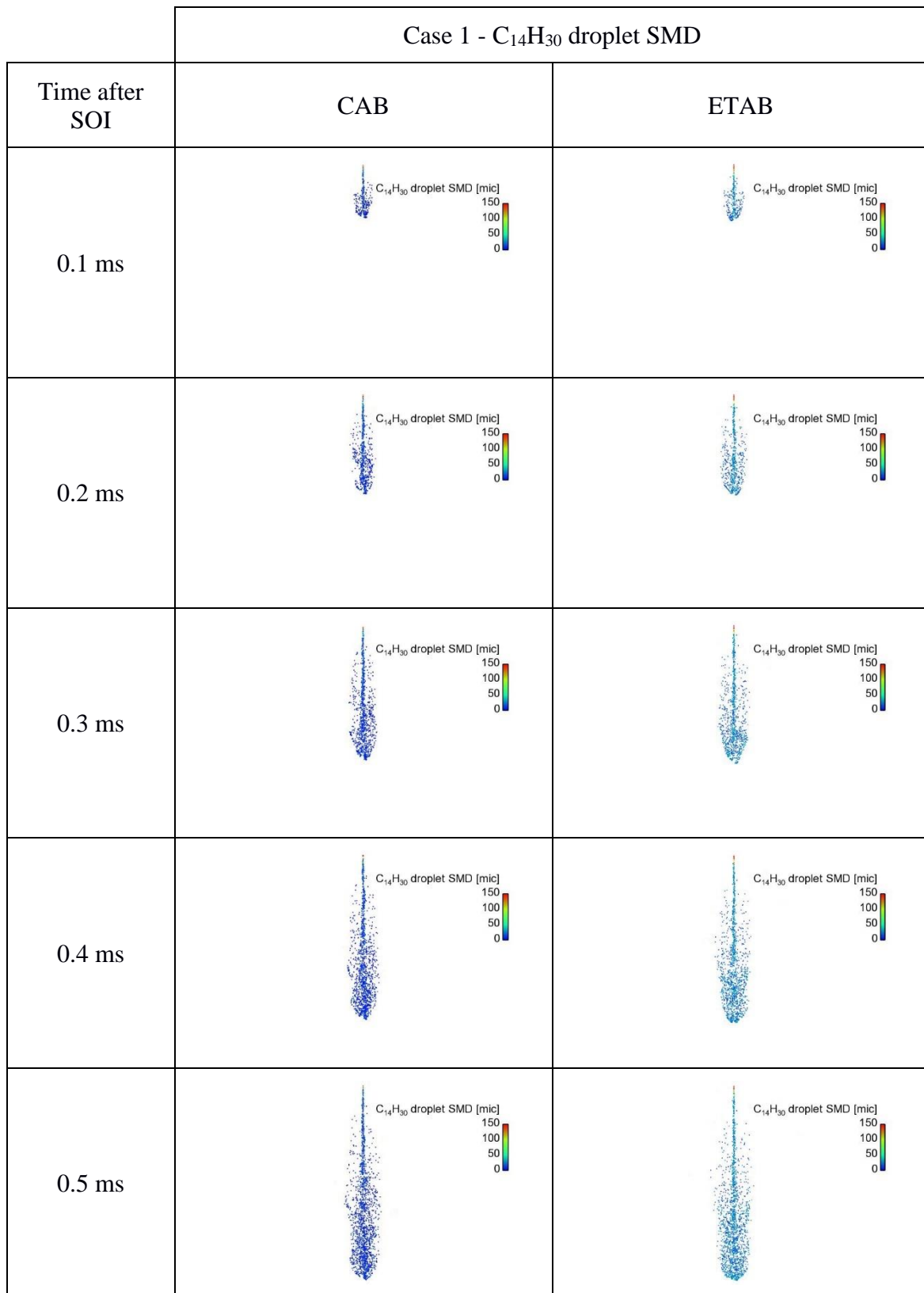


Figure 3.12: Case 1: colour-coded contours of droplet SMD (in microns) for the CAB and ETAB models, at a vertical plane including the injector, at representative time instants.

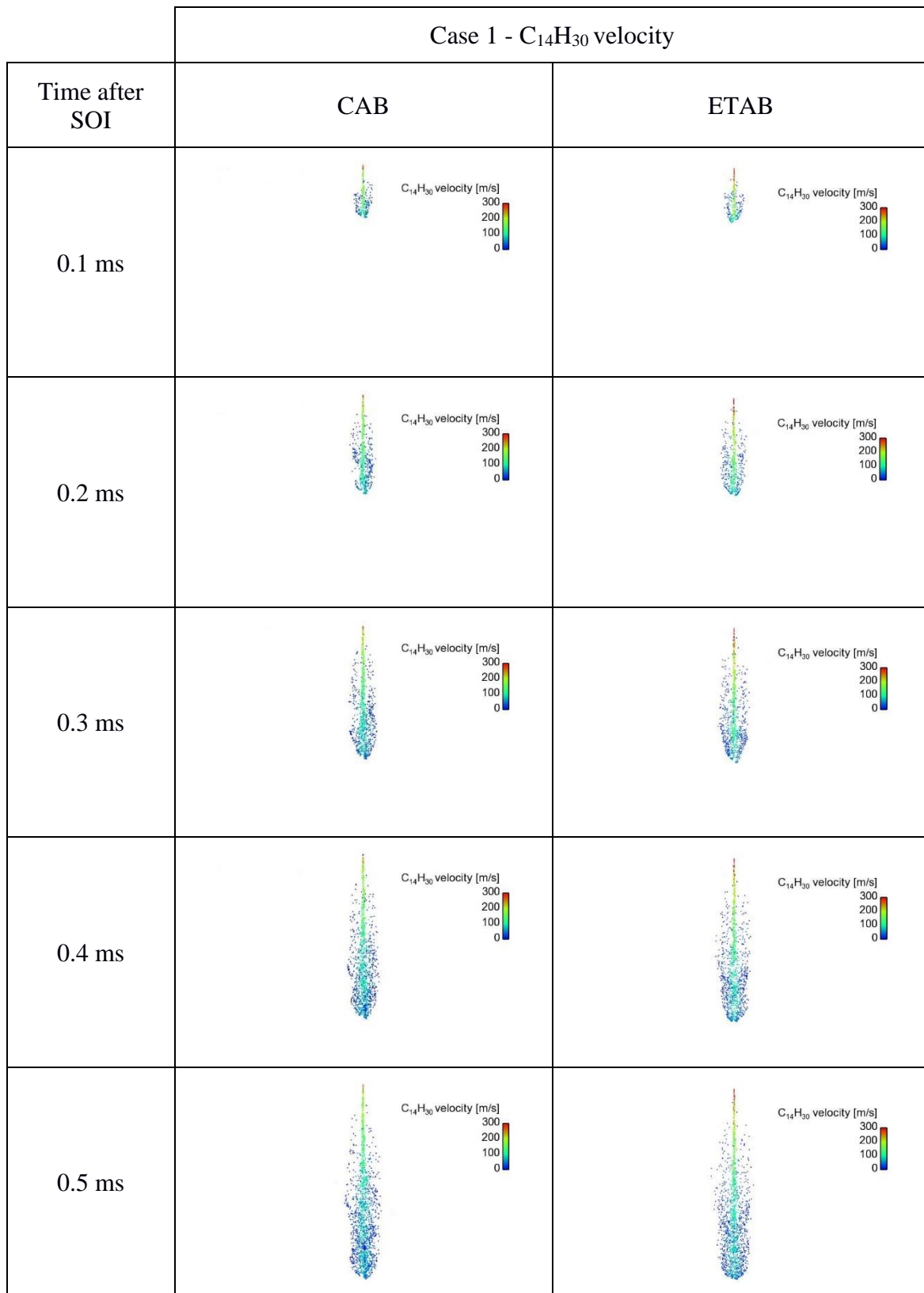


Figure 3.13: Case 1: colour-coded contours of spray droplet velocity for the CAB and ETAB models, at a vertical plane including the injector, at representative time instants.

Finally, Figures 3.14, 3.15 and 3.16 show visualisations of both Case 1 and Case 2, for gas velocity, SMD, and spray droplet velocity, computed with CAB, at the same time instants. All visualisations verify that a similar spray structure is attained for the two Cases.

Overall, the present spray simulations have demonstrated that the CAB model, as adapted in the present study, is proper for simulating sprays characterised by catastrophic droplet breakup. Thus, it is used in all subsequent simulations of the present thesis.

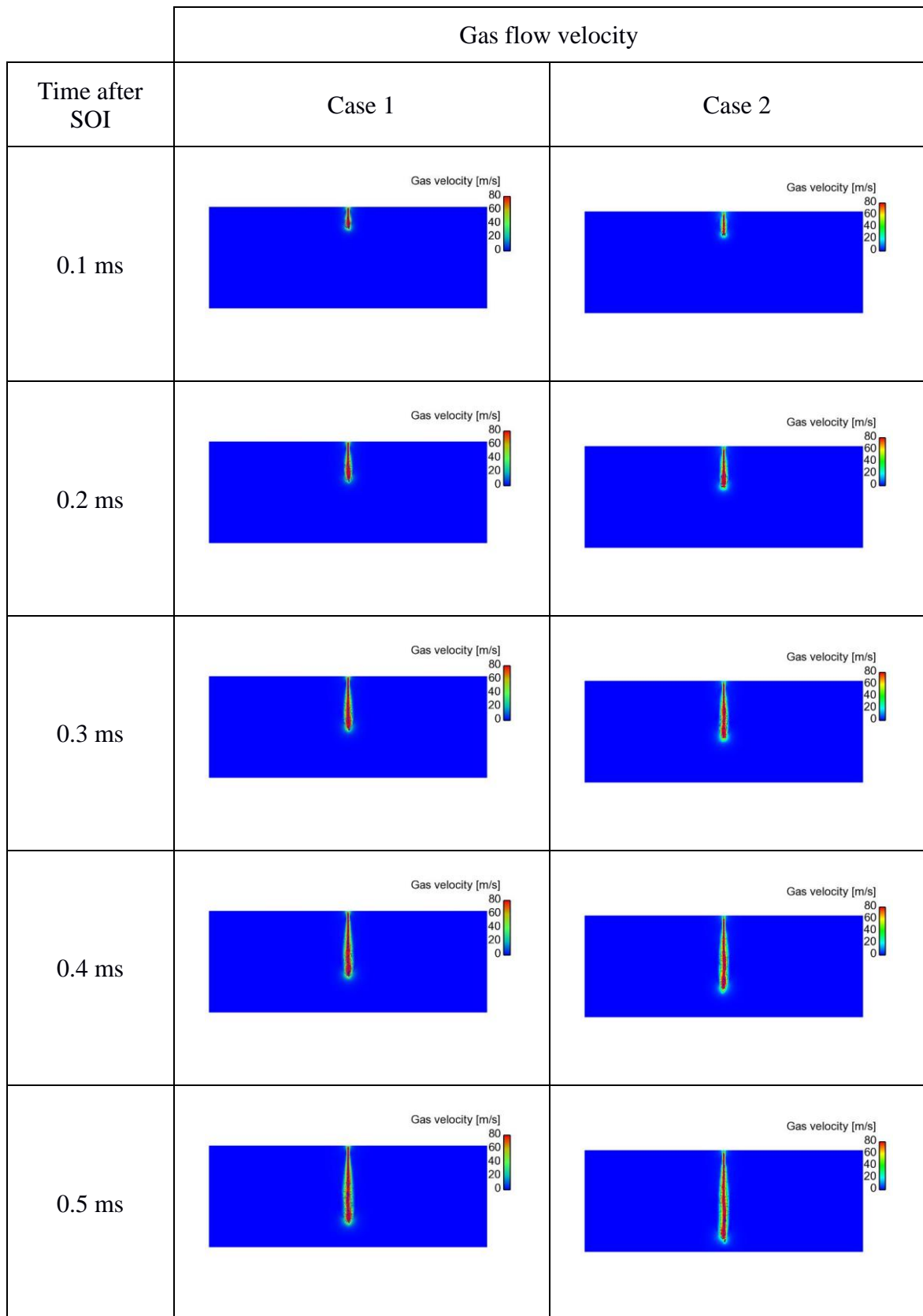


Figure 3.14: Cases 1, 2: colour-coded contours of gas velocity for the CAB and ETAB models, at a vertical plane including the injector, at representative time instants.

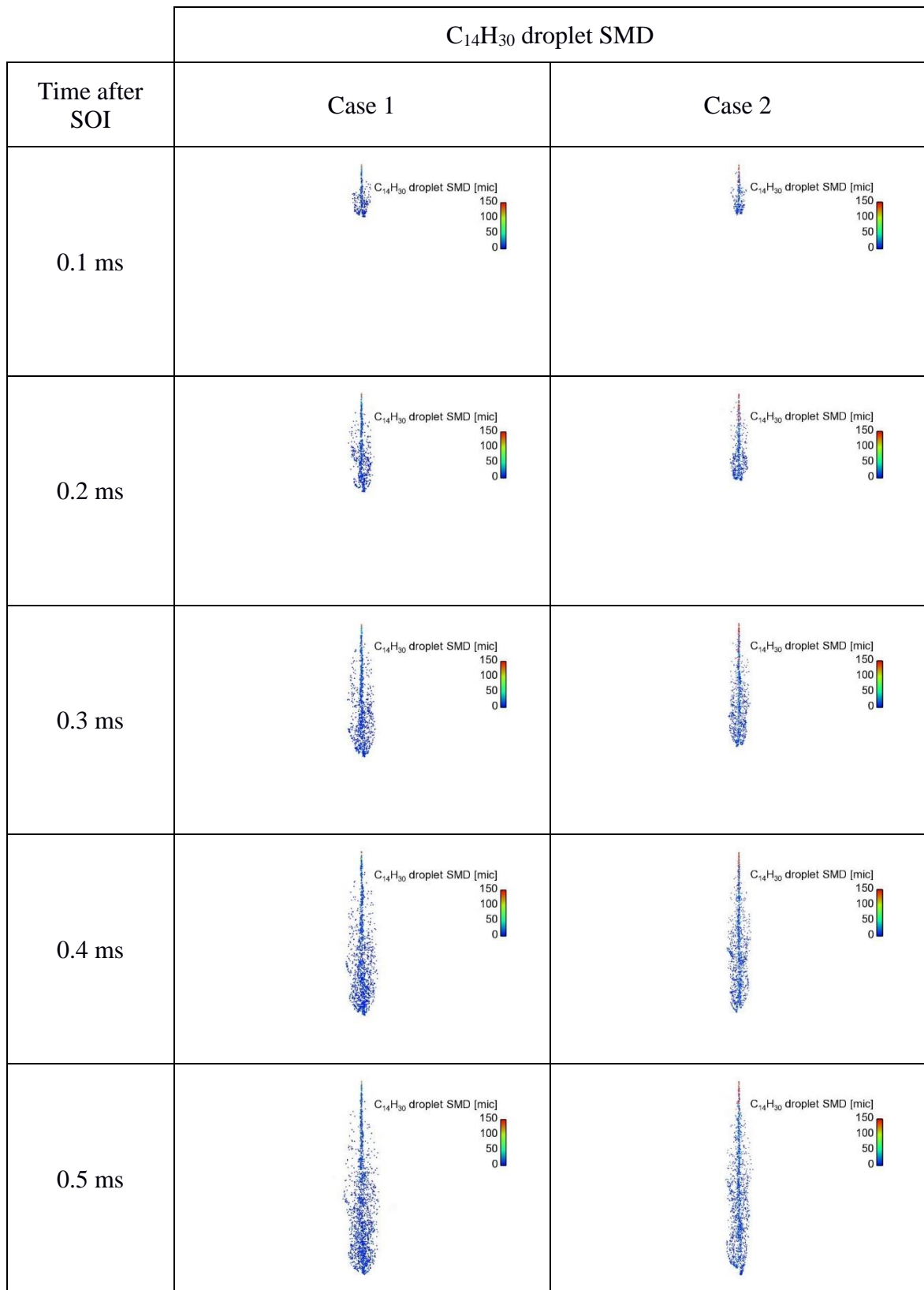


Figure 3.15: Cases 1, 2: colour-coded contours of droplet SMD (in microns) for the CAB and ETAB models, at a vertical plane including the injector, at representative time instants.

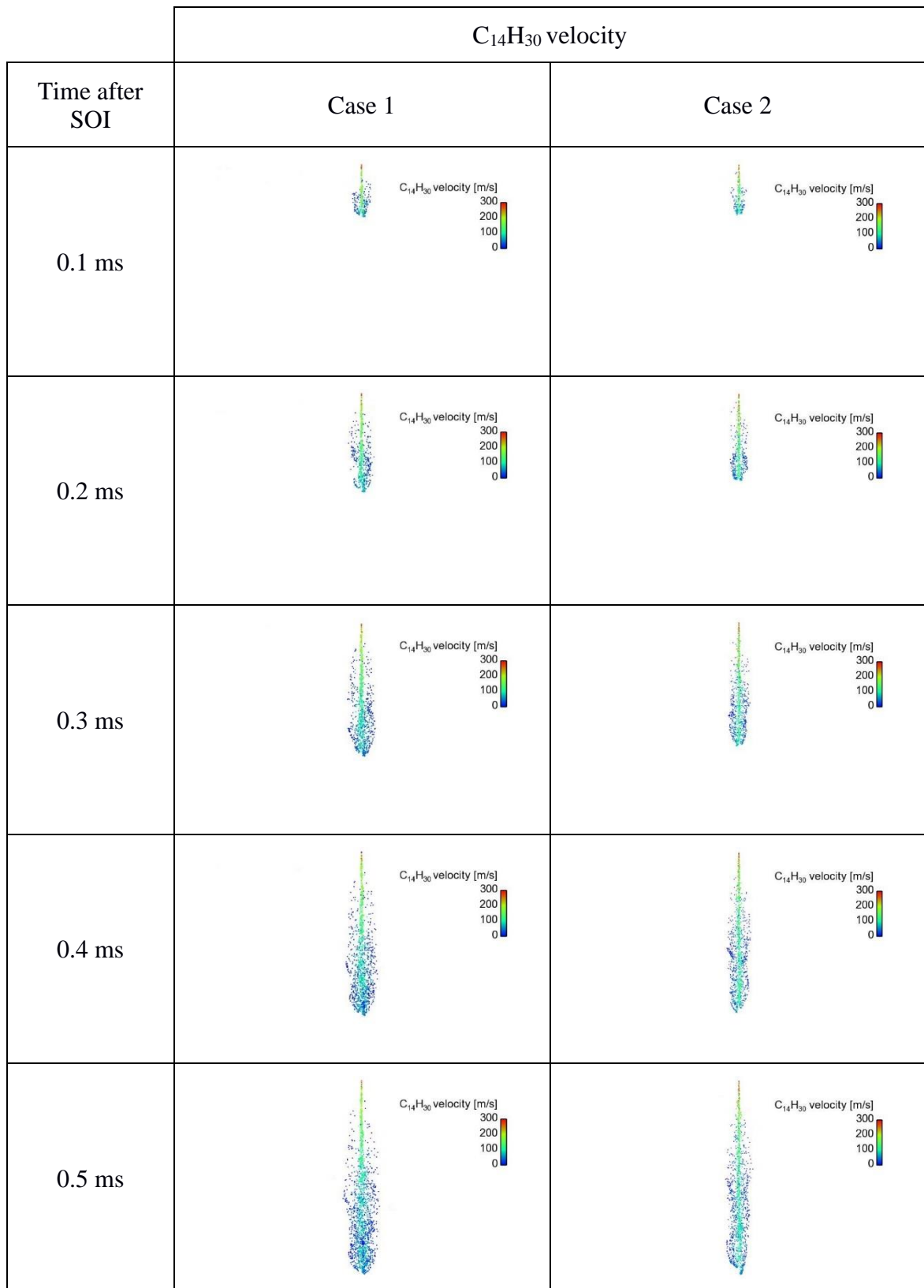


Figure 3.16: Cases 1, 2: colour-coded contours of spray droplet velocity for the CAB and ETAB models, at a vertical plane including the injector, at representative time instants.

3.4 Chapter conclusions

In the present Chapter, spray model adaptation has been performed, using CFD simulations of non-evaporating sprays in a constant volume chamber, against literature experiments. In a first step, resolution tests yielded a proper grid and numerical time step value. Next, model adaptation was performed for ETAB and CAB, using experimental penetration length histories, and verifying computations by detailed visualisations. The present study has demonstrated that, for sprays characterised by catastrophic breakup, the CAB model, as adapted here, is more accurate. Thus, it is selected and will be used in the engine simulations presented in the subsequent Chapters.

4. CFD studies of diesel combustion in an experimental dual fuel engine

The study of flow and combustion phenomena in engines can be performed using Computational Fluid Dynamics (CFD). The one-step chemistry approach is a common valuable method for modelling engine combustion, associated with a low computational cost. In the present study, two reduced-order chemical kinetics mechanisms are also used, in order to characterise and understand deeper combustion in four-stroke engines. In this Chapter, the present modelling framework is applied to the case of a small laboratory four-stroke dual fuel engine (Lister LV1), and is validated the experimental results of Papagiannakis and Hountalas (2003).

4.1 Problem definition

The engine geometry considered in the present study corresponds to the laboratory dual fuel engine Lister LV1 (Papagiannakis and Hountalas, 2003). In the present investigation, CFD studies refer to operation in the diesel mode, in particular to a load regime of 80%, considered in the experiments of Papagiannakis and Hountalas, 2003. The main engine characteristics are listed in Table 9. In the present simulations, only the closed part of the engine cycle is computed, i.e., from -139° CA (Exhaust Valve Closing (EVC)) to 139° CA (Exhaust Valve Opening (EVO)) After Top Dead Centre (ATDC). The profile of swirl velocities at the start of compression stroke is implemented in terms of a Bessel function, and corresponds to a proper value of the Swirl Number, SN (Shi and Reitz, 2008).

$$SN = \frac{\omega_{swirl}}{\omega_{engine}} \quad (4.1)$$

where,

ω_{swirl} is the angular velocity of air flow

$\omega_{engine} = \frac{2\pi N}{60}$ is the angular velocity of engine revolution

N is the engine revolution speed (RPM)

In the present one-step chemistry simulations, fuel thermophysical properties are determined from those of n-tetradecane ($C_{14}H_{30}$), and the values are close to those of the actual fuel used in experiments (Papagiannakis and Hountalas, 2003).

Table 9: Main characteristics of the Lister LV1 engine.

Main engine characteristics	
Bore diameter	8.573 cm
Stroke	8.255 cm
Connecting rod length	14.859 cm
Clearance height at TDC	0.2 cm
IVC	-139 deg
EVO	139 deg
Engine speed at 80% load	2000 rpm
Nozzle diameter	0.23 mm

A modified KIVA-3vr2 code (Amsden, 1999) is used in the present simulations for the one-step combustion. KIVA-3vr2 solves the Reynolds averaged conservation equations for mass, momentum and energy, described by eq. (2.1), (2.3) and (2.12), respectively, utilising physical models to account for the different physical phenomena pertinent to engine aerothermochemistry. Such phenomena include, for instance, the breakup and evaporation of the fuel spray interacting with the turbulent multi-component gas flow. The code has been modified in terms of physical models, to accommodate effectively for operation in the diesel mode. The modifications concern fuel atomisation, ignition, combustion, and pollutant emissions formation. Details regarding the physical models used have been presented in Chapter 2 of the present thesis.

Moreover, this Chapter presents and applies an integrated computational tool, developed by coupling a KIVA-3vr2 based CFD code (Amsden, 1999) with the CHEMKIN-II chemical kinetics code (Kee et al., 1989). The development was initiated by the Laboratory of Aerothermochemistry and Combustion Systems of ETH Zurich, and carried out in a major part by the NTUA research team of Prof. L. Kaiktsis.

In the present study, Re-Normalisation Group (RNG) k - ϵ type of model with wall functions are used for turbulence modelling, with standard values for the model constants (Amsden, 1997). Spray modelling is based on the CAB model (Tanner, 2004), an important extension of the Enhanced Taylor Analogy Breakup (ETAB) model (Tanner, 1997, Tanner and Weisser, 1998). The CAB model adopts the analogy between an oscillating drop penetrating into a gas (with a given relative velocity) and a forced damped spring-mass system, as in ETAB. In the present thesis, the CAB model has been extensively tested and validated against experiments, as presented in Chapter 3. A single-component evaporation model, accounting for the effect of fuel vapor superheating, is used in the present study (Baumgarten, 2006). In addition to the one-step approach, in the present study, combustion modelling uses the coupling of the CFD code with the CHEMKIN-II chemical kinetics code, thus accounting

for a reduced order chemistry description. Here, reduced order mechanisms with 29 species and 52 chemical reactions (Mech.29) (Patel et al., 2004) and 45 species and 142 chemical reactions (Mech.45) (Ra and Reitz, 2008) are used (Table 10). In this context, for a given time step and computational cell, the CFD code provides the initial mass fraction of species, pressure and temperature to the chemical kinetics code. The latter calculates the new production rate of each species included in the reduced order chemistry mechanism. It is noted that in the KIVA code decouples the diffusion and convection calculation terms from the chemical source term due to chemical reactions; therefore, each computational cell can be considered as a homogeneous mixed reactor at every time-step (Kakaee et al., 2015).

The main objectives of the present engine simulations are thus: (a) to account for a proper description of fuel spray breakup, and (b) to properly account for the chemistry of diesel combustion. The expected overall outcome is an improved description of engine aerothermochemistry, including an accurate prediction of global quantities as Rate of Heat Release and pressure.

Table 10: Chemical kinetics mechanisms of s n-heptane combustion.

Literature reference	Name of mechanism	Number of species	Number of chemical reactions
Patel et al., 2004	Mech.29	29	52
Ra and Reitz, 2008	Mech.45	45	124

4.2 Analysis of CFD results

The three-dimensional grids used in the present study correspond to a sector of 120 degrees. Two types of grids were generated in the present work. The first type corresponds to block-structured meshes, uses a polar coordinate system, and is generated by means of the pre-processor module K3PREP; typical grids consist of 12,659 cells. The second type also corresponds to block-structured meshes, uses a cartesian coordinate system, and is generated using the ICEM-CFD grid generator; typical grids consist of 8,314 cells. The two grids are presented in Figure 4.1. It is noted that simulations using one-step chemistry utilised the polar grid, also used for the case of realistic chemistry with the Mech.29 mechanism. Simulations with realistic chemistry using the Mech.45 mechanism have utilised the cartesian grid.

It is noted that engine operation also depends on the intensity of air swirl, as quantified by the Swirl Number, SN. Results of a parametric study in terms of a variation in SN are presented in Appendix A.

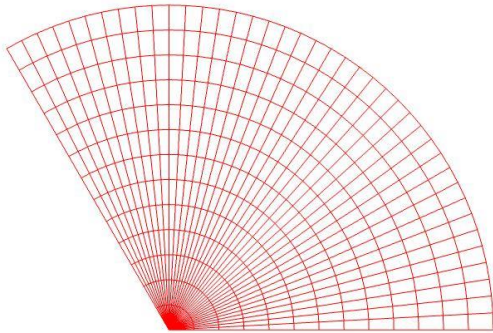
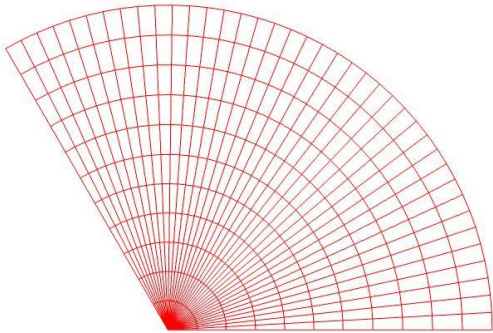
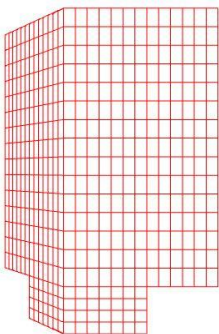
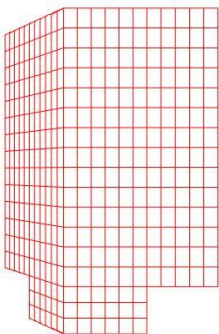
	Polar mesh (K3PREP) 12,659 cells	Cartesian mesh (ICEM) 8,314 cells
Top view		
Front view		

Figure 4.1: Top and front views of the polar and cartesian grid used in the simulations of the Lister LV1 engine.

The Lister LV1 engine is equipped with one central injector, with three identical orifices. The symmetric injection from the three orifices generates a flow and combustion pattern characterised by

a symmetry in mean flow, i.e., the mean flow repeats itself every 120 degrees. Thus, in the frame of RANS simulations, a sector of 120 degrees can be used, with periodic boundary conditions for the lateral boundaries. The injection direction is characterised by the vertical angle β , while, in CFD simulations, a horizontal angle, α , should be also specified; see Figure 4.2. The injection profile is implemented in the present study in terms of square wave, of a proper start and duration (D. Hountalas, private communication); see Figure 4.3.

Important data of the present simulations, including engine data and operational parameters reported in Papagiannakis and Hountalas (2003) are presented in Table 11.

Table 11: Parameters pertinent to operation and injection characteristics of the Lister LV1 engine.

Reference engine operating conditions	
Intake Pressure	1.3 bar
Initial Temperature	320 K
Start of injection	-16.55 deg
Injection duration	26 deg
Injected mass per cycle	0.01636 g
Number of injectors	1
Number of injector nozzle holes	3
Horizontal angle $\hat{\alpha}$	60 deg
Vertical angle $\hat{\beta}$	55 deg
Contraction coefficient	0.8

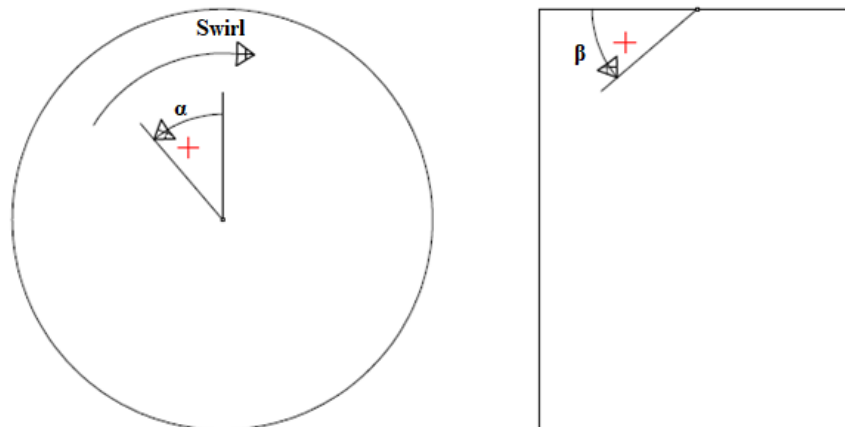


Figure 4.2: Definition of injection direction in terms of angles α and β .

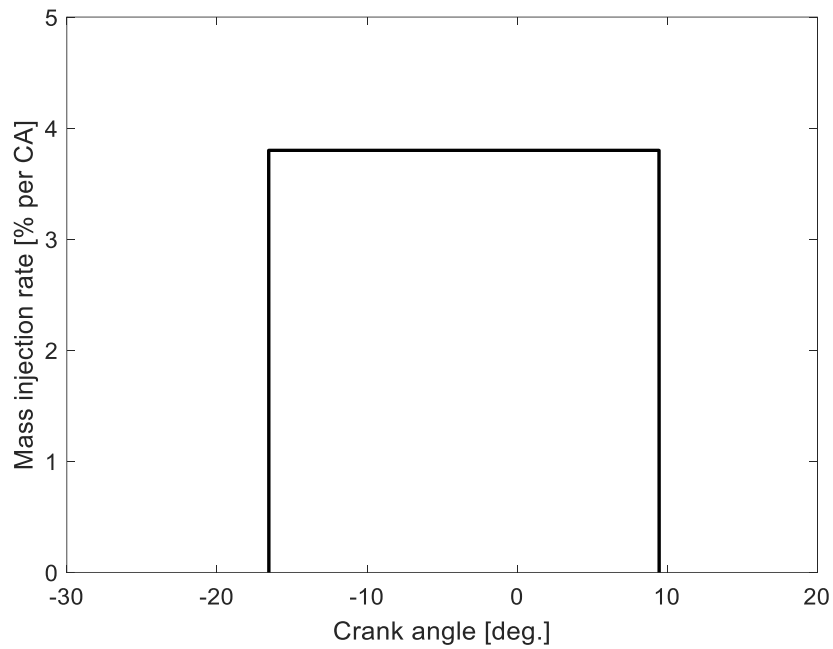


Figure 4.3: Injection profile of the Lister LV1 engine for operation at a load of 80%.

As indicated above, the present engine simulations utilise a computational tool based on coupling a KIVA-3vr2 based CFD code with the CHEMKIN-II chemical kinetics code. The CAB spray model, as adapted based on the constant volume chamber simulation presented in Chapter 3, accounts for spray breakup. Figure 4.4 presents the variation of the value of K_{bu} versus droplet Weber number, and also depicts the transition points between the different modes of drop breakup, including both the ETAB (Tanner, 1997) and the CAB (Tanner, 2004) models. Estimates of droplet Weber number indicate that, in all cases associated with the present simulations of the Lister LV1 engine, droplet breakup corresponds to catastrophic breakup.

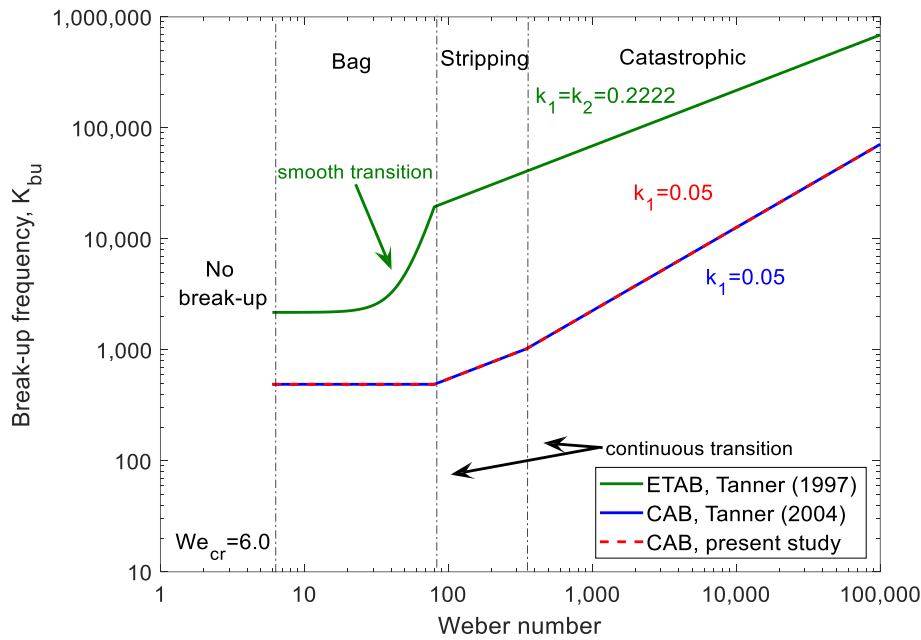


Figure 4.4: Proportionality constant K_{bu} versus Weber number for the ETAB and CAB models.

Figures 4.5 and 4.6 show the computed cylinder pressure and normalized Rate of Heat Release (ROHR) traces, respectively, for the one-step chemistry and the two reduced order chemistry mechanisms, Mech.29 and Mech.45. The corresponding experimental pressure and normalized ROHR curves are also included. In all cases, a very good agreement between the experimental results and the present simulations is demonstrated, which is best for the case of the Mech.45 mechanism. The ROHR curves verify the presence of a premixed and a diffusion phase of combustion. It is noted that the maximum pressure, as predicted for the simulation with Mech.29, is higher, by about 2 bar, in comparison to the experiment and the other two simulations. This should be associated with the longer delay in main ignition with Mech.29 (see Figure 4.6), which accumulates unburned evaporated fuel, which in turn burns at a higher rate after ignition, resulting in a sharper pressure increase; it is noted that a two-stage ignition appears to be present for this simulation. Finally, Figure 4.7 presents the computed history of mean cylinder temperature, verifying the longer ignition delay for the case of Mech.29, and also indicating computed lower temperature levels for the case of Mech.45.

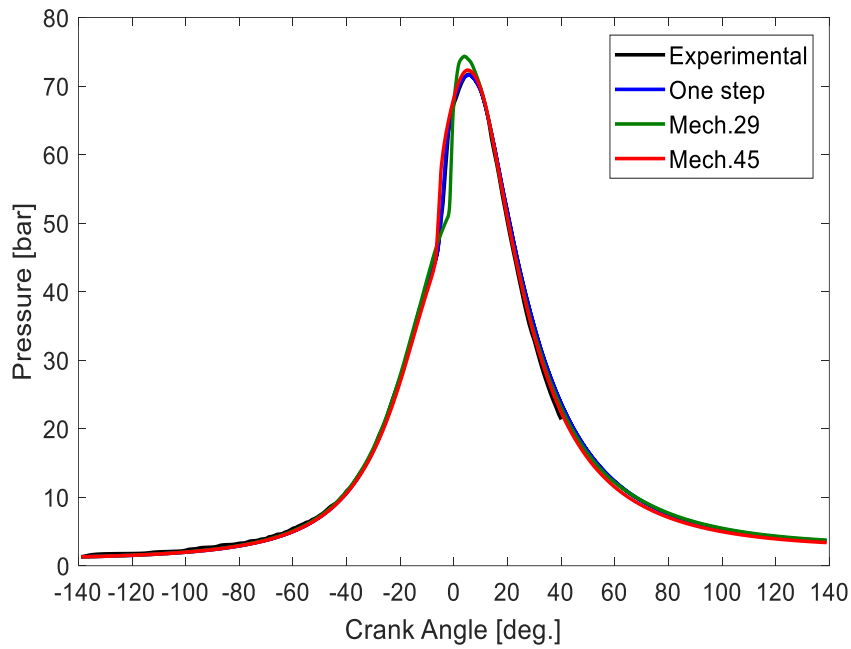


Figure 4.5: Computed traces of cylinder pressure using one-step chemistry and the two reduced order chemical kinetics mechanisms (Mech.29 and Mech.45), at an engine load of 80%. The corresponding experimental curve (Papagiannakis and Hountalas, 2003) is also included.

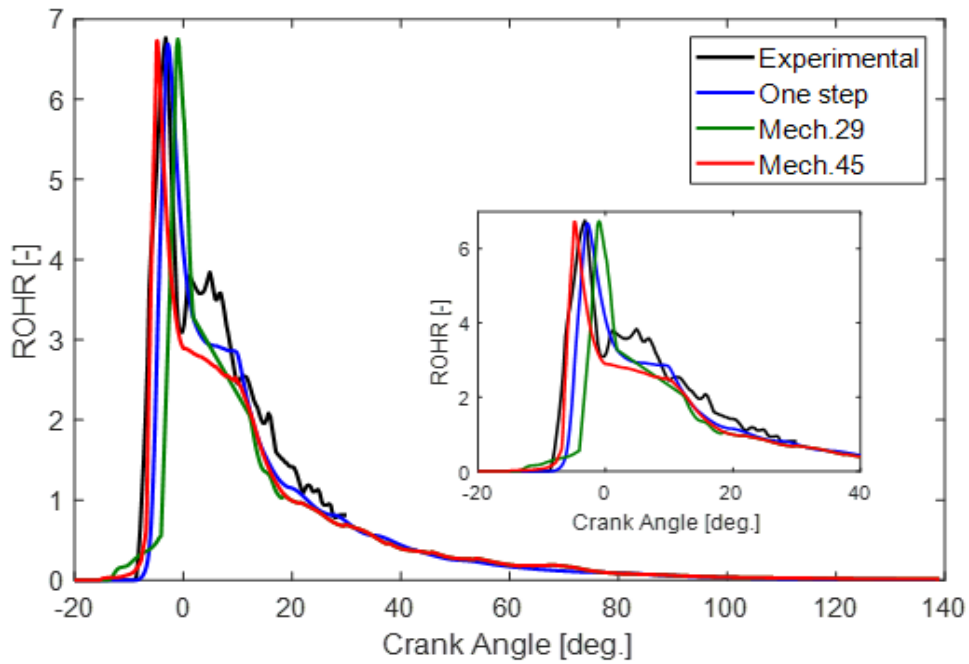


Figure 4.6: Computed traces of normalized Rate of Heat Release using one-step chemistry and the two reduced order chemical kinetics mechanisms (Mech.29 and Mech.45), at an engine load of 80%. The corresponding experimental curve (Papagiannakis and Hountalas, 2003) is also included.

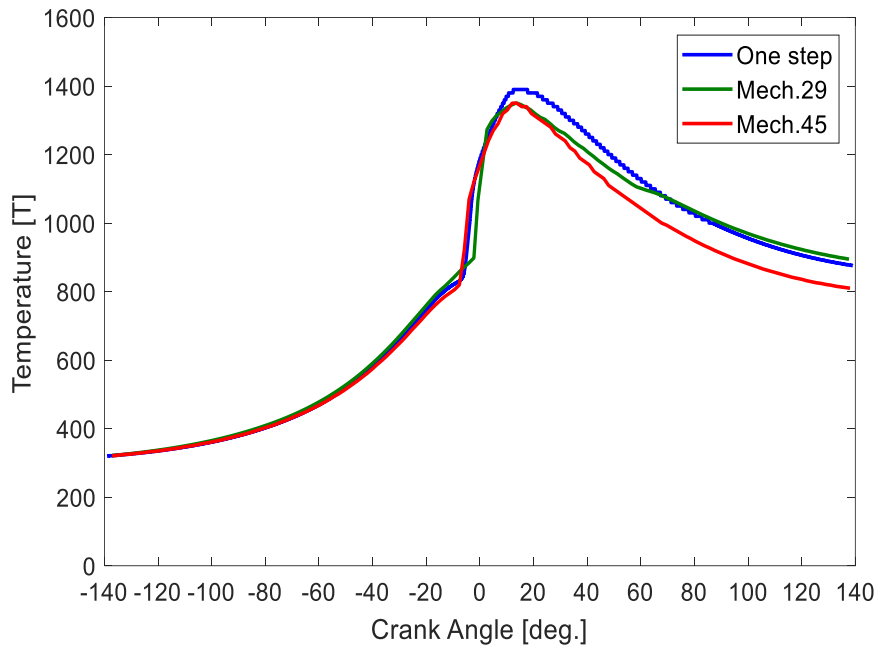


Figure 4.7: Computed traces of mean cylinder temperature using one-step chemistry and the two reduced order chemical kinetics mechanisms (Mech.29 and Mech.45), at an engine load of 80%.

Next, the development of combustion is characterised in terms of visualisation of the computed fields of temperature, equivalence ratio, fuel decomposition rate, and concentration of OH radical, CH₄, CH₂O, CO, CO₂, NO_x and soot, at selected time instants, namely -15°, -10°, -5°, 0°, 5°, 10°, 15°, 20° and 25° of engine crank angle (CA). Visualisation utilises a representative horizontal and a representative vertical plane, both close to injector, which are depicted in Figure 4.8.

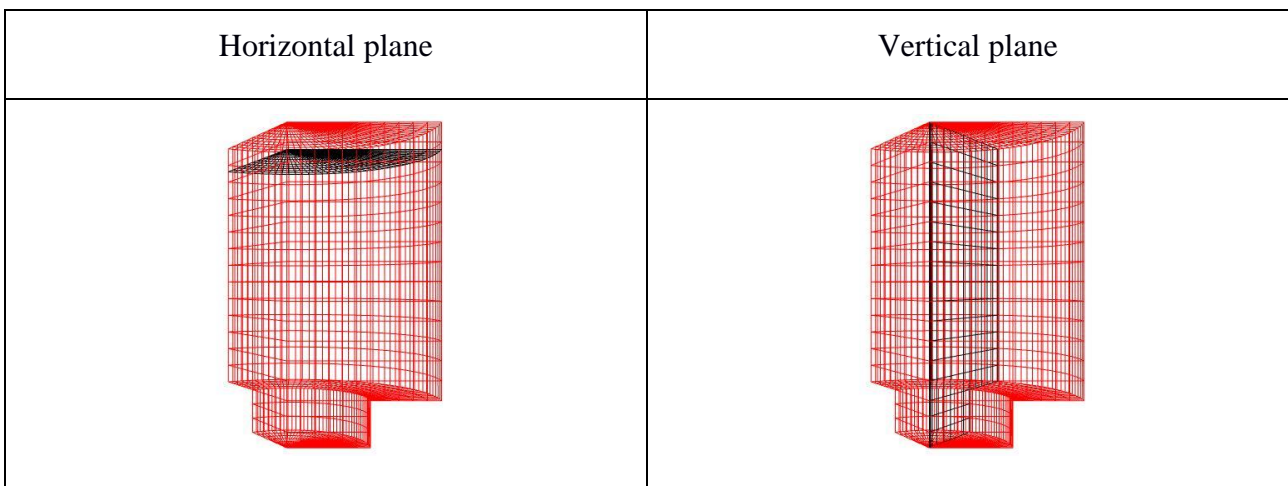
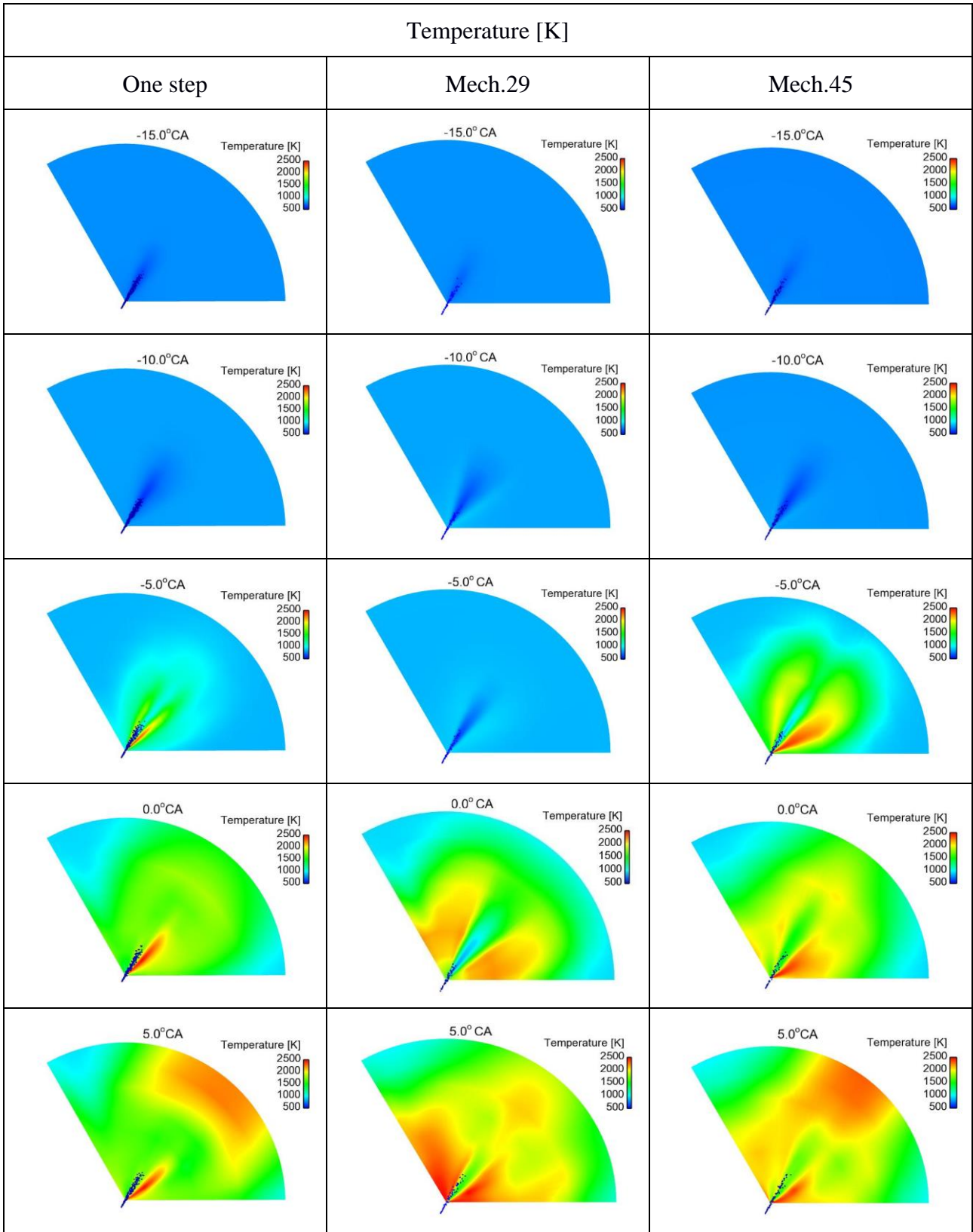


Figure 4.8: Horizontal and vertical planes used in visualisation of the computed fields.

Figure 4.9 presents visualisations (top view) of the distribution of temperature at representative time instants, for simulations using the one-step approach and the two reduced mechanisms (Mech.29 and

Mech.45), at the horizontal plane depicted in Figure 4.8. These visualisations verify the delayed main ignition for the simulation using Mech.29, as well as the rapid combustion development when using the reduced mechanisms, in contrast to the slower one for one-step chemistry. Further, using realistic chemistry results in a more distributed combustion, as compared to a more concentrated one for one-step chemistry. Finally, the asymmetry in the computed fields should be attributed to a convection effect due to the present of (a clockwise) swirl. Figure 4.10 presents visualisations of temperature in the vertical plane. The broader distribution for the cases of realistic chemistry simulations is verified. Figures 4.9 and 4.10 illustrate the presence of hot regions close to piston and liner, associated with high thermal loading. In the case of one-step chemistry, the temperatures in the near-piston region are clearly higher, and this should be associated with the slower development of combustion, which results in local higher burning rates.



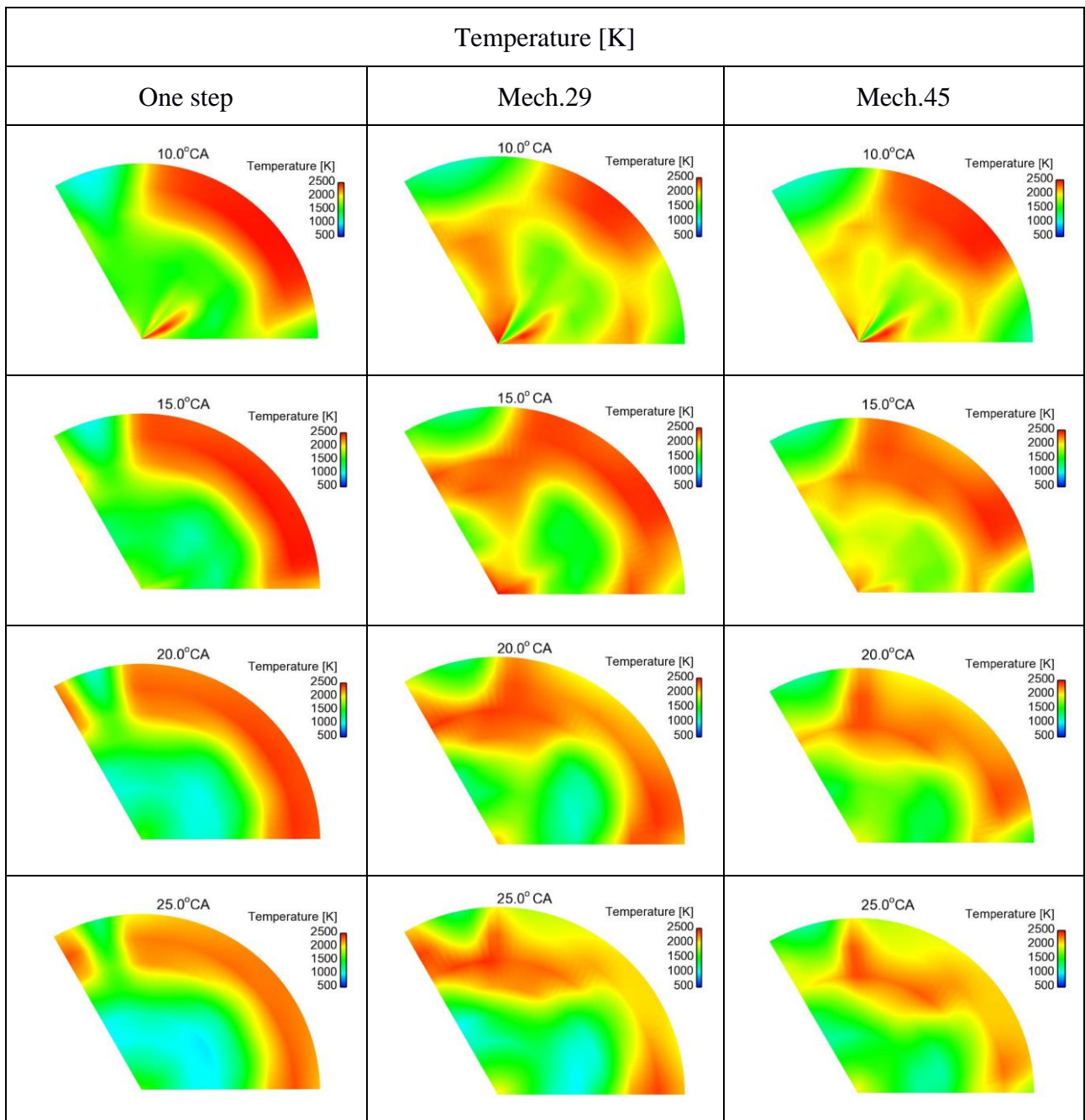
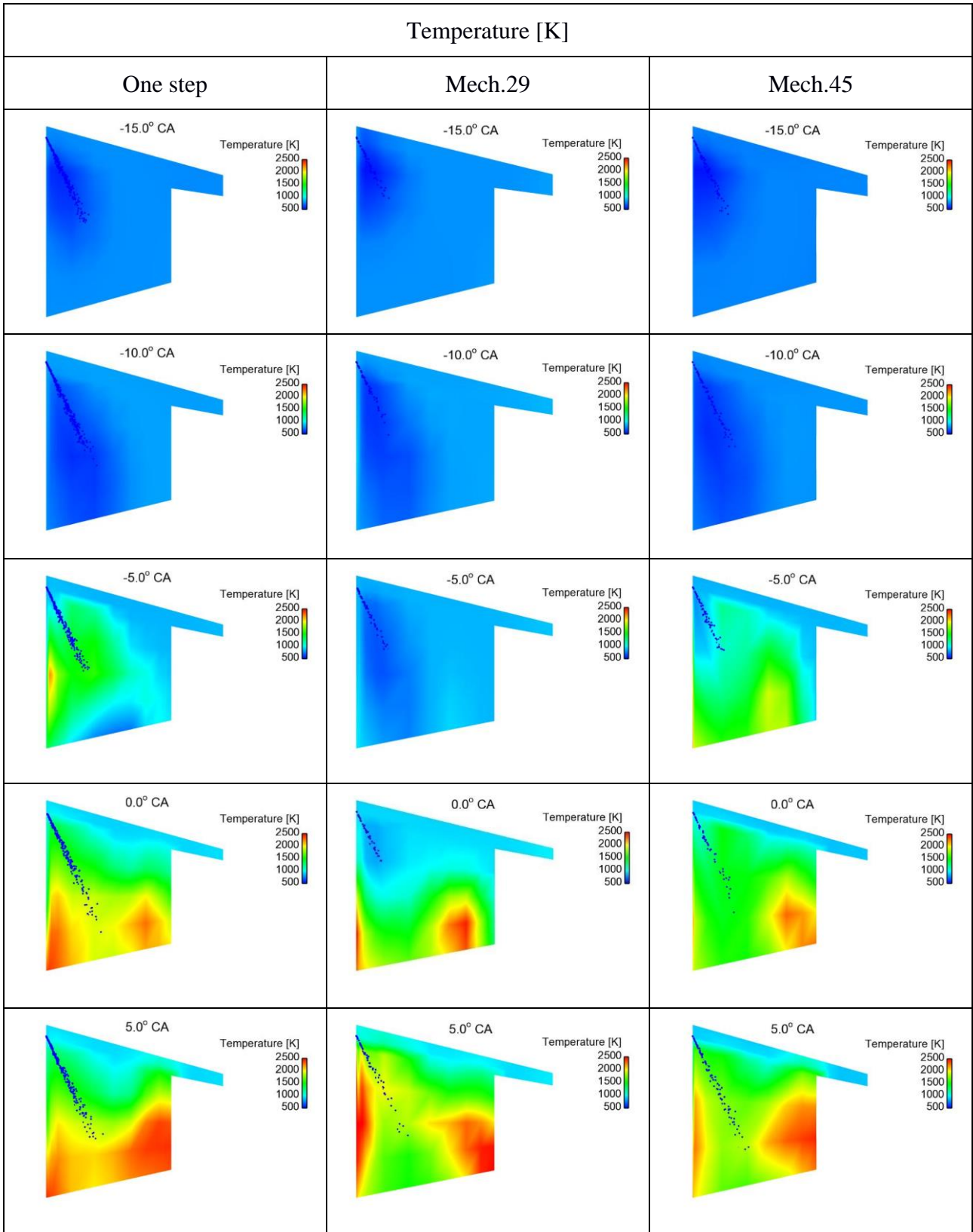


Figure 4.9: Colour-coded contours of temperature for one-step chemistry and reduced order chemistry using mechanisms Mech.29 and Mech.45. A horizontal plane very close to the injector is considered, at selected time instants.



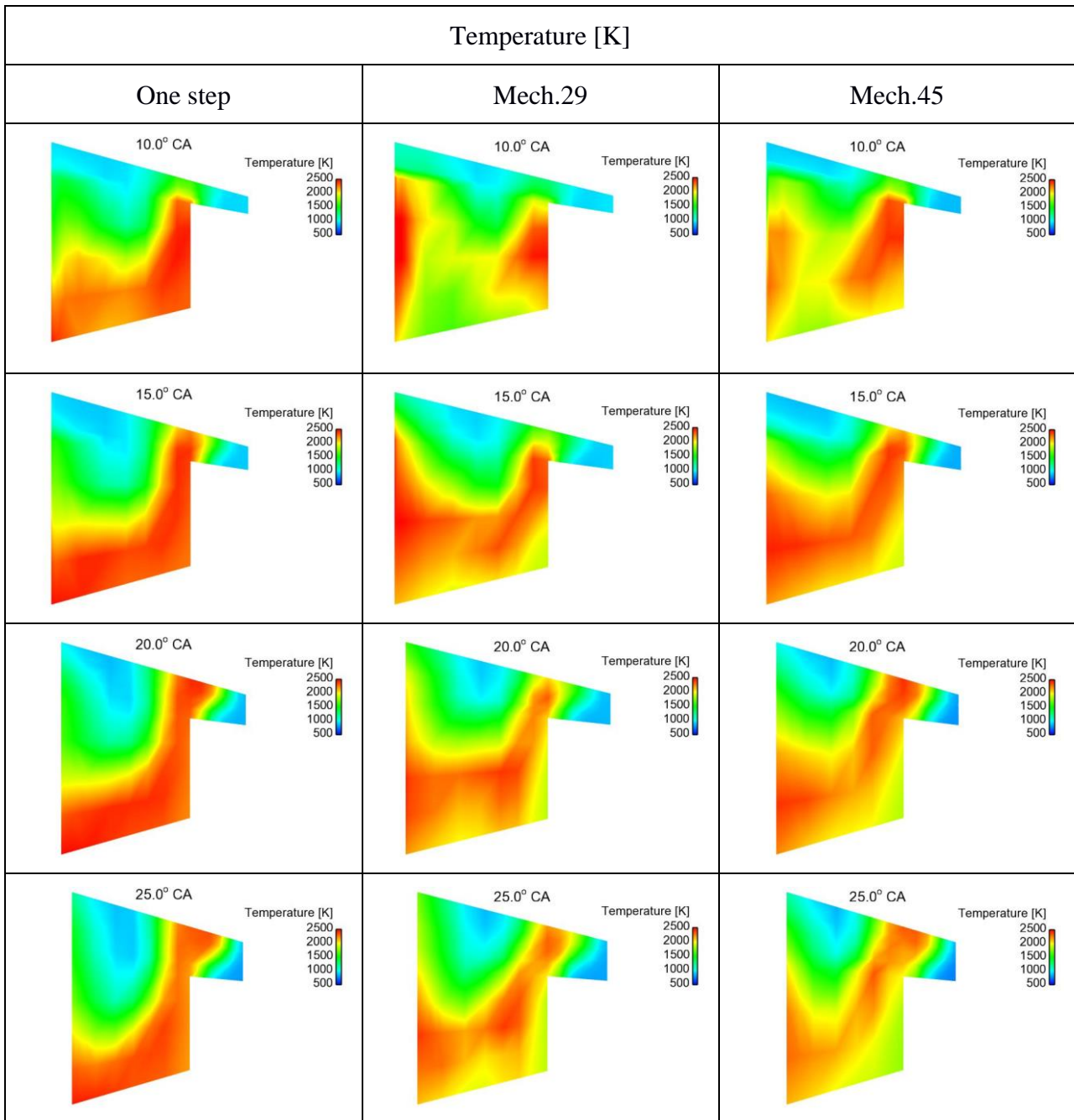
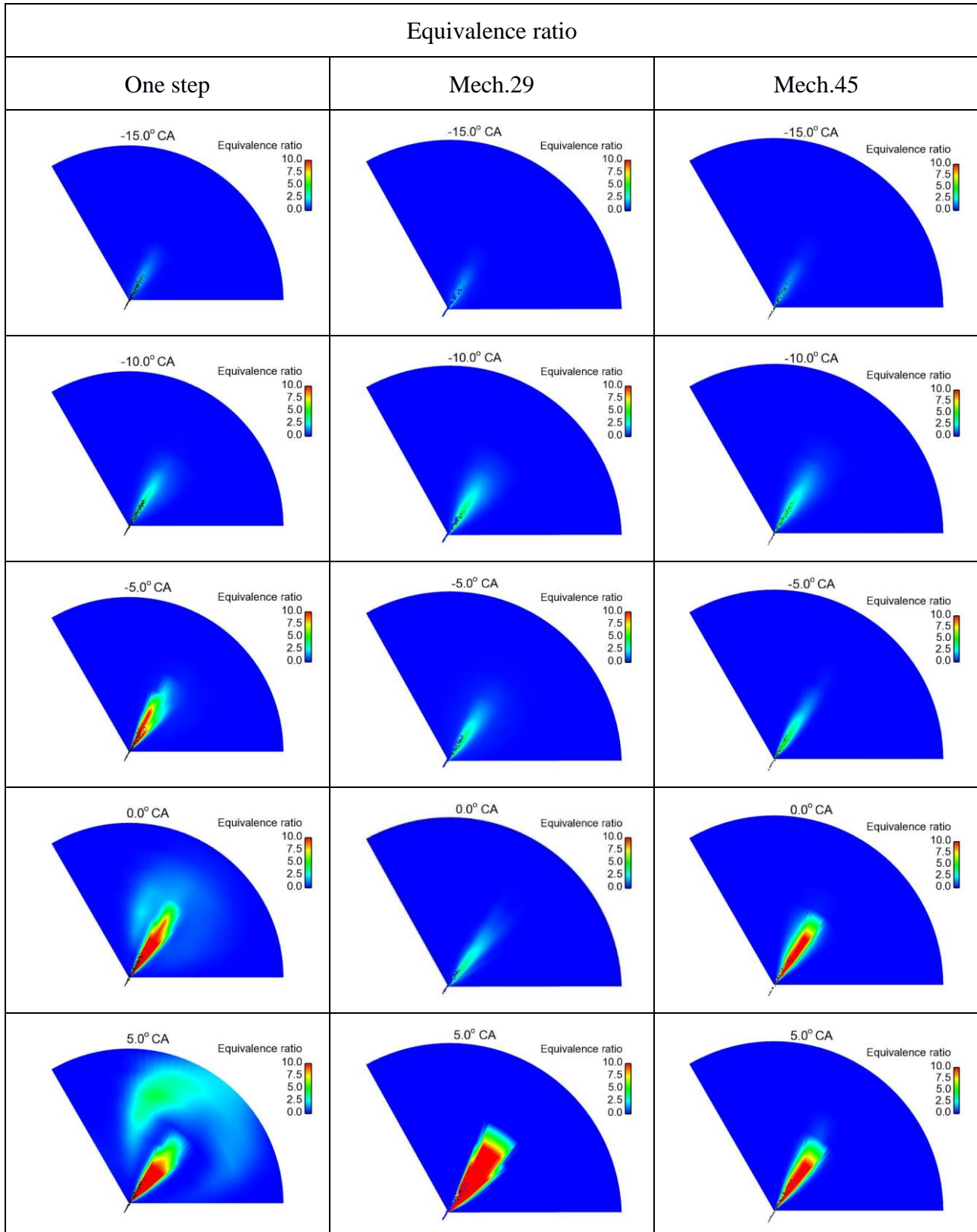


Figure 4.10: Colour-coded contours of temperature for one-step chemistry and reduced order chemistry using mechanisms Mech.29 and Mech.45. A vertical plane including the injector is considered, at selected time instants.

Figure 4.11 presents visualisations of the distribution of equivalence ratio at representative time instants, for simulations using the one-step approach and the two reduced mechanisms (Mech.29 and Mech.45), at the horizontal plane depicted in Figure 4.8. The more rapid consumption of fuel in the cases of reduced chemistry is verified. The slow fuel consumption in the case of one-step chemistry results in the strong presence of fuel close to the cylinder liner, in the late stages of combustion. For Mech.29, a stronger presence of evaporated fuel close to the injector is evident immediately after TDC, verifying a longer main ignition delay.

The process of combustion for one-step chemistry is carried out with deceleration compared to both

reduced mechanisms; this justifies the accumulates fuel and it also burns for a prolonged period. The present snapshots also show the small determination to ignition delay time for the reduced order mechanism with Mech.29. It is noted that in Figure 4.11 displays the evolution of combustion between the one-step chemistry and both reduced order chemistry mechanisms.



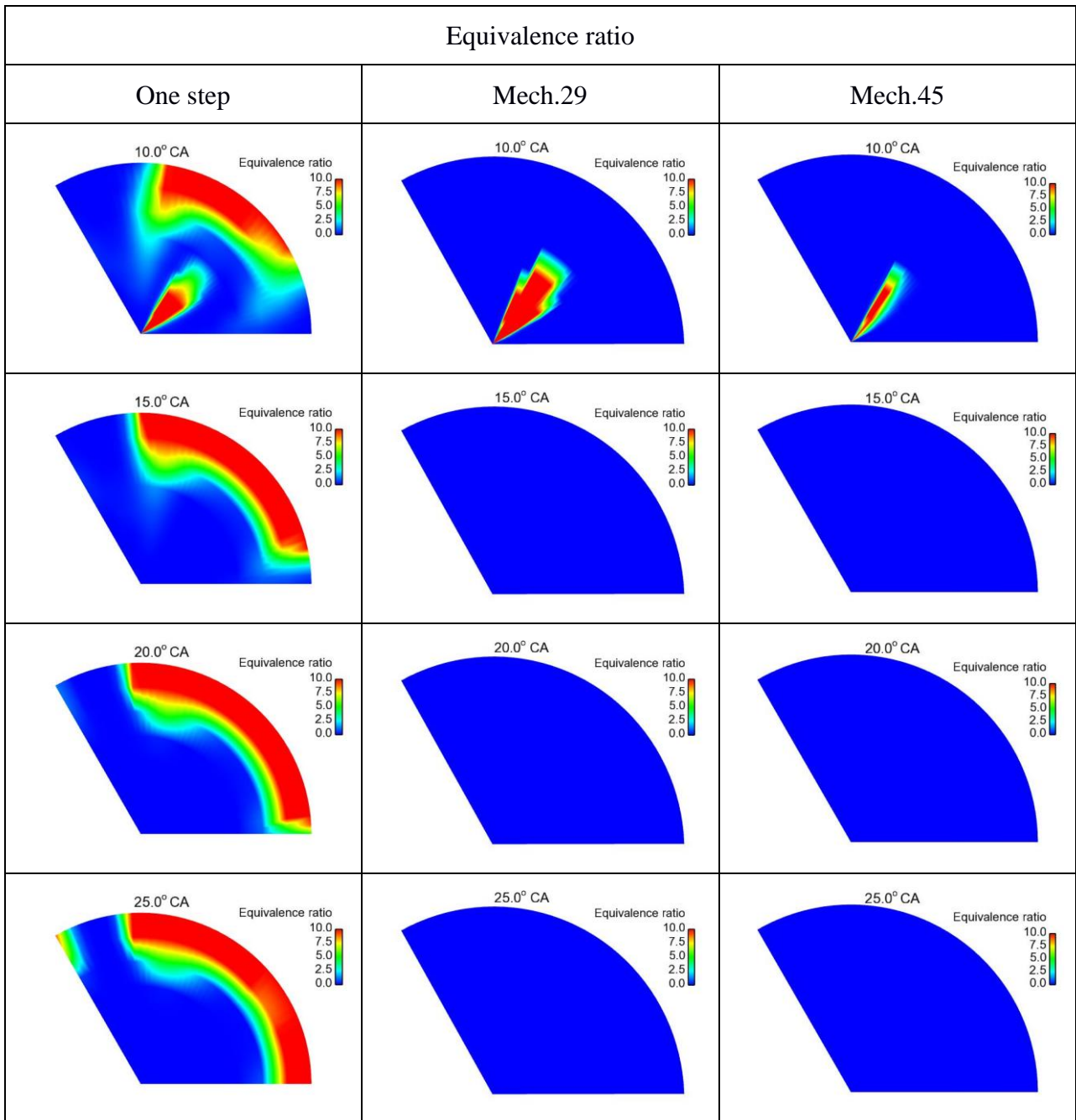


Figure 4.11: Colour-coded contours of equivalence ratio for one-step chemistry and reduced order chemistry using mechanisms Mech.29 and Mech.45. A horizontal plane very close to the injector is considered, at selected time instants.

To further elaborate on the CFD results on ignition delay, the computed ignition delay times based on the present CFD results are presented in Figure 4.12, along with computed values of ignition delay versus temperature, at a pressure close to 90 bar, for representative HFO qualities (Kontoulis, 2019), and ignition delay times of stoichiometric n-heptane – air mixtures as computed by chemical kinetics simulations (Weisser, 2001). Figure 4.12 verifies that the present CFD results correspond to ignition delays shorter than those of HFO ignition, as well as that the present values are close to those of the results in Weisser (2001).

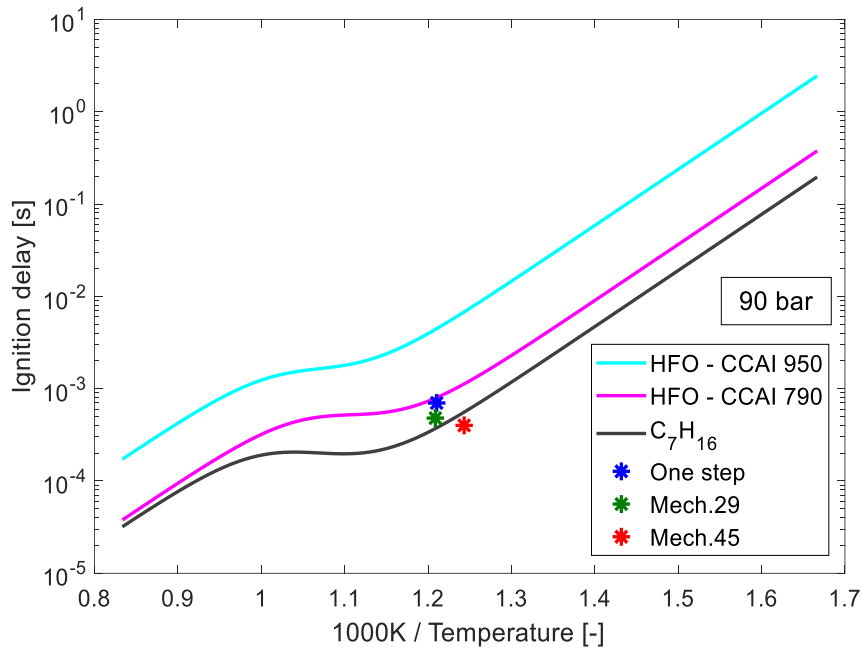


Figure 4.12: Calculated ignition delay times versus temperature for: (a) present CFD simulations using one-step chemistry and realistic chemistry with the reduced mechanisms Mech.29 and Mech.45 in the Lister LV1 engine (colour dots); (b) CFD simulations in a constant volume combustion chamber using two marine fuels with CCAI value in the upper and low limit of marine HFOs, as reported in Kontoulis, 2019; (c) chemical kinetics calculations of n-heptane (C_7H_{16}) combustion at $P=90$ bar and $\Phi=1$, as reported in Weisser, 2001.

Figure 4.13 presents the mean fuel decomposition rate for the three kinetics models of the present study, namely the one-step approach, and the realistic chemistry approaches associated with mechanisms Mech.29 and Mech.45. A first important observation is that, for the realistic chemistry cases, fuel decomposition terminates shortly after the end of injection (close to 9.5 degrees CA), an effect which is very pronounced for Mech.45. On the other hand, for one-step chemistry, fuel decomposition is delayed, in accordance with the visualisation of equivalence ratio, presented in Figure 4.11. In more detail, visualisations of the fuel decomposition rate are present in Figure 4.14 and Figure 4.15, for the horizontal and the vertical plane, respectively, considered here. The visualisations verify the earlier start of fuel decomposition for realistic chemistry, an effect which is very pronounced for Mech.45. They also verify the earlier termination of fuel decomposition for realistic chemistry, as well as the substantial decomposition for the one-step chemistry simulation, which takes place close to the cylinder liner in the late stages of combustion.

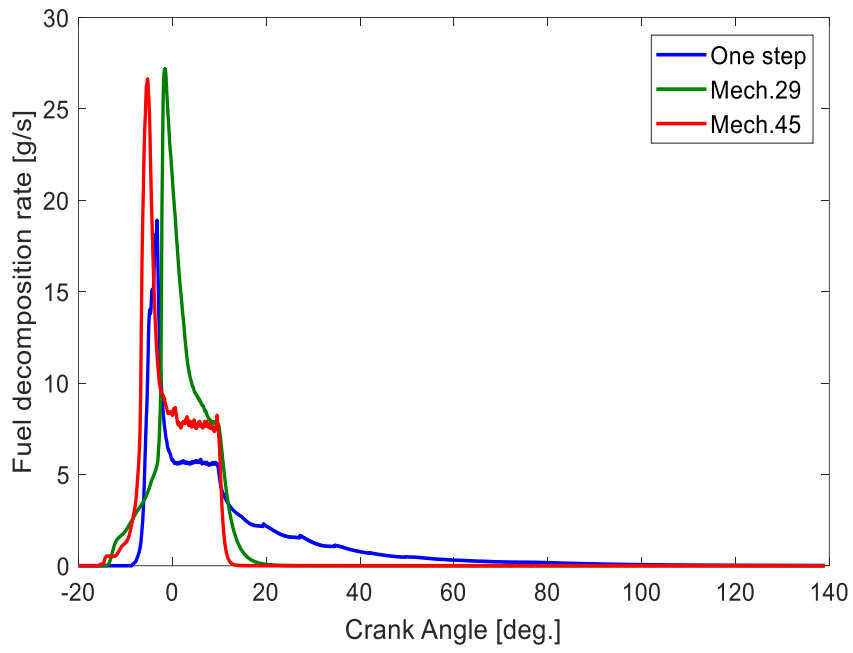
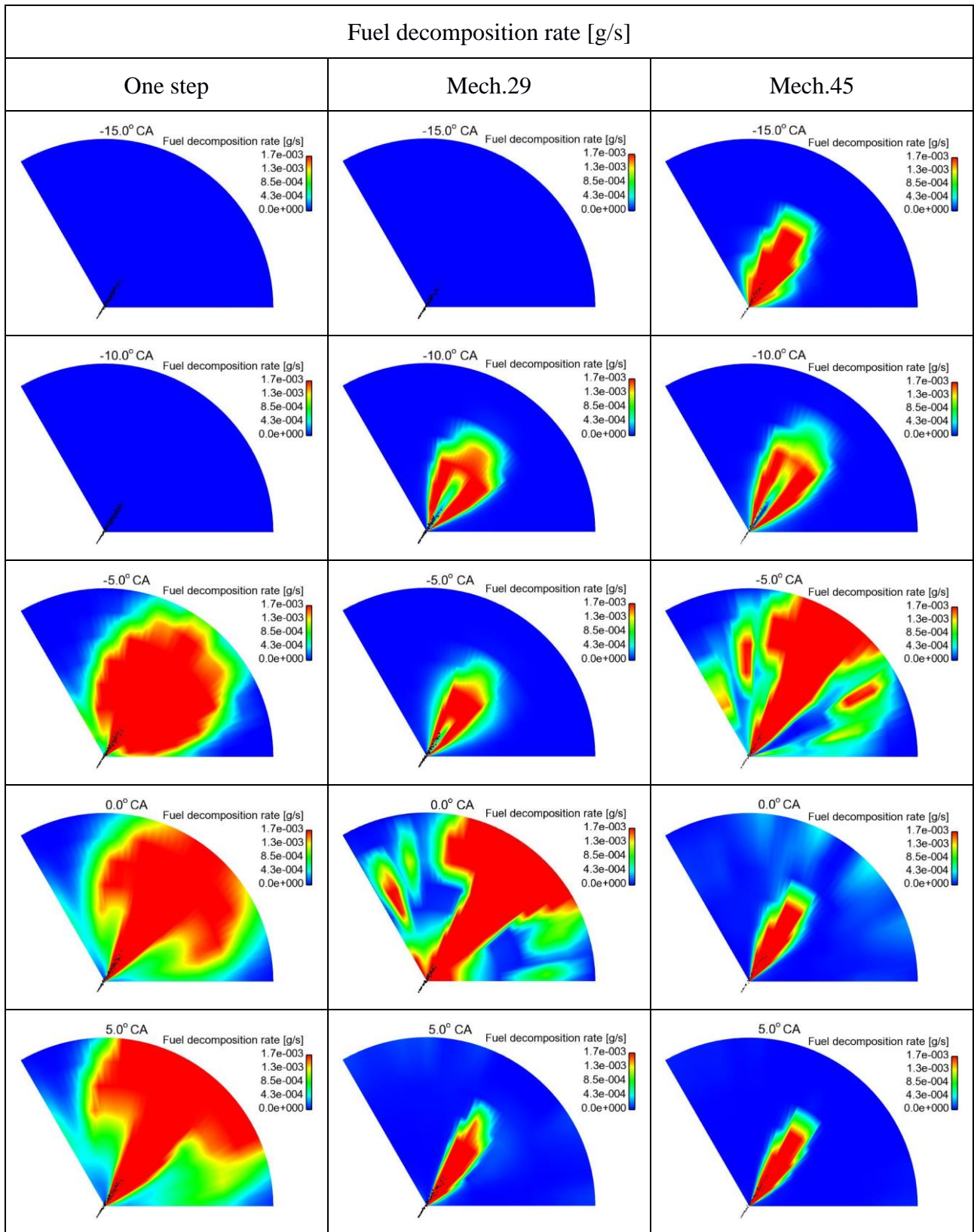


Figure 4.13: Computed traces of mean fuel decomposition rate using one-step chemistry and the two reduced order chemical kinetics mechanisms (Mech.29 and Mech.45), at an engine load of 80%.



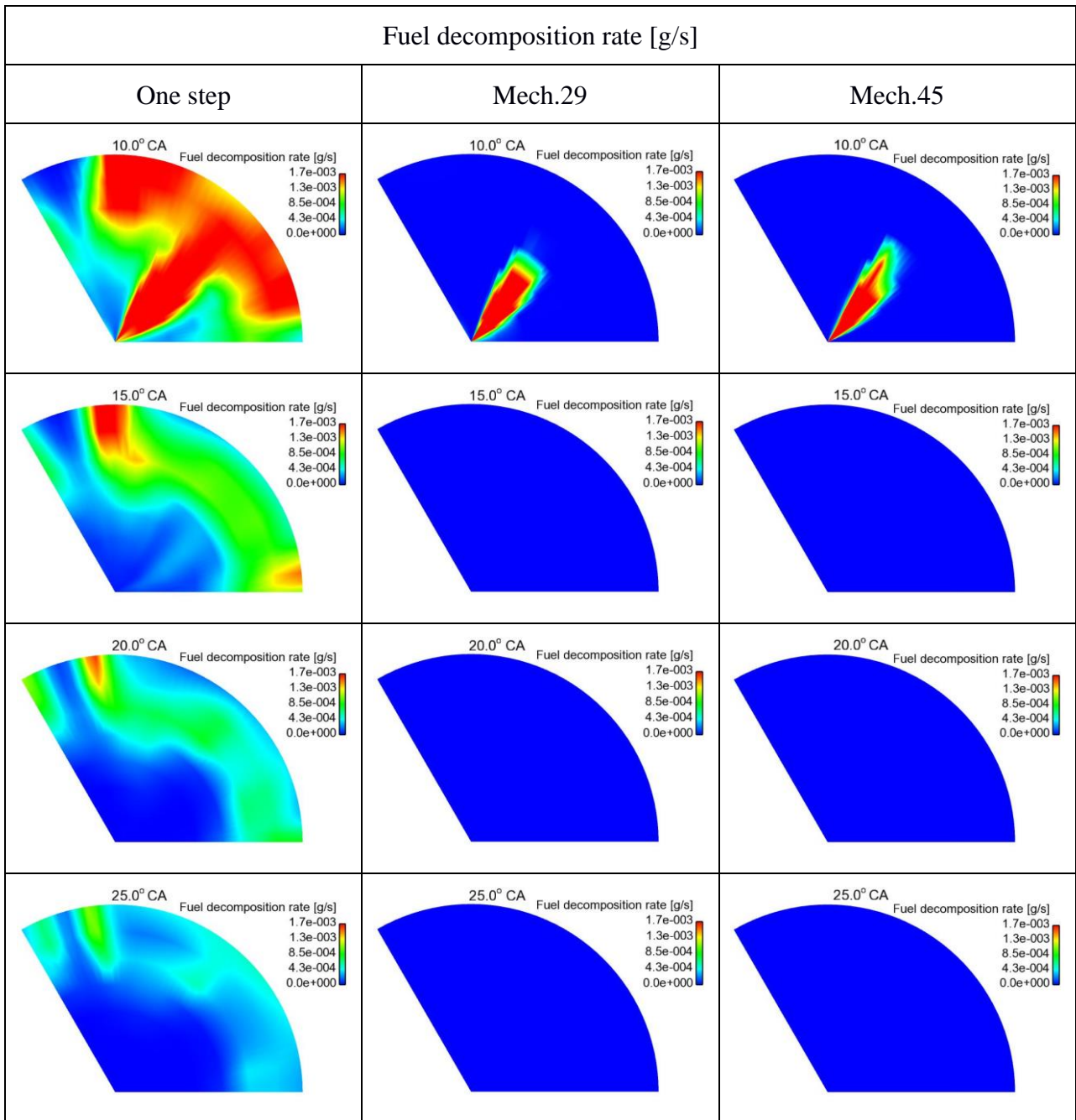
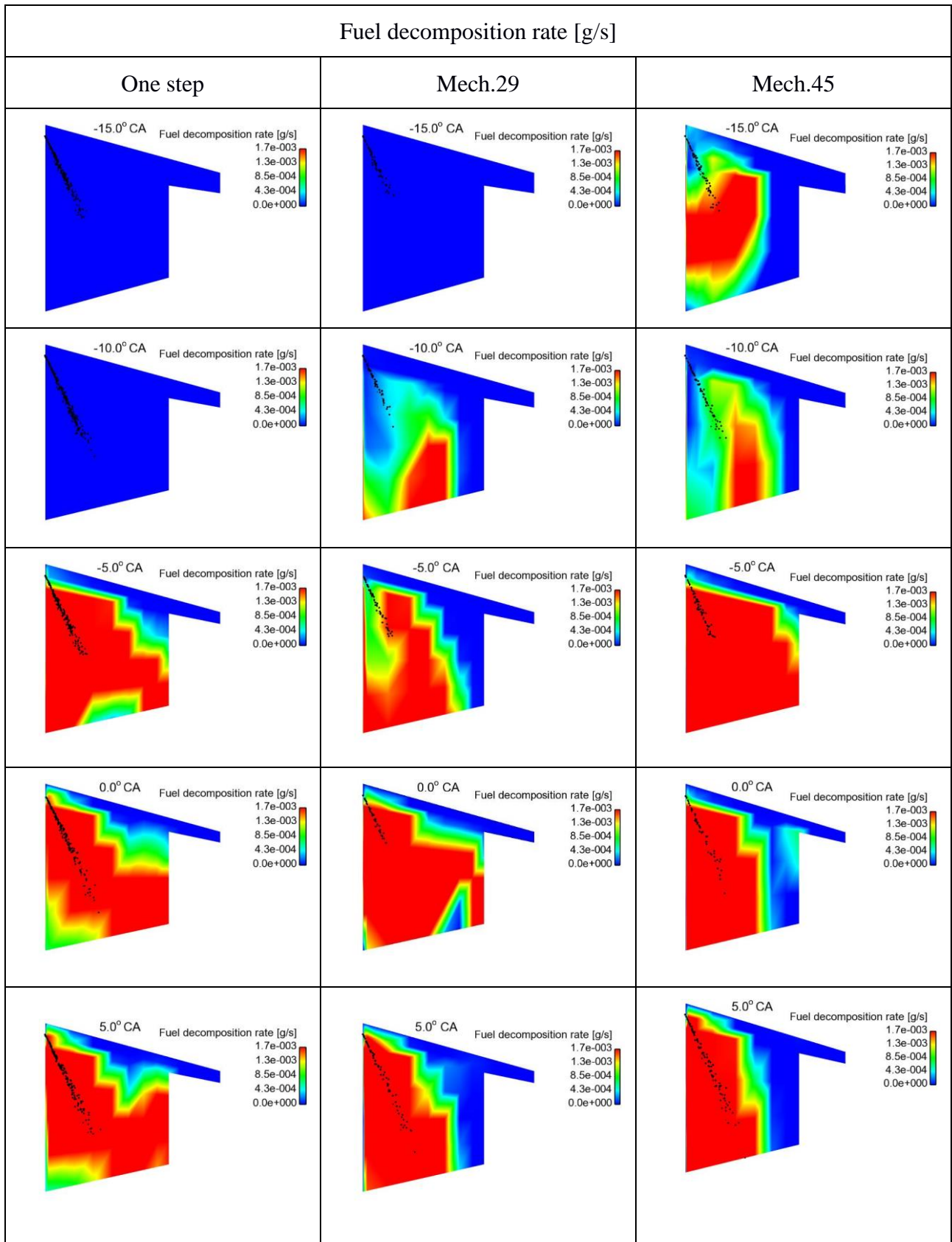


Figure 4.14: Colour-coded contours of fuel decomposition rate for one-step chemistry and reduced order chemistry using mechanisms Mech.29 and Mech.45. A horizontal plane very close to the injector is considered, at selected time instants.



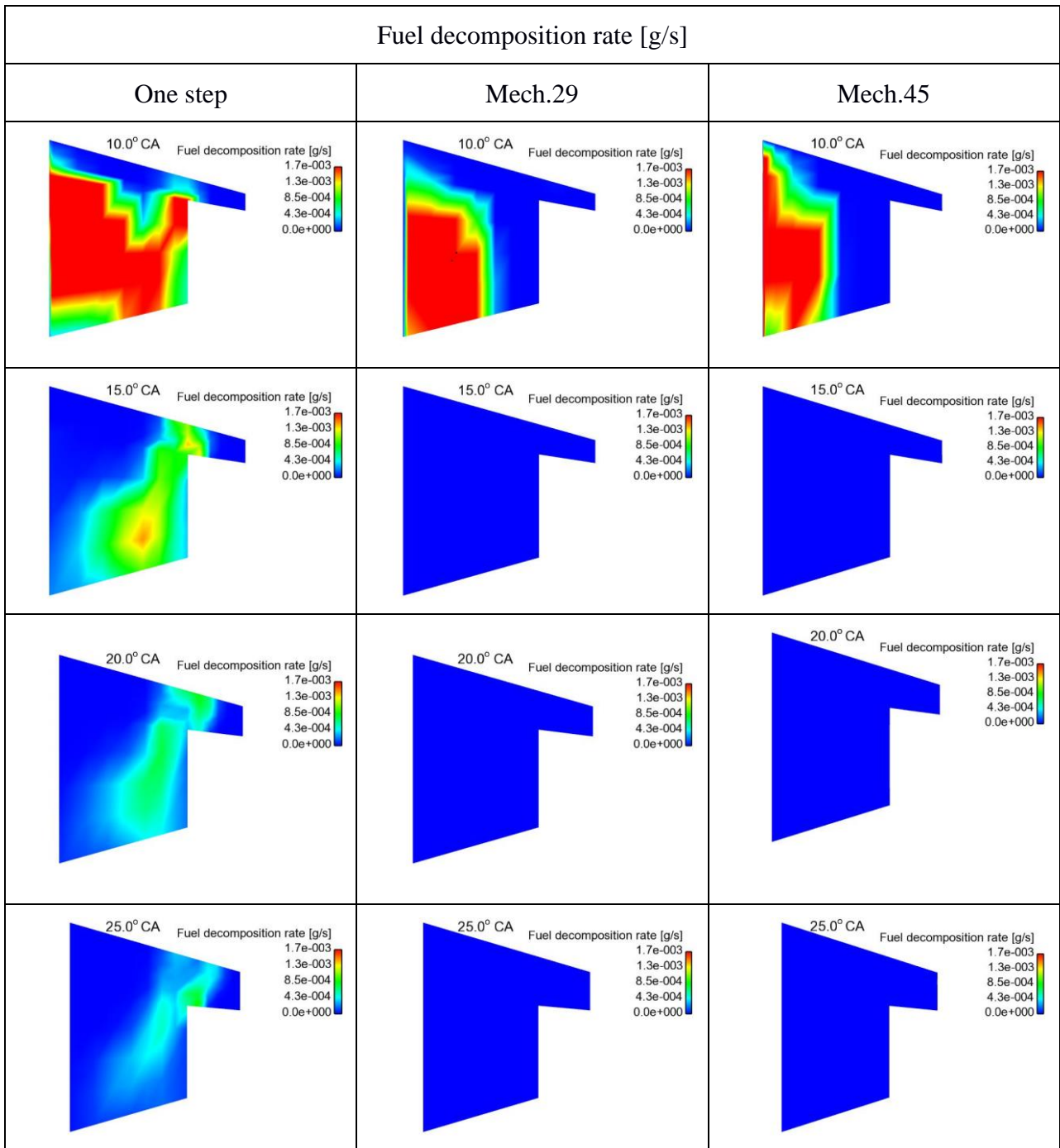


Figure 4.15: Colour-coded contours of fuel decomposition rate for one-step chemistry and reduced order chemistry using mechanisms Mech.29 and Mech.45. A vertical plane including the injector is considered, at selected time instants.

4.2.1 Carbon-based emissions

The present study considers combustion of higher hydrocarbon. During combustion, a representative hydrocarbon molecule, as n-heptane (C_7H_{16}), is decomposed to form hydrocarbons with smaller carbon chain, such as CH_4 , which constitutes a significant precursor for the evolution of combustion and the formation of emissions. Figure 4.16 depicts the reaction pathway analysis for the oxidation of CH_4 over a wide range of conditions (Hashemi et al., 2016). The oxidation of methane leads to major products of combustion, including CO and CO_2 . The intermediate species of combustion of CH_4 include, among others, formaldehyde (CH_2O) and formyl radical (HCO).

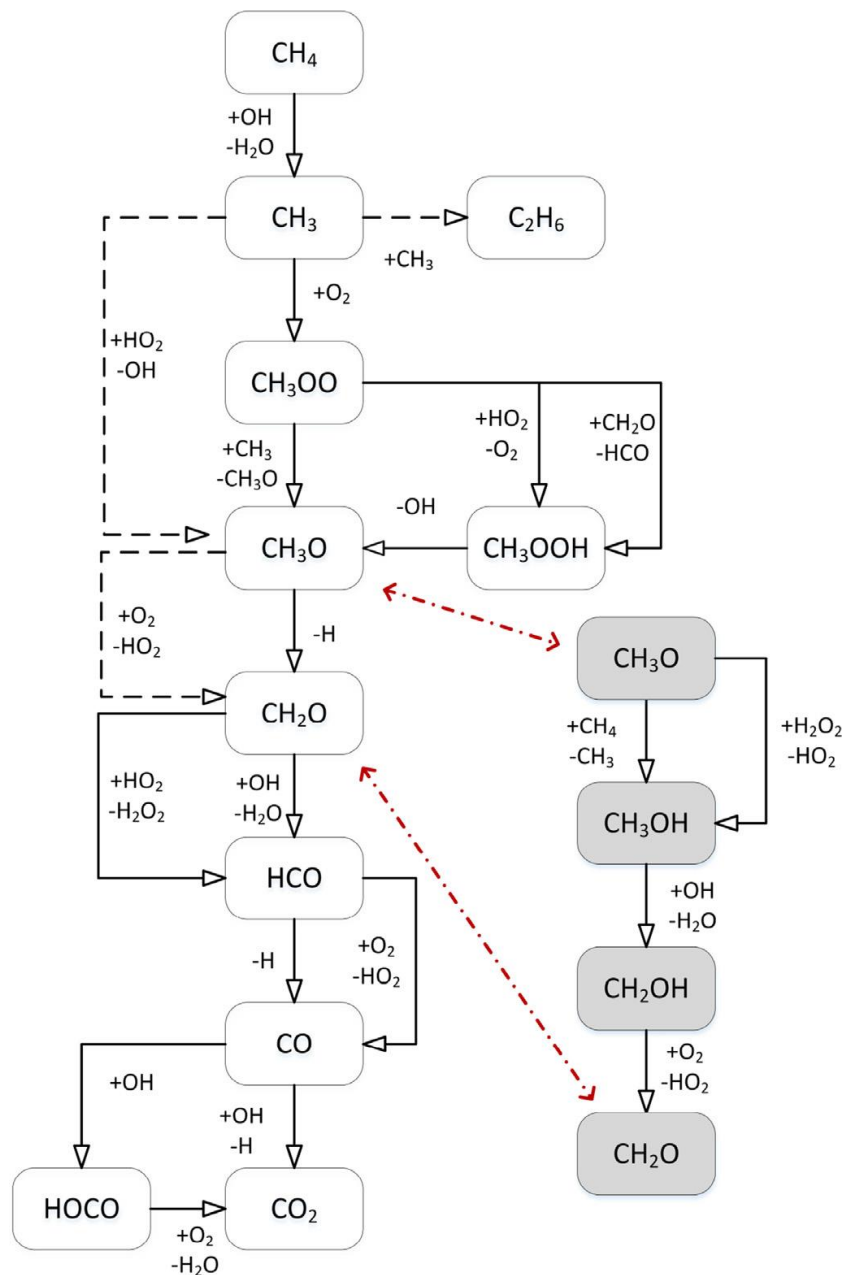


Figure 4.16: Reaction pathways for methane consumption. The dashed lines correspond to paths active only under specific conditions (Hashemi et al., 2016).

The temporal evolution of combustion can be characterised in terms of the evolution of the concentration of important species, such as Hydroxyl radical (OH), Oxygen radical (O), Hydrogen radical (H), Methane (CH₄), Methyl radical (CH₃), Formaldehyde (CH₂O), Formyl radical (HCO), Carbon Monoxide (CO) and Carbon Dioxide (CO₂). The coupled computational tool used in the present study enables calculating the temporal evolution of the above species, including important ones which cannot be calculated with an one-step type of approach; these include CH₃, CH₄, HCO and CH₂O.

Central to ignition and combustion is the production of important radicals, namely OH, H and O. Further, ignition is dominated by the production of OH radical, which can thus be directly associated with an ignition criterion in one-step approaches (Weisser, 2001). As discussed in section 2.6.1, in the one-step approach, the concentration of OH, H and O radicals is the outcome of six equilibrium reactions, which have been implemented in KIVA-3vr2, following Weisser, 2001.

Figure 4.17 shows the computed histories of mean (space-averaged) OH concentration, for the one-step chemistry and realistic chemistry calculations of the present study. The earlier ignition for the Mech.45 mechanism is demonstrated, and is in accordance with the fuel decomposition rate curve (Figure 4.13). The decay of OH concentration to low levels in the late stages of combustion is demonstrated for the case of one-step chemistry, and is in agreement with the presence of unburned fuel, especially close to the liner, demonstrated in the equivalence ratio visualisations of Figure 4.11. The strong presence of OH radical for one-step chemistry up to a value of crank angle of about 25 degrees is demonstrated in the visualisations of OH concentration presented in Figure 4.18.

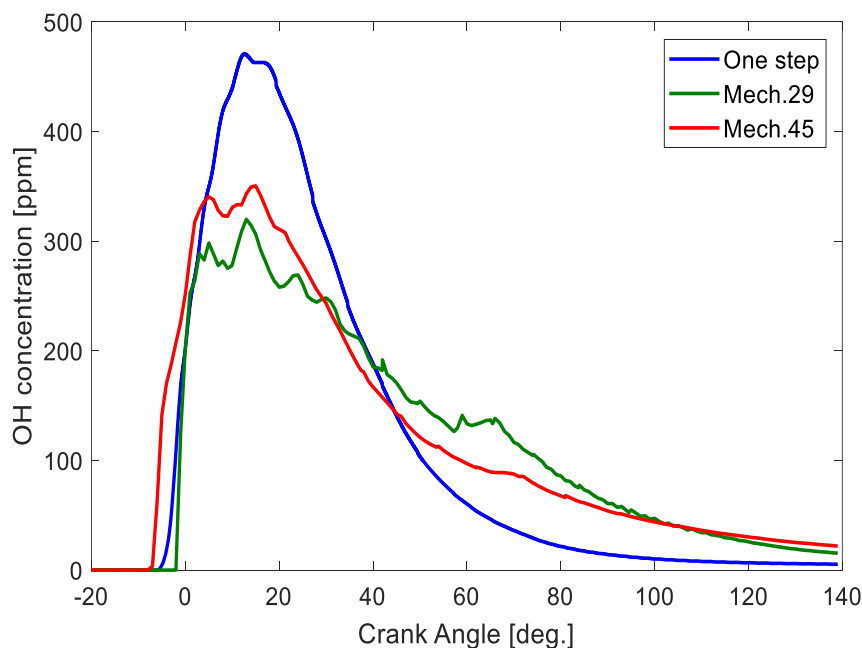
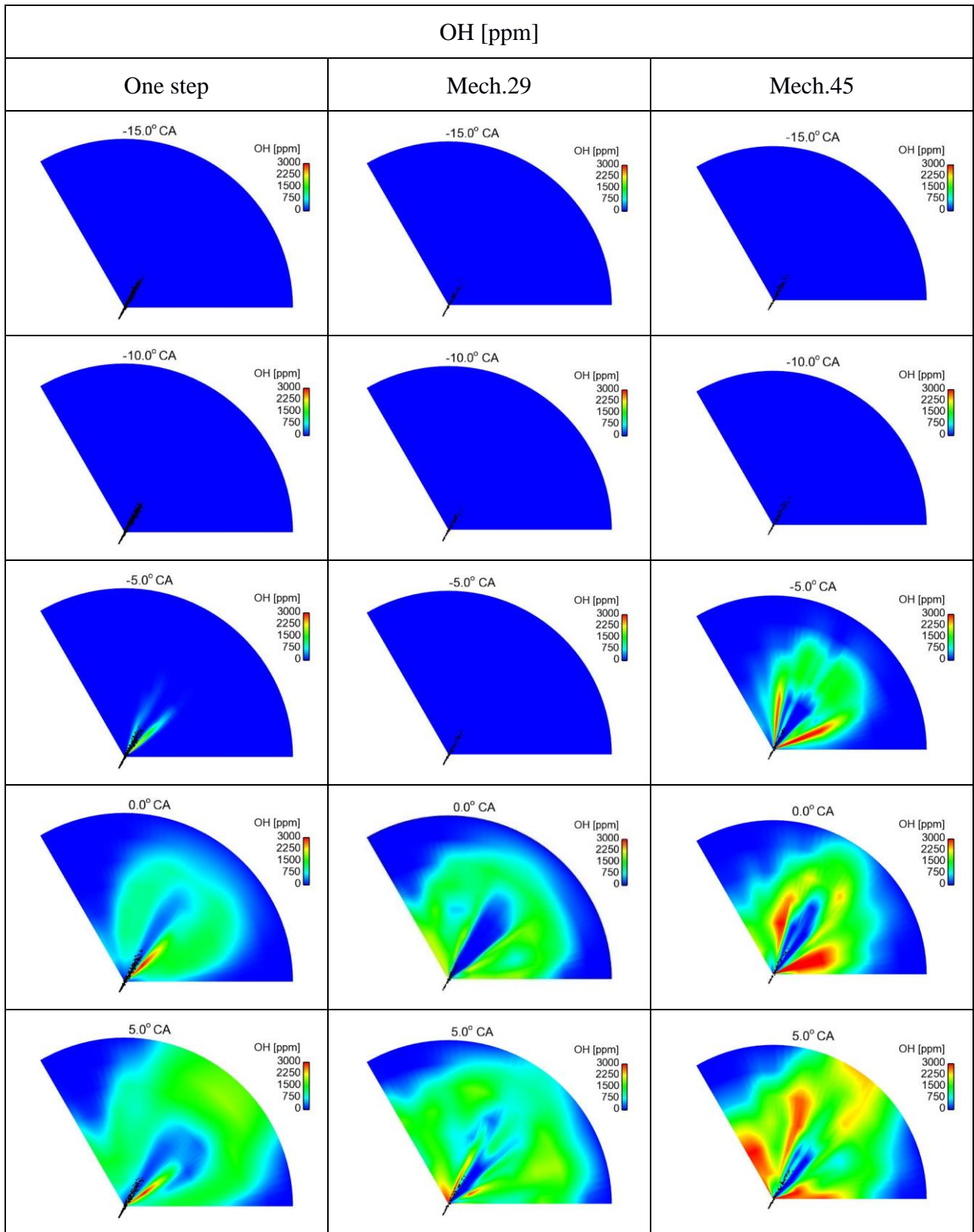


Figure 4.17: Computed traces of mean OH (Hydroxyl radical) concentration using one-step chemistry and the two reduced order chemical kinetics mechanisms (Mech.29 and Mech.45), at an engine load of 80%.



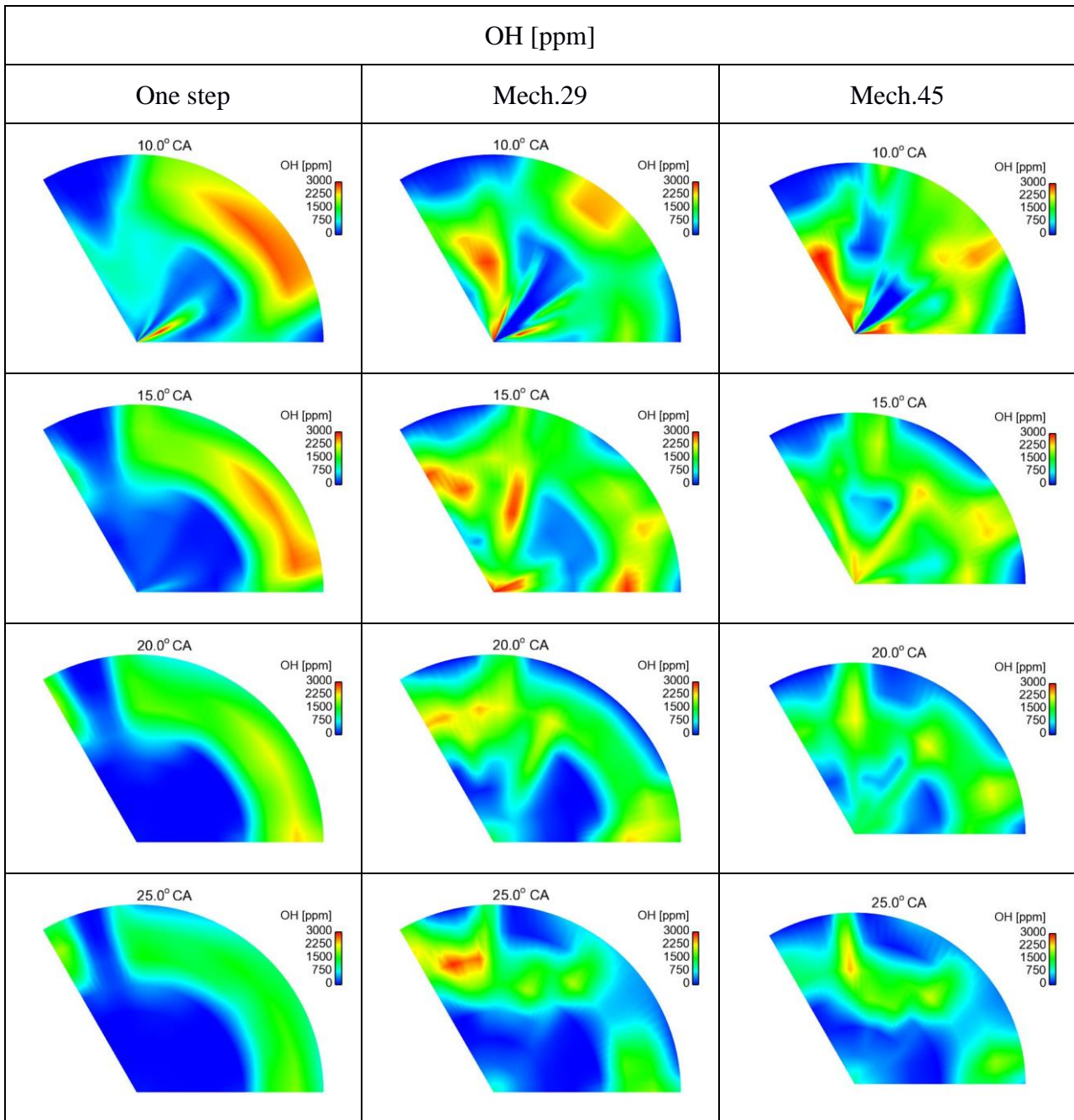


Figure 4.18: Colour-coded contours of OH concentration for one-step chemistry and reduced order chemistry using mechanisms Mech.29 and Mech.45. A horizontal plane very close to the injector is considered, at selected time instants.

Figure 4.19 presents the computed histories of space-averaged concentration of O radical for the one-step chemistry and the two reduced order chemistry mechanisms (Mech.29 and Mech.45). The evolution of O radical is found to be very similar for the two cases of realistic chemistry. For one-step chemistry, the mean O concentration is maximum before 20°CA and diminishes to negligible levels in the late expansion, similarly to the evolution of the OH radical (Figure 4.17).

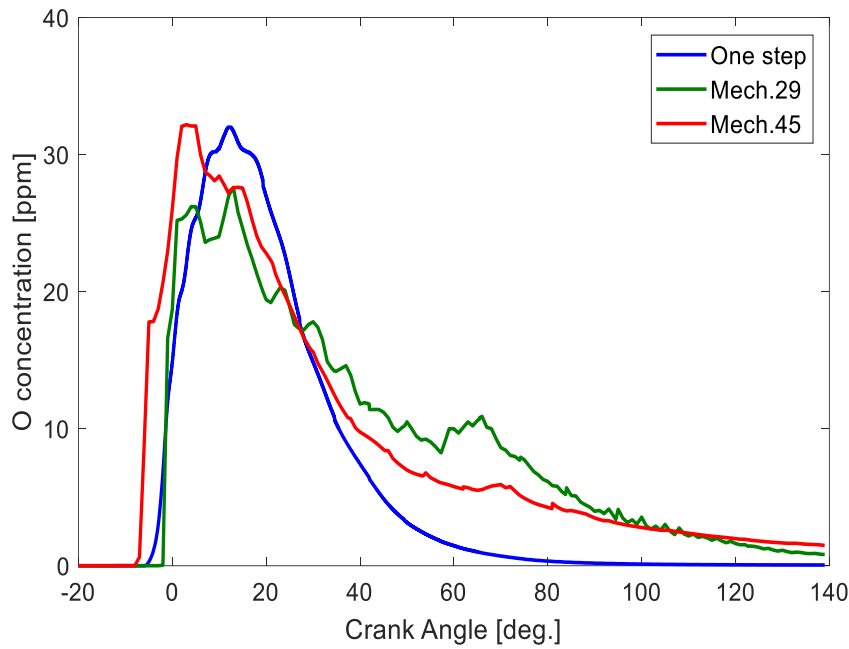


Figure 4.19: Computed traces of mean O (Oxygen radical) concentration using one-step chemistry and the two reduced order chemical kinetics mechanisms (Mech.29 and Mech.45), at an engine load of 80%.

Figure 4.20 presents the computed histories of mean concentration of H radical for the one-step chemistry and the cases of realistic chemistry of the present study. For one-step chemistry, low levels of H concentration are verified, as well as an early decay to zero levels; this infers a simplified representation of combustion in fuel-rich regions. The early H decay may contribute to the longer overall duration of combustion, in the case of one-step chemistry. Higher levels of H are persistent for Mech.29, in comparison to Mech.45.

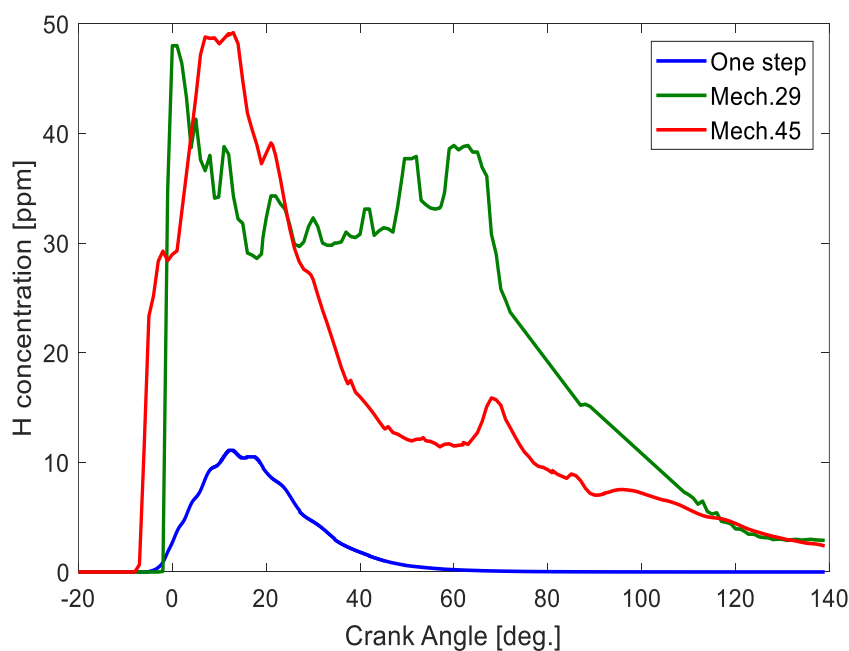


Figure 4.20: Computed traces of mean H (Hydrogen radical) concentration using one-step chemistry and the two reduced order chemical kinetics mechanisms (Mech.29 and Mech.45), at an engine load of 80%.

In the combustion of higher hydrocarbons, fuel decomposition leads to the formation of smaller hydrocarbon molecules and carbon-centred radicals, the chemistry of which forms main building blocks towards an overall characterisation of combustion chemistry. In particular, the chemistry of methane (CH_4) is in all cases crucial for understanding hydrocarbon chemistry of fuels of different molecule size. In methane combustion, a reaction path towards forming CO and CO_2 , valid in a wide range of conditions, has been suggested by Hashemi et al. (2016); it is shown in Figure 4.16.

Figure 4.21 presents the computed histories of space-averaged concentration of CH_4 for the two realistic chemistry mechanisms of the present study, Mech.29 and Mech.45. It is demonstrated that, in the case of Mech.29, higher levels of methane are maintained, in comparison to Mech.45; nonetheless, in the late expansion stages, the methane concentration predicted by Mech.29 diminishes to near-zero values. In more detail, visualisations of the computed methane fields, at representative time instants, are presented in Figure 4.22. A stronger initial build-up of methane for Mech.45 is demonstrated, nonetheless, for Mech.29, a more rapid subsequent development of methane leads to higher levels of concentration around 20° CA, in accordance with the observations from Figure 4.21. The earlier initial development of CH_4 for Mech.45 is in accordance with the associated stronger decomposition rate, as demonstrated in Figure 4.13.

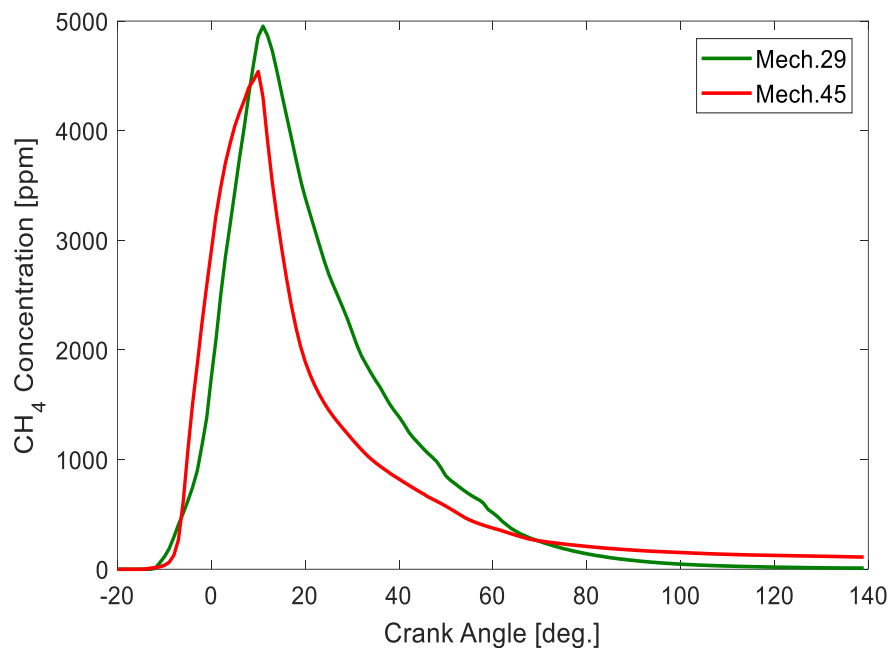
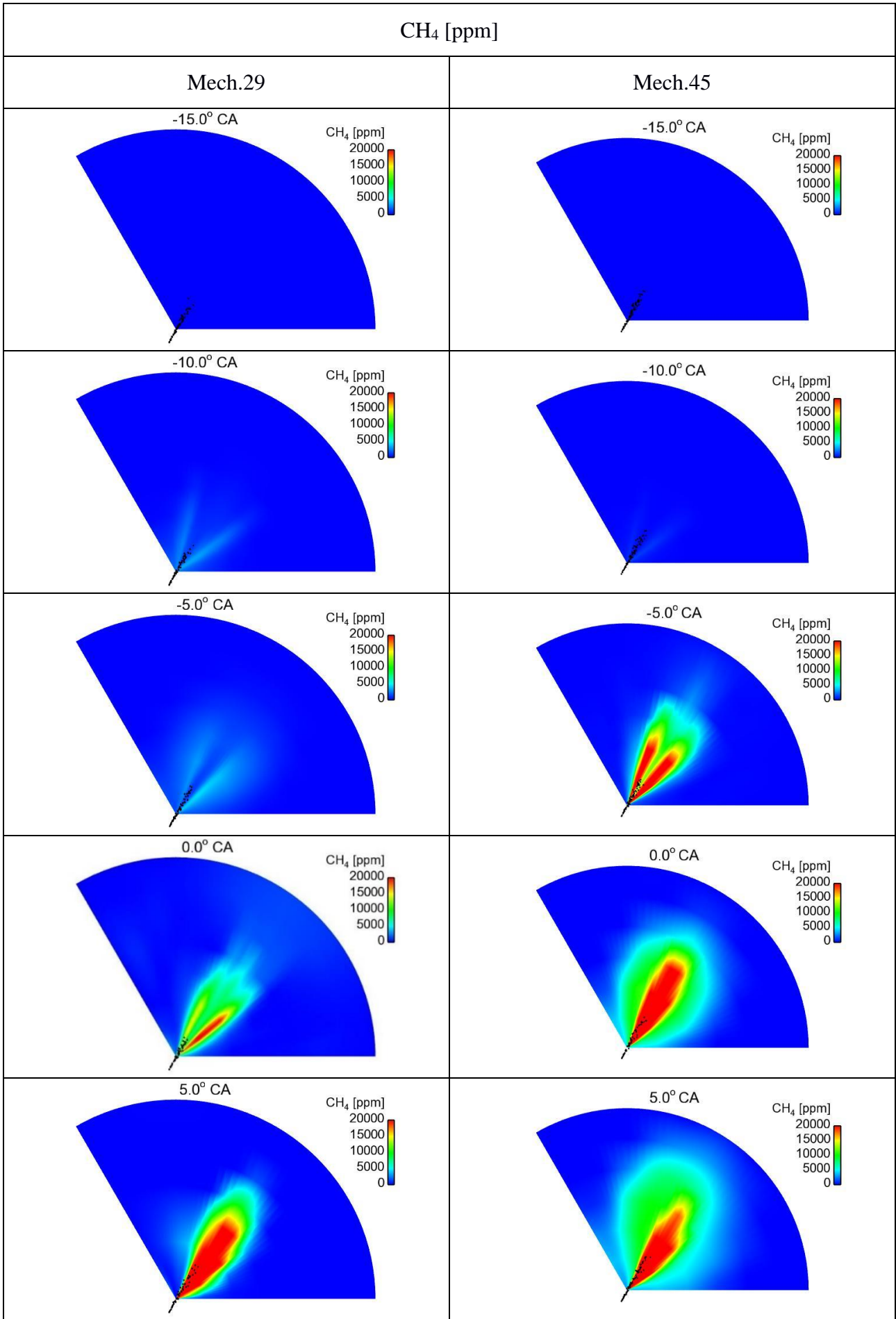


Figure 4.21: Computed traces of mean CH_4 (Methane) concentration using the two reduced order chemical kinetics mechanisms (Mech.29 and Mech.45), at an engine load of 80%.



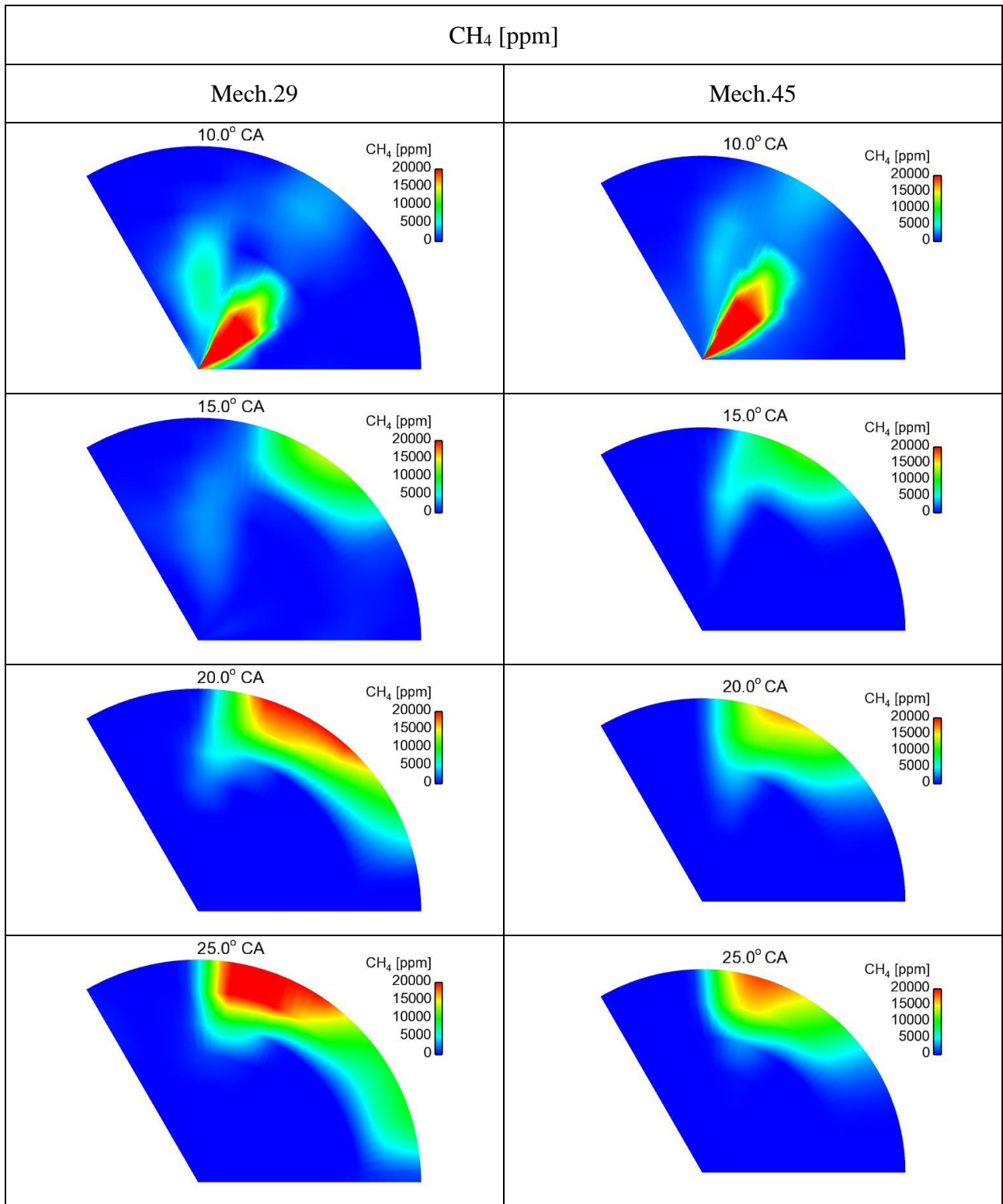


Figure 4.22: Colour-coded contours of CH₄ concentration for reduced order chemistry using mechanisms Mech.29 and Mech.45. A horizontal plane very close to the injector is considered, at selected time instants.

Figure 4.23 shows the computed histories of space-averaged concentration of the CH_3 radical, for Mech.29 and Mech.45. An initial stronger formation of CH_3 is demonstrated for Mech.45, in accordance with the faster fuel decomposition (Figure 4.13). The resulting faster development of combustion leads to convergence to near-zero levels at larger times.

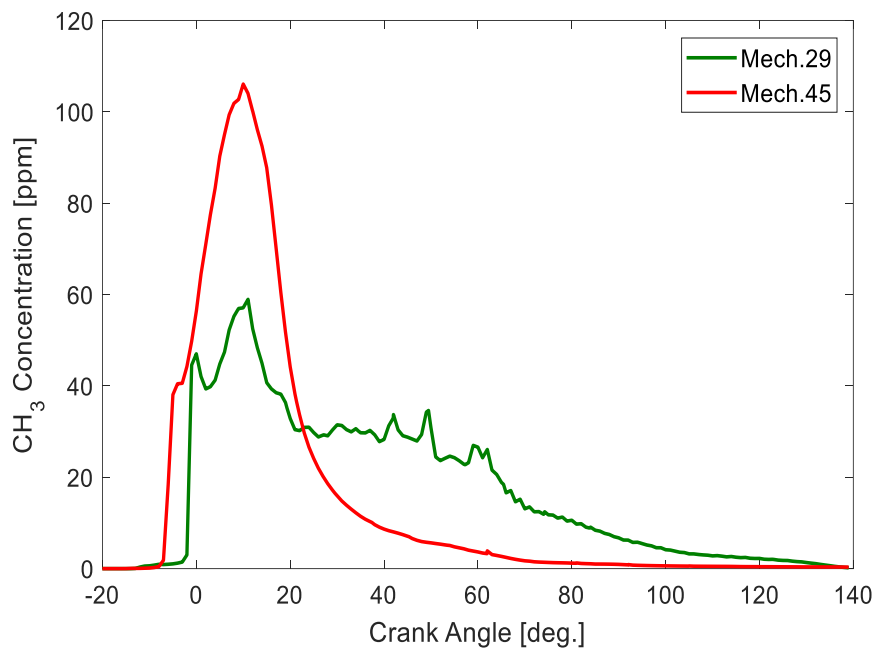


Figure 4.23: Computed traces of mean CH_3 (methyl radical) concentration using the two reduced order chemical kinetics mechanisms (Mech.29 and Mech.45), at an engine load of 80%.

Figure 4.24 shows the computed history of mean concentration of formaldehyde (CH_2O), for Mech.29 and Mech.45. As CH_2O is a known inhibitor of soot production (Yuan et al., 2015), the associated higher production with Mech.29 is expected to correspond to lower soot production, and a decreased exhaust soot concentration, in comparison to Mech.45. The trend of Figure 4.24 complies with the spatial distributions presented in Figure 4.25.

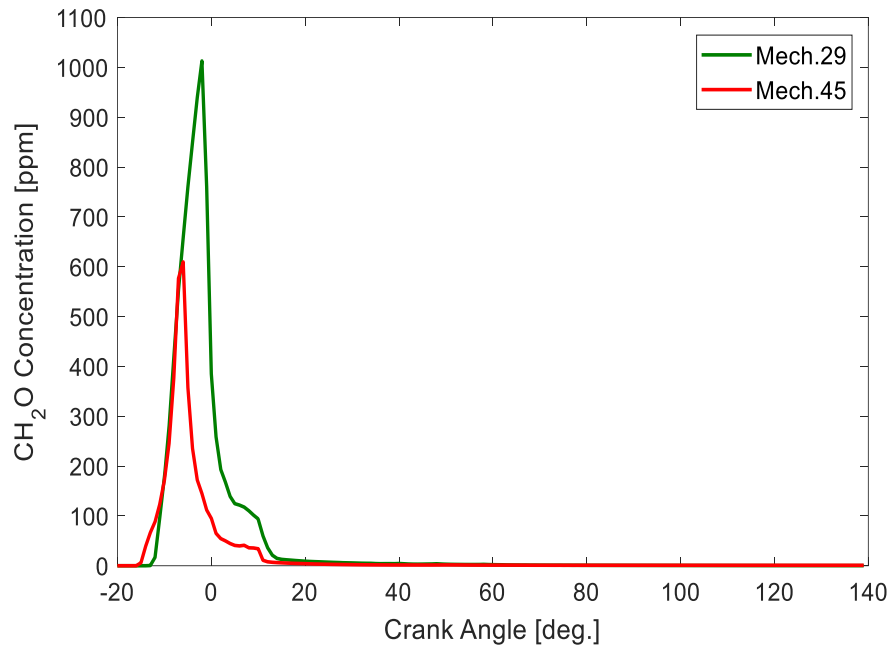
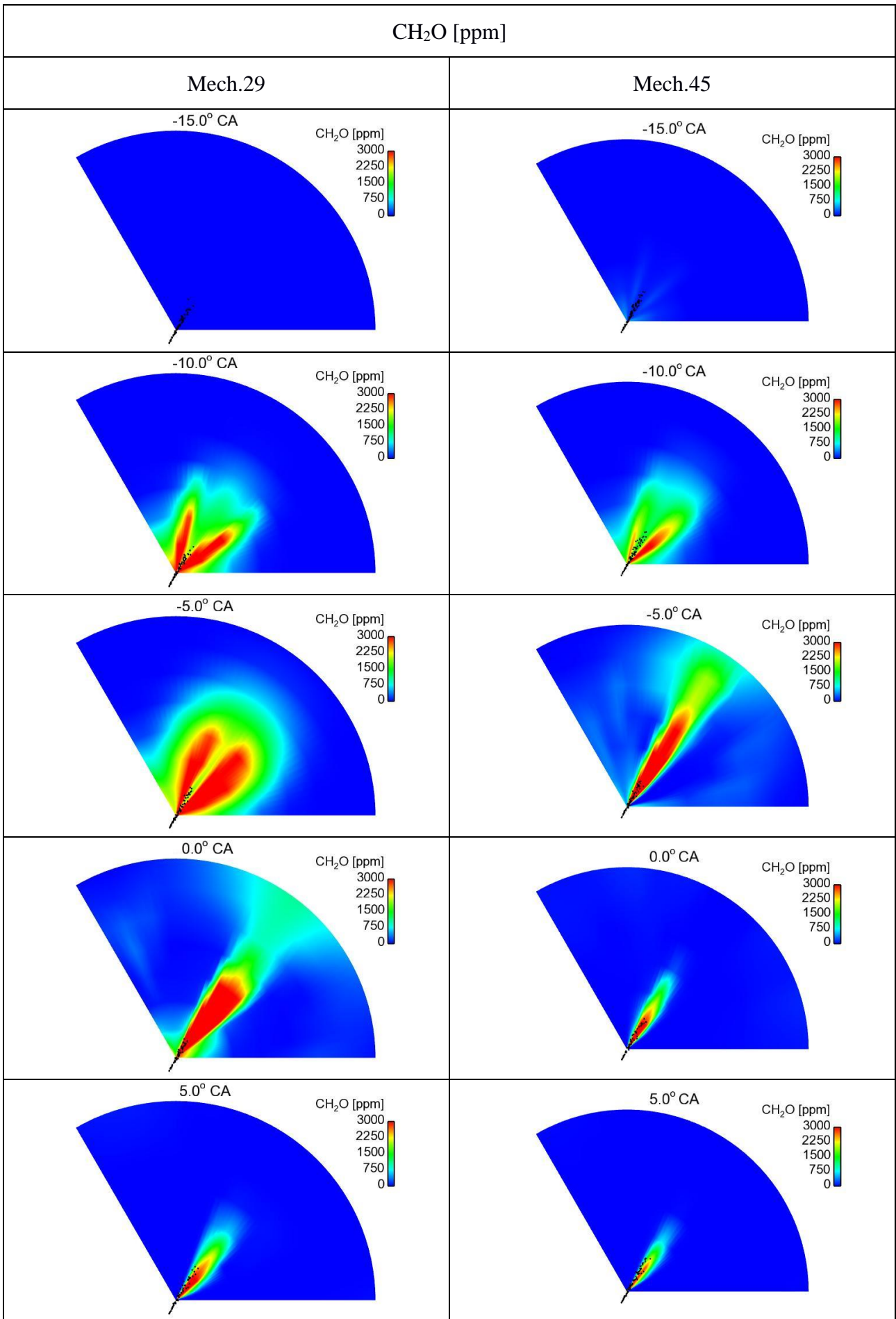


Figure 4.24: Computed traces of mean CH₂O (formaldehyde) concentration using the two reduced order chemical kinetics mechanisms (Mech.29 and Mech.45), at an engine load of 80%.



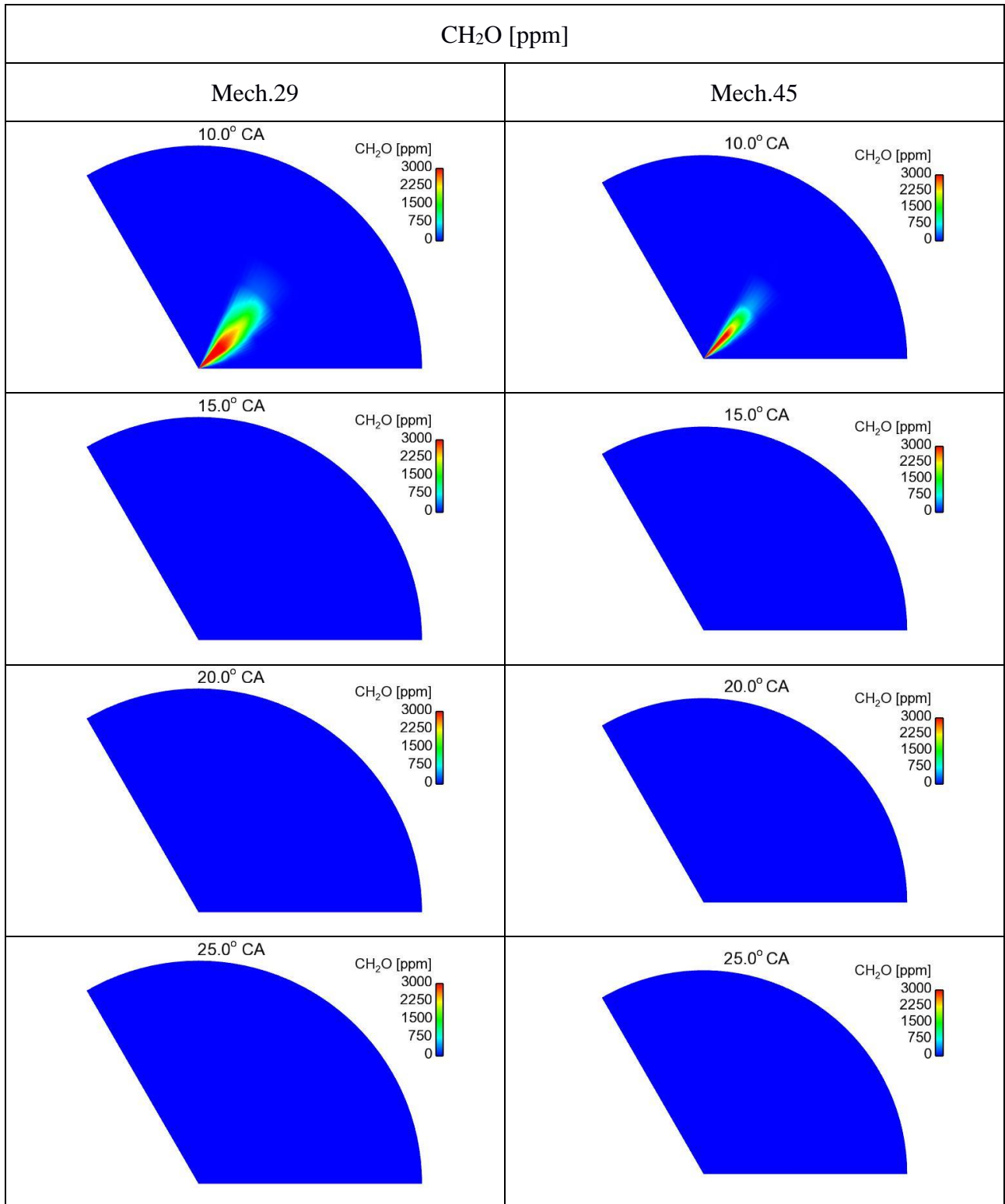


Figure 4.25: Colour-coded contours of CH₂O concentration for reduced order chemistry using mechanisms Mech.29 and Mech.45. A horizontal plane very close to the injector is considered, at selected time instants.

Figure 4.26 presents the computed traces of mean concentration of formyl radical (HCO), for Mech.29 and Mech.45; HCO is an important precursor to the CO formation. Low levels of produced HCO are demonstrated. The earlier development of HCO with Mech.45 may suggest an earlier formation of CO. This is in accordance with the calculated development of CO, presented in Figure 4.27, in which the results of one-step chemistry are also included, and correspond to substantially lower, by more than an order of magnitude, CO levels, in comparison to the realistic chemistry calculations. Interestingly, Figure 4.27 shows that, for realistic chemistry, the exhaust concentration of CO is non-zero, and is higher for the calculation with Mech.45. The practically zero final value of the CO concentration in the case of one-step chemistry is an outcome of the fact that only one (equilibrium) reaction accounts for its production/consumption: $O_2 + 2CO \rightleftharpoons 2CO_2$. Further, Figure 4.28 presents visualisations of the CO concentration at different values of crank angle, for the one-step chemistry and the realistic chemistry cases considered. The low levels of CO for the one-step chemistry are verified, as well as the existence of a CO zone in the near-liner region in the later stages of combustion, in accordance with the local presence of fuel, as shown in the equivalence ratio visualisations of Figure 4.11. For the realistic chemistry simulations, a similar development of CO is demonstrated for the two mechanisms considered, with higher predicted levels for Mech.45 just before TDC.

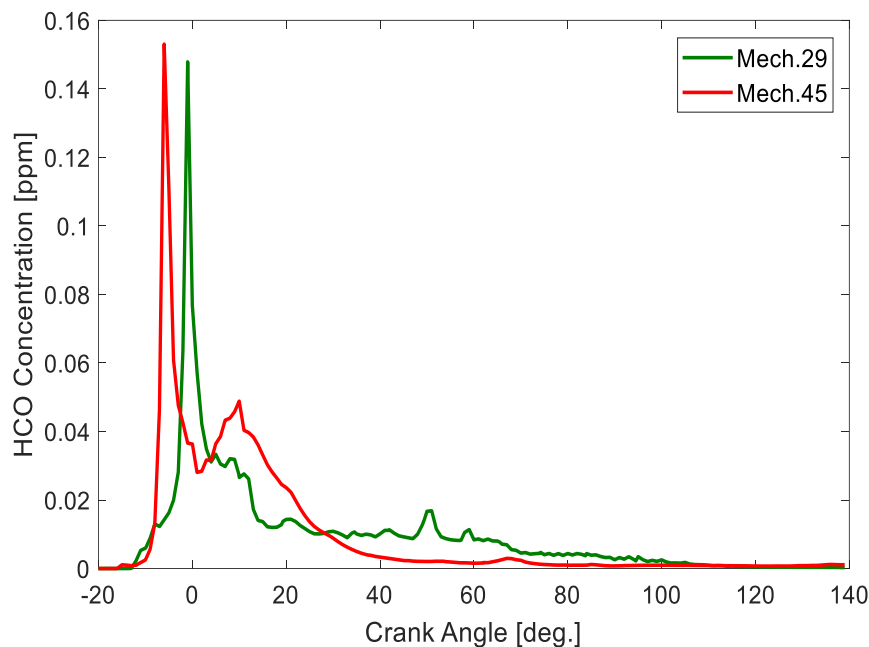


Figure 4.26: Computed traces of mean HCO (formyl radical) concentration using the two reduced order chemical kinetics mechanisms (Mech.29 and Mech.45), at an engine load of 80%.

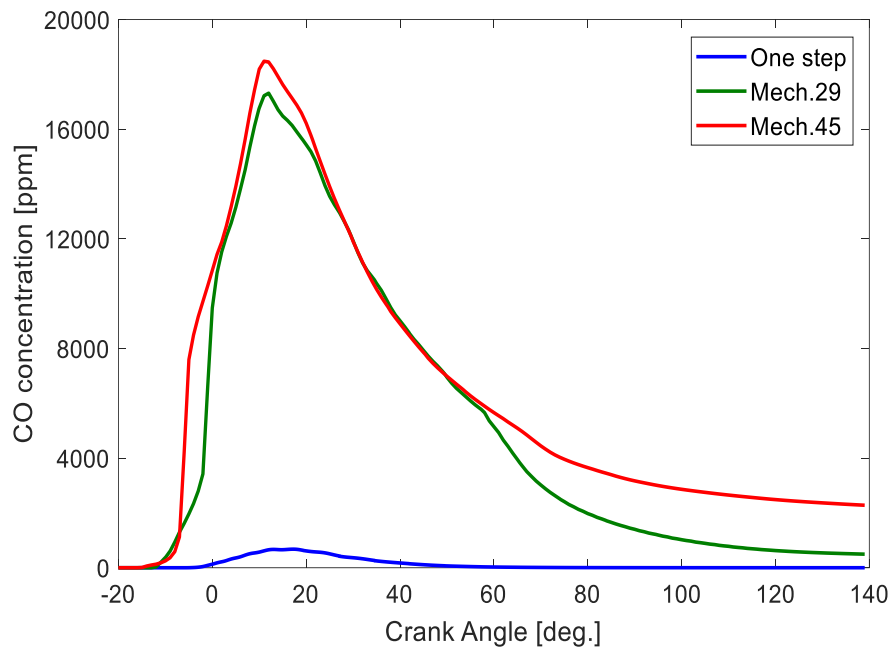
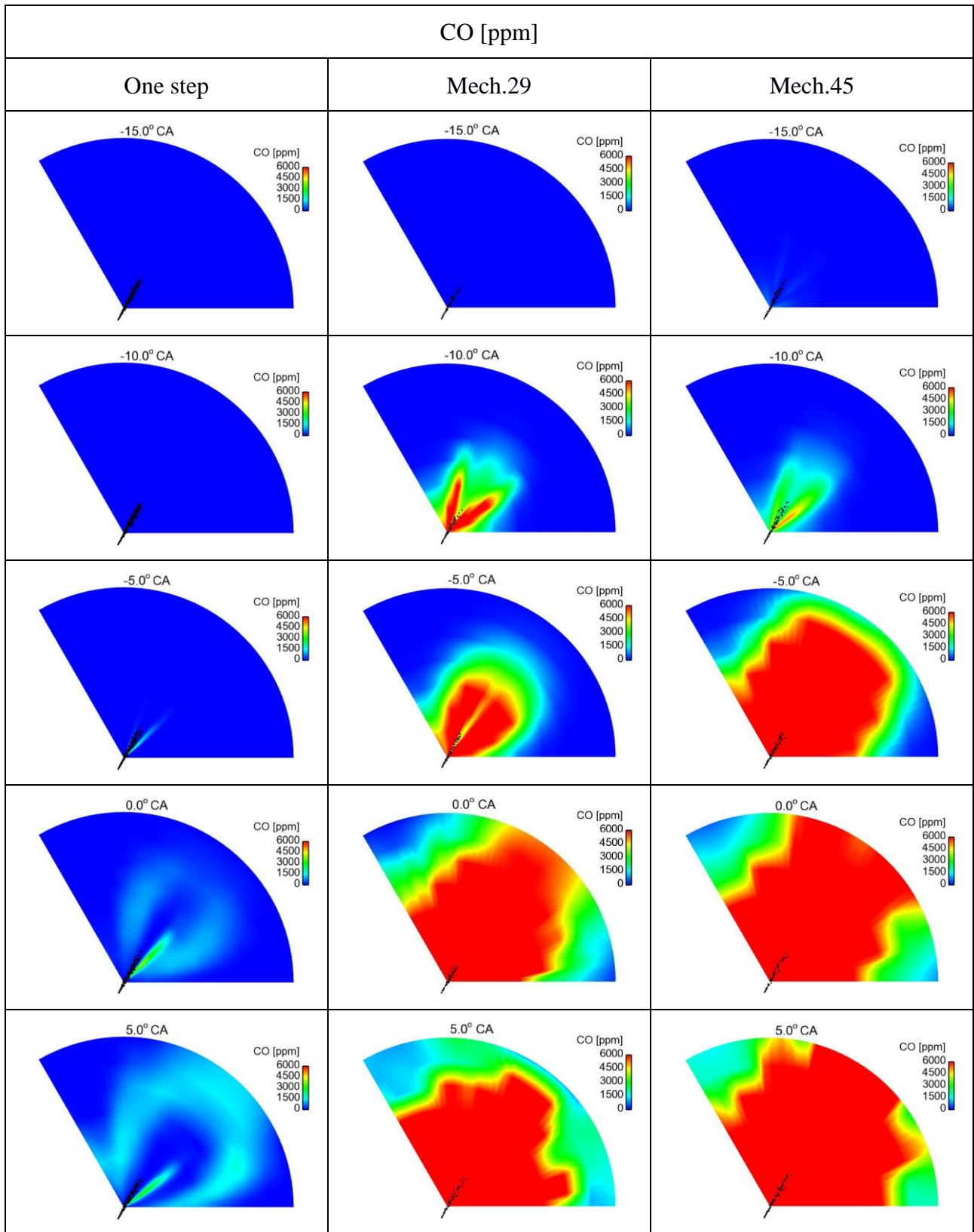


Figure 4.27: Computed traces of mean CO (Carbon monoxide) concentration using the one-step chemistry and the two reduced order chemical kinetics mechanisms (Mech.29 and Mech.45), at an engine load of 80%.



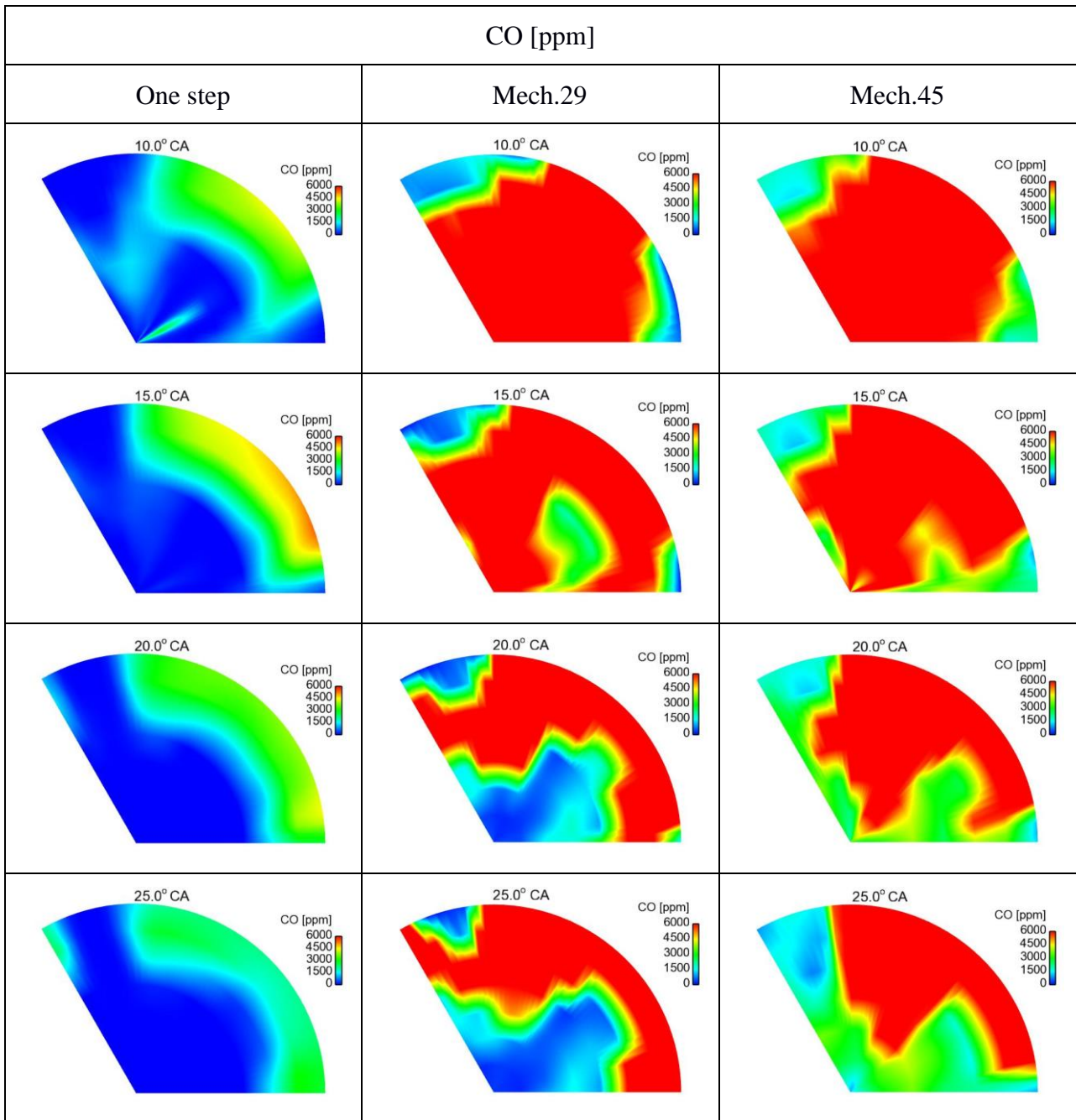


Figure 4.28: Colour-coded contours of CO concentration for reduced order chemistry using mechanisms Mech.29 and Mech.45. A horizontal plane very close to the injector is considered, at selected time instants.

Figure 4.29 presents the computed evolution of space-averaged concentration of CO_2 , for the one-step chemistry and the two realistic chemistry cases. A stronger initial production of CO_2 is demonstrated for the case of one-step chemistry, nonetheless comparative levels are attained at large times. The earlier development of CO_2 for one-step chemistry is verified by the visualisations of CO_2 concentration of Figure 4.30, which also verify the strong presence of CO_2 close to the cylinder liner for values of crank angle between 10 and 25 degrees, and are in accordance with the temperature isocontours in the vertical plane presented in Figure 4.10. Visualisation of the two fields thus suggests that the production of CO_2 takes place mainly in the near-piston region, and CO_2 is subsequently

convected upwards by a tumble-type of motion.

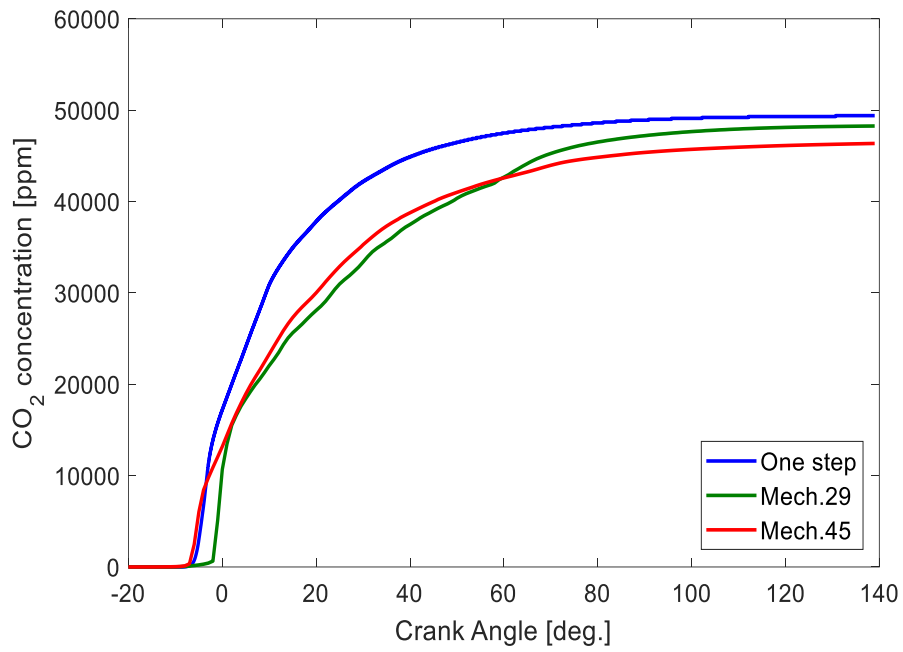
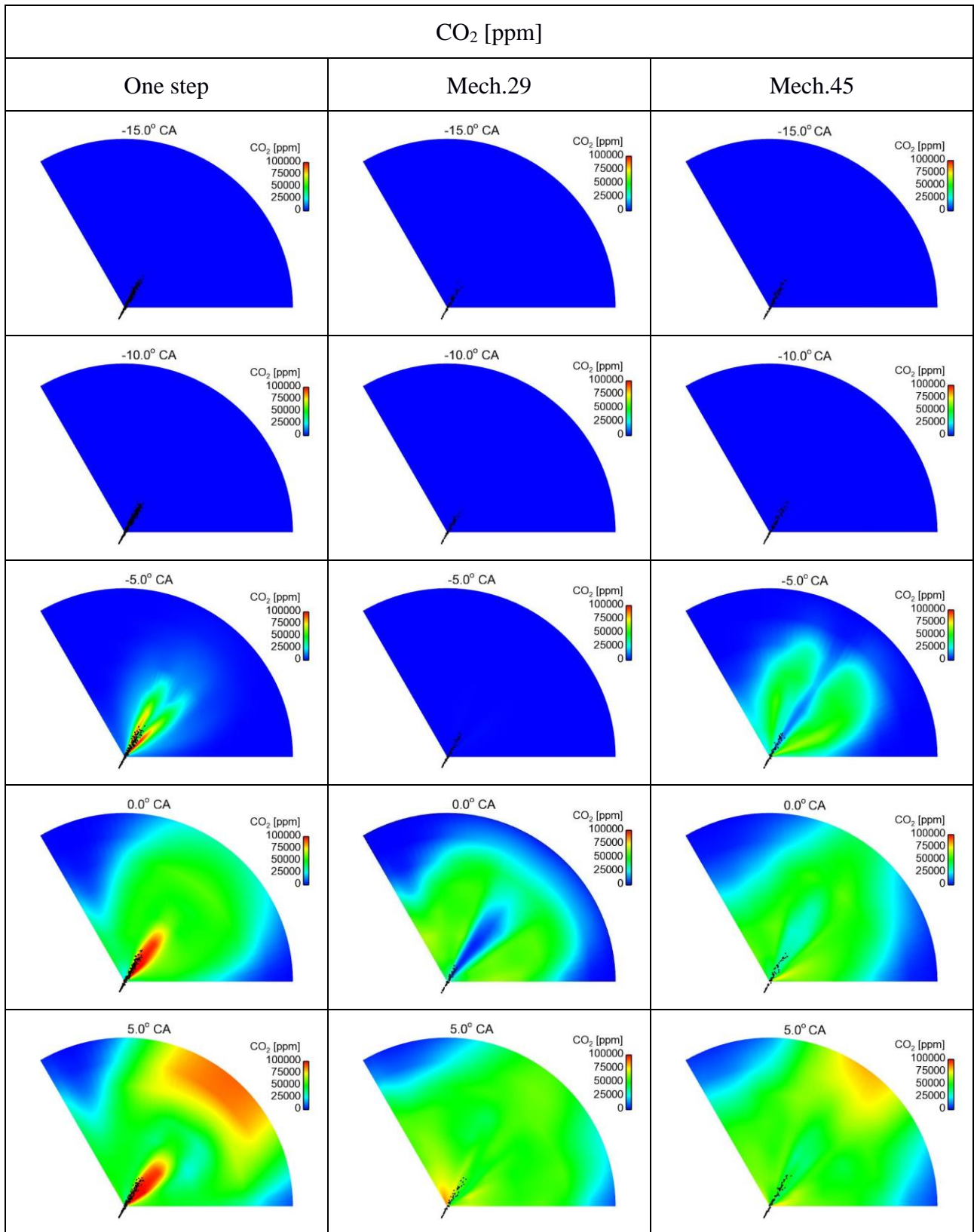


Figure 4.29: Computed traces of mean CO₂ (Carbon dioxide) concentration using the one-step chemistry and the two reduced order chemical kinetics mechanisms (Mech.29 and Mech.45), at an engine load of 80%.



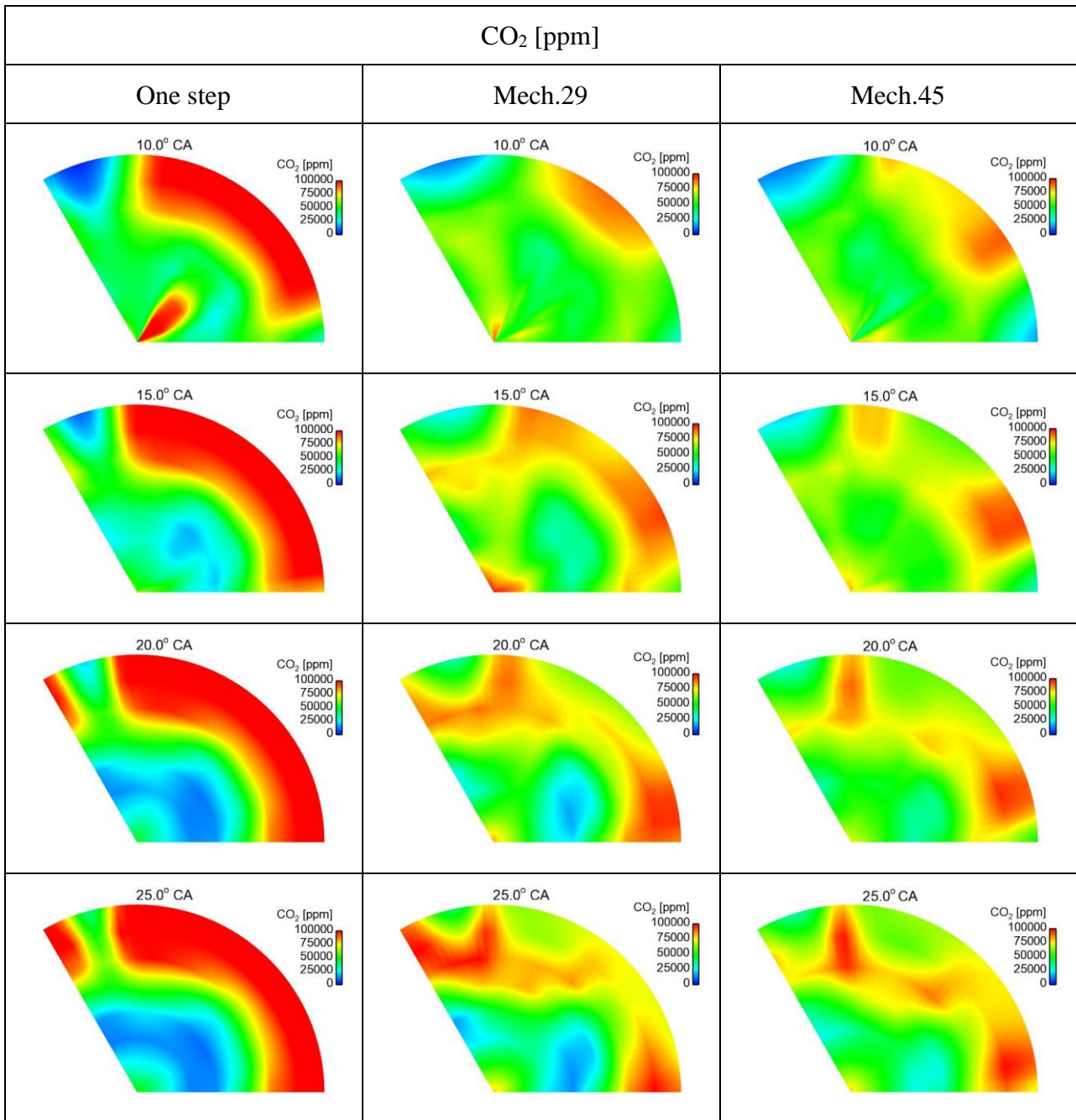


Figure 4.30: Colour-coded contours of CO₂ concentration for one-step chemistry and reduced order chemistry using mechanisms Mech.29 and Mech.45. A horizontal plane very close to the injector is considered, at selected time instants.

Soot modelling has been considered for the case of one-step chemistry, using the phenomenological model of Hiroyasu et al. (1983), as adapted by the NTUA research team (Douladiris, 2010). The computed history of total soot mass is presented in Figure 4.31, and illustrates the common build-up and oxidation of soot in Diesel engines. Nearly zero values at exhaust are attained here. The visualisations of soot concentration presented in Figure 4.32 verify the initial high production in the spray flame region, as well the high concentration in the near-liner region at larger times; the latter should be associated to both a convection effect (as also outlined above for CO₂) and to rather high local production rates due to the strong local presence of evaporated fuel (see equivalence ratio

visualisations in Figure 4.11).

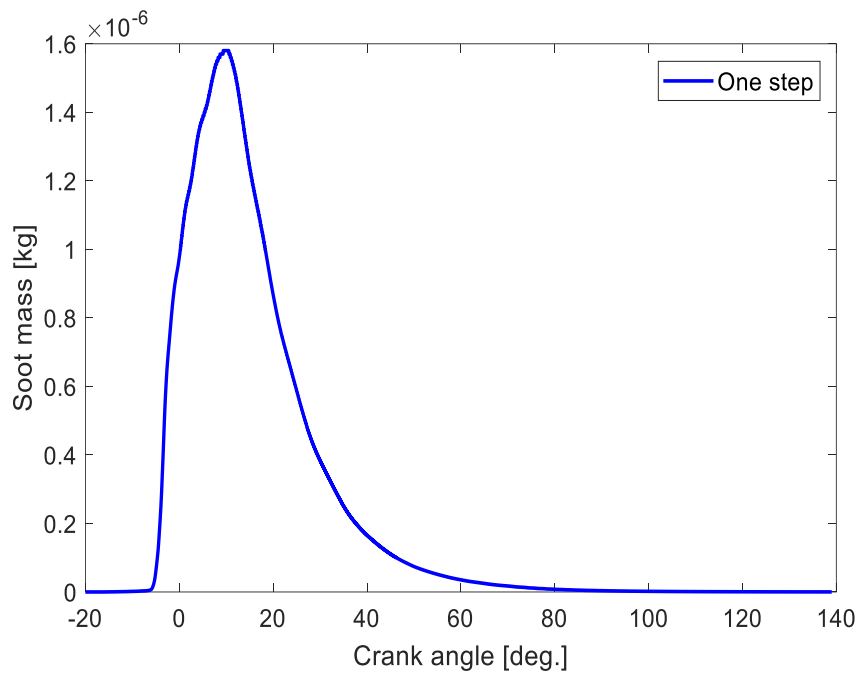
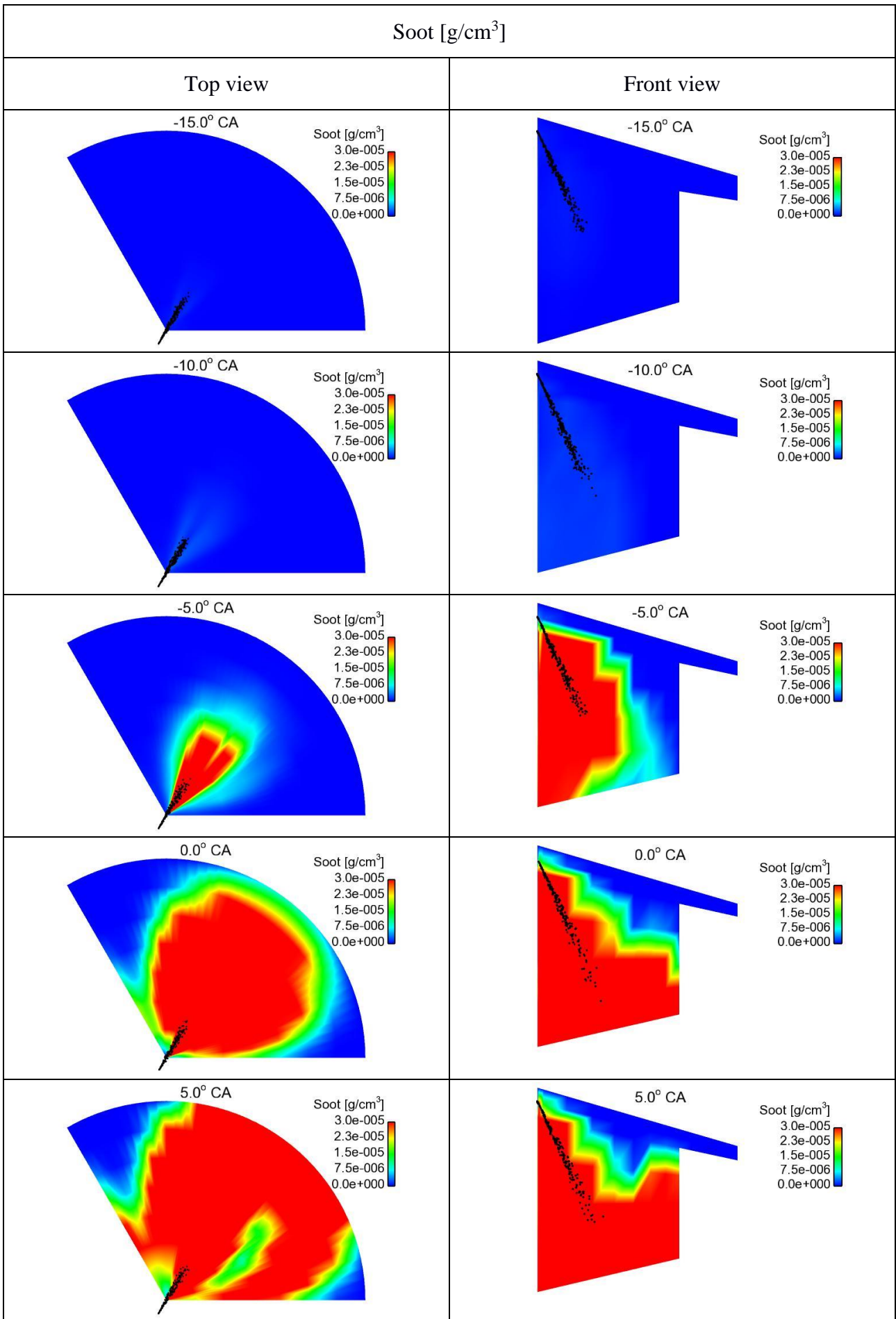


Figure 4.31: Computed traces of total soot mass using the one-step chemistry, at an engine load of 80%.



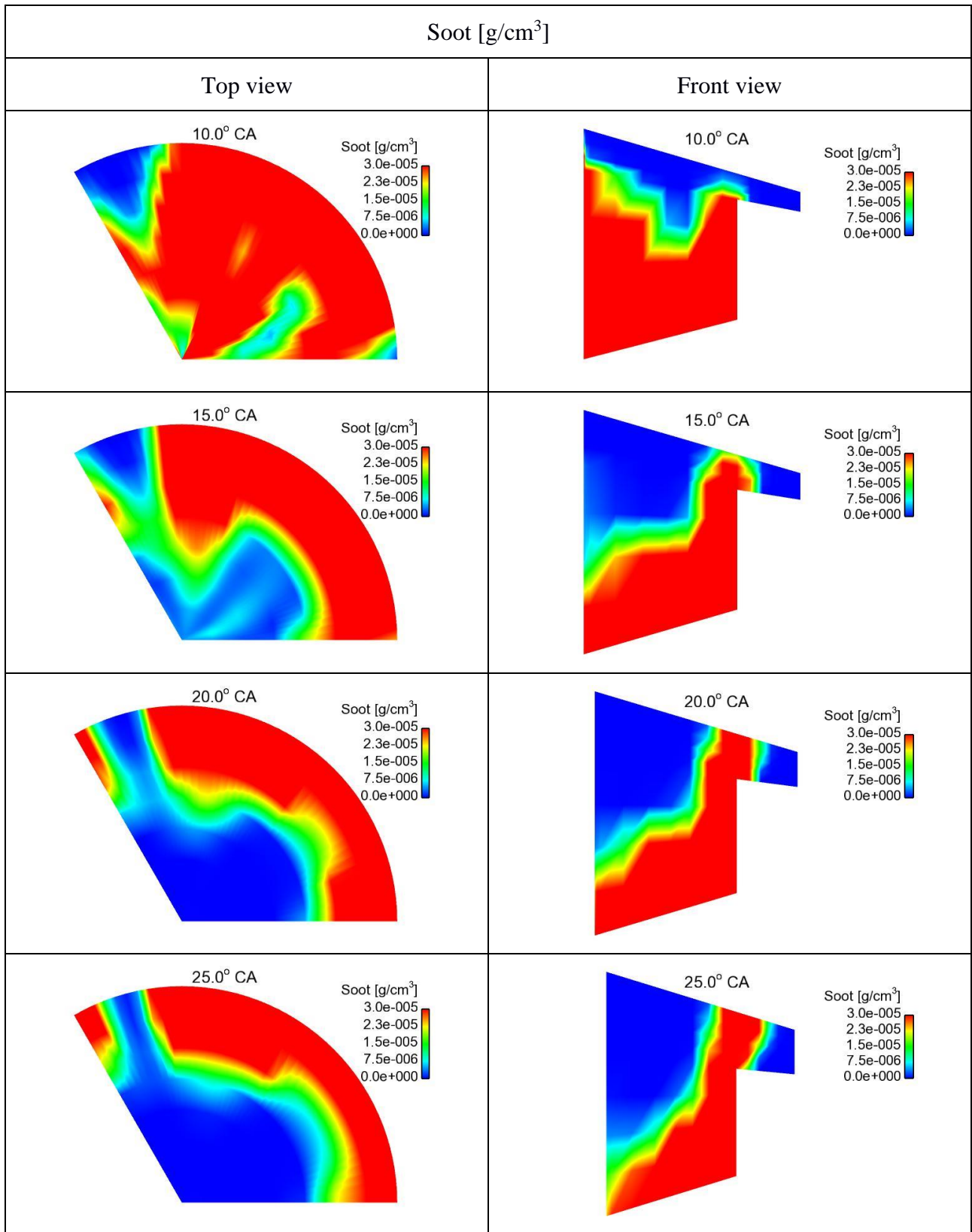


Figure 4.32: Colour-coded contours of soot density for one-step chemistry. A horizontal plane close to the injector and a vertical plane including the injector are considered, at selected time instants.

4.2.2 NO_x emissions

Nitrogen oxides (NO_x) consist mainly of Nitric Oxide (NO) and Nitrogen Dioxide (NO₂). The exhaust concentration of NO in Diesel engines ranges from 80% to 90% of the total NO_x concentration, and the rest 10% to 20 % corresponds to NO₂. Thermal NO (Glassman and Yetter, 2008) is the main source of NO_x. NO is initially formed due to high temperatures but may be transformed to NO₂ in the presence of the colder air. Typical NO_x mechanisms build on the extended Zeldovich model (Weisser 2001), as highlighted in section 2.8.1.

Figure 4.33 presents the computed histories of space-averaged NO_x concentration for the one-step and realistic chemistry cases considered here; the measured value of exhaust concentration is also included. A similar development is demonstrated in all cases, with the final values of NO_x concentration being very close (about 700 ppm) for one-step chemistry and Mech.45 being higher, by about 15%, in comparison to the value computed with Mech.29. In all cases, computations underpredict the experimental value (880 ppm). The higher production of NO_x for one-step chemistry and Mech.45 can be associated with the calculated earlier start of combustion (see heat release rates, presented in Figure 4.6), which results in local higher temperatures prior to TDC, as shown in the temperature visualisations of Figure 4.9 and 4.10. Correspondingly, regions of higher levels of produced NO_x emerge for the two calculations, with the differences persisting up to values of about 25° CA, where the temperature decrease due to expansion terminates the NO_x production, and results in a steady state.

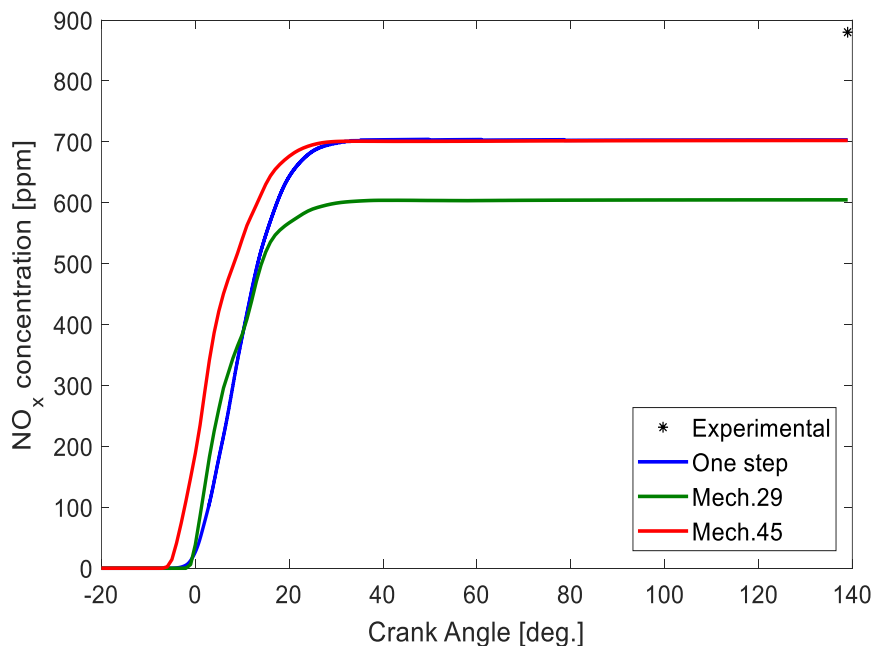
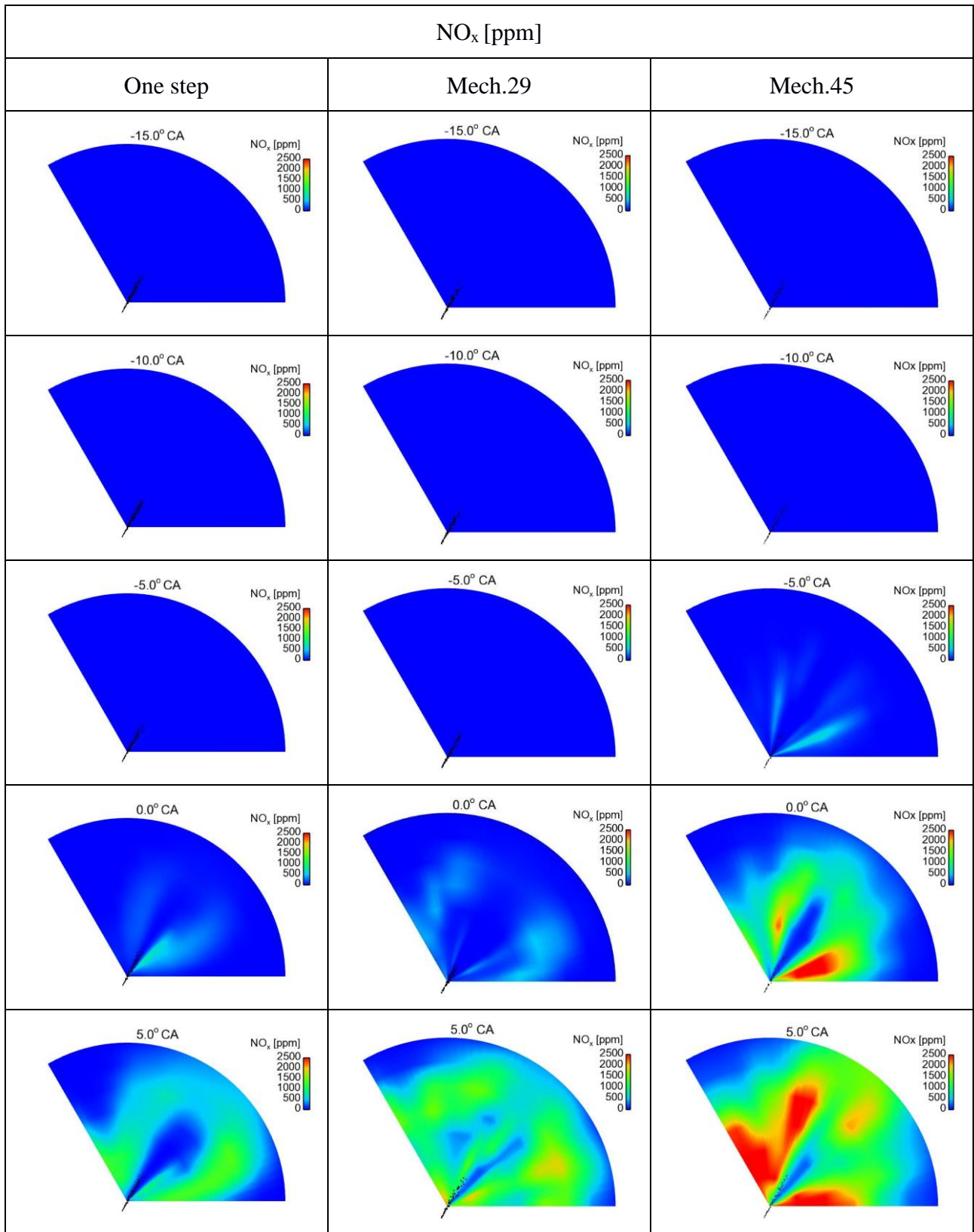


Figure 4.33: Computed traces of mean NO_x (Nitrogen Oxides) concentration using the one-step chemistry and the two reduced order chemical kinetics mechanisms (Mech.29 and Mech.45), at an engine load of 80%. A measured value of final NO_x concentration is also included (Papagiannakis and Hountalas, 2003).



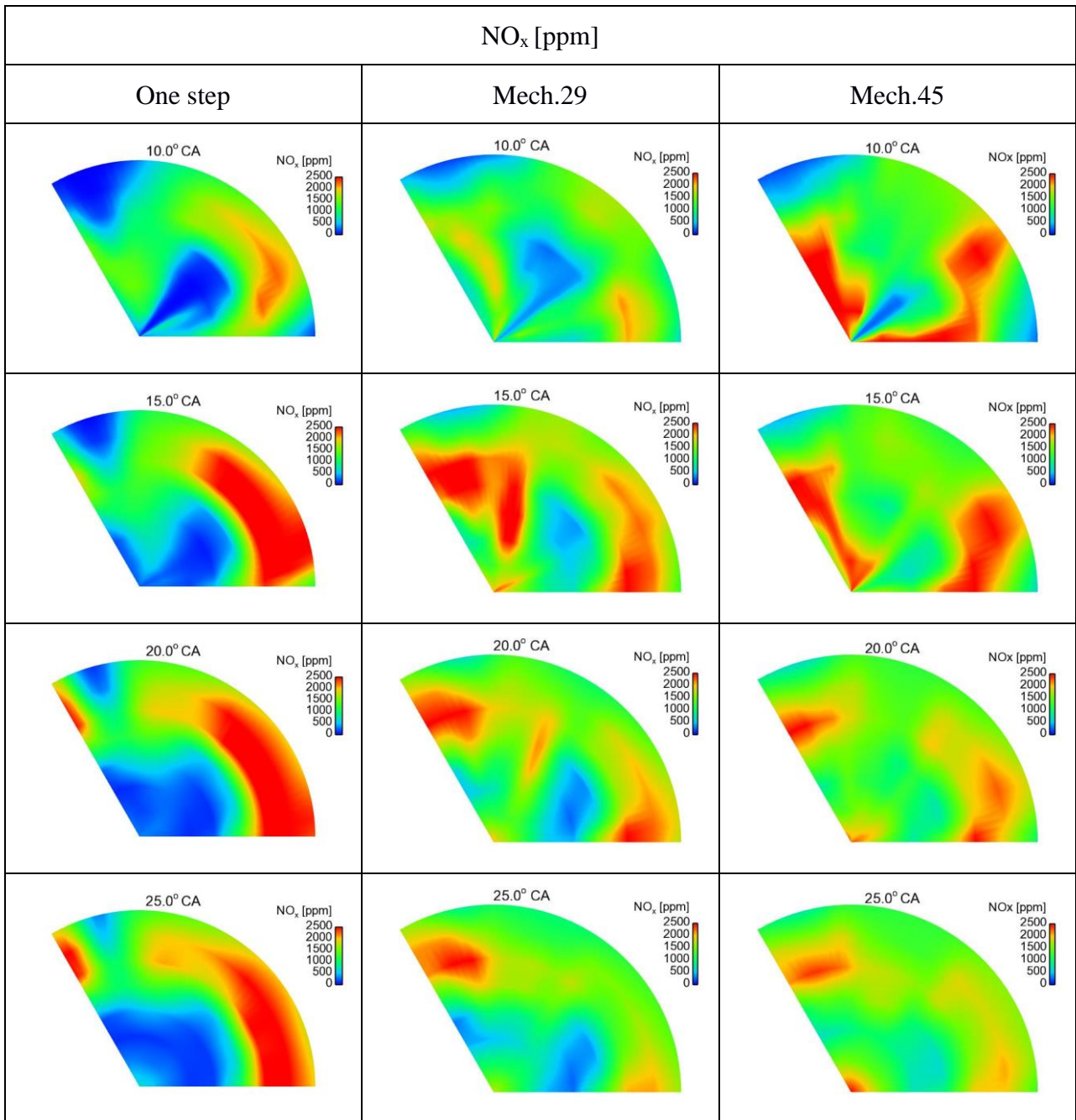
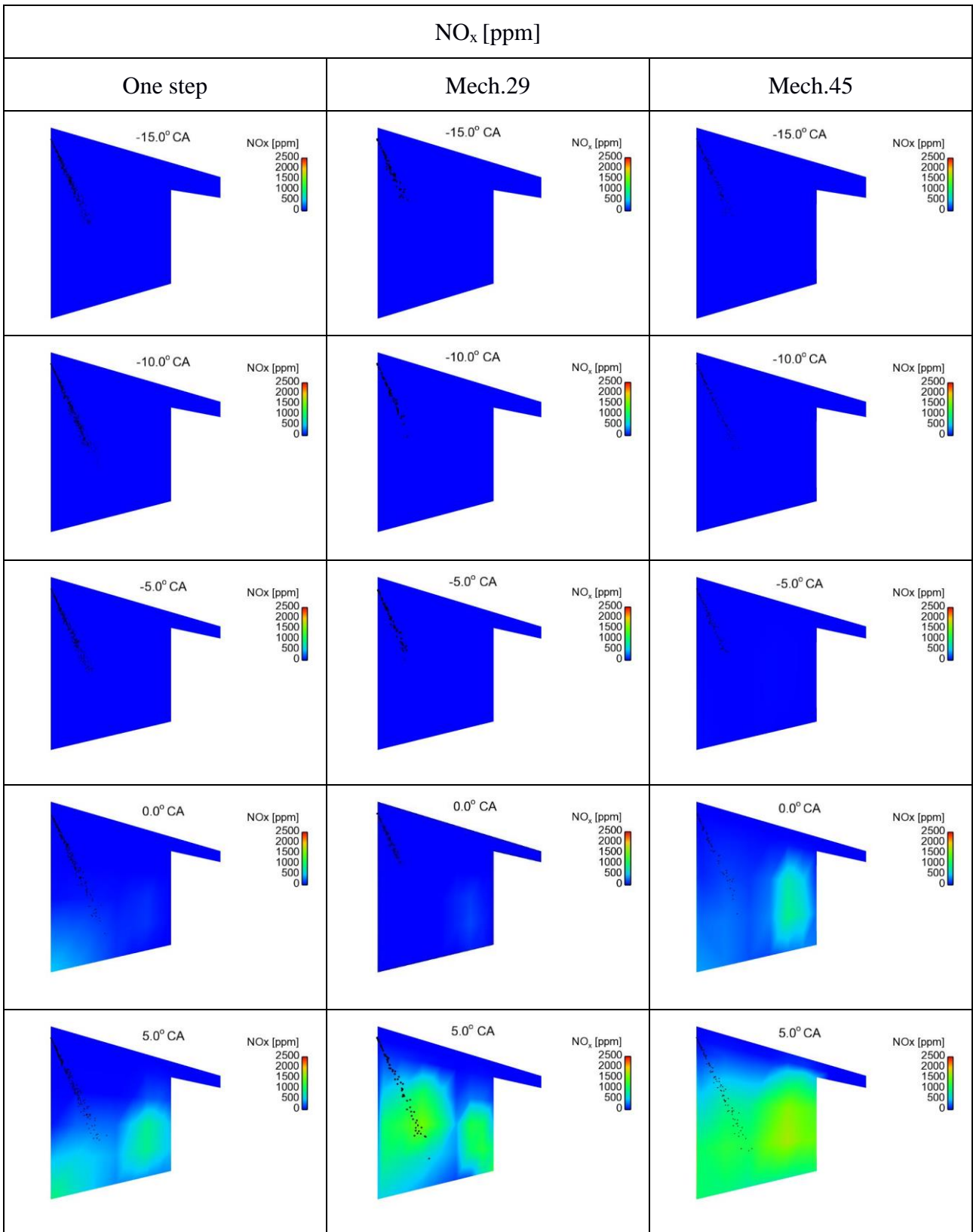


Figure 4.34: Colour-coded contours of NO_x concentration for one-step chemistry and reduced order chemistry using mechanisms Mech.29 and Mech.45. A horizontal plane very close to the injector is considered, at selected time instants.



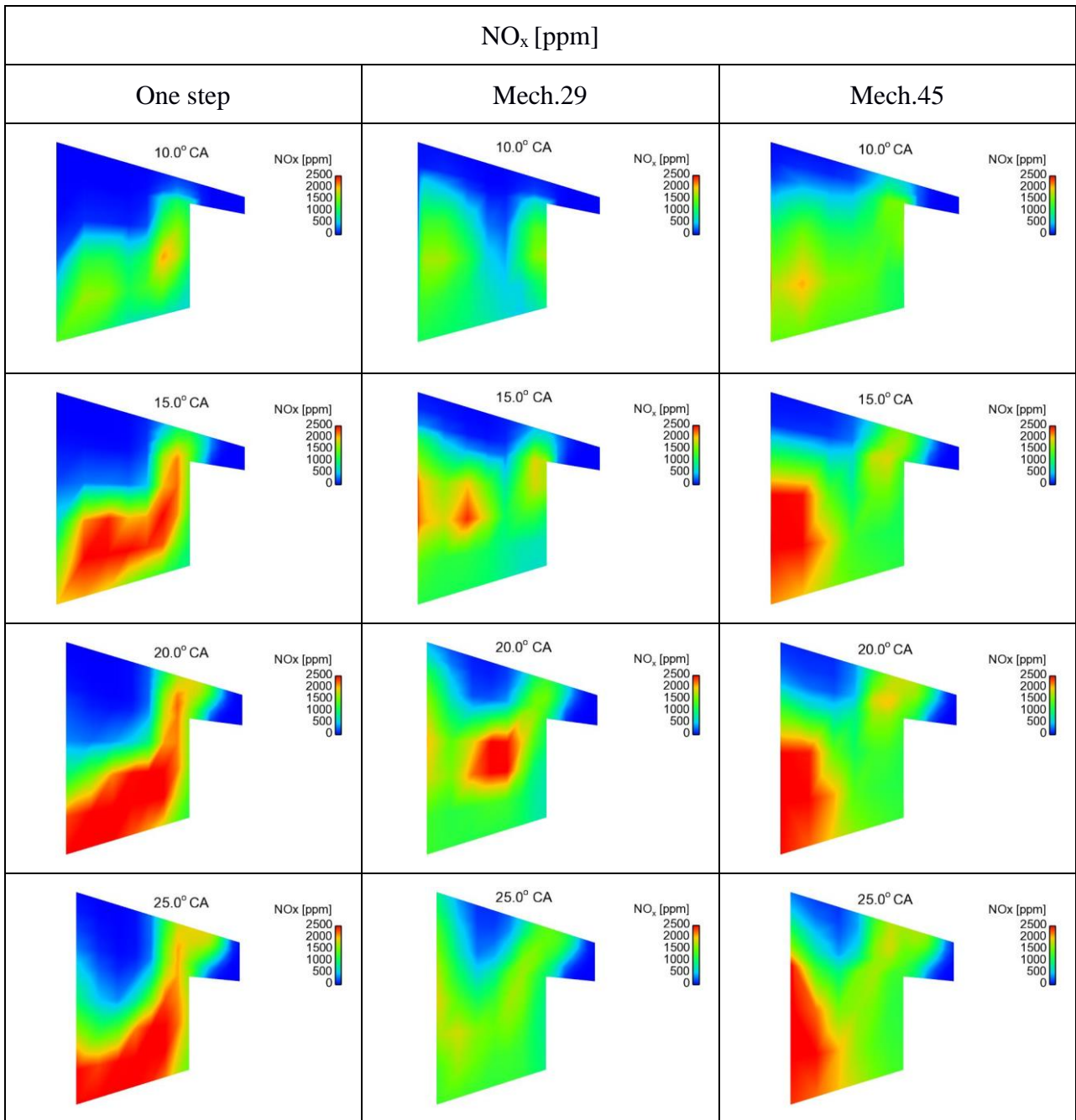


Figure 4.35: Colour-coded contours of NO_x concentration for one-step chemistry and reduced order chemistry using mechanisms Mech.29 and Mech.45. A vertical plane very close to the injector is considered, at selected time instants.

4.3 Chapter conclusions

This Chapter has presented the CFD results for the Lister LV1 engine, for operation at a load of 80%. Here, a single-step approach was used, as well as a realistic chemistry one, in terms of the reduced order mechanisms Mech.29 and Mech.45. Results were compared against the experiments, for the pressure and Rate of Heat Release traces, as well for the exhaust NO_x concentration. Overall, a very good agreement was demonstrated. Computational results were processed to yield traces of global quantities, such as mean temperature and species concentration, as well as associated spatial distributions, at representative time instants. The main outcome of the present analysis can be summarised as follows.

- A longer delay in main ignition is calculated with Mech.29, thus accumulating higher levels of unburned evaporated fuel.
- A more rapid fuel decomposition and combustion development is calculated with realistic chemistry, in comparison to one-step chemistry. In the latter case, more fuel thus accumulates, and is decomposed and burns at later stages of combustion.
- The prolonged fuel decomposition associated with one-step chemistry accumulates fuel in the near-piston region, which converts towards the liner region, due to the presence of a tumbling-type of motion. These effects increase the associated local burning rates and thermal loads.
- For the realistic chemistry cases, fuel decomposition terminates shortly after the end of injection, an effect which is very pronounced for Mech.45.
- For one-step chemistry, the OH radical is dominant, persisting up to late stages of combustion. For realistic chemistry, the role of H and O radical is upgraded, contributing to a faster development of combustion. This faster development is reflected in the early production and destruction of intermediate species, especially CH₄, CH₂O (a soot inhibitor) and HCO.
- The production of CO is very minor in the case of one-step chemistry, but very pronounced for realistic chemistry. An adequate characterisation of the combustion development is thus only feasible by means of detailed/realistic chemistry.
- In the initial stages of combustion, an intense soot production, predicted with one-step chemistry, takes place in the spray flame region, while a high soot concentration is subsequently present in the piston and liner regions, associated with local high concentration of evaporated fuel. Nearly all of the soot produced during the engine cycle is subsequently oxidised.

- The longer effective ignition delay for Mech.29 results in a lower initial formation of NO_x , which leads to a lower exhaust NO_x concentration, in comparison to both one-step chemistry and Mech.29.

5. CFD studies of diesel combustion in a marine dual fuel engine

In the present Chapter, following the simpler cases of constant volume chamber and a laboratory dual fuel engine analysed in the previous two chapters, the CFD modelling approach and tools of this thesis are applied to the study of flow and combustion in a four-stroke dual fuel marine engine, namely the Wärtsilä 50DF engine. As in the previous chapter, chemistry is accounted for by either an one-step approach, or by two mechanisms of moderate size, namely Mech.29 and Mech.45.

5.1 Problem definition

The Wärtsilä 50DF marine engine (Wärtilä, 2015) is simulated for diesel mode operation at full (100%) load. The main engine characteristics are listed in Table 12. Here, only the closed part of the engine cycle is computed, i.e., from -150° CA (Exhaust Valve Closing (EVC)) to 120° CA (Exhaust Valve Opening (EVO)). In the present one-step chemistry simulations, fuel thermophysical properties are determined from those of n-tetradecane ($C_{14}H_{30}$).

Table 12: Main characteristics of the Wärtilä 50DF engine.

Main engine characteristics	
Bore diameter	50 cm
Stroke	58 cm
Connecting rod length	130 cm
Clearance height at TDC	3.85 cm
IVC	-150 deg
EVO	120 deg
Engine speed	514 rpm
Nozzle diameter	0.78 mm

A computational tool, developed by coupling a modified KIVA-3vr2 code with the CHEMKIN-II chemical kinetics code, also used for the simulations presented in the previous chapter, is used in the present simulations; the same chemical kinetics mechanisms, Mech.29 and Mech.45, are considered. The same modified KIVA-3vr2 code used for the one-step chemistry simulations of the previous chapter is used here.

5.2 Analysis of CFD results

The three-dimensional grids used in this chapter correspond to a sector of 36 degrees. Two types of grids were generated: (i) block-structured meshes, using a polar coordinate system, generated by means of the pre-processor module K3PREP, with a typical grid consisting of 147,858 cells; (ii) block-structured meshes, using a cartesian coordinate system, generated using the ICEM-CFD grid generator, with a typical grid consisting of 46,400 cells. The two grids are presented in Figure 5.1. It is noted that simulations using one-step chemistry utilised the polar grid, while simulations with realistic chemistry, with Mech.29 and Mech.45, have utilised the cartesian grid.

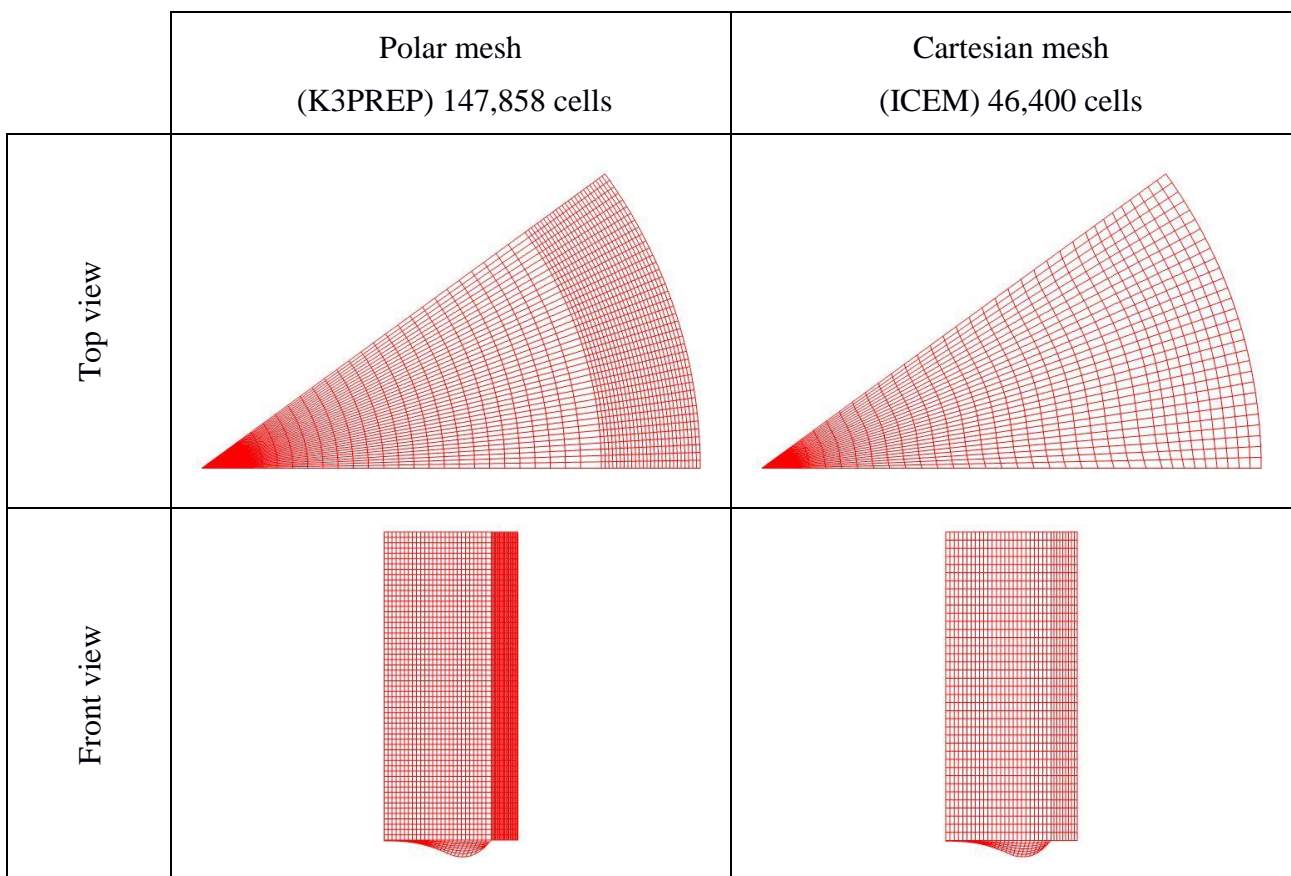


Figure 5.1: Top and front views of the polar and cartesian grid used in the simulations of the Wärtsilä 50DF engine.

The Wärtsilä 50DF engine has one central injector, with ten identical orifices. The symmetric injection from the ten orifices generates a flow and combustion pattern characterised by a symmetry in mean flow, i.e., the mean flow repeats itself every 36 degrees. Thus, in the present RANS simulations, a sector of 36 degrees is used, with periodic boundary conditions for the lateral boundaries. The injection direction is characterised by the vertical angle, β , while, in CFD simulations, a horizontal angle, α , should be also specified; as illustrated in Figure 5.2. The injection profile is prescribed in the present study in terms of square wave, of a proper start and duration; see

Figure 5.3. Important data of the present simulations, including engine data and operational parameters, are presented in Table 13 (P. Kontoulis, private communication). In the same table, the initial conditions for pressure and temperature are included; they are based on estimates using the GT-ISE software for a 0-D two-zone approach, using a Woschni heat transfer model, and a single Wiebe function (Stoumpos et al., 2018).

Table 13: Parameters pertinent to operation and injection characteristics of the Wärtilä 50DF engine.

Reference engine operating conditions	
Intake Pressure	3.8 bar
Initial Temperature	340 K
Start of injection	-12 deg
Injection duration	33 deg
Injected mass per cycle	12.197 g
Number of injectors	1
Number of injector nozzle holes	10
Horizontal angle $\hat{\alpha}$	18 deg
Vertical angle $\hat{\beta}$	17.5 deg
Contraction coefficient	0.8

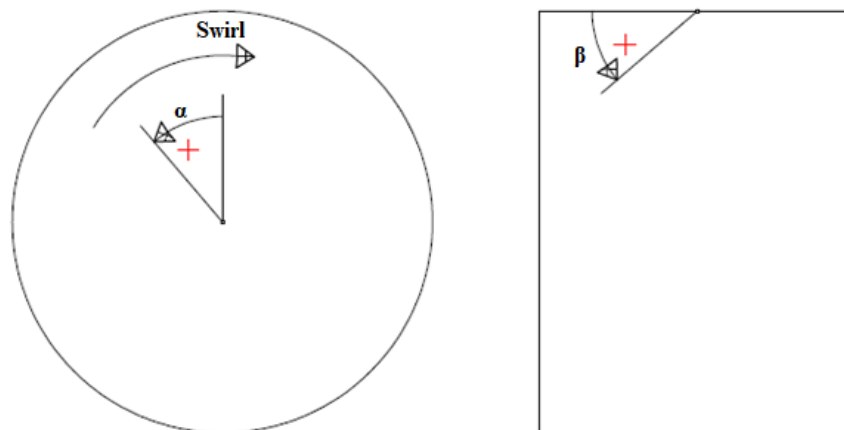


Figure 5.2: Definition of injection direction in terms of angles α and β .

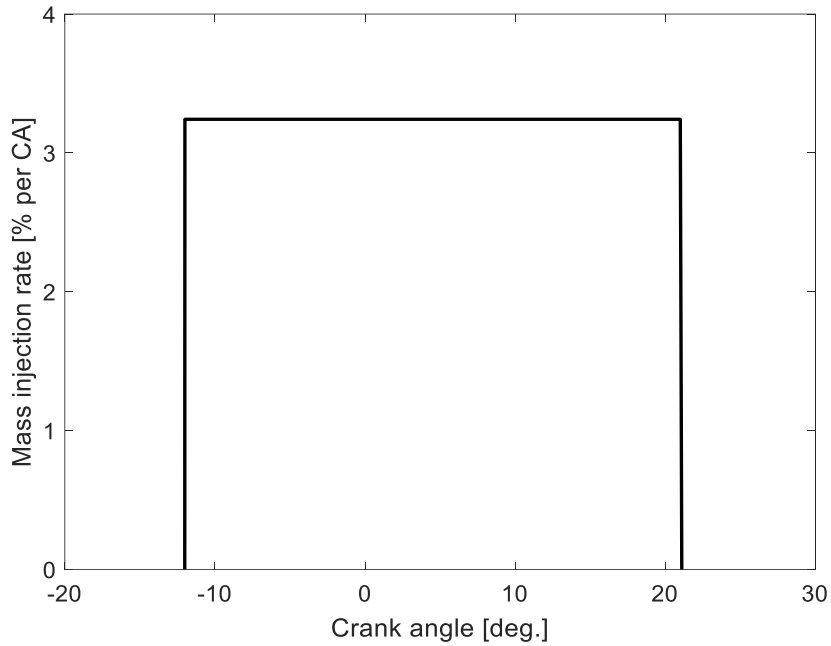


Figure 5.3: Injection profile of the Wärtsilä 50 DF for operation at a load of 100%.

The modelling frame used in the previous chapter has been maintained here, including the details (values of constants) of the physical models. Regarding the CAB spray model, the computed range of droplet Weber number, and associated values of the K_{bu} constant, are presented in Figure 5.4; the case of ETAB model has been maintained, for completeness. For the present engine (Wärtsilä 50DF), estimates of droplet Weber number verify that, in all cases, catastrophic droplet breakup occurs.

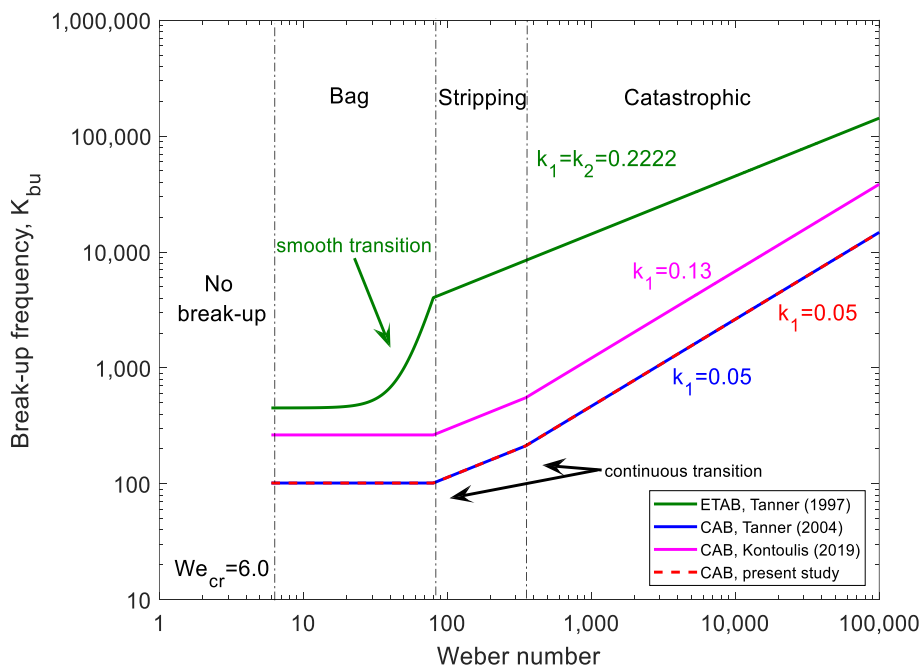


Figure 5.4: Proportionality constant K_{bu} versus Weber number for the ETAB and CAB models.

Figure 5.5 presents the computed p-V diagrams corresponding to the closed part of the engine cycle, for one-step chemistry, as well as for realistic chemistry with Mech.29 and Mech.45. The corresponding values of mean useful power are presented in Table 14, and are close to the value of Nominal Power per cylinder (975 kW), provided by the manufacturer.

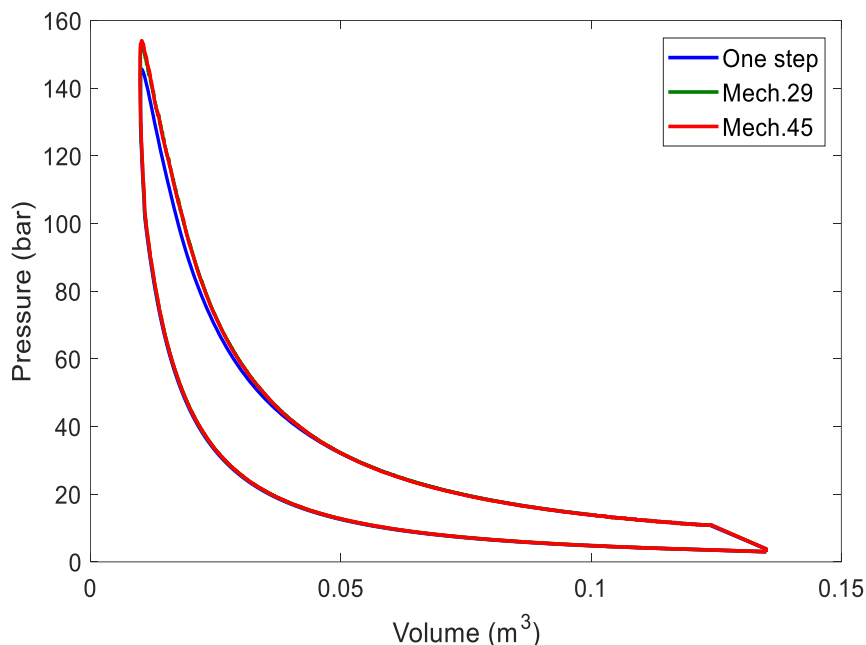


Figure 5.5: P-V diagrams calculated using one-step chemistry and the two reduced order chemical kinetics mechanisms (Mech.29 and Mech.45), at an engine load of 100%.

Table 14: Calculated values of power for the closed part of the cycle using one-step chemistry and the two reduced order chemical kinetics mechanisms (Mech.29 and Mech.45), at an engine load of 100%. The value of Nominal Power (provided by the engine manufacturer) is also included.

Nominal Power: 975 kW/cylinder	
One-step chemistry	Power: 968 kW/cylinder
Mech.29	Power: 979 kW/cylinder
Mech.45	Power: 981 kW/cylinder

Figures 5.6 and 5.7 show the computed cylinder pressure and normalised ROHR traces, respectively, for the one-step chemistry and the two reduced order chemistry mechanisms, Mech.29 and Mech.45. The corresponding maximum value of experimental pressure, for an undetermined crank angle (G. Theotokatos, private communication), as well as the corresponding trace of the 0-D simulation, are also included. In all cases, a good agreement among the present CFD simulations is demonstrated. A

first important observation is that the one-step combustion and both the reduced order mechanisms have similar ignition delay times; in contrast, a substantially longer ignition delay characterises the 0-D results, which affects the subsequent development of pressure. The detailed chemistry predicts higher levels of maximum pressure, in comparison to the experiment and the one-step chemistry. The ROHR curves, presented in Figure 5.7, verify the presence of a premixed and a diffusion phase of combustion. The results corresponding to Mech.45 are in qualitative agreement with the CFD results for four-stroke marine engines presented in Weisser (2001). The same trends are pertinent to the one-step chemistry and Mech.29 simulations, with the premixed phase being more pronounced. Finally, Figure 5.8 presents the computed history of mean cylinder temperature, verifying the very good agreement between the present CFD simulations, and also indicating a deviation from the corresponding temperature trace of the burned zone of the 0-D simulation.

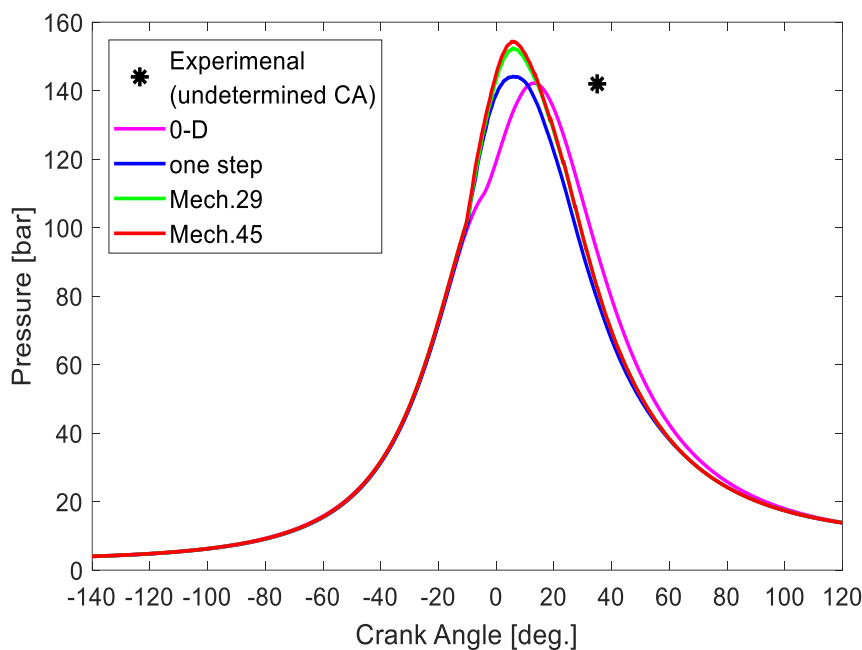


Figure 5.6: Computed traces of cylinder pressure using one-step chemistry and the two reduced order chemical kinetics mechanisms (Mech.29 and Mech.45), at an engine load of 100%. The corresponding trace from the 0-D simulation (Stoumpos et al., 2018)), as well as the maximum experimental value of pressure for an undetermined crank angle, are also included.

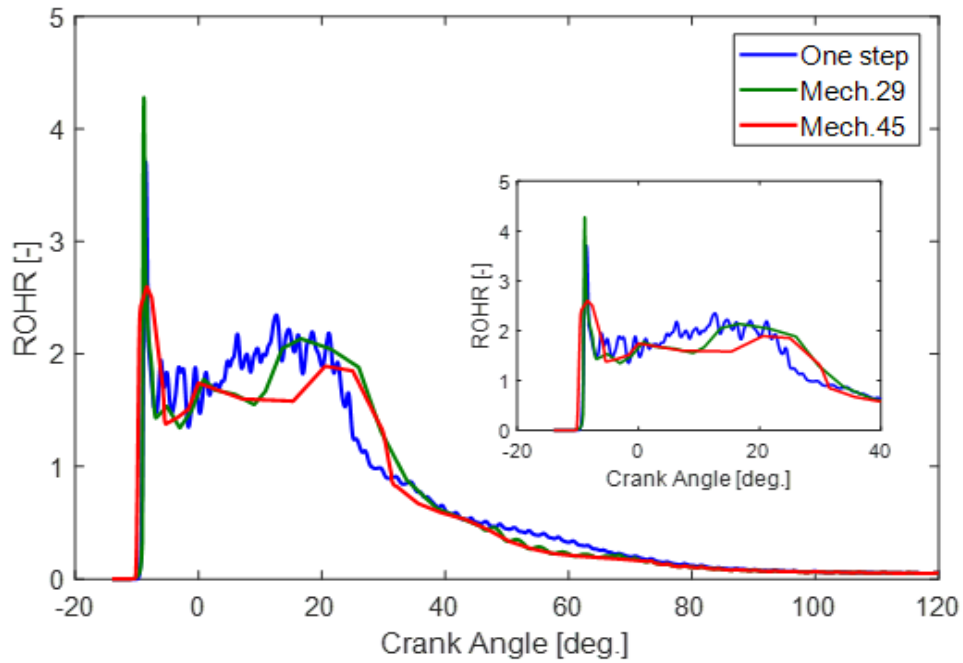


Figure 5.7: Computed traces of normalized Rate of Heat Release using one-step chemistry and the two reduced order chemical kinetics mechanisms (Mech.29 and Mech.45), at an engine load of 100%.

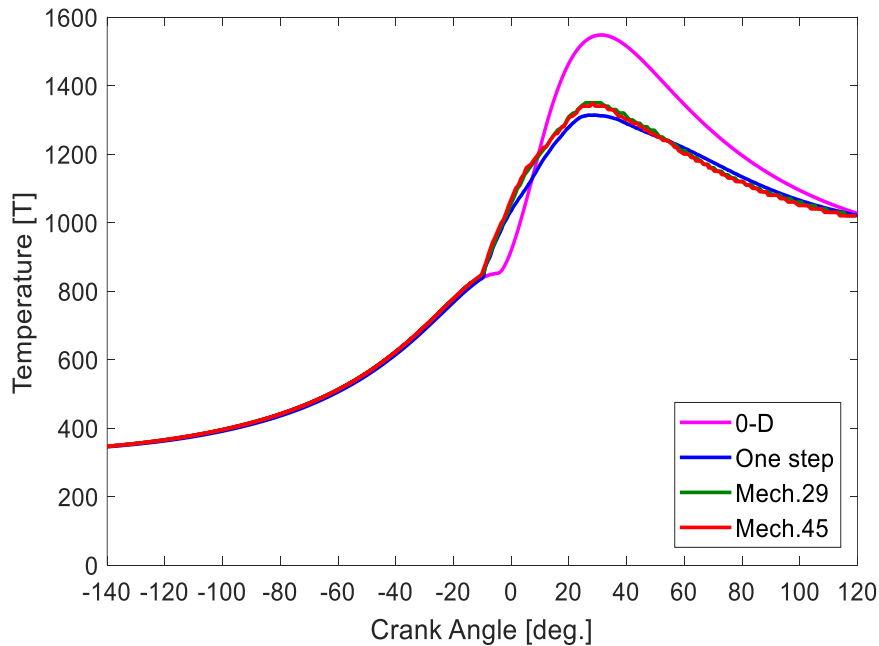


Figure 5.8: Computed traces of mean cylinder temperature using one-step chemistry and the two reduced order chemical kinetics mechanisms (Mech.29 and Mech.45), at an engine load of 100%. The corresponding burned zone trace from the 0-D simulation (Stoumpos et al., 2018) is also included.

Next, visualisations of the computed fields of temperature, equivalence ratio, fuel decomposition rate, and concentration of OH radical, CH₄, CH₂O, CO, CO₂, NO_x and soot, at selected time instants, namely -10°, -5°, 0°, 5°, 10°, 15°, 20°, 25° and 30° of engine crank angle (CA), are presented, to characterise the development of combustion. Visualisation utilises a representative horizontal plane,

close to the injector, and a representative vertical plane, including the injector, shown in Figure 5.9.

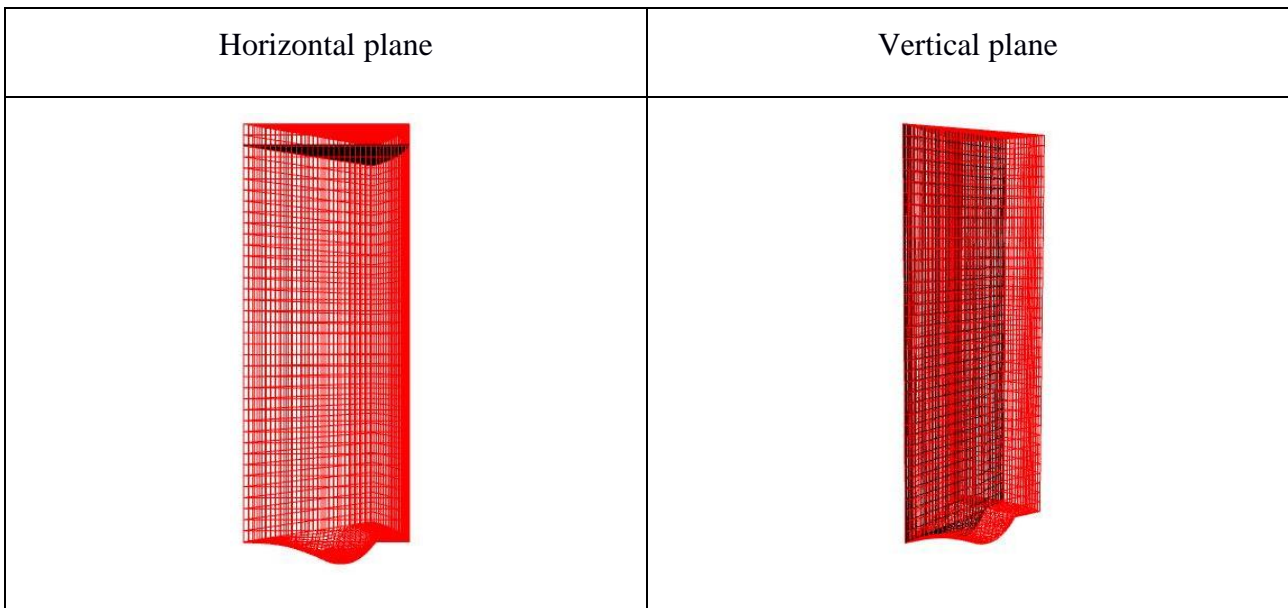
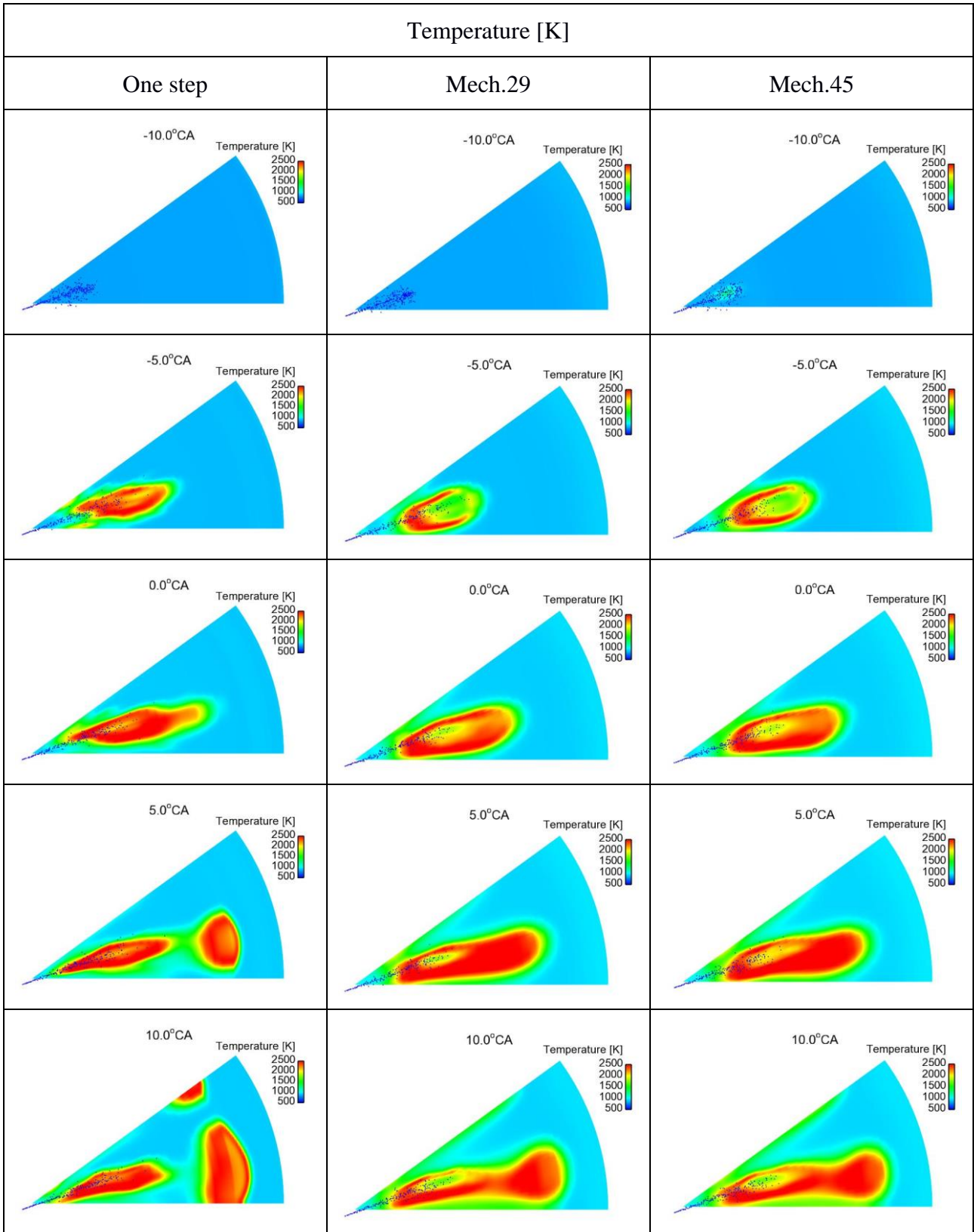


Figure 5.9: Horizontal and vertical planes used in visualisation of the computed fields.

Figure 5.10 presents visualisations (top view) of the distribution of temperature at representative time instants, for simulations using the one-step approach and the two reduced mechanisms (Mech.29 and Mech.45), at the horizontal plane of Figure 5.9, suggesting a similar development of combustion, for the three calculations performed. The discontinuous distribution of temperature in the one-step chemistry simulation during the later stages of combustion is the outcome of a tumbling-type of motion, shown in Figure 5.11, supported by the shape of bowl. A similar development is assessed from the visualisations of equivalence ratio, shown in Figure 5.12, which also suggest an earlier termination of fuel decomposition, for the realistic chemistry cases.



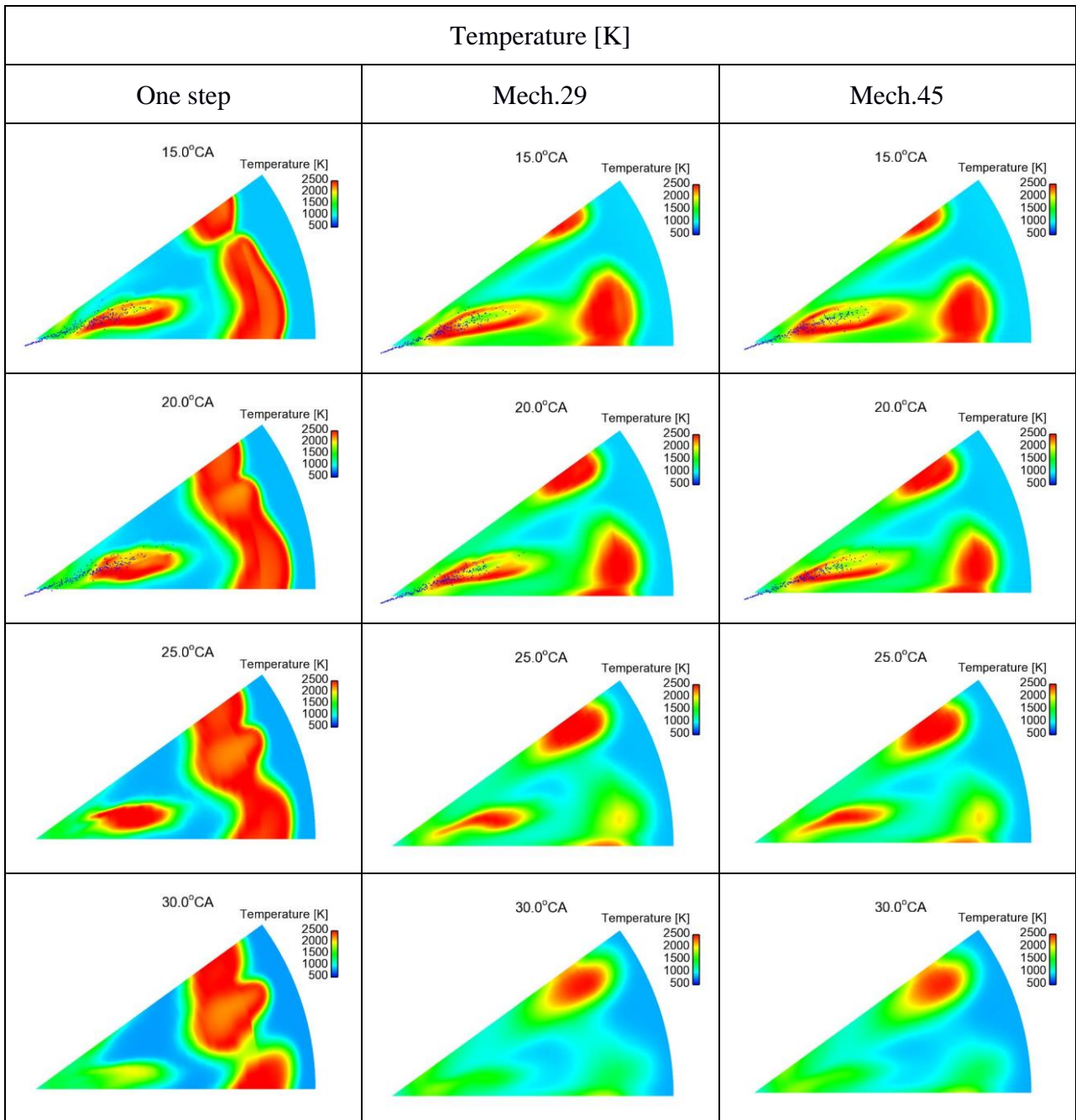
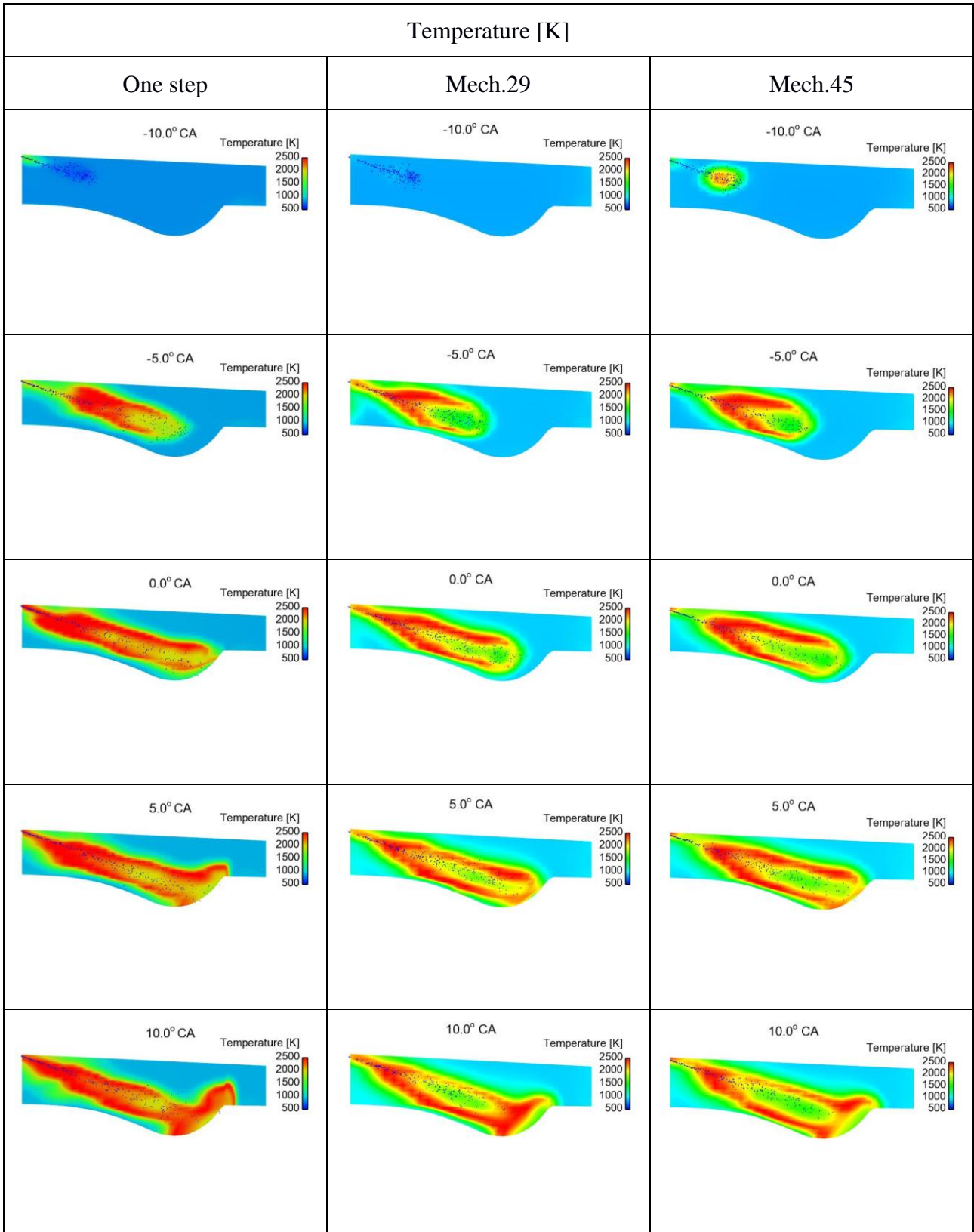


Figure 5.10: Colour-coded contours of temperature for one-step chemistry and reduced order chemistry using mechanisms Mech.29 and Mech.45. A horizontal plane very close to the injector is considered, at selected time instants.



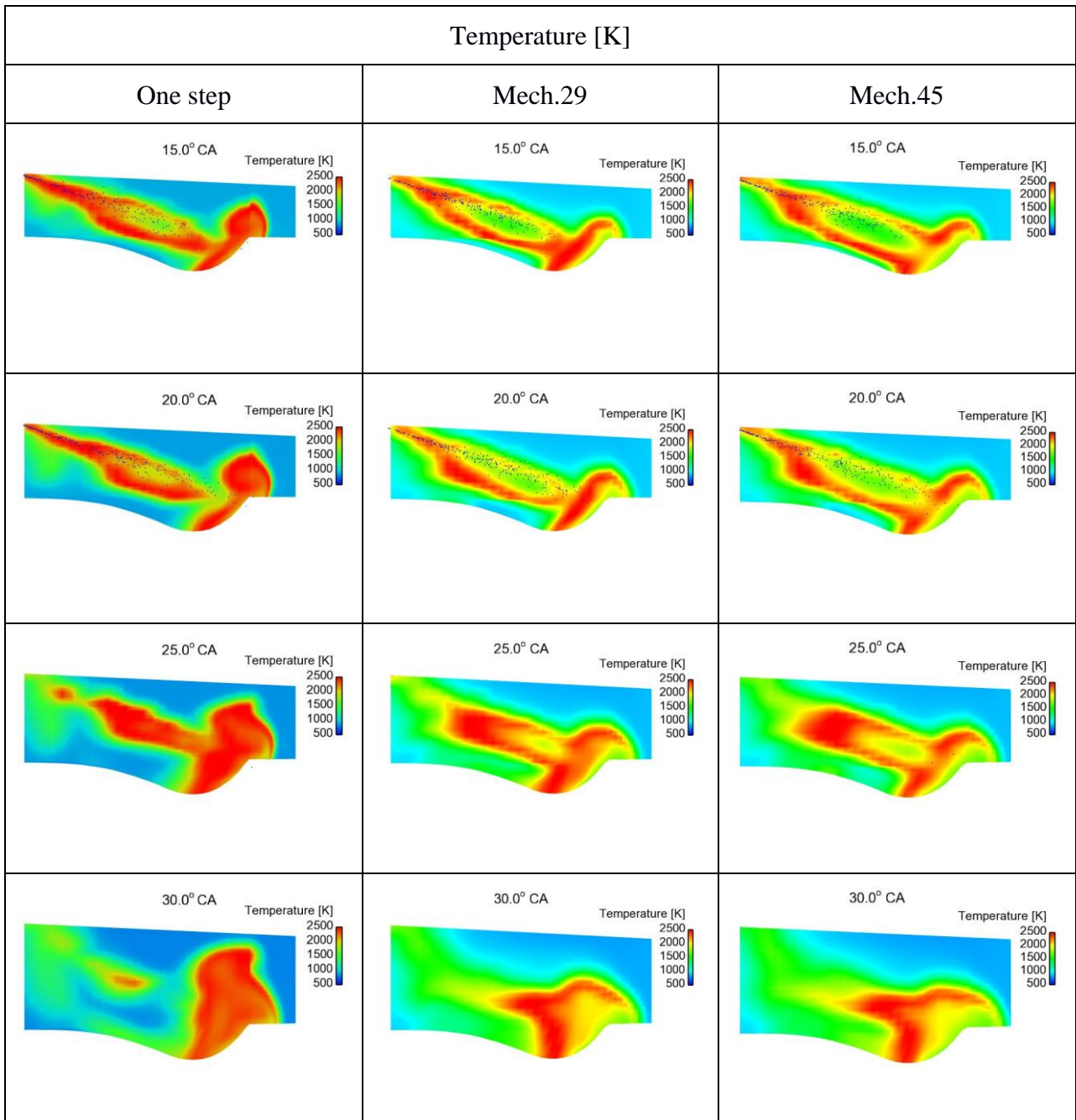
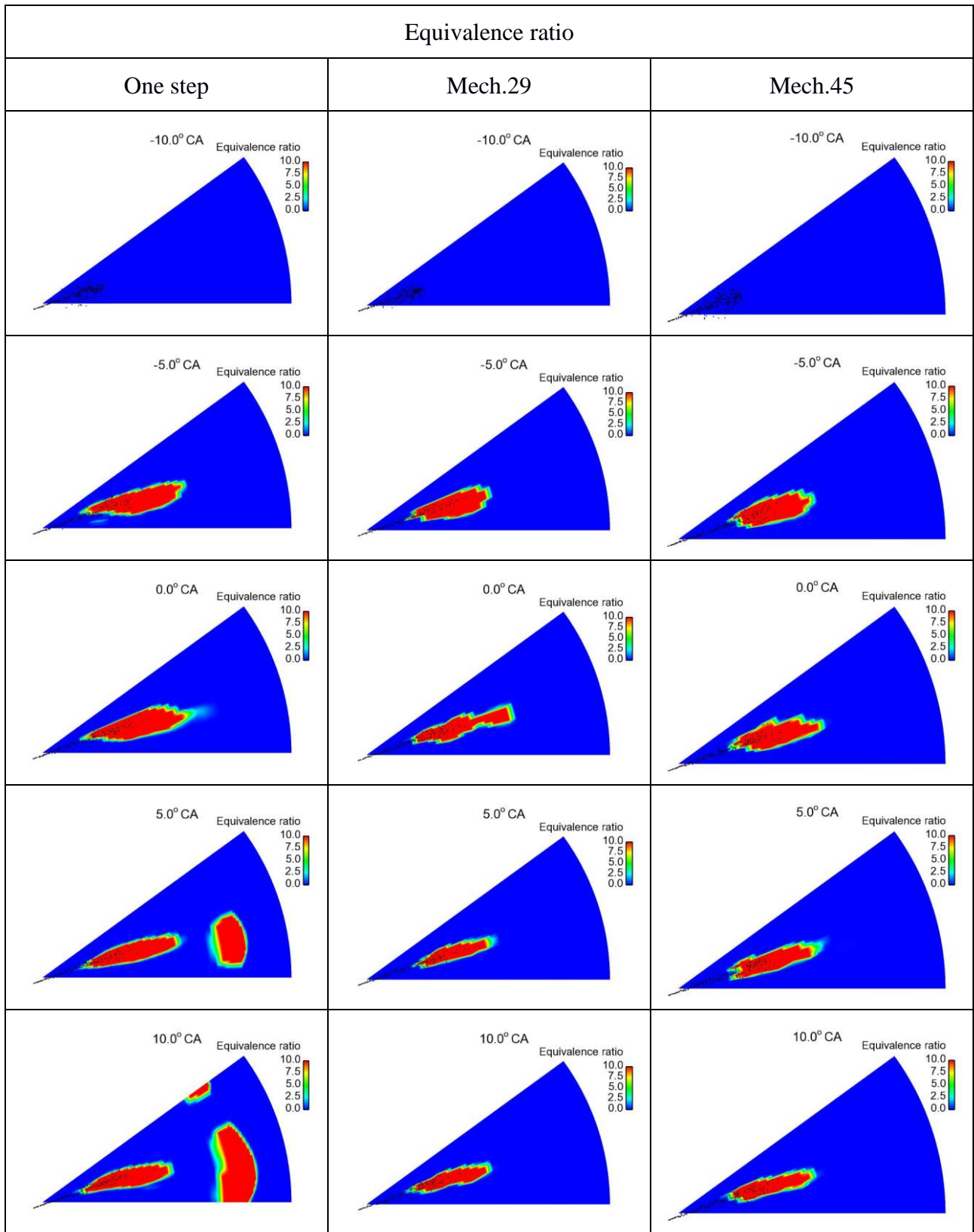


Figure 5.11: Colour-coded contours of temperature for one-step chemistry and reduced order chemistry using mechanisms Mech.29 and Mech.45. A vertical plane including the injector is considered, at selected time instants.



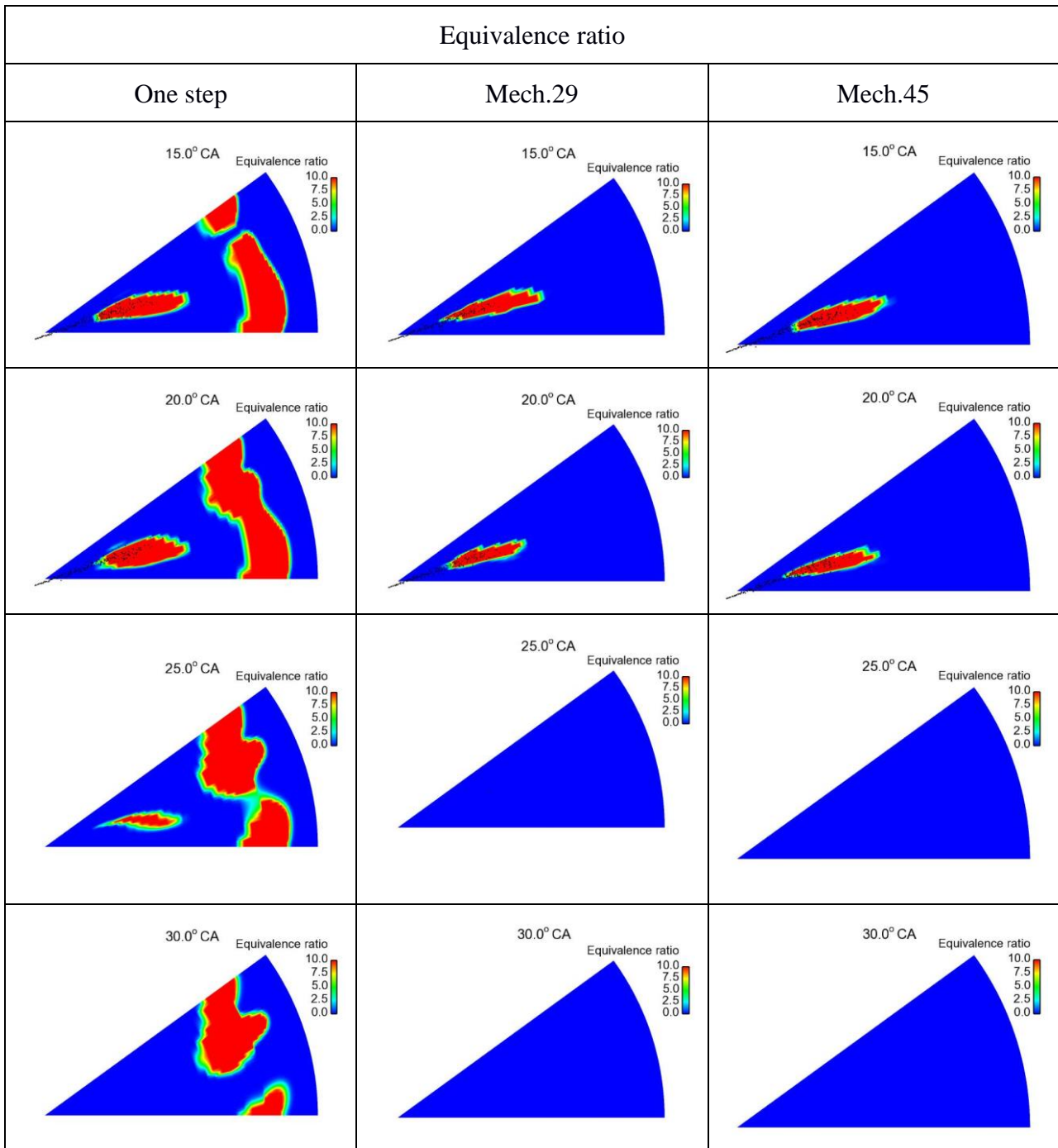


Figure 5.12: Colour-coded contours of equivalence ratio for one-step chemistry and reduced order chemistry using mechanisms Mech.29 and Mech.45. A horizontal plane very close to the injector is considered, at selected time instants.

To elaborate on the CFD results on ignition delay, the computed ignition delay times are presented in Figure 5.13, along with computed values of ignition delay versus temperature, at a pressure close to 90 bar, for representative HFO qualities (Kontoulis, 2019); ignition delay times of stoichiometric n-heptane – air mixtures, as calculated from chemical kinetics simulations (Weisser, 2001), are included. As shown in Figure 5.13, the present CFD results correspond to ignition delays shorter than those of HFO ignition. The present values of ignition delay are close to those of Weisser (2001).

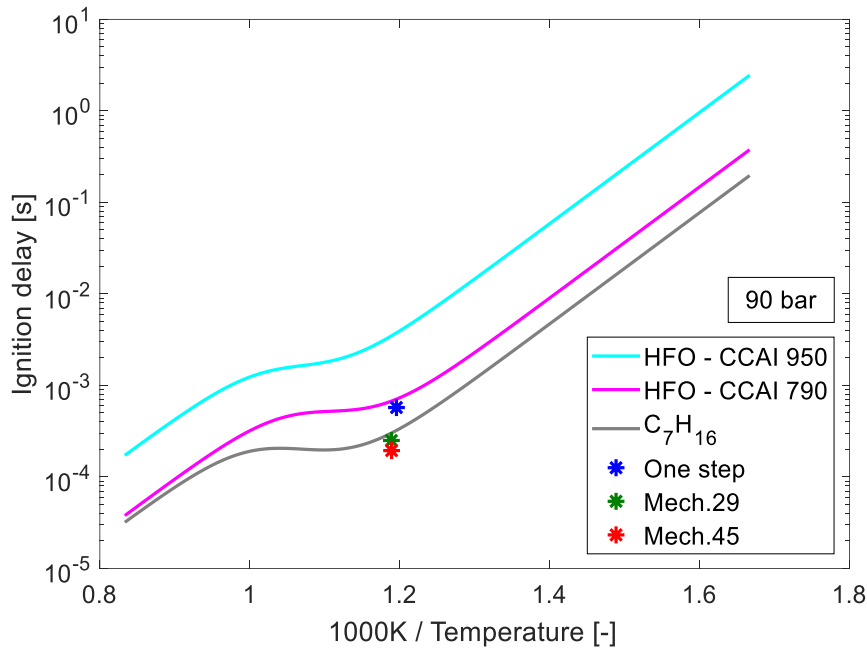


Figure 5.13: Calculated ignition delay times versus temperature for: (a) present CFD simulations using one-step chemistry and realistic chemistry with the reduced mechanisms Mech.29 and Mech.45 in the Wärtilä 50DF engine (colour dots); (b) CFD simulations in a constant volume combustion chamber using two marine fuels with CCAI value in the upper and low limit of marine HFOs, as reported in Kontoulis, 2019; (c) chemical kinetics calculations of n-heptane (C_7H_{16}) combustion at $P=90$ bar and $\Phi=1$, as reported in Weisser, 2001.

Figure 5.14 presents the mean fuel decomposition rate for the three kinetics models of the present study. An important observation is that, for the realistic chemistry cases, fuel decomposition terminates shortly after the end of injection (close to 21 degrees CA); it is in accordance with the equivalence ratio visualisations of Figure 5.12. In more detail, visualisations of the fuel decomposition rate are presented in Figure 5.15 and Figure 5.16, for the horizontal and the vertical plane, respectively, considered here. The visualisations verify the earlier start of fuel decomposition for realistic chemistry, which is slightly more pronounced for Mech.45. They also verify the earlier termination of fuel decomposition for realistic chemistry.

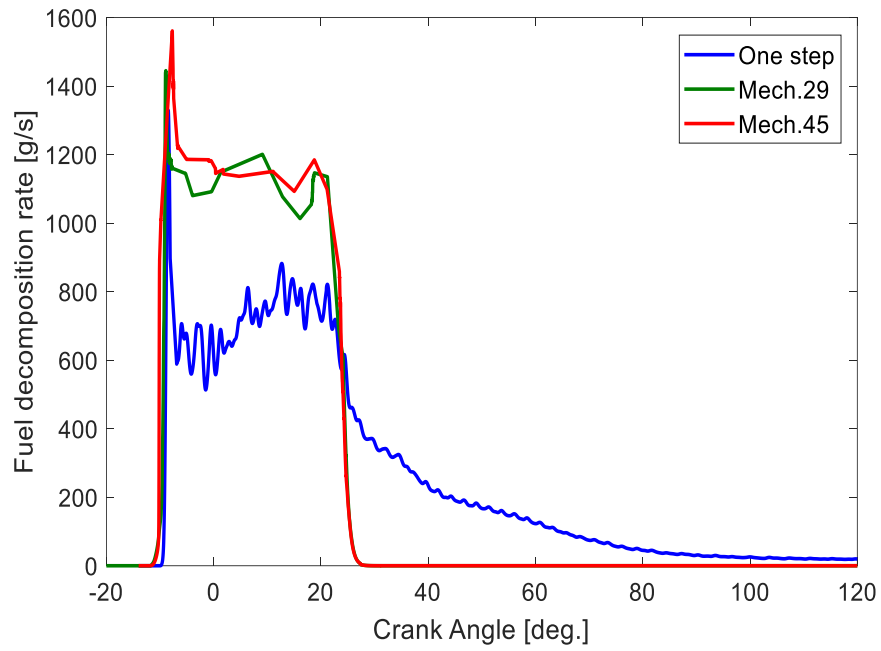
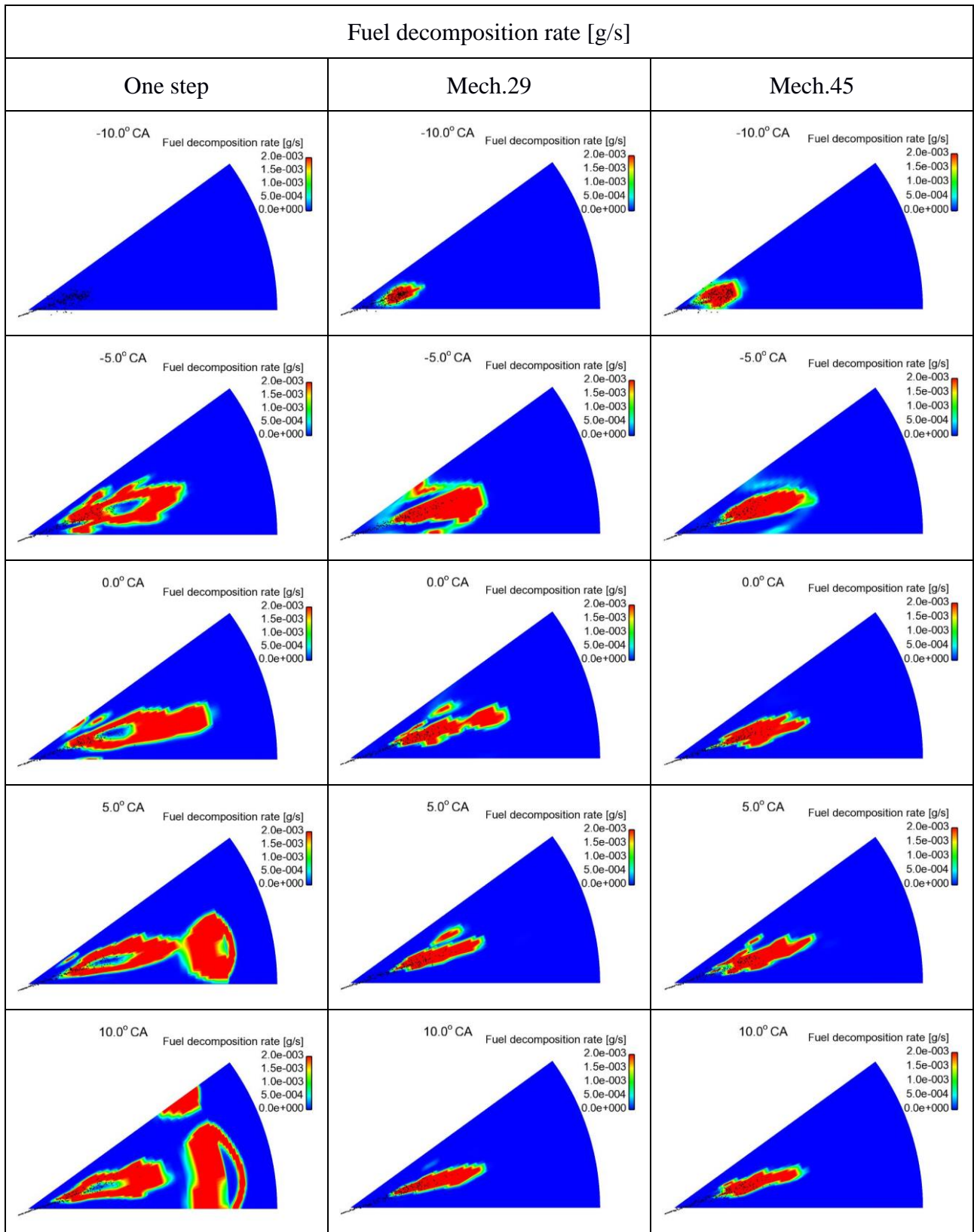


Figure 5.14: Computed traces of mean fuel decomposition rate using one-step chemistry and the two reduced order chemical kinetics mechanisms (Mech.29 and Mech.45), at an engine load of 100%.



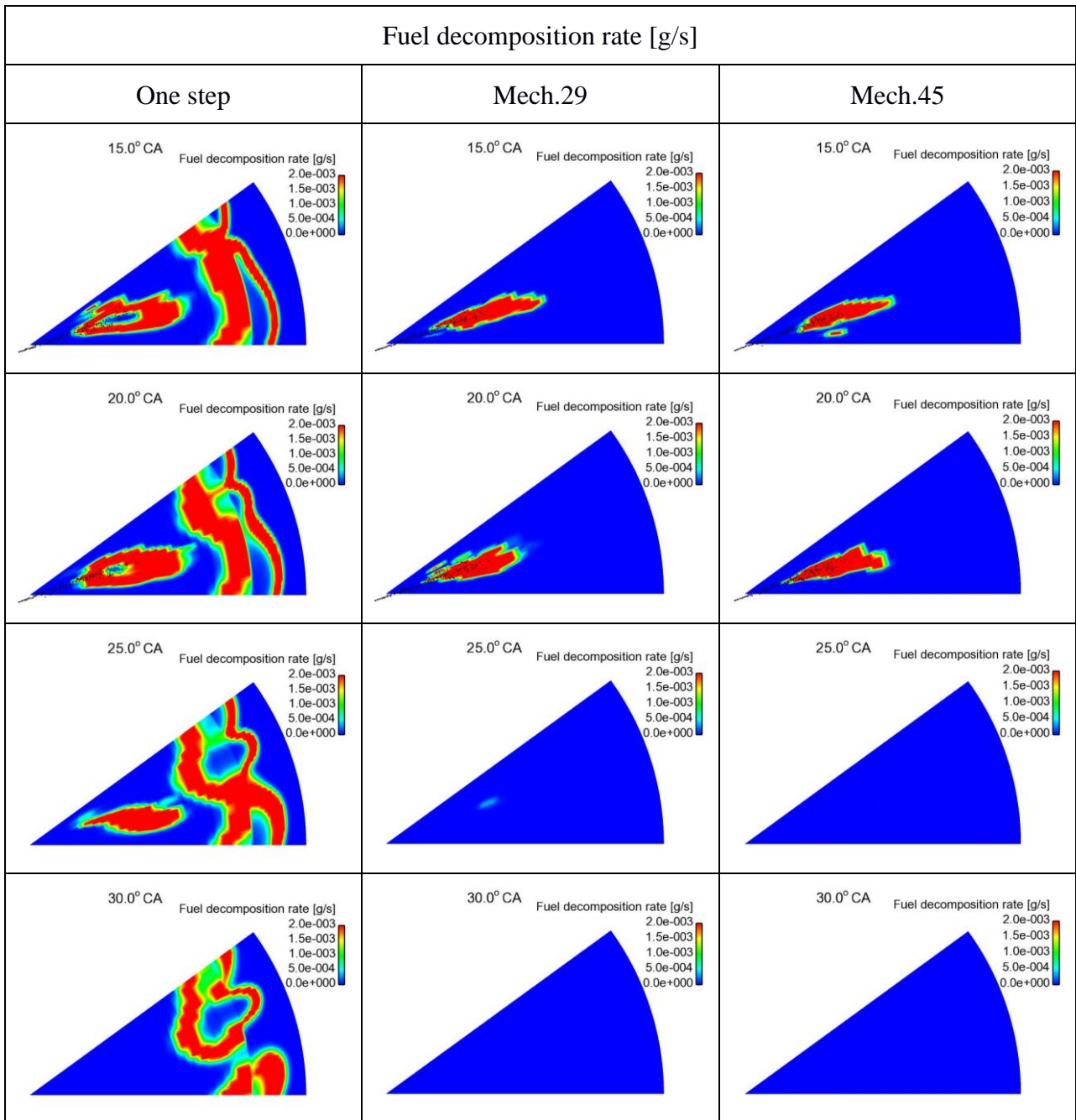
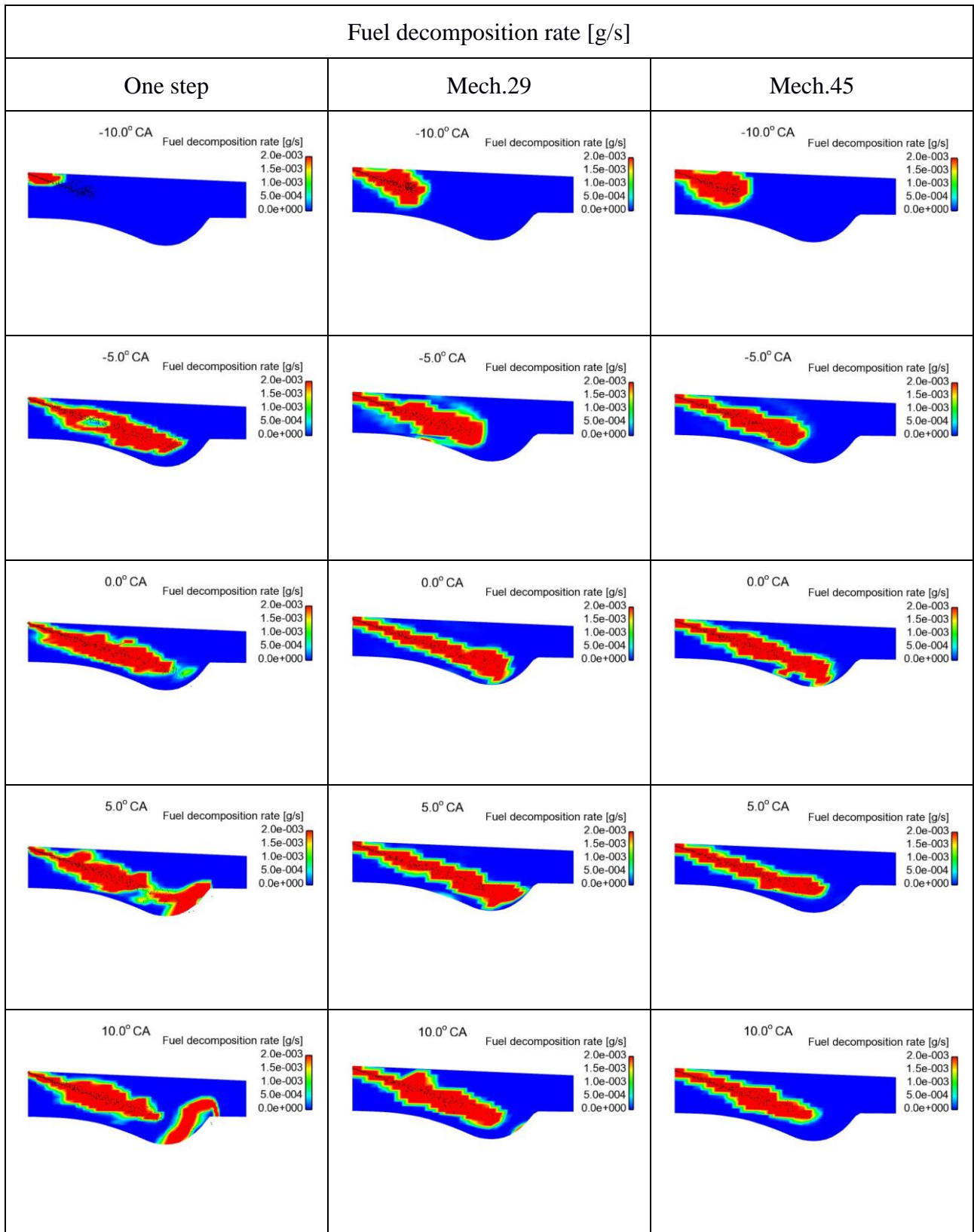


Figure 5.15: Colour-coded contours of fuel decomposition rate for one-step chemistry and reduced order chemistry using mechanisms Mech.29 and Mech.45. A horizontal plane very close to the injector is considered, at selected time instants.



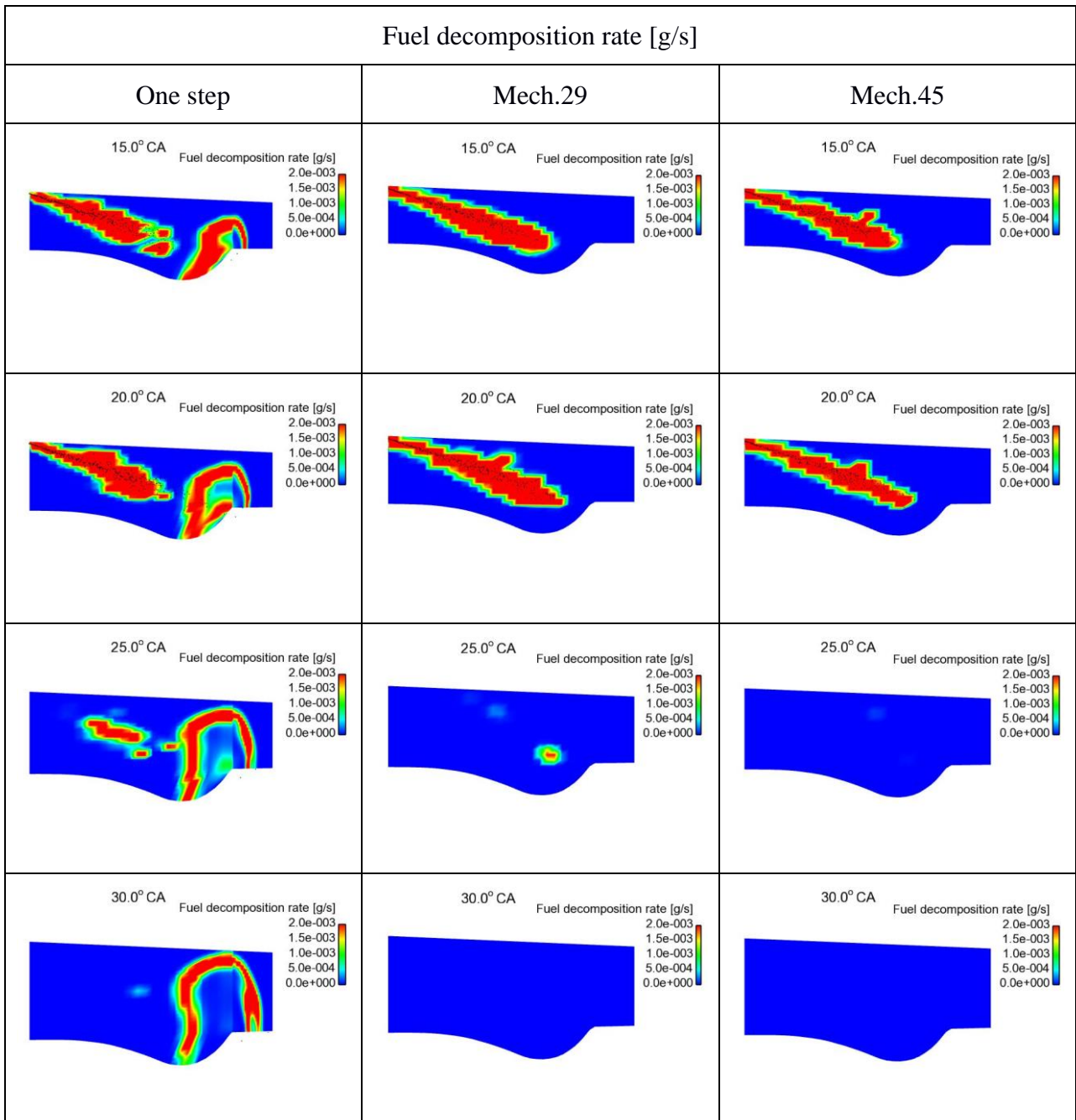


Figure 5.16: Colour-coded contours of fuel decomposition rate for one-step chemistry and reduced order chemistry using mechanisms Mech.29 and Mech.45. A vertical plane including the injector is considered, at selected time instants.

5.2.1 Carbon-based emissions

Similarly, to the previous chapter, the temporal evolution of combustion can be characterised in terms of the evolution of the concentration of important species, such as Hydroxyl radical (OH), Oxygen radical (O), Hydrogen radical (H), Methane (CH₄), Methyl radical (CH₃), Formaldehyde (CH₂O), Formyl radical (HCO), Carbon Monoxide (CO) and Carbon Dioxide (CO₂). The coupled computational tool used in the present study enables calculating the temporal evolution of the above species, including important ones which cannot be calculated with an one-step type of approach; these include CH₃, CH₄, HCO and CH₂O.

Figure 5.17 shows the computed histories of space-averaged OH concentration, for the one-step chemistry and the realistic chemistry calculations of the present study. The earlier ignition for the Mech.45 mechanism is demonstrated and is in accordance with the details of fuel decomposition rate curve (Figure 5.14). An interesting observation is that the two cases of realistic chemistry nearly coincide regarding OH, whilst the one-step chemistry gives higher concentration values after TDC. Similar values are attained in all cases at large values of engine crank angle. The visualisations of OH radical, presented in Figure 5.18, verify very similar distributions for the two cases of realistic chemistry. They also demonstrate the stronger presence of OH radical for one-step chemistry and values of crank angle around 20 degrees, as well as the associated presence of combustion within the pattern induced by the tumble-type of motion.

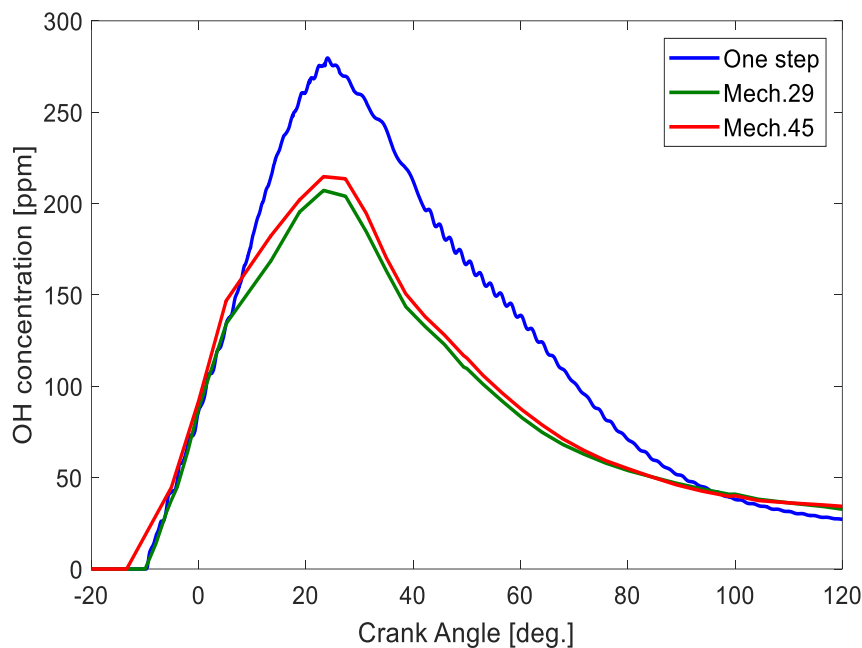
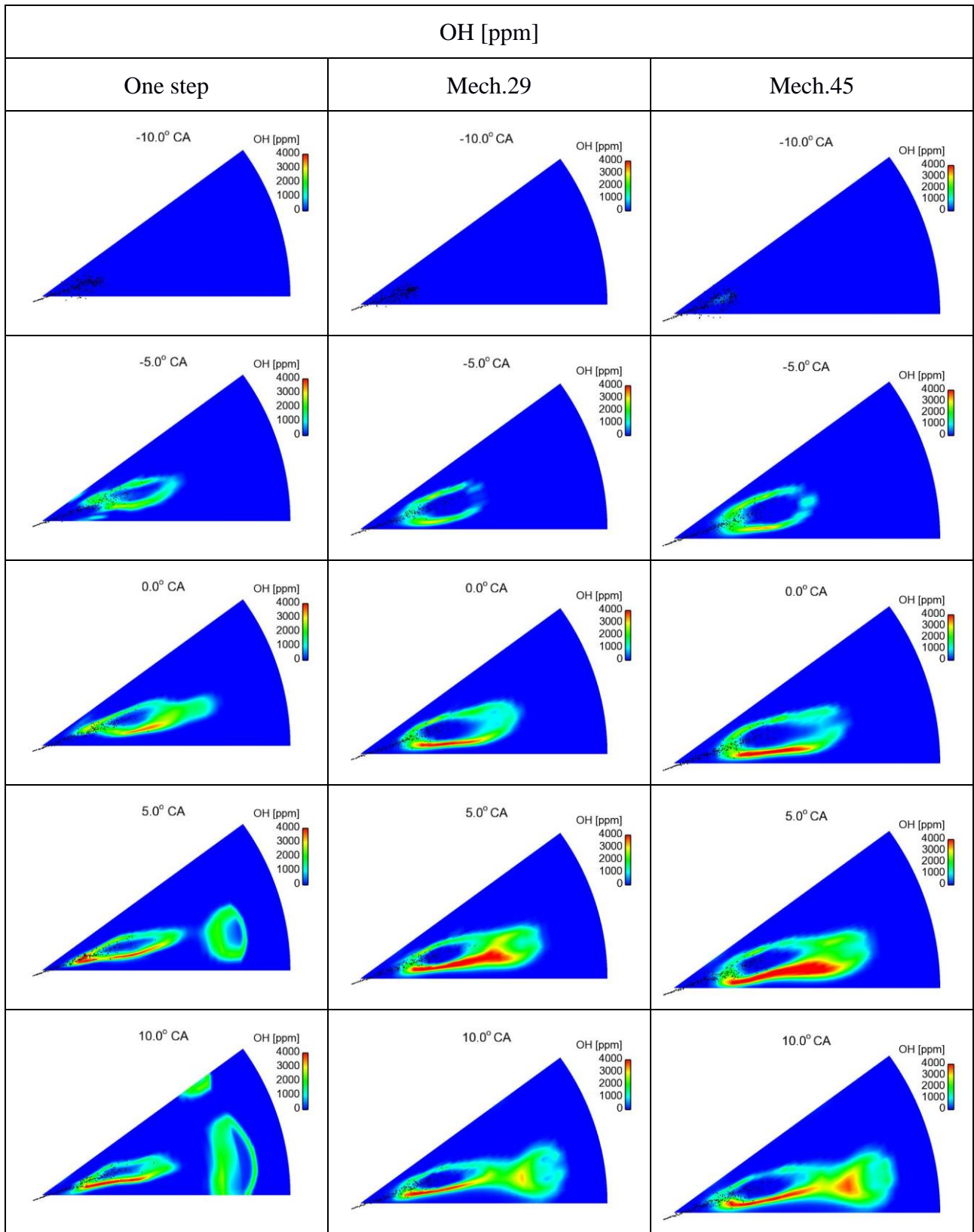


Figure 5.17: Computed traces of mean OH (Hydroxyl radical) concentration using one-step chemistry and the two reduced order chemical kinetics mechanisms (Mech.29 and Mech.45), at an engine load of 100%.



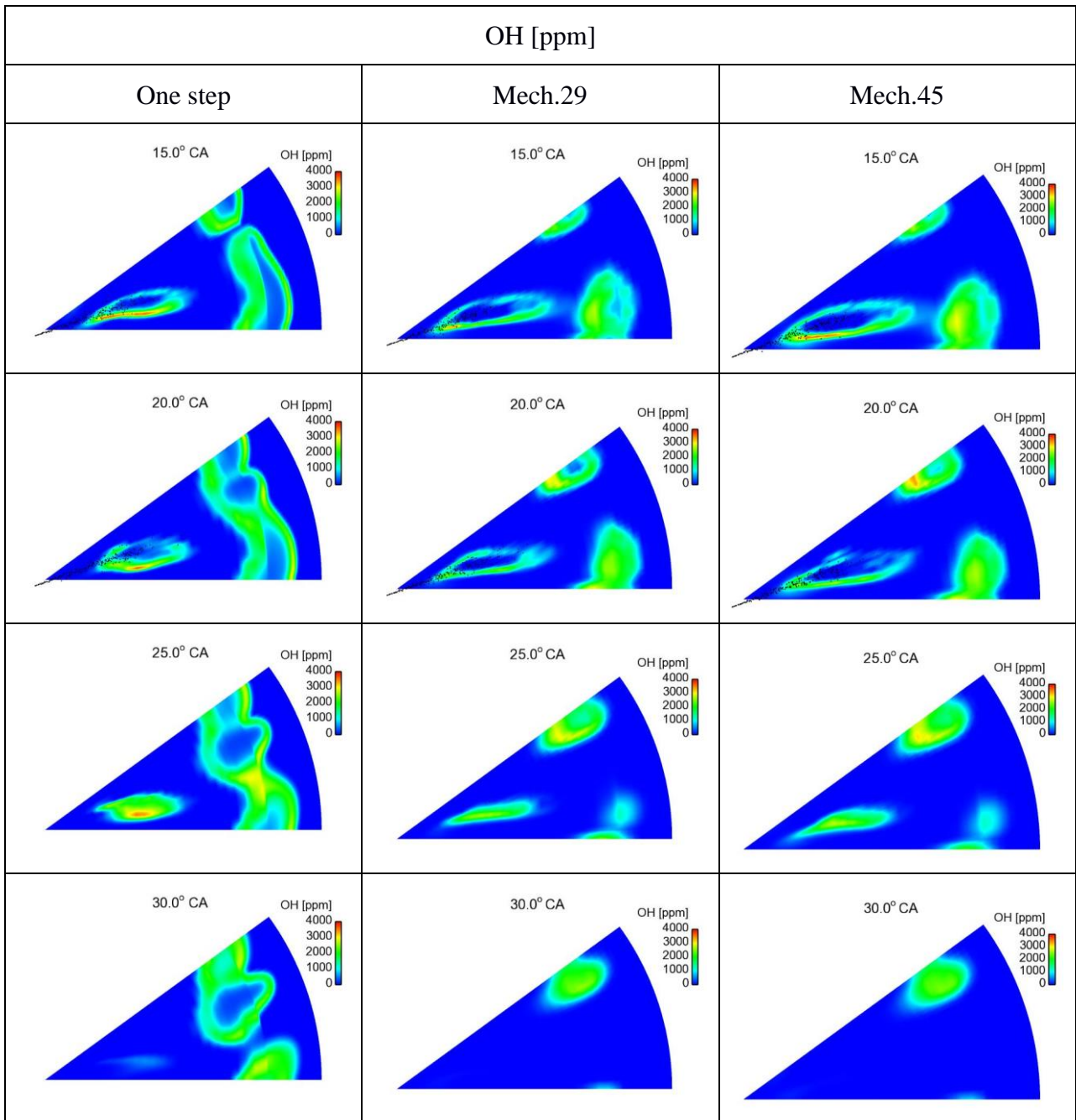


Figure 5.18: Colour-coded contours of OH concentration for one-step chemistry and reduced order chemistry using mechanisms Mech.29 and Mech.45. A horizontal plane very close to the injector is considered, at selected time instants.

Figure 5.19 presents the computed histories of mean concentration of O radical for one-step chemistry and the two reduced order chemistry mechanisms. The evolution of O radical is found to be very similar in all cases.

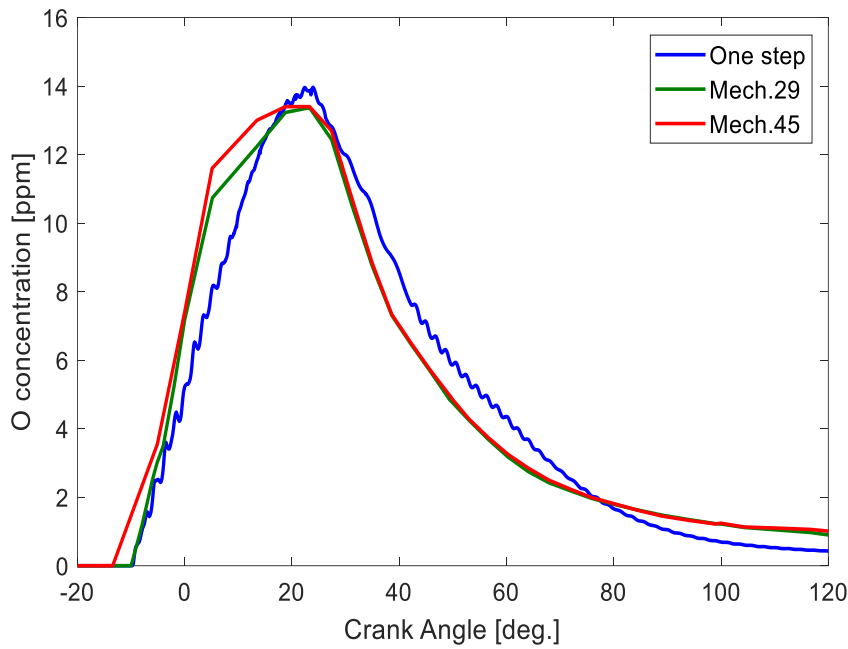


Figure 5.19: Computed traces of mean O (Oxygen radical) concentration using one-step chemistry and the two reduced order chemical kinetics mechanisms (Mech.29 and Mech.45), at an engine load of 100%.

Figure 5.20 presents the computed histories of mean concentration of H radical for the one-step chemistry and the cases of realistic chemistry of the present study. It is shown that Mech.45 results in high levels of produced H, while the maximum values of the one-step and Mech.29 cases are similar. The two realistic chemistry cases give similar concentrations at exhaust, while very low exhaust levels are computed for the one-step case.

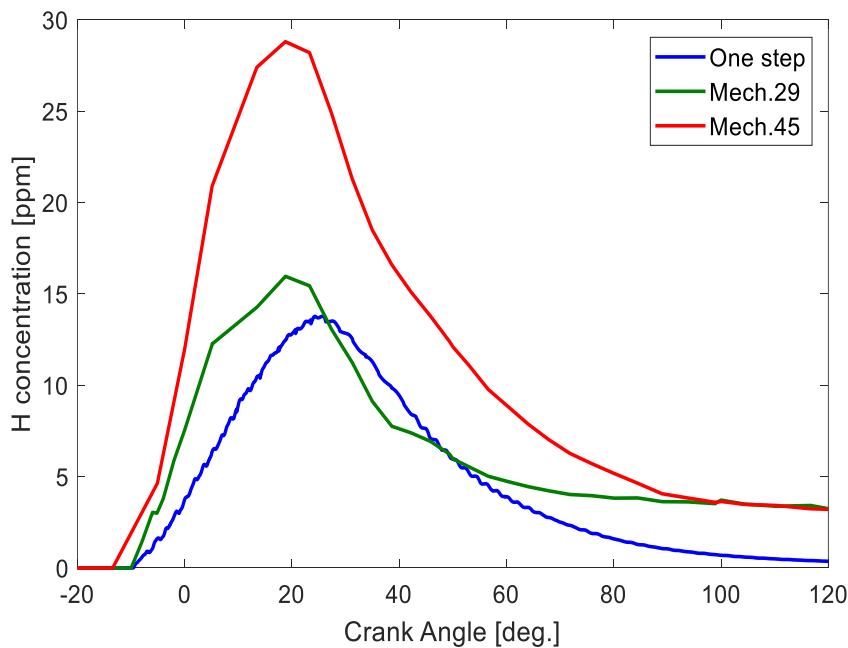


Figure 5.20: Computed traces of mean H (Hydrogen radical) concentration using one-step chemistry and the two reduced order chemical kinetics mechanisms (Mech.29 and Mech.45), at an engine load of 100%.

Figure 5.21 presents the computed histories of space-averaged concentration of CH₄ for the two realistic chemistry mechanisms of the present study, Mech.29 and Mech.45. It is demonstrated that, similar levels of methane are maintained up to a crank angle of about 20 degrees; nonetheless, in the late expansion stages, the methane concentration predicted by Mech.45 diminishes to near-zero values. The similar development up to a crank angle of 20 degrees is verified by the visualisation of CH₄ concentration presented in Figure 5.22.

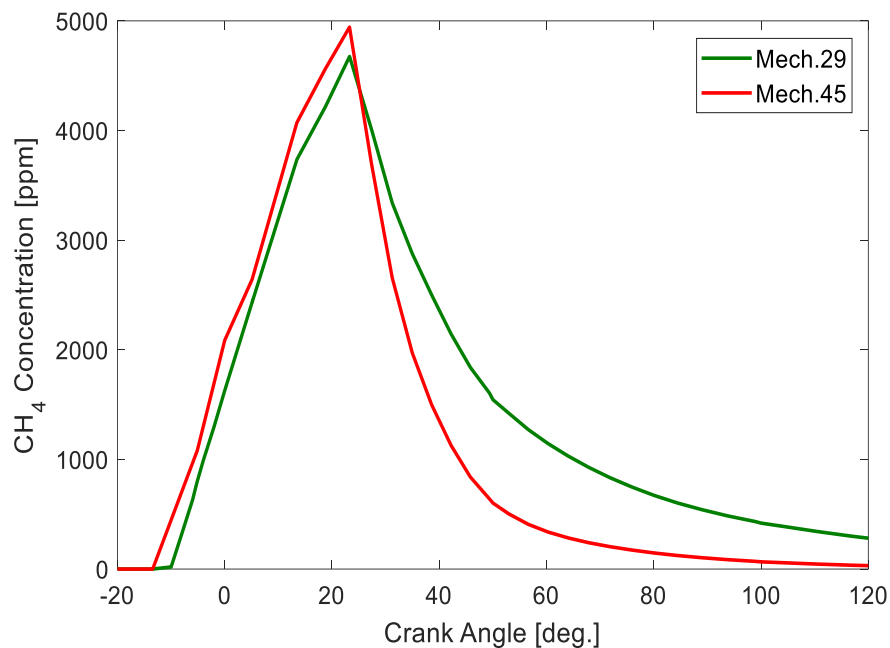
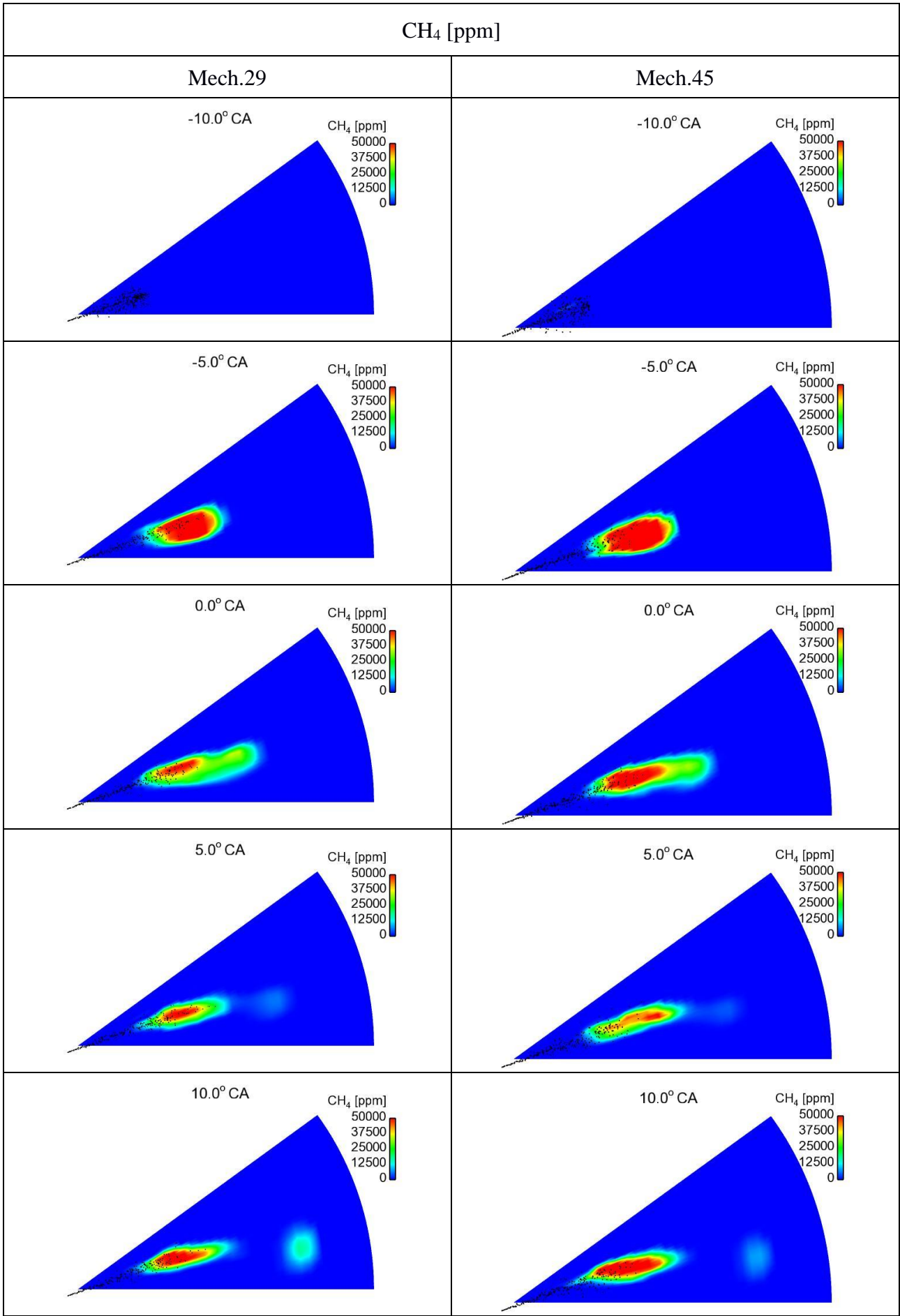


Figure 5.21: Computed traces of mean CH₄ (Methane) concentration using the two reduced order chemical kinetics mechanisms (Mech.29 and Mech.45), at an engine load of 100%.



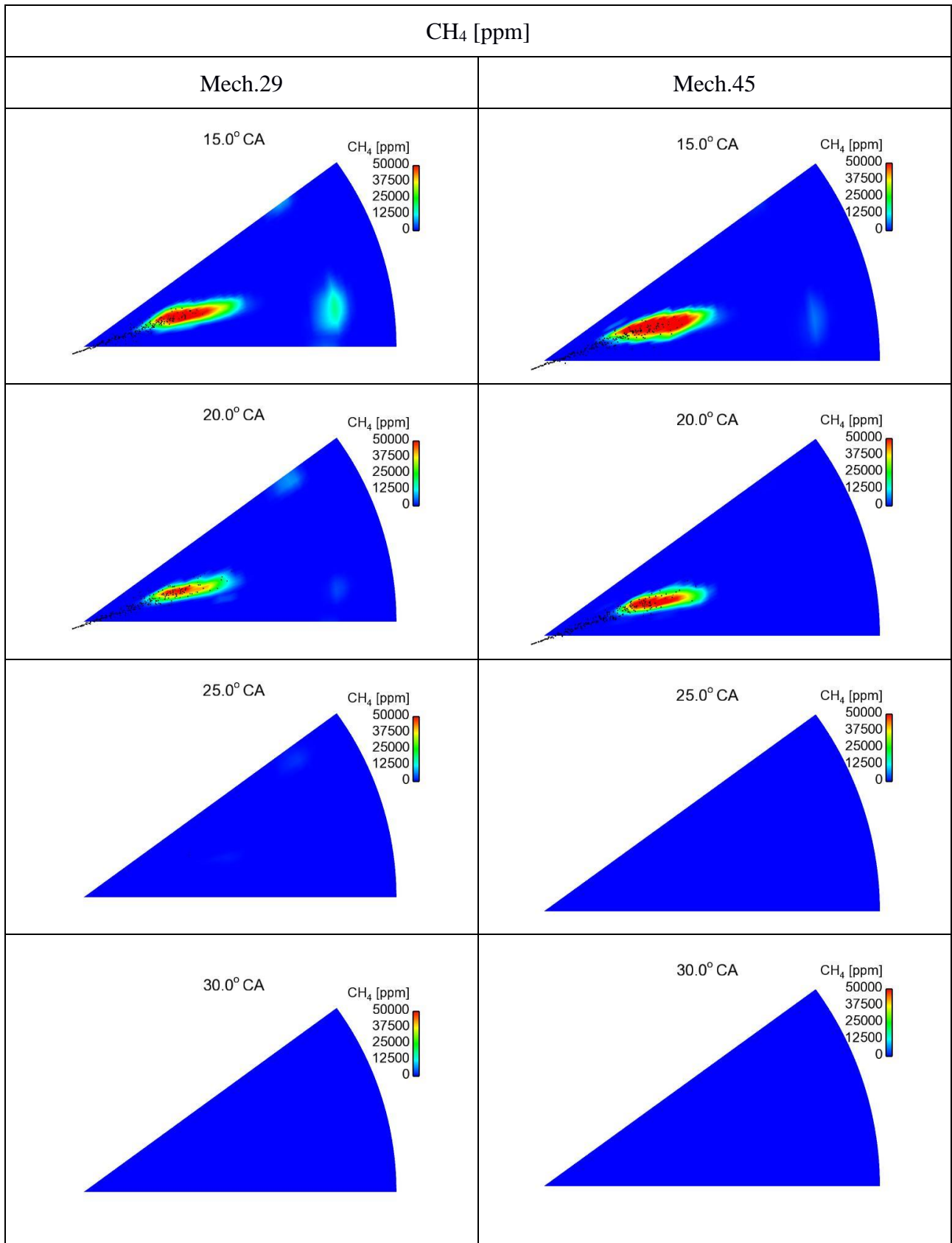


Figure 5.22: Colour-coded contours of CH₄ concentration for reduced order chemistry using mechanisms Mech.29 and Mech.45. A horizontal plane very close to the injector is considered, at selected time instants.

Figure 5.23 shows the computed histories of space-averaged concentration of the CH_3 radical, for Mech.29 and Mech.45. An initial stronger formation of CH_3 is demonstrated for Mech.45. The resulting faster development of combustion leads to convergence to near-zero levels at larger times.

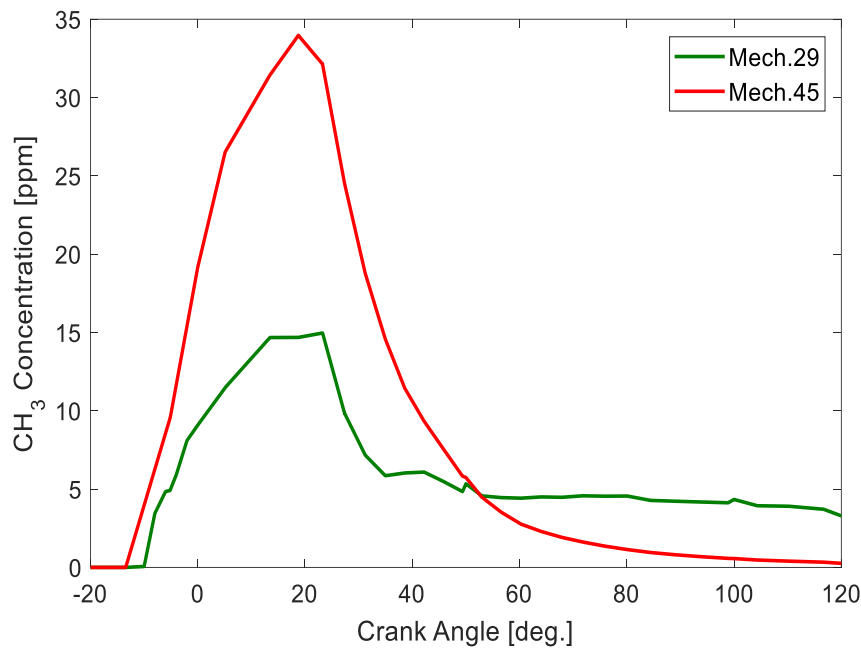


Figure 5.23: Computed traces of mean CH_3 (methyl radical) concentration using the two reduced order chemical kinetics mechanisms (Mech.29 and Mech.45), at an engine load of 100%.

Figure 5.24 shows the computed history of mean concentration of formaldehyde (CH_2O), for Mech.29 and Mech.45. As CH_2O is a known inhibitor of soot production (Yuan et al., 2015), the associated higher production with Mech.29 is expected to correspond to lower soot production, and a decreased exhaust soot concentration, in comparison to Mech.45. The trend of Figure 5.24 complies with the spatial distributions presented in Figure 5.25.

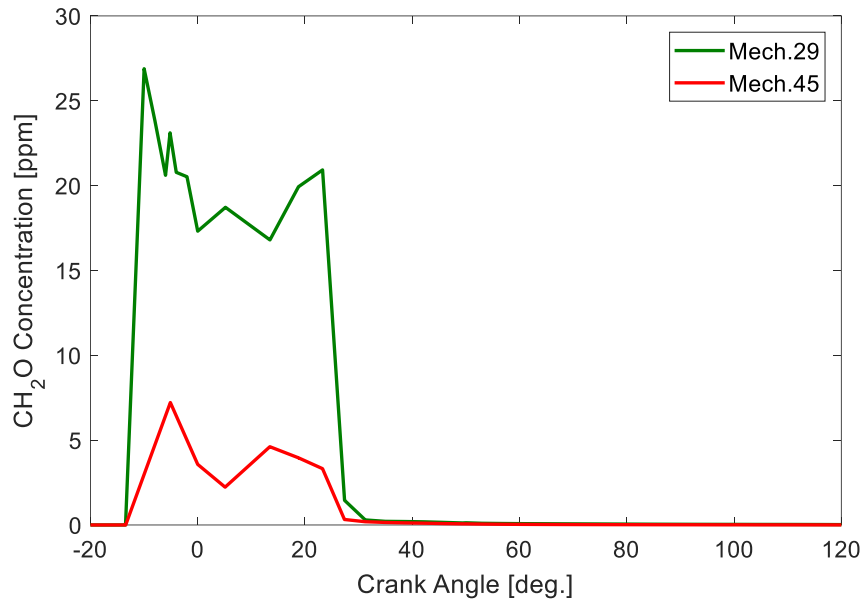
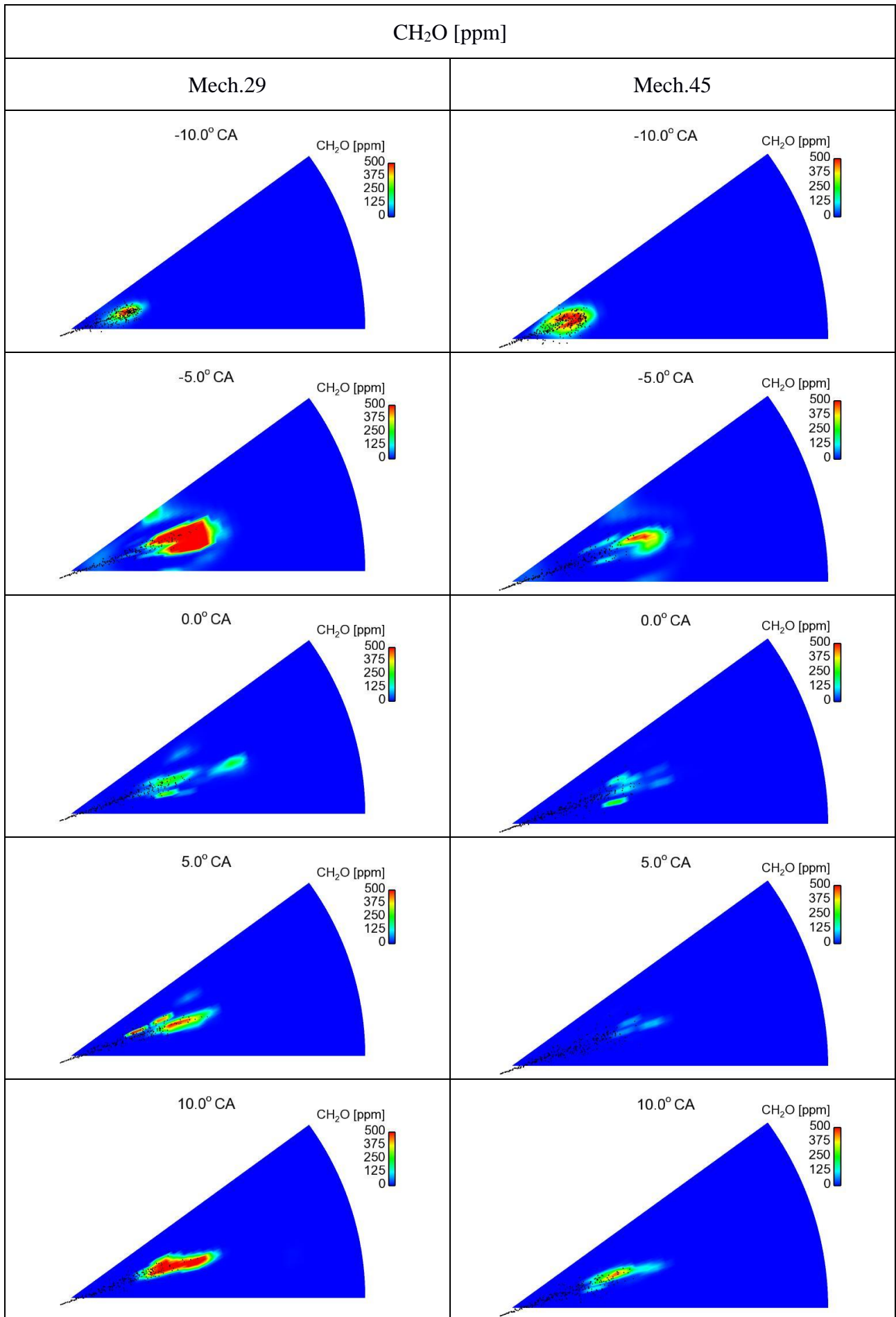


Figure 5.24: Computed traces of mean CH₂O (formaldehyde) concentration using the two reduced order chemical kinetics mechanisms (Mech.29 and Mech.45), at an engine load of 100%.



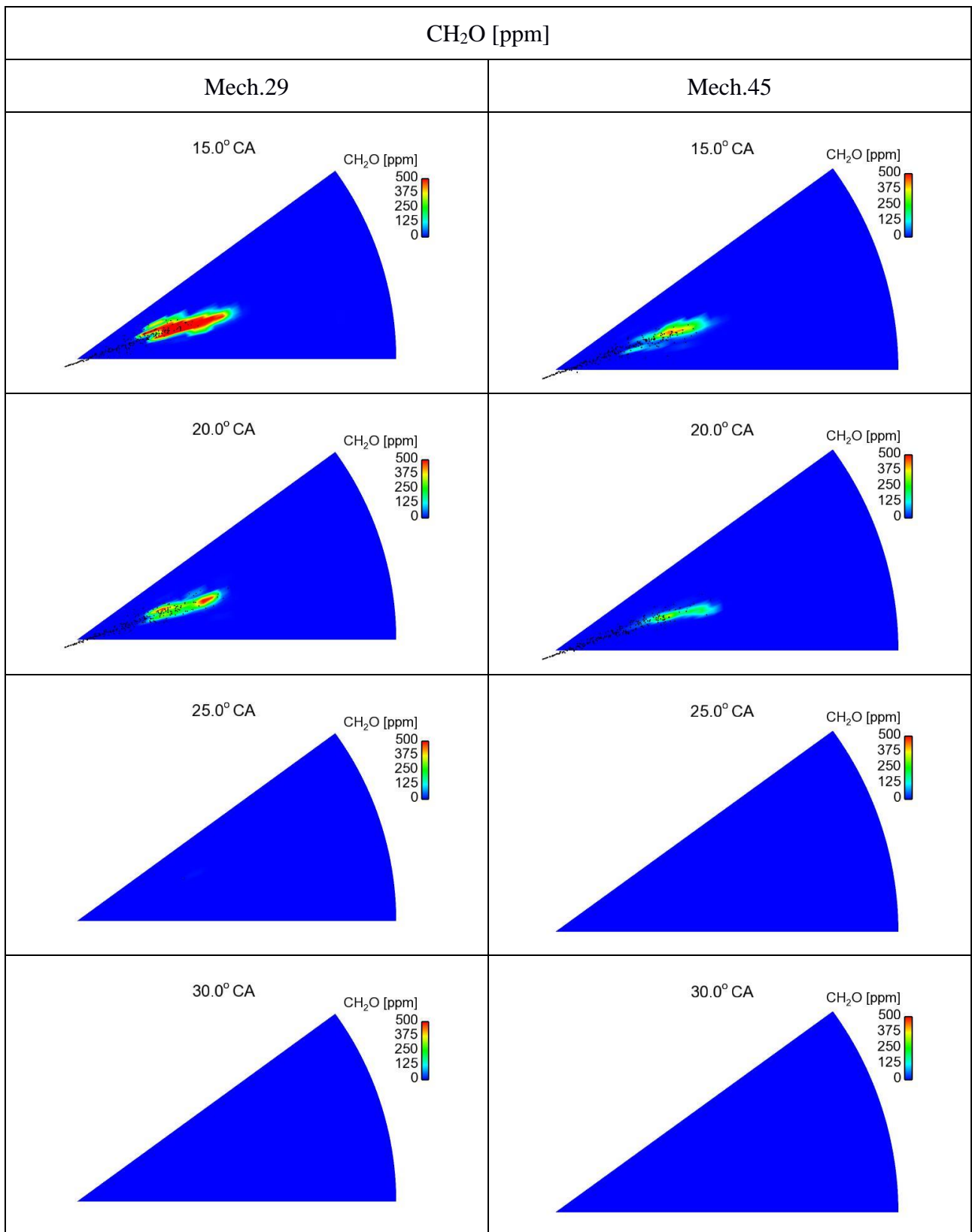


Figure 5.25: Colour-coded contours of CH₂O concentration for reduced order chemistry using mechanisms Mech.29 and Mech.45. A horizontal plane very close to the injector is considered, at selected time instants.

Figure 5.26 presents the computed traces of mean concentration of formyl radical (HCO), for Mech.29 and Mech.45; HCO is an important precursor to the formation of CO. Very low levels of HCO are demonstrated.

The calculated development of CO is presented in Figure 5.27, both for one-step and realistic chemistry. One-step chemistry gives substantially lower, by more than an order of magnitude, CO levels, in comparison to the realistic chemistry calculations. Further, Figure 5.27 shows that, for realistic chemistry, the exhaust concentration of CO is non-zero for two mechanisms. The very low final value of CO concentration in the case of one-step chemistry could be attributed to the fact that only one (equilibrium) reaction accounts for its production/consumption: $O_2 + 2CO \rightleftharpoons 2CO_2$. Figure 5.28 presents visualisations of the CO concentration at different values of crank angle, for the one-step chemistry and the realistic chemistry cases calculated. The low levels of CO for the one-step chemistry are verified. For the realistic chemistry simulations, a similar development of CO is demonstrated for the two mechanisms considered, with slightly higher predicted levels for Mech.45 during engine expansion.

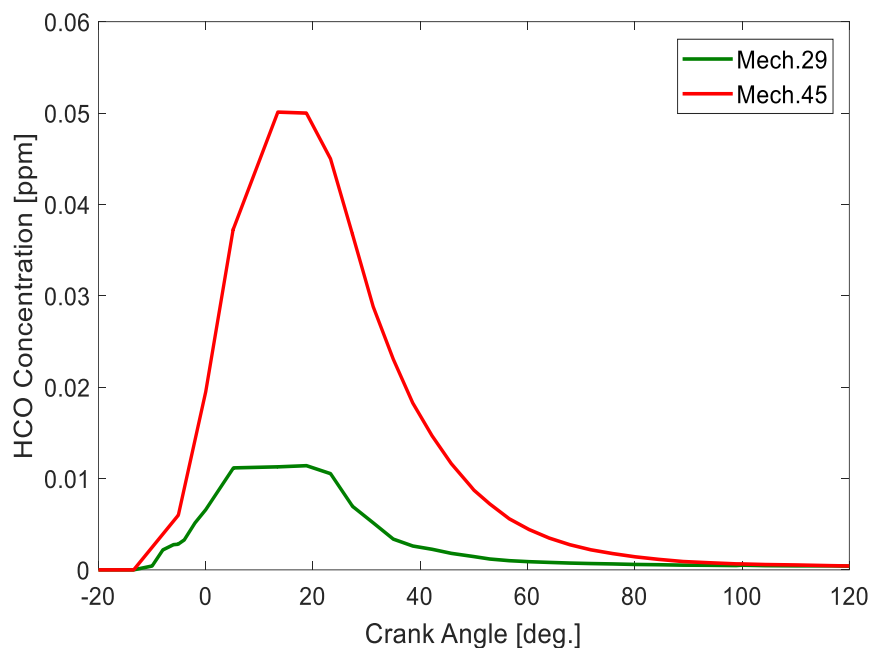


Figure 5.26: Computed traces of mean HCO (formyl radical) concentration using the two reduced order chemical kinetics mechanisms (Mech.29 and Mech.45), at an engine load of 100%.

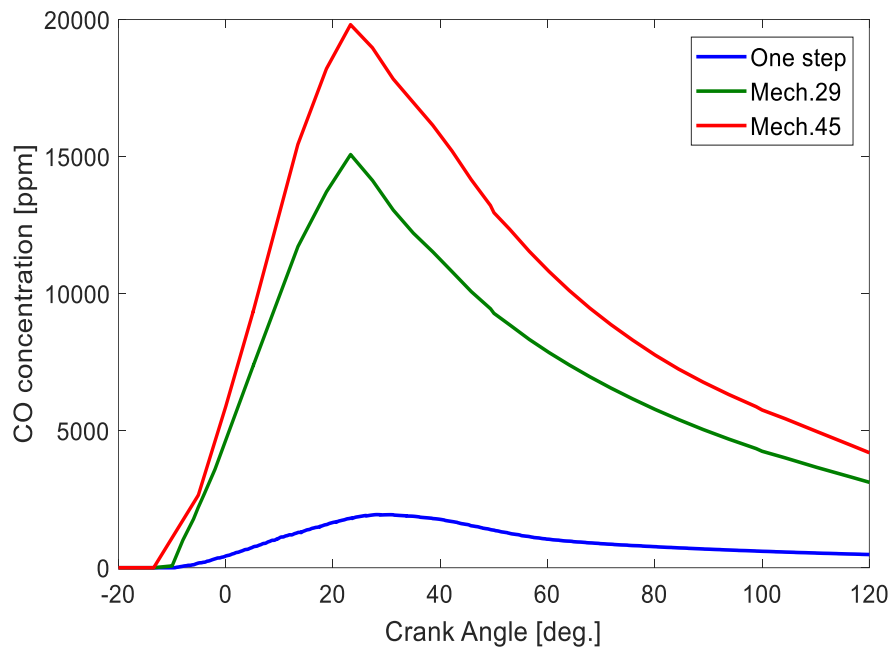
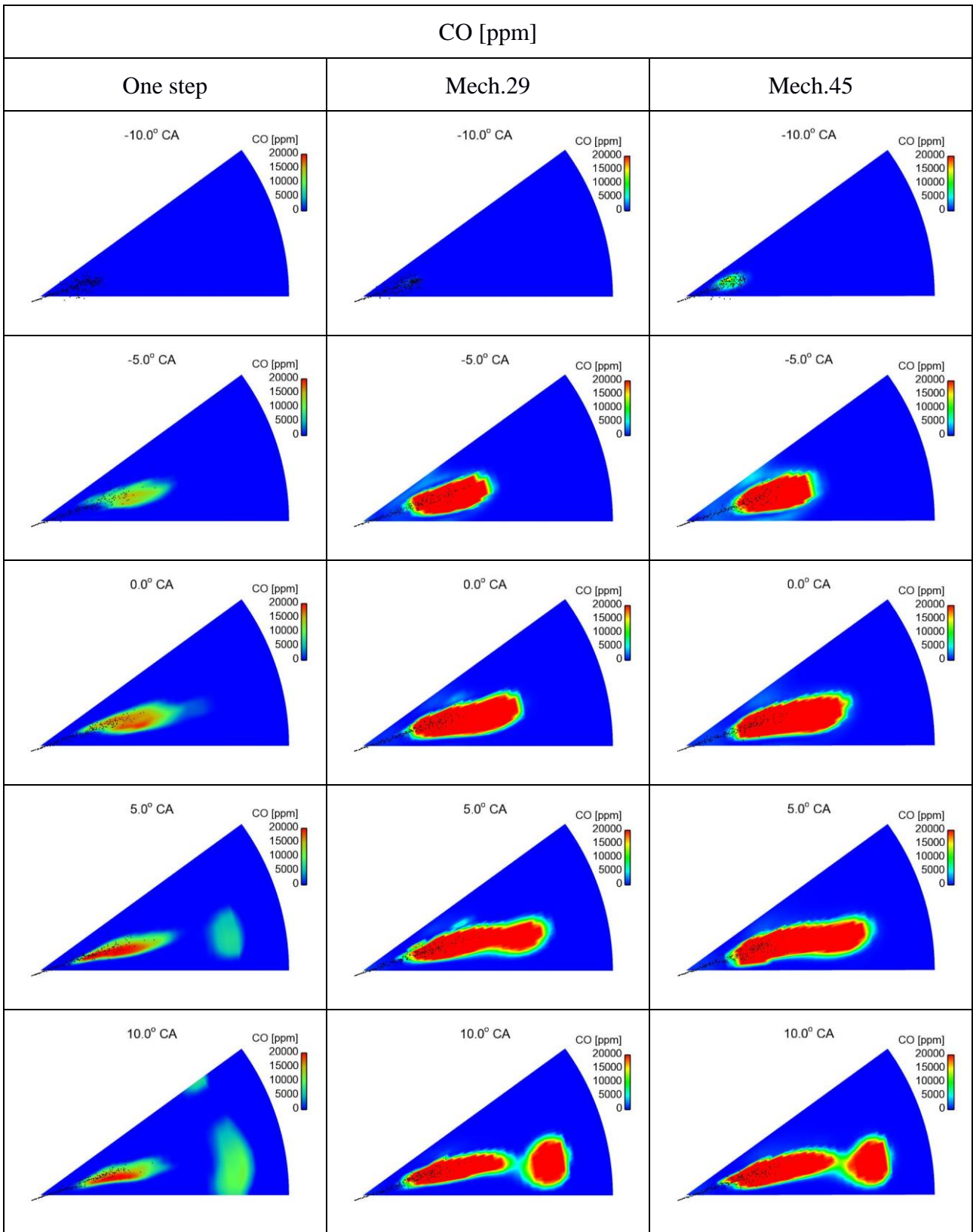


Figure 5.27: Computed traces of mean CO (Carbon monoxide) concentration using one-step chemistry and the two reduced order chemical kinetics mechanisms (Mech.29 and Mech.45), at an engine load of 100%.



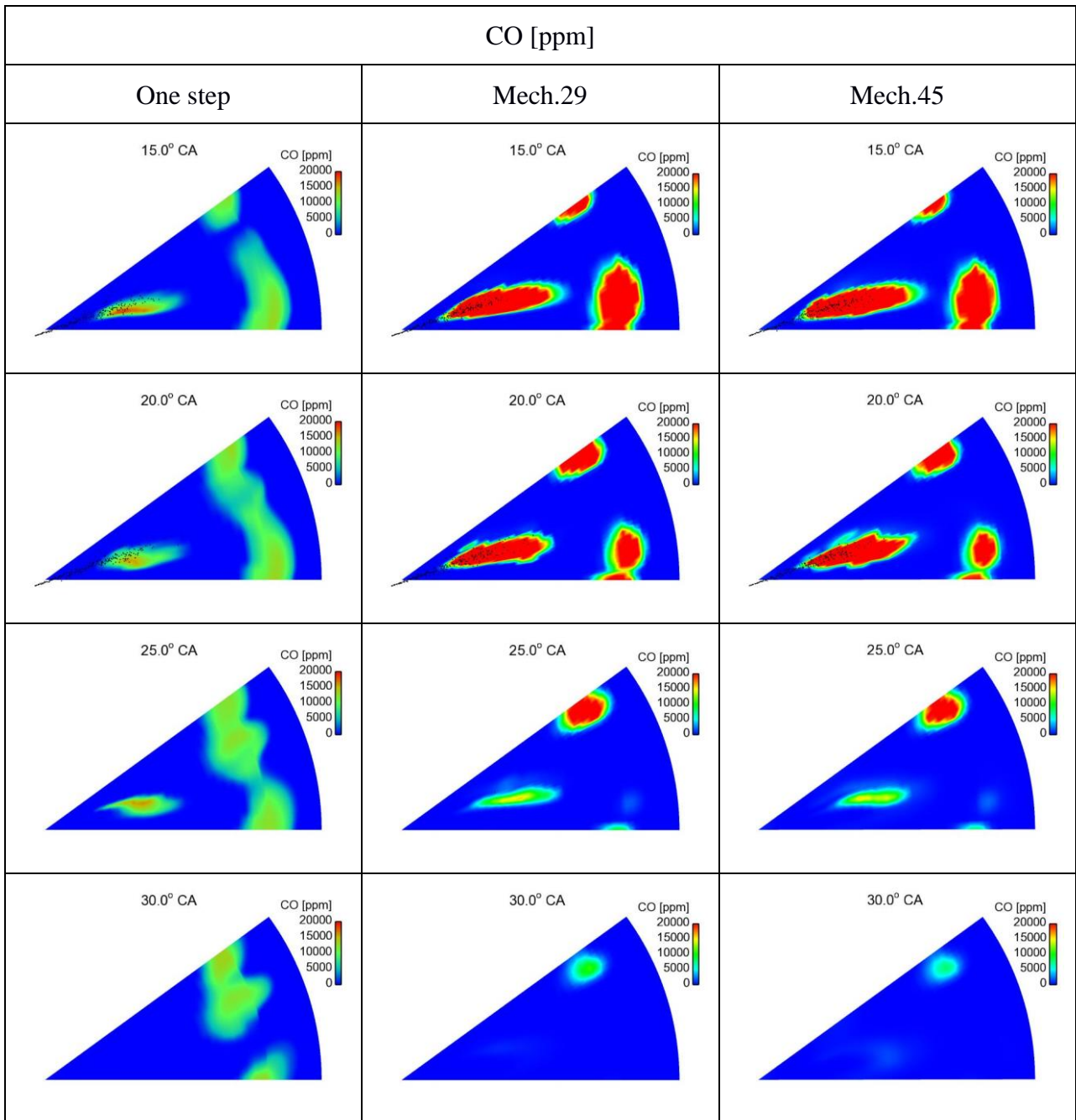


Figure 5.28: Colour-coded contours of CO concentration for one-step chemistry and reduced order chemistry using mechanisms Mech.29 and Mech.45. A horizontal plane very close to the injector is considered, at selected time instants.

Figure 5.29 presents the computed evolution of mean concentration of CO₂, for the one-step chemistry and the two realistic chemistry cases. A stronger initial production of CO₂ is demonstrated for the case of one-step chemistry, and comparative levels are attained at large times. The earlier development of CO₂ for one-step chemistry is verified by the visualisations of the CO₂ concentration of Figure 5.30.

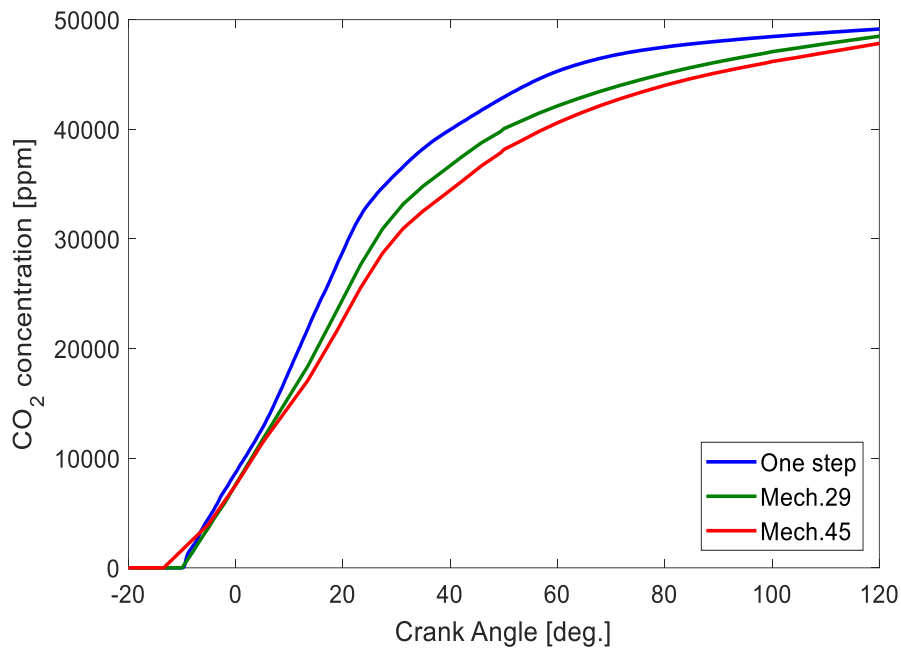
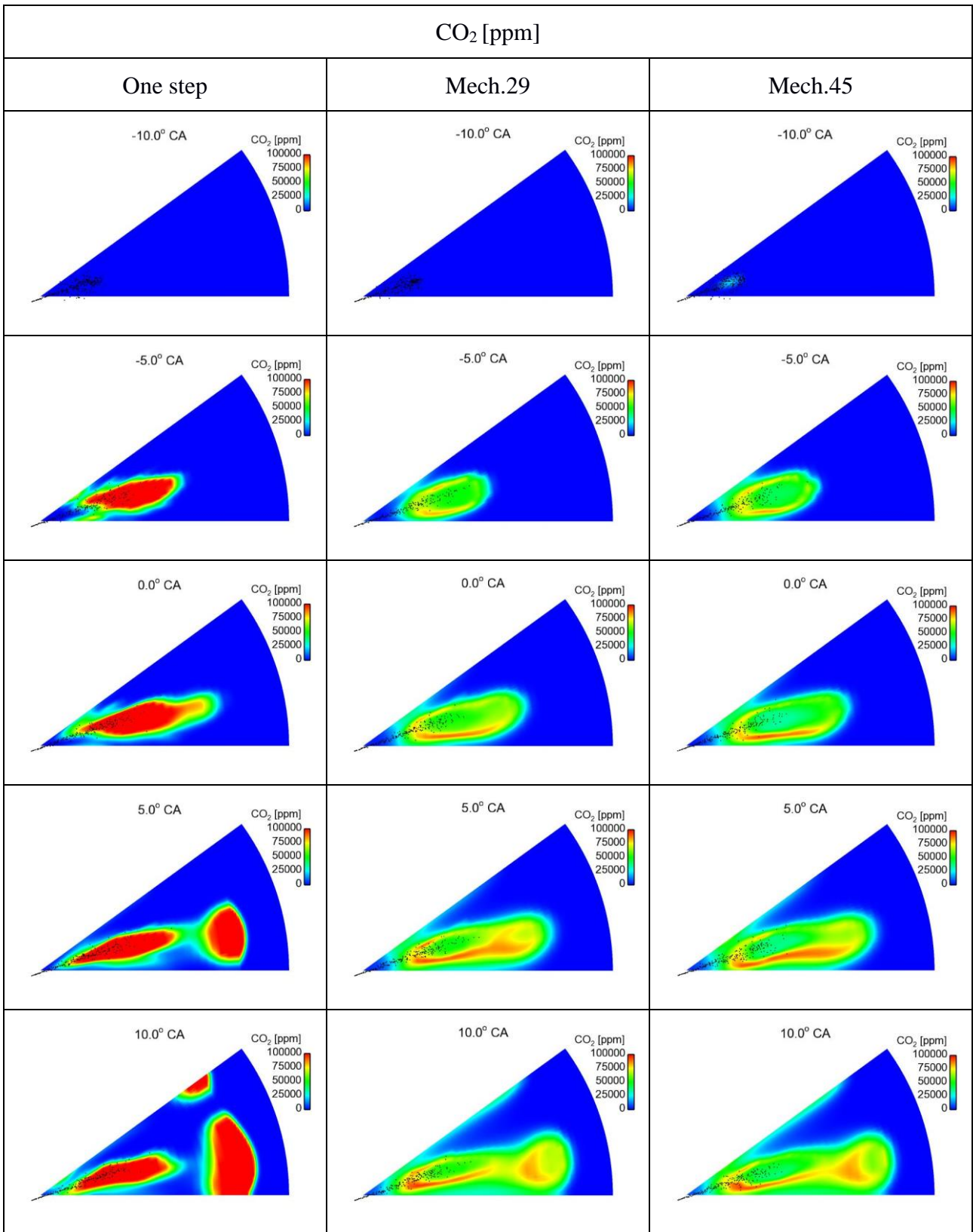


Figure 5.29: Computed traces of mean CO₂ (Carbon dioxide) concentration using one-step chemistry and the two reduced order chemical kinetics mechanisms (Mech.29 and Mech.45), at an engine load of 100%.



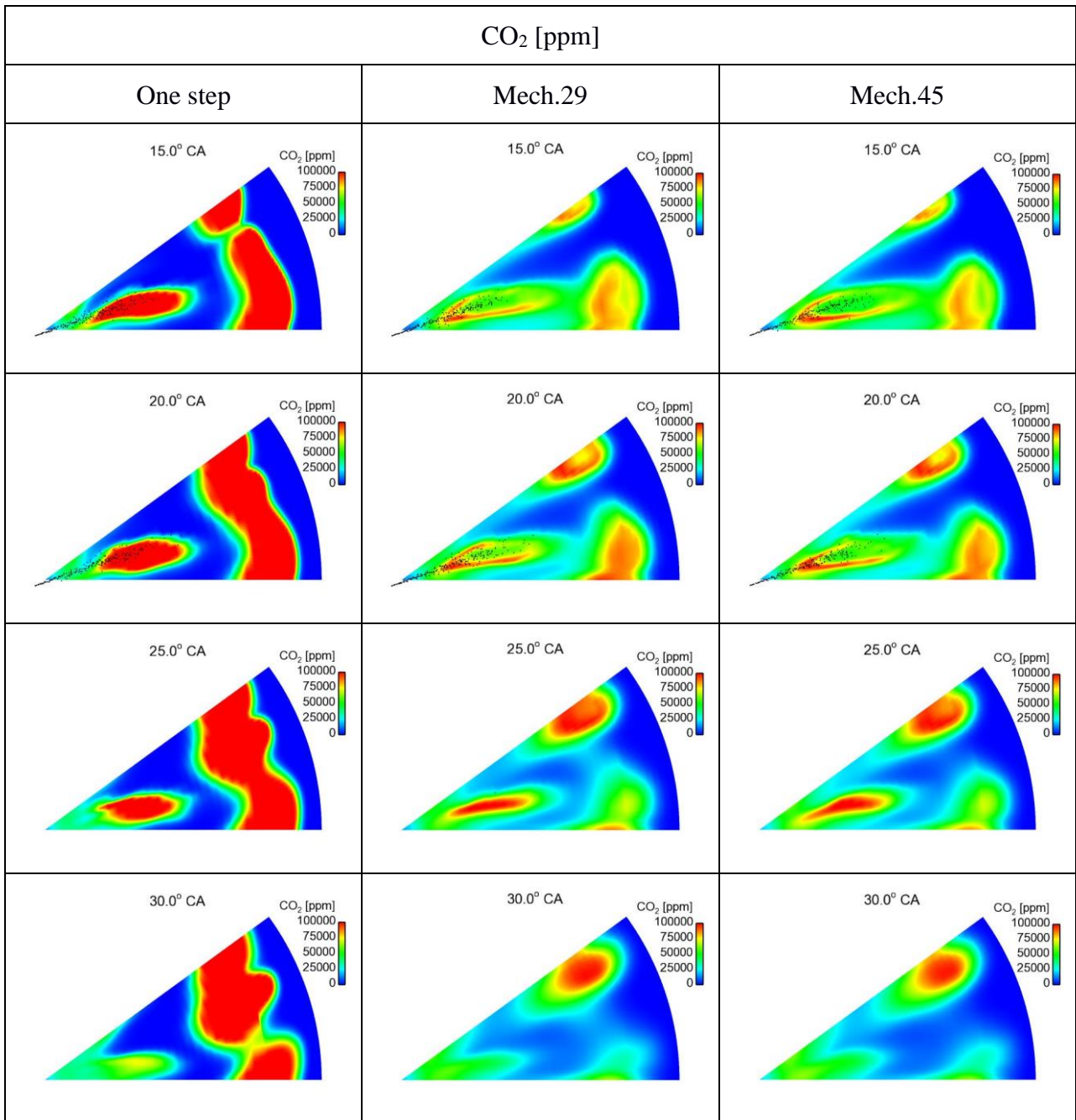


Figure 5.30: Colour-coded contours of CO₂ concentration for one-step chemistry and reduced order chemistry using mechanisms Mech.29 and Mech.45. A horizontal plane very close to the injector is considered, at selected time instants.

The soot modelling approach of the present study has been applied for the case of one-step chemistry. The computed history of total soot mass is presented in Figure 5.31, and illustrates the common build-up and oxidation of soot in marine Diesel engines. Non-zero values at exhaust are attained. The visualisations of soot concentration presented in Figure 5.32 verify the initial high production in the spray flame region, as well the high concentration in the flow pattern formed by the tumble-type of motion.

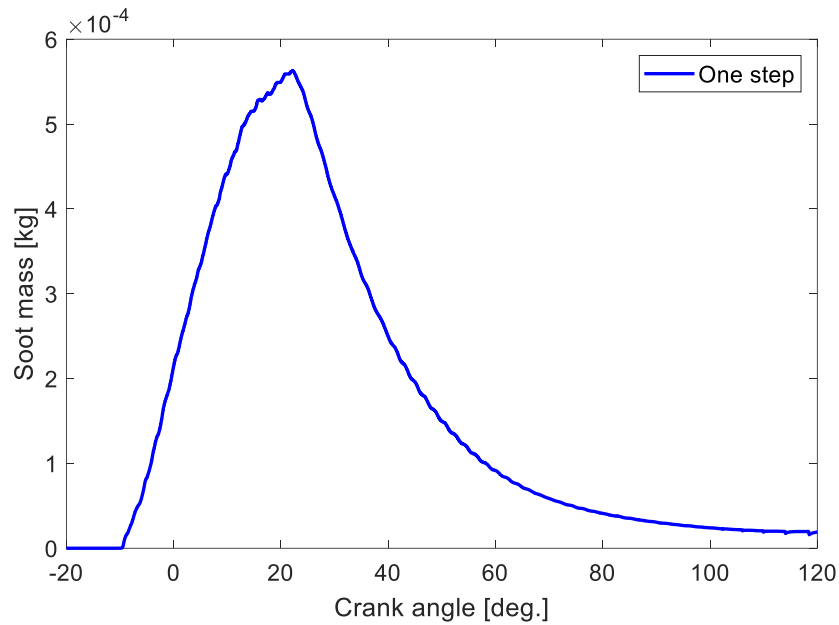
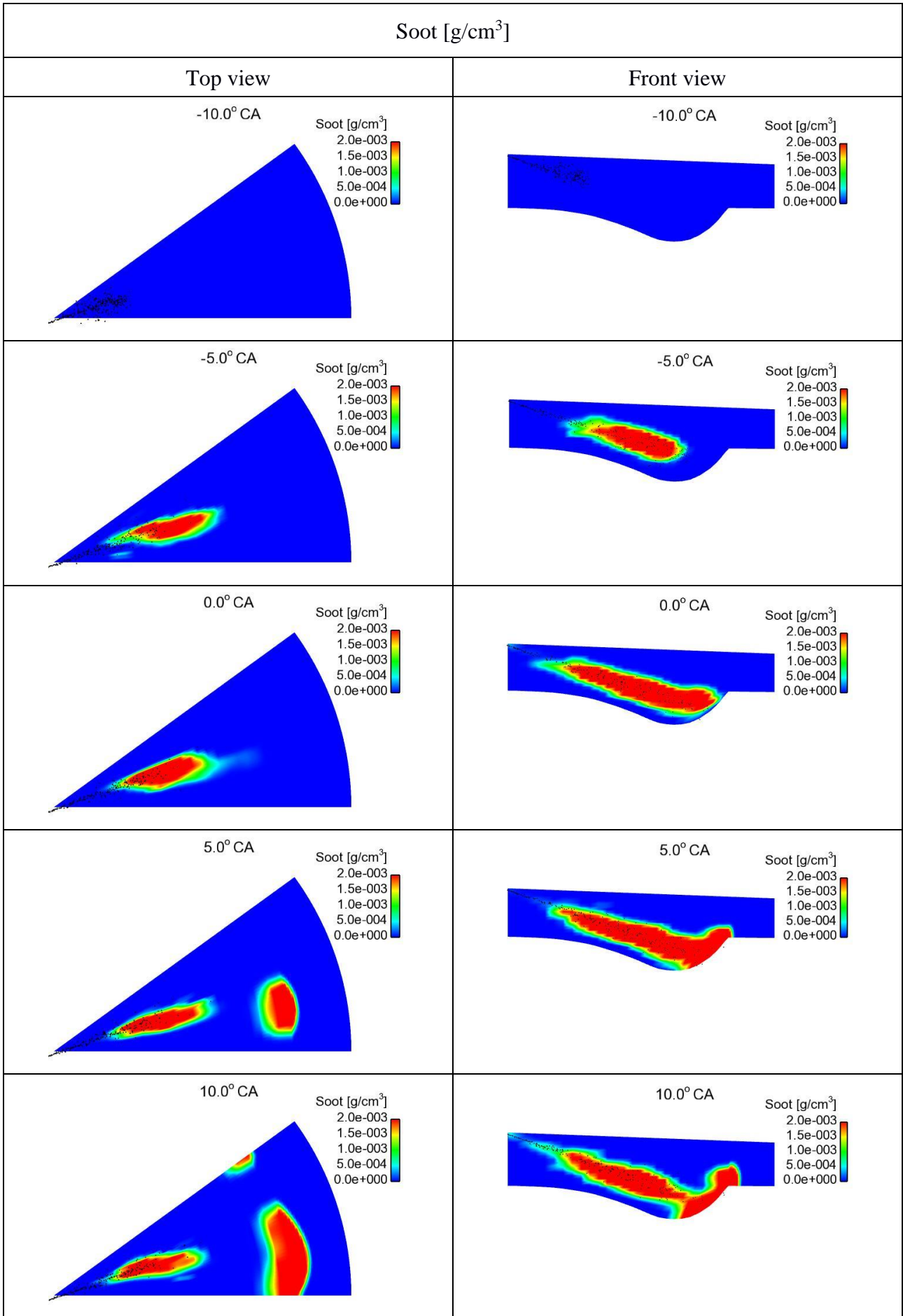


Figure 5.31: Computed traces of mean soot mass using the one-step chemistry, at an engine load of 100%.



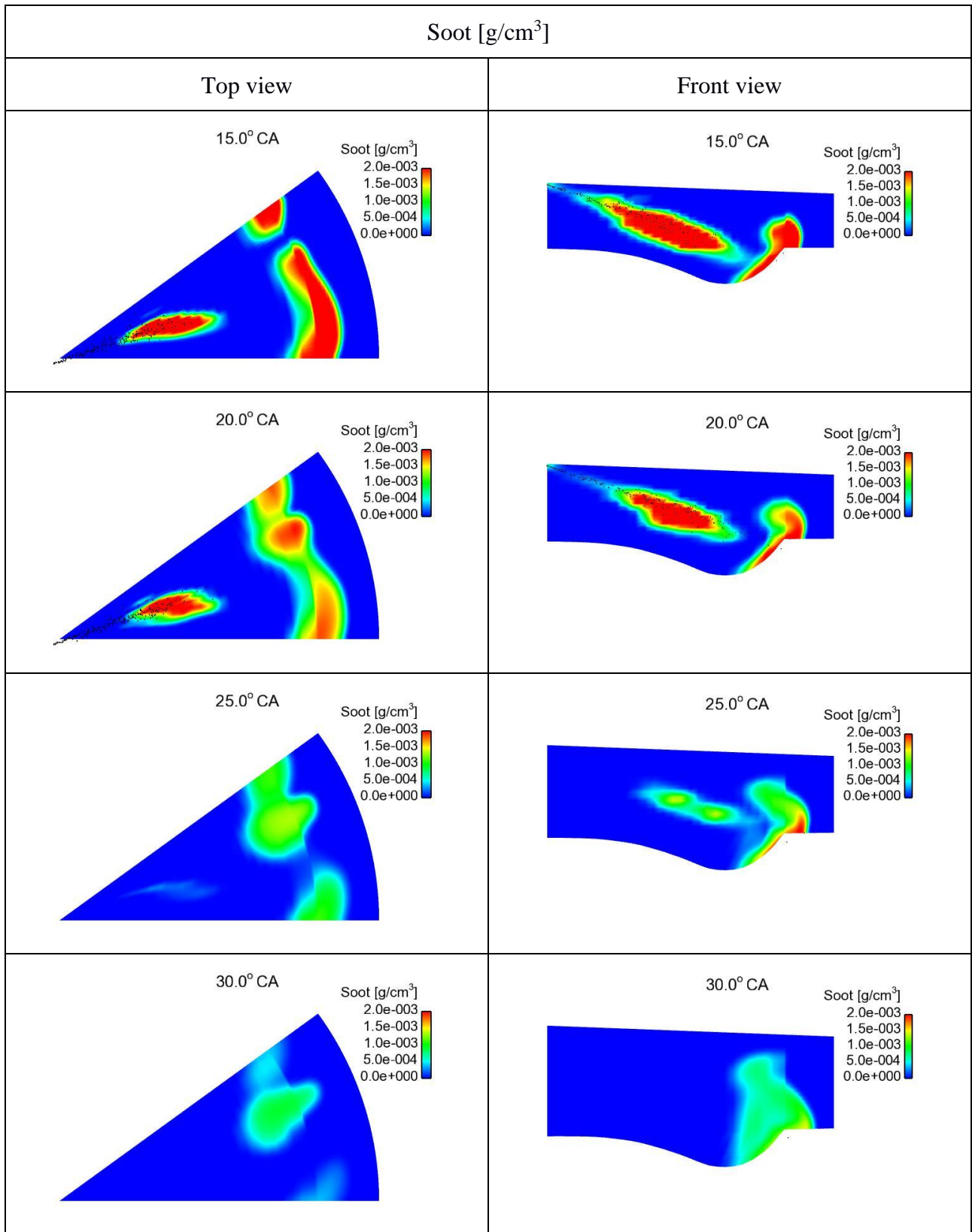


Figure 5.32: Colour-coded contours of soot density for one-step chemistry. A horizontal plane close to the injector and a vertical plane including the injector are considered, at selected time instants.

5.2.2 NO_x emissions

Figure 5.33 presents the computed histories of the space-averaged NO_x concentration for the one-step and realistic chemistry cases considered here; the measured value of exhaust concentration is also included. A similar development is demonstrated in all cases, with the final values of NO_x concentration being very close (about 1200 ppm) for one-step chemistry and Mech.29. The value for Mech.45 is predicted lower, by order 10%. In all cases, computations overpredict the experimental value (900 ppm). The visualisations of the computed NO_x concentration, presented in Figures 5.34 and 5.35 show a qualitatively different distribution for the case of one-step chemistry, associated with a stronger impact on the tumble-type of motion in the NO_x distribution.

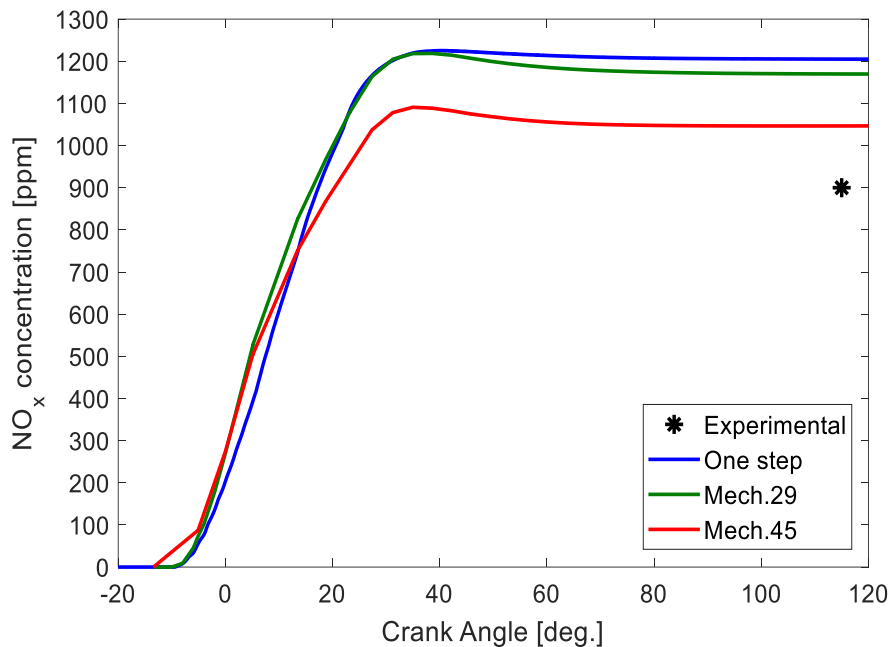
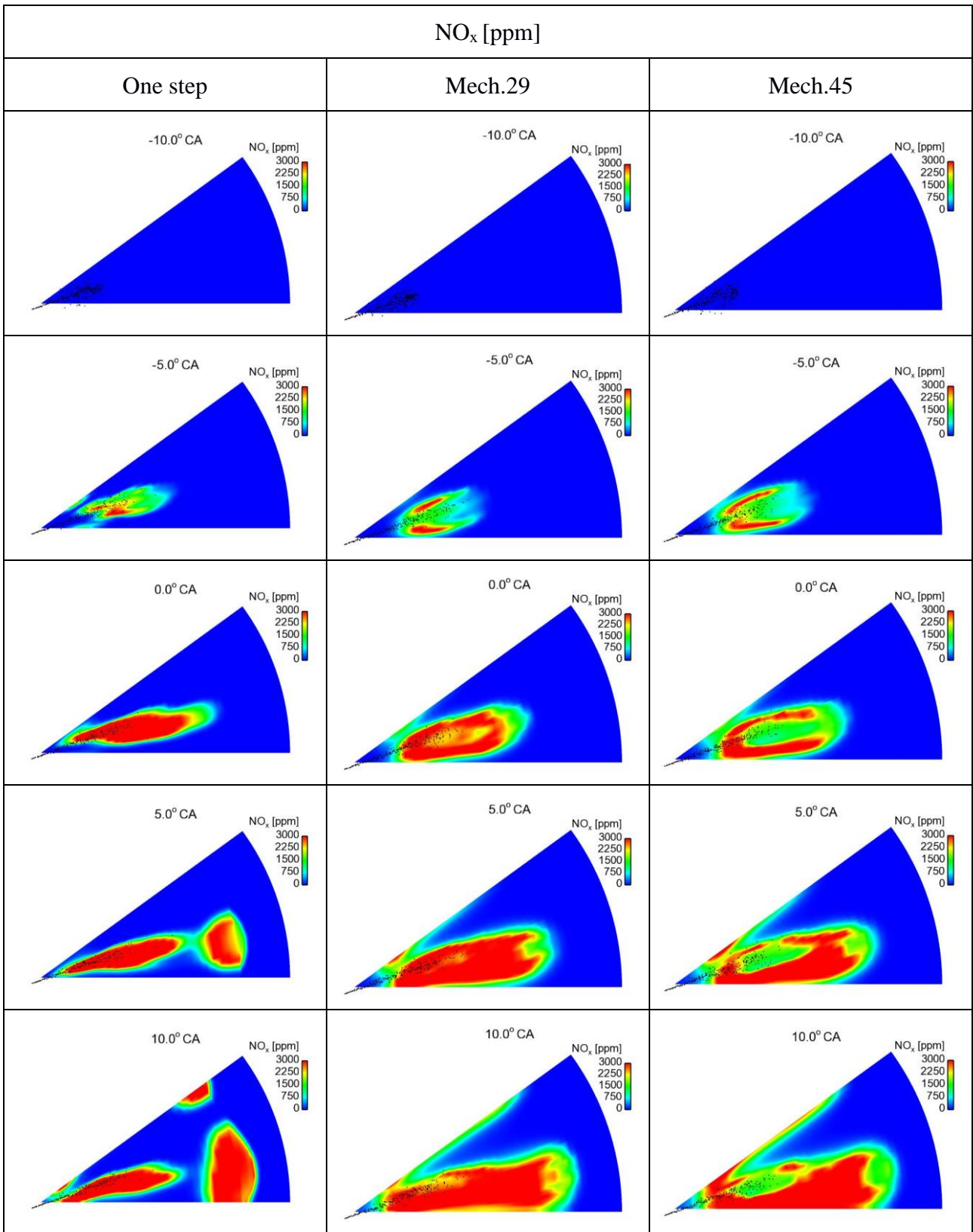


Figure 5.33: Computed traces of mean NO_x (Nitrogen Oxides) concentration using the one-step chemistry and the two reduced order chemical kinetics mechanisms (Mech.29 and Mech.45), at an engine load of 100%. A measured value of final NO_x concentration is also included (G. Theotokatos, private communication).



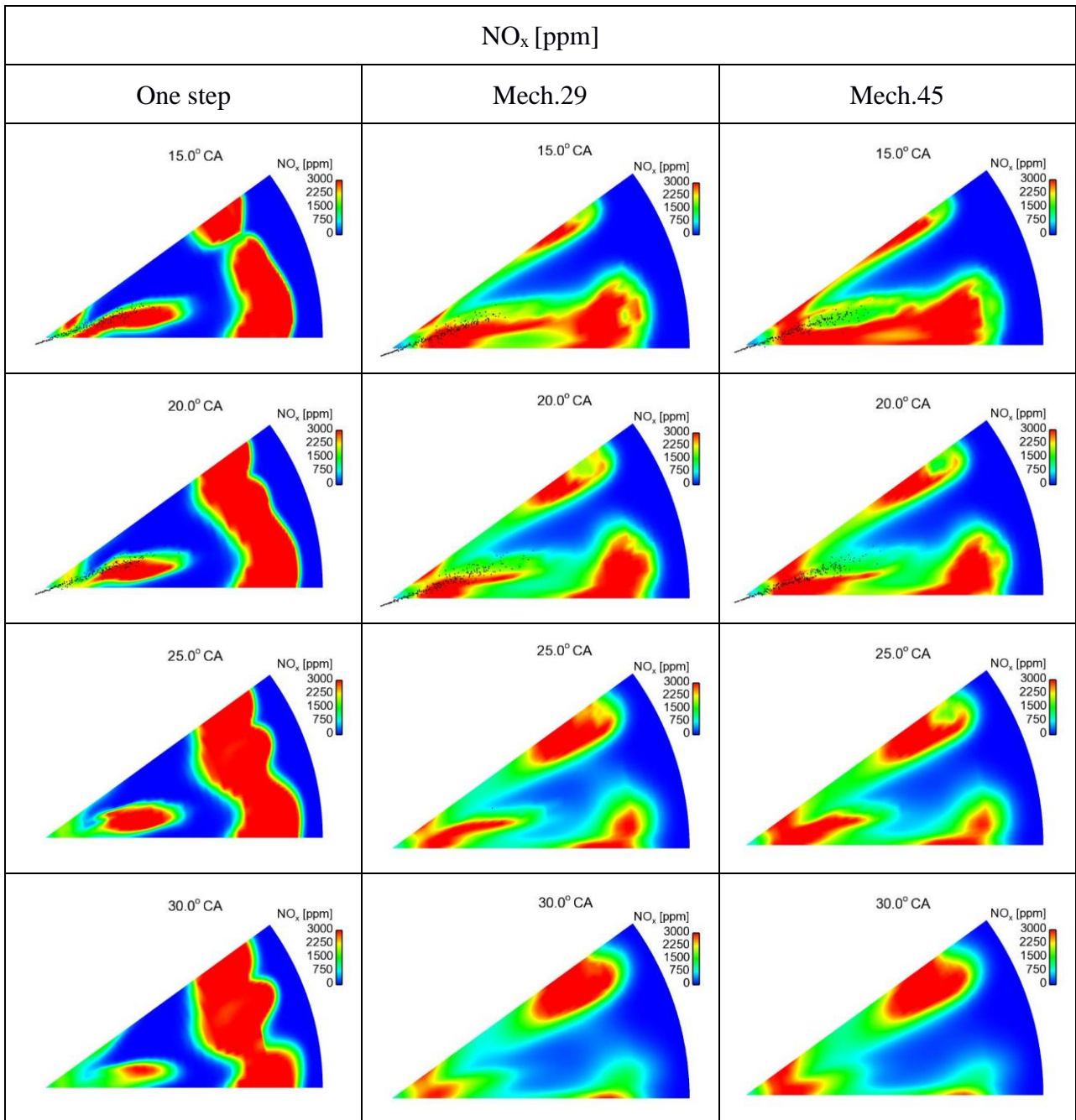
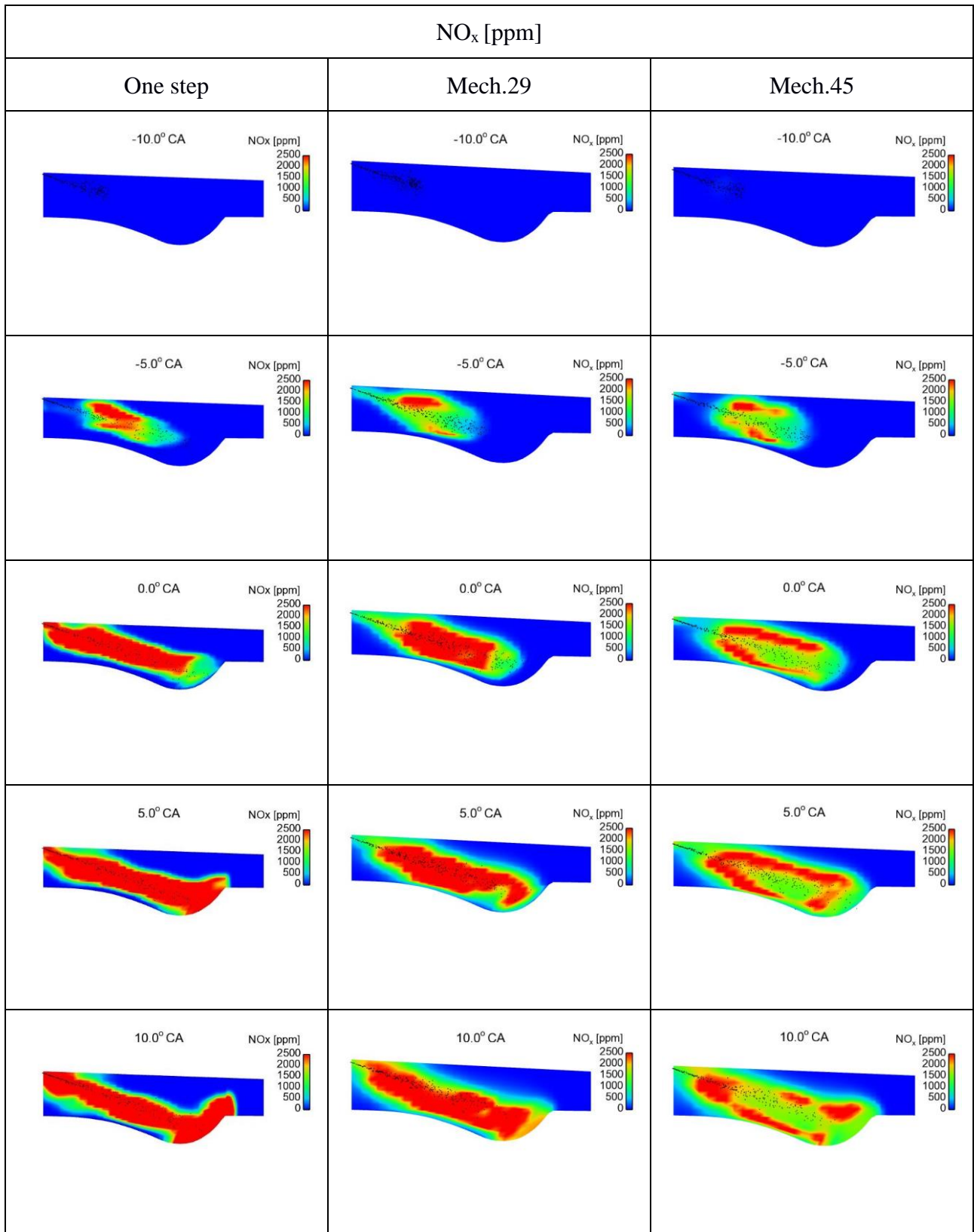


Figure 5.34: Colour-coded contours of NO_x concentration for one-step chemistry and reduced order chemistry using mechanisms Mech.29 and Mech.45. A horizontal plane very close to the injector is considered, at selected time instants.



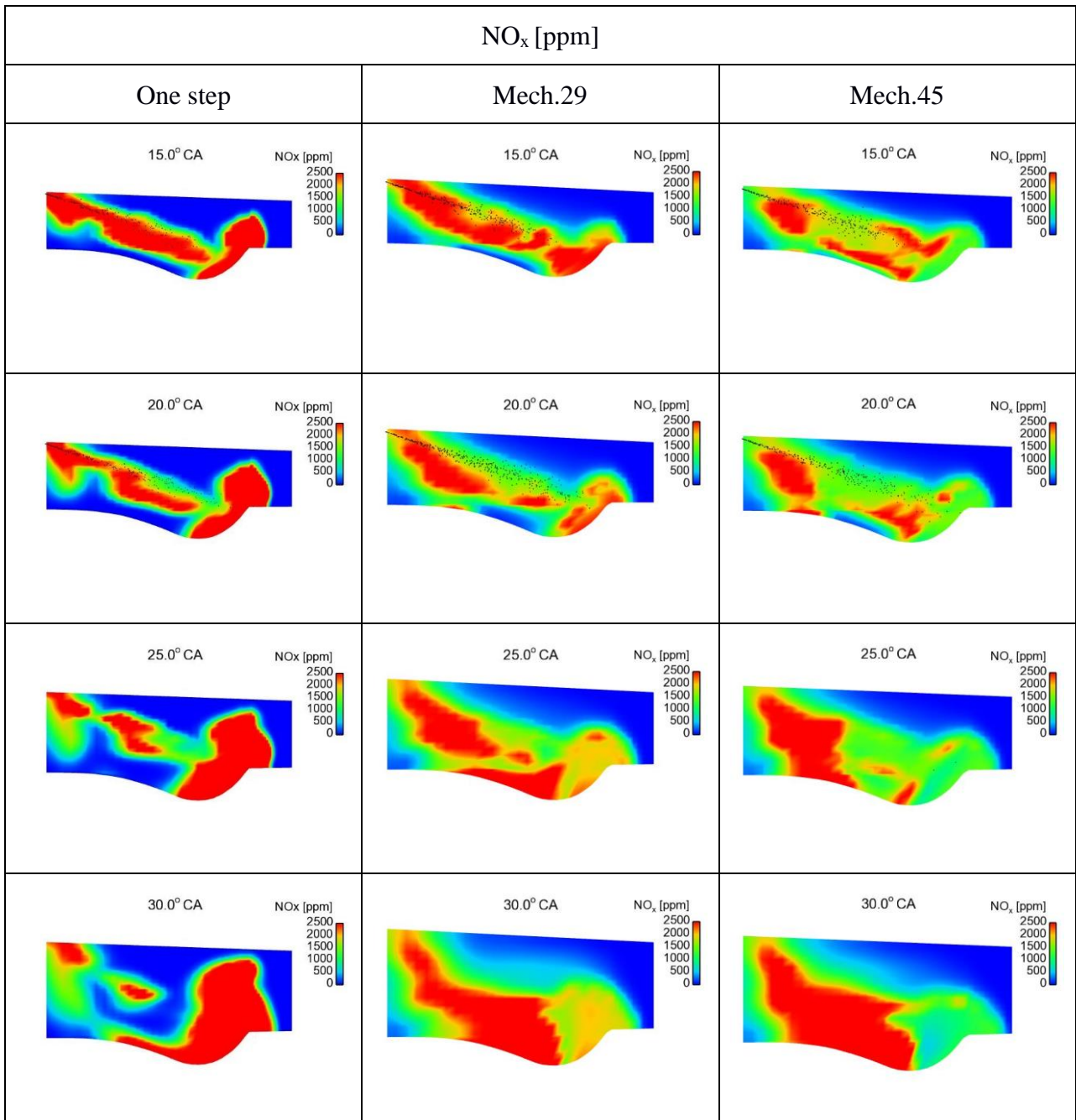


Figure 5.35: Colour-coded contours of NO_x concentration for one-step chemistry and reduced order chemistry using mechanisms Mech.29 and Mech.45. A vertical plane very close to the injector is considered, at selected time instants.

5.3 Chapter conclusions

This Chapter has presented CFD results for the Wärtsilä 50DF engine, for operation at full load. Here, a single-step approach was used, as well as a realistic chemistry one, in terms of the reduced order mechanisms Mech.29 and Mech.45. Results were referred to a measured value of maximum pressure, and to one of final NO_x concentration. Overall, a very good agreement was demonstrated. Computational results were processed to yield traces of global quantities, such as mean temperature and species concentration, as well as associated spatial distributions, at representative time instants. The main outcomes of the present analysis can be summarised as follows.

- A slightly longer ignition delay was calculated for one-step chemistry.
- A more rapid fuel decomposition and combustion development is calculated with realistic chemistry, in comparison to one-step chemistry. In the latter case, more fuel thus accumulates, and is decomposed and burns at later stages of combustion.
- A tumble-type of motion is present in the engine, with more pronounced effects in the case of one-step chemistry, in terms of the distribution of evaporated fuel distribution, and temperature and species distributions.
- For the realistic chemistry cases, fuel decomposition terminates shortly after the end of injection.
- For one-step chemistry, the OH radical is dominant, persisting up to late stages of combustion. For realistic chemistry, the role of H radical is upgraded for Mech.45. For realistic chemistry, an early production and destruction of intermediate species is identified.
- The production of CO is very minor in the case of one-step chemistry, but very pronounced for realistic chemistry. An adequate characterisation of the combustion development is thus only feasible by means of detailed/realistic chemistry.
- In the initial stages of combustion, an intense soot production, predicted with one-step chemistry, takes place in the spray flame region, while a high soot concentration is subsequently present in the flow pattern induced by the tumble-type of motion. Non-zero levels of soot are present at the engine exhaust.
- NO_x distributions differ qualitatively between the one-step and the realistic chemistry cases.

6. Novelty of the present work and contribution to scientific research

6.1 Methodology aspects

In an initial step of the present study, a modified KIVA-3vr2 code (Amsden, 1999) has been used, in which physical models of the open literature have been implemented, including the CAB spray model. In the present study, the CAB model was properly adapted for conditions representative of the engines considered here, which correspond to catastrophic secondary breakup. Adaptation of the CAB model was in terms of CFD studies of non-reactive sprays in a constant volume chamber, and has utilised experiments performed at ETH Zurich. In particular, adaptation has been performed in terms of the model constants, considering the comparison of CFD results against experiments regarding the temporal evolution of the spray penetration tip.

A main novelty of this thesis is that, to the best of the author's knowledge, it presents the first CFD studies in marine engines operating in the diesel mode, including realistic combustion chemistry. To this end, a recent version of a coupled CHEMKIN II - KIVA-3vr2 tool, developed by the NTUA team, was properly adapted. In particular, two validated reduced mechanisms of the open literature have been incorporated: (i) a mechanism with 29 species and 52 chemical reactions (Mech.29) (Patel et al., 2004), (ii) a mechanism with 45 species and 142 chemical reactions (Mech.45) (Ra and Reitz, 2008). Simulations have been performed for two four-stroke dual fuel engines operating in the diesel mode, and yielded important details regarding the development of combustion, such as the evolution of important species, and an enhanced overall understanding of engine combustion. Comparisons with CFD results using the one-step approach have been presented. The outcome of the present approach, which utilises realistic combustion chemistry, is shown to be an improved description of engine aerothermochemistry, which also includes an accurate prediction of global quantities as Rate of Heat Release and pressure. An outline of this modelling framework is presented in Figure 6.1.

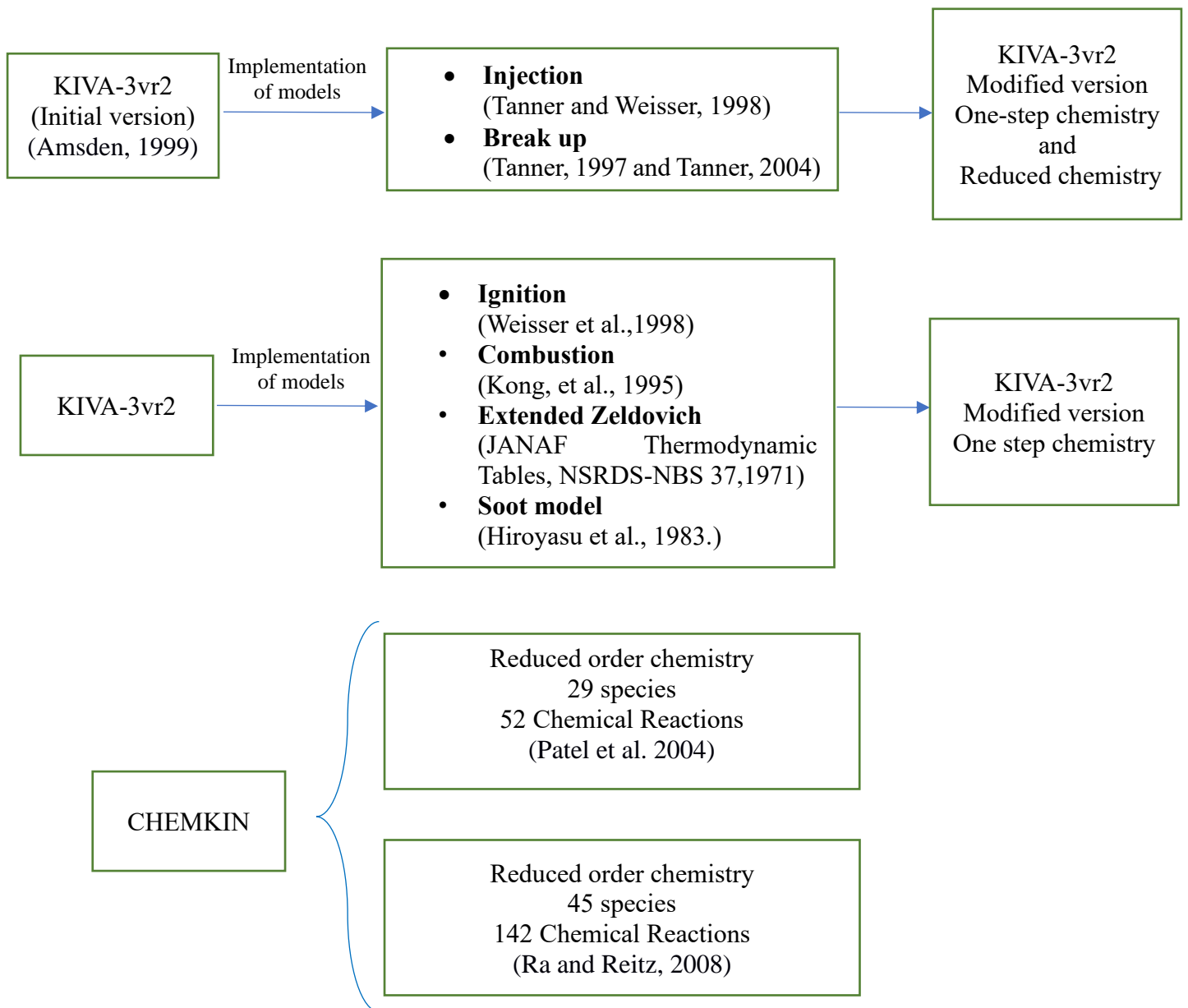


Figure 6.1: Sketch of modelling approach of the present study.

6.2 New findings of the present thesis

As already highlighted, a main novelty of the proposed project is associated with enabling accurate CFD calculations of marine engine combustion with realistic chemistry, thus leading to an accurate calculation of combustion development. Further, it is associated with an accurate prediction of global quantities, which are of interest from an engineering point of view, as the evolution of Rate of Heat Release and pressure, and the final concentration of main pollutant emissions. The present development has enabled a cross-evaluation with the standard approach of one-step chemistry, demonstrating that the latter can still be useful for the prediction of global engine quantities (at a reduced computational cost). The availability of two validated CFD tools can potentially be important for cases in which experimental data are not available.

In terms of combustion evolution, the present study has demonstrated that the realistic chemistry approach gives a termination of fuel decomposition at an earlier time instant, in comparison to the one-step approach; the former is deemed more realistic. In terms of understanding and characterising the combustion chemistry, the present study has demonstrated the following: (i) The role of the OH radical is less dominant for realistic chemistry versus one-step chemistry, whereas the inverse is the case for the H and O radicals; this is in accordance with the strong spatial variation of local air–fuel ratio within the combustion chamber. (ii) The evolution of CH_2O , important inhibitor of soot formation, has been demonstrated by means of CFD simulations with realistic chemistry. (iii) The formation of the major combustion products is properly accounted for by the present CFD simulations with realistic chemistry. In particular, the production of CO and CO_2 is shown to strongly depend on the decomposition of fuel to CH_4 and subsequently to CH_3 , followed by the formation of CH_2O and HCO, finally forming CO and CO_2 .

6.3 Journal publications under preparation

Based on the present results, the following journal publications are currently under preparation:

[1] A. Kiourtzis, D. Kazangas, G. Theotokatos and L. Kaiktsis, “Combustion characterisation in four-stroke engines using CFD with realistic chemical kinetics”, *Energy & Fuels*.

[2] D. Kazangas, A. Kiourtzis, G. Theotokatos and L. Kaiktsis, “Study of emissions formation in four-stroke engines using CFD with realistic chemical kinetics”, *International Journal of Engine Research*.

7. Concluding remarks

In the present thesis, CFD coupled with realistic chemistry has been implemented to characterise the combustion processes in four-stroke dual fuel engines of interest for marine applications, for operation in the diesel mode. Two representative engines have been considered. A systematic sequence has been followed. In a first step, the CAB spray model has been adapted, by performing CFD simulations of non-reactive spray in a constant volume chamber, and comparing results against experiments. CFD simulations with realistic chemistry have been enabled by further adapting a computational tool which couples the chemical kinetics CHEMKIN-II code with the KIVA-3vr2 CFD code; two validated reduced mechanisms of n-heptane combustion have been implemented, supplemented with a NO_x sub-mechanism. These engine CFD simulations have corresponded to operation in the high load range, and were compared against one-step chemistry CFD simulations, also performed here, as well as experiments, where available. Thus, this thesis presents CFD results of marine engine operation in the diesel mode, incorporating realistic combustion chemistry, for the first time, to the author's knowledge.

The results of the present study indicate that, for the same mechanisms, ignition delay times, as predicted by the present integrated computational tool, are in accordance with chemical kinetics calculations. In comparison to one-step CFD simulations, the ones of realistic chemistry predict a (physically plausible) earlier disintegration of the fuel, and give an accurate overall characterisation of chemistry, as reflected in the temporal evolution of important species.

The present approach accurately predicts the evolution of global quantities, as the Rate of Heat Release and pressure, as well as the level of emitted pollutants. The availability of two distinct CFD tools, corresponding to both realistic and one-step chemistry, is useful for cross-validating CFD results, as well as for computational studies for cases and conditions where experimental data are not available.

In terms of characterising and understanding the physics of engine combustion, the results have demonstrated the superiority of the present approach, i.e., the importance of incorporating realistic chemistry in engine CFD. Important findings in this context include a proper, earlier, calculation of fuel decomposition, a demonstration of a less pronounced role of OH radical, in comparison to one-step simulations, and a more pronounced one for the H and O radicals. Other important findings include a characterisation of the evolution of CH₂O, which is an important inhibitor of soot formation, as well as the identification of important paths towards the formation of major combustion products. Finally, it is noted that, as also shown by the present study, the one-step chemistry approach can still be a useful engineering tool, providing a basic characterisation of engine combustion.

8. Suggestion for future work

Following the outcomes of this study as presented and discussed in the preceding chapters, the recommendations for future work, can include:

- A more detailed study of the formation of main pollutant emissions, namely NO_x , SO_x and soot. This will require extending the reduced order chemical kinetics mechanisms of the present study, Mech.29 and Mech.45, with proper sub-mechanisms regarding the individual pollutant emissions.
- Optimisation studies of reduced order chemical kinetics mechanisms can yield improved mechanisms, which can be used, as in the context of the present work, for an improved representation of diesel mode engine combustion, as well as for engine optimisation studies.
- The computational tool of the present study can be applied to the study of marine engine combustion using alternative liquid fuels of current interest, such as methanol and Liquefied Petroleum Gas (LPG). Further, with a proper extension in terms of implementing the G-equation, the tool can be used to simulate marine engine operation in the gas mode, using Liquefied Natural Gas (LNG) as fuel.
- Applying the above to the simulation of two-stroke marine engines, for operation in both the diesel and in the gas mode.
- Implementing the present development in a parallel integrated computational tool, consisting of a parallel engine CFD code (such as KIVA-4mpi) and a parallel chemical kinetics tool (such as SpeedCHEM).

References

- Aceves, S. M., Flowers, D. L., Westbrook, C. K., Smith, J. R., Pitz, W., Dibble, R., Christensen, M., and Johansson, B. (2000). "A Multi-Zone Model for Prediction of HCCI Combustion and Emissions", SAE Technical Paper Series 2000-01-0327.
- Aceves, S. M., Martinez-Frias, J., Flowers, D. L., Smith, J. R., Dibble, R. W., Wright, J. F., and Hessel, R. P. (2001). "A Decoupled Model of Detailed Fluid Mechanics Followed by Detailed Chemical Kinetics for Prediction of Iso-Octane HCCI Combustion", SAE Technical Paper Series 2001-01-3612.
- Amsden, A. A. (1997). "KIVA-3V: A Block-Structured KIVA Program for Engines with Vertical or Canted Valves".
- Amsden, A.A. (1999). "KIVA-3V, Release 2, Improvements to KIVA-3V", LA-12503-MS, Los Alamos National Laboratory, Los Alamos, CA.
- Amsden, A.A. (1992). "KIVA-3: A KIVA program with block-structured mesh for complex geometries", Los Alamos National Laboratory, LA-12503-MS.
- Amsden, A.A., O'Rourke, P.J., and Butler, T.D. (1989). "KIVA-II: A computer program for chemically reactive flows with sprays", Los Alamos National Laboratory, LA-11560-MS.
- Andreadis, P., Zompanakis, A., Chryssakis, C., and Kaiktsis, L. (2011). "Effects of the fuel injection parameters on the performance and emissions formation in a large-bore marine Diesel engine", *Int. J. Engine Res.* 12:14-29.
- Aneja, R., and Abraham, J. (1998). "How far does the liquid penetrate in a Diesel engine: Computed results vs. measurements?", *Combustion Science and Technology*, 138(6):233–255.
- ANSYS ICEM CFD, version 18.0 - © SAS IP.
- Arcoumanis, C., Gavaises, M., and French, B. (1997). "Effect of Fuel Injection Processes on the Structure of Diesel Sprays", SAE Technical Paper Series 970799.
- Ashgriz, N. (2011). "Handbook of Atomization and sprays", Springer, USA.
- Babajimopoulos, A., Assanis, D. N., Flowers, D. L., Aceves, S. M., and Hessel, R. P. (2005). "A fully coupled computational fluid dynamics and multi-zone model with detailed chemical kinetics for the simulation of premixed charge compression ignition engines", *International Journal of Engine Research*, 6(5), 497–512.
- Baumgarten, C. (2006). "Mixture formation in internal combustion engines", Springer, Germany.

- Bolla, M., Srna, A., Wright, Y. M., Von Rotz, B., Herrmann, K., and Boulouchos, K. (2014). "Influence of Injector Diameter (0.2-1.2 mm range) on Diesel Spray Combustion: Measurements and CFD Simulations", SAE Technical Paper Series 2014-01-1419.
- Borman, G.L., and Johnson, J.H. (1962). "Unsteady vaporization histories and trajectories of fuel drops injected into swirling air", SAE Technical paper 598 C.
- Dent, J. C. (1971). "A Basis for the Comparison of Various Experimental Methods for Studying Spray Penetration", SAE Technical Paper Series 710571.
- Det Norske Veritas (DNV GL). (2018). "Maritime Forecast to 2050".
- Douladiris, K. (2010). "Computational study of soot formation in marine diesel engines", Diploma Thesis, National Technical University of Athens (NTUA), Greece.
- Fink, C., Buchholz, B., Niendorf, M., and Harndorf, H. (2008). "Injection Spray Analysis from Medium Speed Engines using Marine Fuels", In 22nd European Conference on Liquid Atomization and Spray Systems (ILASS). Como Lake, Italy.
- Galetakis, P. (2019). "Coupling of Computational Fluid Dynamics code with code of Chemical Kinetics and applications in two-stroke naval Diesel engines", Diploma Thesis, National Technical University of Athens (NTUA), Greece.
- Glassman, I., and Yetter, R. A. (2008). "Combustion", Elsevier.
- Golovitchev, V. I., and Nordin, N. (2001). "Detailed Chemistry Spray Combustion Model for the KIVA Code", 11th International Multidimensional Engine Modeling User's Group Meeting at the SAE Congress. Detroit, MI: Engine Research Center.
- Golovitchev, V. I., Nordin, N., Jarnicki, R., and Chomiak, J. (2000). "3-D Diesel Spray Simulations Using a New Detailed Chemistry Turbulent Combustion Model", SAE Technical Paper Series 2000-01-1891.
- Hashemi, H., Christensen, J. M., Gersen, S., Levinsky, H., Klippenstein, S. J., and Glarborg, P. (2016). "High-pressure oxidation of methane. Combustion and Flame", 172, 349–364.
- Haynes, B. S., and Wagner, H. G. (1981). "Soot formation", Progress in Energy and Combustion Science, 7(4), 229–273.
- Hensel, S., Herrmann, K., Schulz, R. and Weisser, G. (2012). "Numerical analysis and statistical description of the primary breakup in fuel nozzles of large two stroke engines for application in CFD engine simulations", The Eighth International Conference on Modeling and Diagnostics for Advanced Engine System, Fukuoka, Japan.

- Heywood, J.B. (1998). "Internal Combustion Engine Fundamentals", McGraw – Hill International Editions.
- Hiroyasu, H., and Arai, M. (1990). "Structures of Fuel Sprays in Diesel Engines", SAE Technical Paper, No. 900475.
- Hiroyasu, H., Kadota, T., and Arai, M. (1983). "Development and Use of a Spray Combustion Modeling to Predict Diesel Engine Efficiency and Pollutant Emissions, part 1: Combustion Modeling", Bull JSME 26, pp. 569 – 575.
- Hong, S., Wooldridge, M., Im, H, Assanis, D., and Kurtz, E. (2008). "Modeling of Diesel Combustion, Soot and NO Emissions Based on a Modified Eddy Dissipation Concept", Combustion Science and Technology, 180(8), 1421–1448.
- Hult, J., and Mayer, S. (2013). "A methodology for laser diagnostics in large bore marine two-stroke diesel engines", Measurement Science and Technology, 24(4):045204.
- Hult, J., Matlok, S., and Mayer, S. (2014). "Optical Diagnostics of Fuel Injection and Ignition in a Marine Two-Stroke Diesel Engine", SAE International Journal of Engines, 7(3), 1195–1206.
- Humair, D., Cartier, P., Süess, P., Wüthrich, S., Herrmann, K., Barro, C., Schneider, B., Schürch C., and Boulouchos, K. (2020). "Characterization of dual-fuel combustion processes", ISBN 978-3-941554-22-1, Rostock Large Engine Symposium.
- Imhof, D., and Takasaki, K. (2012). "Visual combustion research using the rapid compression expansion machine", MTZ Industrial, 2(2), 28–39.
- IMO (International Maritime Organization). (2008). "Amendments to the annex of the protocol of 1997 to amend the international convention for the prevention of pollution from ships, 1973, as modified by the protocol of 1978 relating thereto (revised MARPOL Annex VI)." MEPC.176 (58), London
- Kakaee, A.-H., Rahnama, P., and Paykani, A. (2015). "CFD Study of Reactivity Controlled Compression Ignition (RCCI) Combustion in a Heavy-Duty Diesel Engine", Periodica Polytechnica Transportation Engineering, vol. 43, no. 4, pp. 177–183.
- Kee R. J., Rupley F. M., and Miller J. A. (1989). "CHEMKIN-II: A Fortran chemical kinetics package for the analysis of gas-phase chemical kinetics", Sandia National Laboratories: Livermore, CA, Technical Report SAND-89-8009.
- Kong, S.-C., Han, Z., and Reitz, R.D. (1995). "The Development and Application of a Diesel Ignition and Combustion Model for Multidimensional Engine Simulation", SAE 950278.
- Kong, S.-C., Marriott, C. D., Reitz, R. D., and Christensen, M. (2001). "Modeling and Experiments

- of HCCI Engine Combustion Using Detailed Chemical Kinetics with Multidimensional CFD”, SAE Technical Paper 2001-01-1026.
- Kong, S.-C., Reitz, R. D. (2002). “Use of Detailed Chemical Kinetics to Study HCCI Engine Combustion with Consideration of Turbulent Mixing Effects”, *Journal of Engineering for Gas Turbines and Power*, v. 124, p. 702-707.
- Kong, S.-C., Reitz, R. D. (2003). “Numerical Study of Premixed HCCI Engine Combustion and its Sensitivity to Computational Mesh and Model Uncertainties”, *Combustion Theory and Modelling*, v. 7, p. 417-433.
- Kontoulis, P. (2019). “Computational Study and Optimization of Flow and Combustion Processes in Marine Engines Operating with Heavy Fuel Oil”, Ph.D. Thesis, National Technological University of Athens, Athens, Greece.
- Kontoulis, P., Kaiktsis, L., von Rotz, B., and Boulouchos, K. (2019). “CFD Modeling and Experimental Spray Studies for Different Heavy Fuel Oil Qualities with Respect to Large Two-Stroke Marine Engines”, *Journal of Energy Engineering*, 145(5), 04019014.
- Kontoulis, P., Kaiktsis, L., von Rotz, B., Schmid A., Weisser, G., Herrmann, K., and Boulouchos, K. (2014). “CFD and experimental studies of Heavy Fuel Oil sprays for marine engine applications”, ILASS – Europe 2014, Bremen, Germany.
- Kontoulis, P., Kazangas, D., Doss, T. P., and Kaiktsis, L. (2018). “Development and CFD Validation of an Integrated Model for Marine Heavy Fuel Oil Thermophysical Properties”, *Journal of Energy Engineering*, 144(5), 04018059.
- Laboratory Report LA-13608-MS, (1999), Los Alamos, New Mexico.
- Lacoste, J., Crua, C., Heikal, M. and Kennaïrd, D. (2003). “PDA Characterisation of Dense Diesel Sprays Using a Common-Rail Injection System”, SAE International 2003-10-27.
- Lavoie, G., Heywood, J., and Keck, J. (1970). “Experimental and Theoretical Investigation of Nitric Oxide Formation in Internal Combustion Engine”, *Combustion Science Technology*, vol. 1, pp. 313 – 326.
- Liang, L., Kong, S.-C., Jung, C., and Reitz, R. D. (2007). “Development of a Semi-implicit Solver for Detailed Chemistry in Internal Combustion Engine Simulations”, *Journal of Engineering for Gas Turbines and Power*, 129(1), 271.
- Liu, A.B., and Reitz, R.D. (1993). “Mechanisms of air-assisted liquid atomization”, *Atomization and Sprays*, 3: 55-75.
- Liu, Z., and Karim, G. A. (1997). “Simulation of combustion processes in gas-fuelled Diesel engines.

- Proceedings of the Institution of Mechanical Engineers”, Part A: Journal of Power and Energy, 211(2), 159–169.
- Maghbouli, A., Saray, R. K., Shafee, S., and Ghafouri, J. (2013). “Numerical study of combustion and emission characteristics of dual-fuel engines using 3D-CFD models coupled with chemical kinetics”, *Fuel*, 106, 98–105.
- Malte, P.C., and Pratt, D.T. (1974). "The role of energy-releasing kinetics in NO_x formation: Fuel-lean, jet-stirred CO-air combustion. " *Combust. Sci. Technol.*, 9(5–6), 221–231.
- Marine Engines & Systems. (2017). <http://marine.man.eu>.
- Mazi, H. A. (2009). “Coupling of Chemical Kinetics with Computational Fluid Dynamics in a Three-Dimensional Engine Model”, Master’s Thesis in Mechanical Engineering, University of Illinois at Urbana-Champaign.
- Naber, J., and Siebers, D. L. (1996). “Effects of Gas Density and Vaporization on Penetration and Dispersion of Diesel Sprays”, SAE Technical Paper, No. 960034.
- Najar, I., Fink, C., Pinkert, F. and Harndorf, H. (2014). “A New Spray Penetration Model Developed for Large Engine Diesel Injectors”, In 26th European Conference on Liquid Atomization and Spray Systems (ILASS). Bremen, Germany.
- Nakagawa, H., Oda, Y., Kato, S., Nakashima, M. and Tateishi, M. (1990). “Fuel Spray Motion in Side-Injection Combustion System for Diesel Engines”, In 2nd International Symposium on Diagnostics and Modeling of Combustion in Internal Combustion engines (COMODIA). Kyoto, Japan.
- Nordin., N. (2000). “Complex chemistry modeling of Diesel spray combustion”, PhD Thesis, Chalmers University of Technology.
- O’Rourke, P. J., and Amsden, A. A. (1987). “The Tab Method for Numerical Calculation of Spray Droplet Breakup”, SAE Technical Paper Series 872089.
- Pananakis, E. Kontoulis, P. Chryssakis, C., and Kaiktsis, L. (2013). “Investigation of Fuel Injection Strategies for Partially Premixed Compression Ignition Combustion in Two-Stroke Marine Diesel Engines”, ILASS – Europe 2013, 25th European Conference on Liquid Atomization and Spray Systems, Chania, Greece.
- Pang K.M., Karvounis N., Walther J.H., Schramm J., Glaborg P., and Mayer S. (2017). “Modelling of temporal and spatial evolution of sulphur oxides and sulphuric acid under large, two-stroke marine engine-like conditions using integrated CFD-chemical kinetics”, *Appl Energy* 2017;193:60–73.
- Pang, K. M., Karvounis, N., Walther, J. H., and Schramm, J. (2016). “Numerical investigation of soot

formation and oxidation processes under large two-stroke marine Diesel engine-like conditions using integrated CFD-chemical kinetics”, *Applied Energy*, 169, 874–887.

Papagiannakis, R., and Hountalas, D. (2003). “Experimental investigation concerning the effect of natural gas percentage on performance and emissions of a DI dual fuel Diesel engine”, *Applied Thermal Engineering*, 23(3), 353–365.

Papagiannakis, R., and Hountalas, D. (2004). “Combustion and exhaust emission characteristics of a dual fuel compression ignition engine operated with pilot Diesel fuel and natural gas”, *Energy Conversion and Management*, 45, 2971-2987.

Patel, A., Kong, S.-C., and Reitz, R. (2004). “Development and Validation of a Reduced Reaction Mechanism for HCCI Engine Simulations”, SAE Technical Paper Series 2004-01-0558.

Perini, F., Das Adhikary, B., Lim, J. H., Su, X., Ra, Y., Wang, H., and Reitz, R. (2014). “Improved Chemical Kinetics Numerics for the Efficient Simulation of Advanced Combustion Strategies”, *SAE International Journal of Engines*, 7(1), 243–255.

Pizza, G., Wright, Y. M., Weisser, G., and Boulouchos, K. (2007). “Evaporating and non-evaporating diesel spray simulation: comparison between the ETAB and wave breakup model”, *International Journal of Vehicle Design*, 45(1/2), 80.

Prescher, K., Astachow, A., Krüger, G., and Hintze, K. (1999). “Investigation of the Atomization and Evaporation of Diesel Fuel and Heavy Fuel Sprays Using Optical Measurement Techniques”, SAE Technical Paper, No. 1999-01-0520.

Ra, Y., and Reitz, R. (2008). “A reduced chemical kinetic model for IC engine combustion simulations with primary reference fuels”, *Combustion and Flame*, 155(4), 713–738.

Ranz, W.E., and Marshall, W.R. (1952). “Internal combustion engine modelling”, New York: Hemisphere.

Reitz, R., and Rutland, C. (1993). “Three-dimensional modeling of Diesel engine intake flow, combustion and emissions-2”, University of Wisconsin-Madison, Wisconsin.

Reitz, R. (2012). “Reciprocating internal combustion engines”, summer program on combustion, University of Wisconsin-Madison, USA.

Rodatz, P., Weisser, G., and Tanner, F. X. (2000). “Assessment of CFD Methods for Large Diesel Engines Equipped with a Common Rail Injection System”, SAE Technical Paper Series 2000-01-0948.

Schmid, A., Von Rotz, B., Weisser, G., and Herrmann, K. (2014). “Ignition Behaviour of Marine Diesel Fuels under Engine Like Conditions”, SAE Technical Paper Series 2014-01-2656.

- Schmidt, P. D., and Rutland, J. C. (2004). "Reducing grid dependency in droplet collisions modeling. *Journal of Engineering for Gas Turbines and Power*", 127:227255.
- Schneider, B. (2003). "Experimentelle Untersuchungen zur Spraystruktur in Transienten, Verdampfenden und Nicht Verdampfenden Brennstoffstrahlen unter Hochdruck." Doctoral Thesis, ETH Zurich.
- Schneider, B., Schürch, C., Boulouchos, K., Herzig, S., Hangartner, M., Herzig, S., Hangartner M., Humair, D., Wuthrich S., Gossweiler, C., and Herrmann, K. (2020). "The Flex-OeCoS-a Novel Optically Accessible Test Rig for the Investigation of Advanced Combustion Processes under Engine-Like Conditions", *Energies*, 13(7), 1794.
- Shi, Y., and Reitz, R. (2008). "Optimization study of the effects of bowl geometry, spray targeting, and swirl ratio for a heavy-duty Diesel engine operated at low and high load", *International Journal of Engine Research*, 9(4), 325–346.
- Shi, Y., Hessel, R., and Reitz, R. (2009). "An Adaptive Multi-Grid Chemistry (AMC) Model for Efficient Simulation of HCCI and DI Engine Combustion", *Combustion Theory and Modeling*, p. 1-22.
- Spahni, M., and Kyrtatos, A. (2014). "New Generation Low Speed Two-stroke Engines", *MTZ Industrial*, 4(2), 12–19.
- Stiesch, G. (2003). "Modeling engine spray and combustion processes", Springer, Germany.
- Stoumpos, S., Theotokatos, G., Boulougouris, E., Vassalos, D., Lazakis, I., and Livanos, G. (2018). "Marine dual fuel engine modelling and parametric investigation of engine settings effect on performance-emissions trade-offs", *Ocean Engineering*, 157, 376–386.
- Stratsianis V., Kontoulis P., and Kaiktsis L. (2016). "Effects of fuel post-injection on the performance and pollutant emissions of a large marine engine", *J. Energy Eng.* 142(2):E4016001 1-19.
- Takasaki, K., Fukuyoshi, T., Abe, S., Nakashima, M. and Osafune, S.-n. (1999). "Visual Study about Combustion Characteristics of Heavy Fuel in Diesel Engines", *Bulletin of the M.E.S.J.*, Vol. 27(No.1)22-28.
- Takasaki, K., Fukuyoshi, T., Abe, S., Nakashima, M., and Osafune, S.-n. (1999). "Visual Study about Combustion Characteristics of Heavy Fuel in Diesel Engines", *Bulletin of the M.E.S.J.*, Vol. 27(No.1)22-28.
- Tanner, F.X. (1997). "Liquid jet atomization and droplet break-up modeling of non-evaporating diesel fuel sprays", SAE Technical paper 970050.
- Tanner, F. X. (2003). "A Cascade Atomization and Drop Breakup Model for the Simulation of High-

Pressure Liquid Jets”, SAE Technical Paper Series 2003-01-1044.

Tanner, F.X. (2004). “Development and validation of a cascade atomization and drop breakup model for high-velocity dense sprays”, *Atomization and Sprays*, Vol. 14, No. 3.

Tanner, F. X., and Weisser, G. (1998). “Simulation of Liquid Jet Atomization for Fuel Sprays by Means of a Cascade Drop Breakup Model”, SAE Technical Paper Series 980808.

Taylor, D. H. C., and Walsham, B. E. (1969). “Combustion Processes in a Medium-Speed Diesel Engine. Proceedings of the Institution of Mechanical Engineers”, *Conference Proceedings*, 184(10):67{76.

Turns, S.R. (1996). “An Introduction to Combustion – Concepts and Applications”, McGraw-Hill, pp. 80-87.

von Rotz, B. (2015). “Experimental investigation of spray characteristics and ignition processes at conditions representative of large two-stroke marine Diesel engine”, Ph.D. Thesis, Swiss Federal Institute of Technology, Zurich, Switzerland.

von Rotz, B., Herrmann, K., and Boulouchos, K., (2015). “Experimental Investigation on the Characteristics of Sprays Representative for Large 2-Stroke Marine Diesel Engine Combustion Systems”, SAE Technical Paper 2015-01-1825.

von Rotz, B., Schmid A., Hensel S., Herrmann, K., and Boulouchos, K. (2016). “Comparative Investigations of Spray Formation, Ignition and Combustion for LFO and HFO at Conditions relevant for Large 2-Stroke Marine Diesel Engine Combustion Systems”, Paper No. 253, CIMAC Congress Helsinki, Finland.

Wärtilä, (2015). “Product Guide Wärtilä 50DF”, Wärtilä.

Wärtilä, (2009). “Wärtilä 50DF Engine Technology”, Wärtilä

Weisser, G. (2001). “Modelling of combustion and nitric oxide formation for medium - speed DI Diesel engines: a comparative evaluation of zero- and three - dimensional approaches”, Ph.D. Thesis, Swiss Federal Institute of Technology, Zurich, Switzerland.

Weisser, G. (2013). “Current trends in the development of large two-stroke marine Diesel engines in the light of significantly changing market requirements and environmental regulations”, 3rd Technical meeting of SNAME Greece.

Weisser, G., Tanner, F. X., and Boulouchos, K. (1998). “Modeling of Ignition and Early Flame Development with Respect to Large Diesel Engine Simulation”, SAE Technical Paper Series 981451.

Wüthrich, S., Humair, D., Herrmann, K., and Bertola, A. (2020). “Enhanced instrumentation of an optical research engine with unique combustion chamber”, ISBN Nummer 978-3-9816971-6-2, 14th

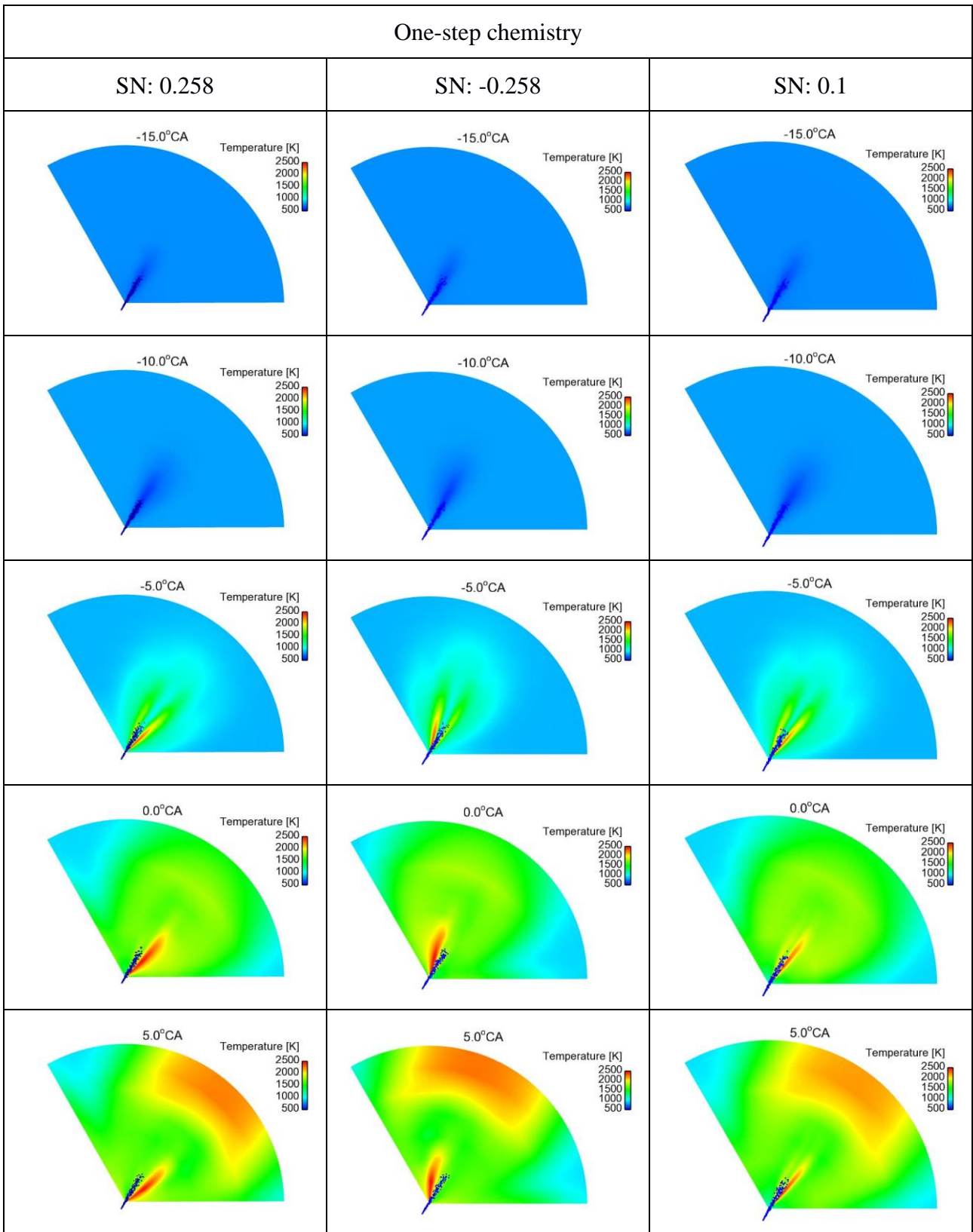
Int. AVL Symposium on Propulsion Diagnostics, Kurhaus Baden-Baden, Germany.

Yuan, R., Kariuki, J., Dowlut, A., Balachandran, R., and Mastorakos, E. (2015). “Reaction zone visualisation in swirling spray n -heptane flames”, *Proceedings of the Combustion Institute*, 35(2), 1649–1656.

Appendix A

For the Lister LV1 engine, the effect of Swirl Number (SN) was investigated for both of the grids considered (polar grid and cartesian grid). Figures A-1 and A-2 present colour-coded contours of temperature as derived from (a) one-step chemistry using polar mesh (Figure A-1), and (b) reduced order chemistry with mechanism Mech.45 and a cartesian mesh (Figure A-1). In both cases, three values of swirl number, SN, are considered. The three cases of SN correspond to: (i) $SN = 0.258$ (clockwise swirl), (ii) $SN = -0.258$ (counterclockwise swirl), (iii) a very low value of SN. The visualisations of Figures A-1 and A-2 verify that a nearly symmetric field is attained at very low swirl, whereas, for $SN = 0.258$ and $SN = -0.258$, the fields are antisymmetric to each other.

One-step chemistry



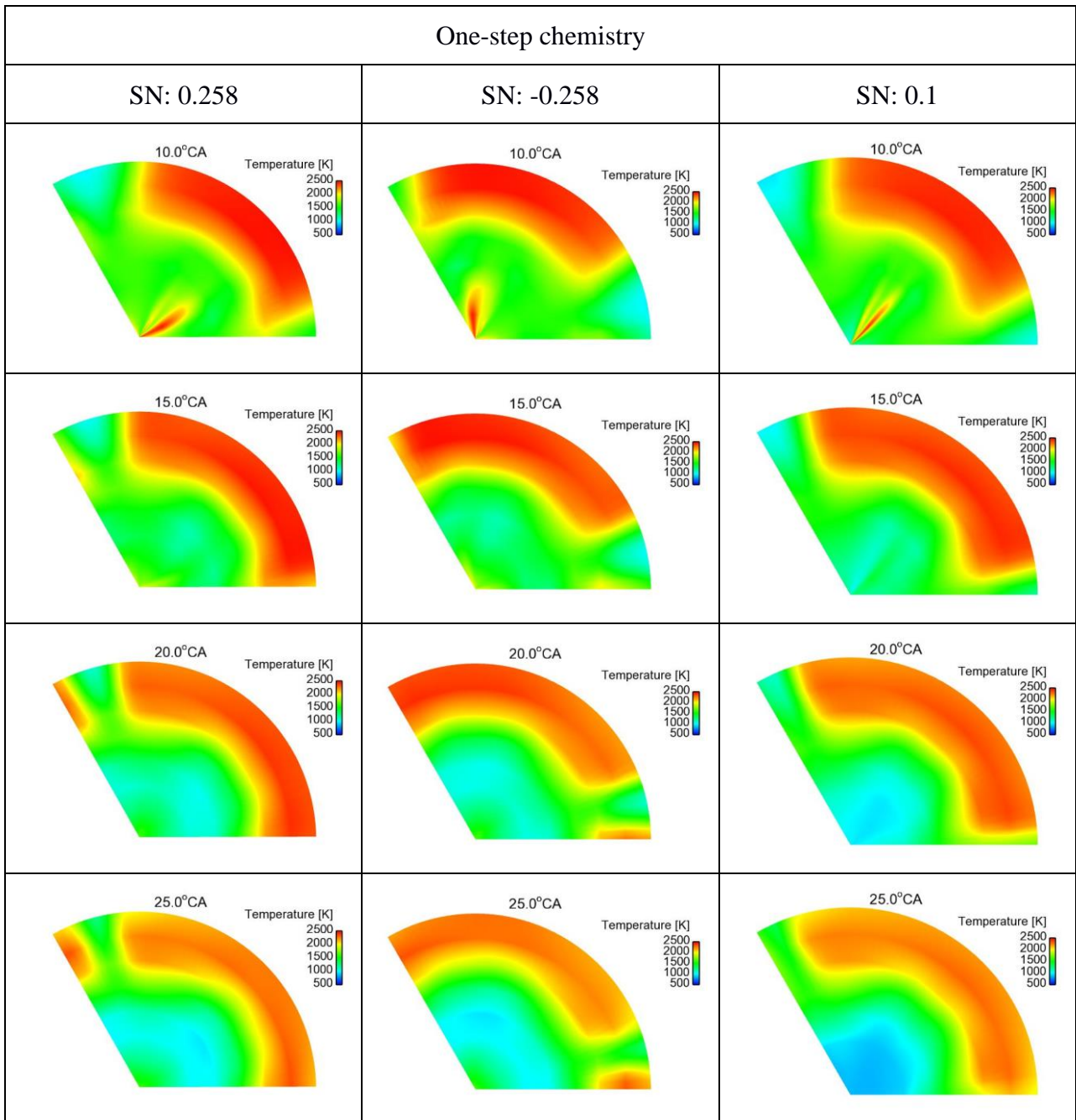
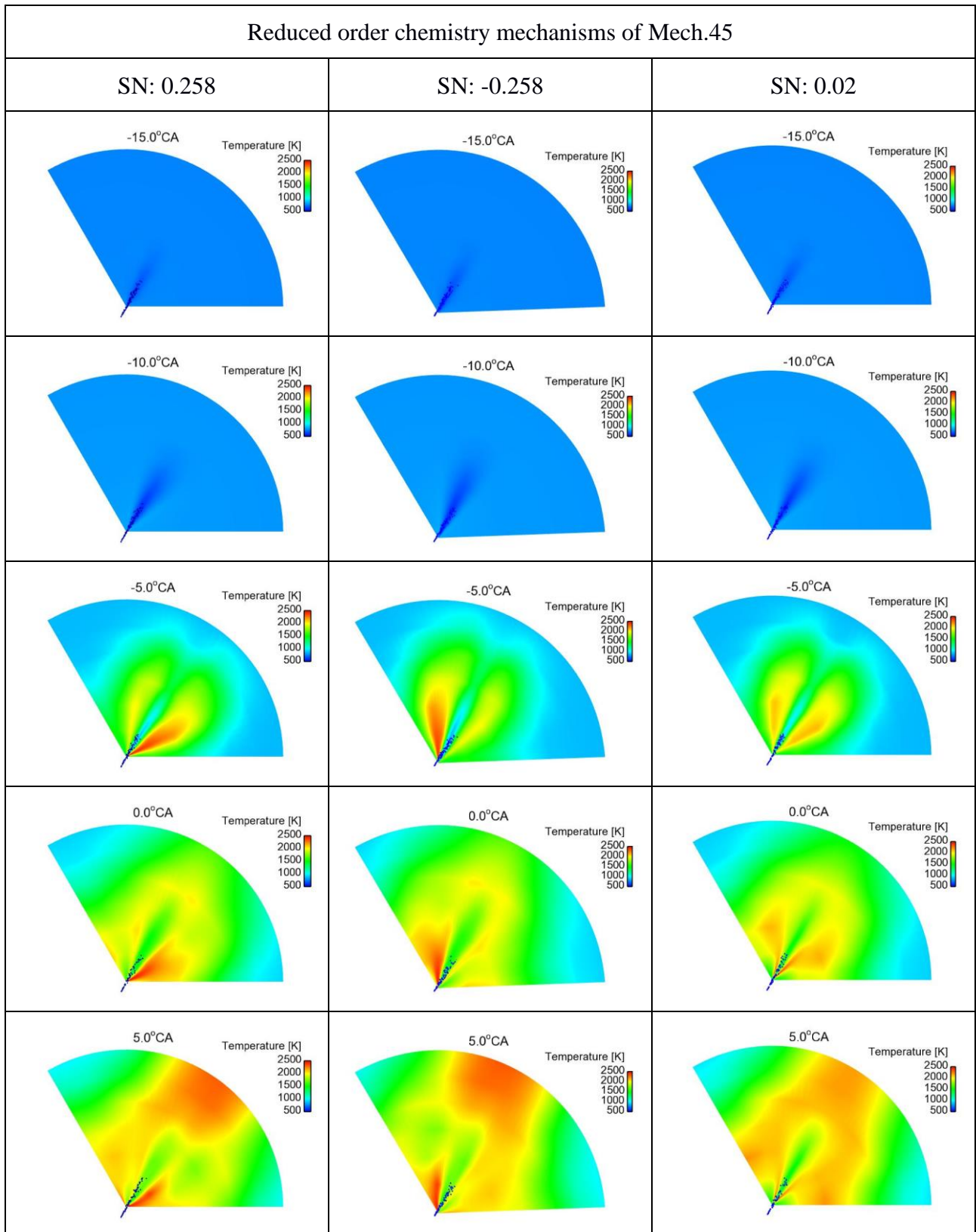


Figure A-1: Colour-coded contours of temperature using one-step chemistry with polar mesh for three different values of SN (Swirl Number). A horizontal plane very close to the injector is considered, at selected time instants.

Reduced order chemistry mechanisms of Mech.45



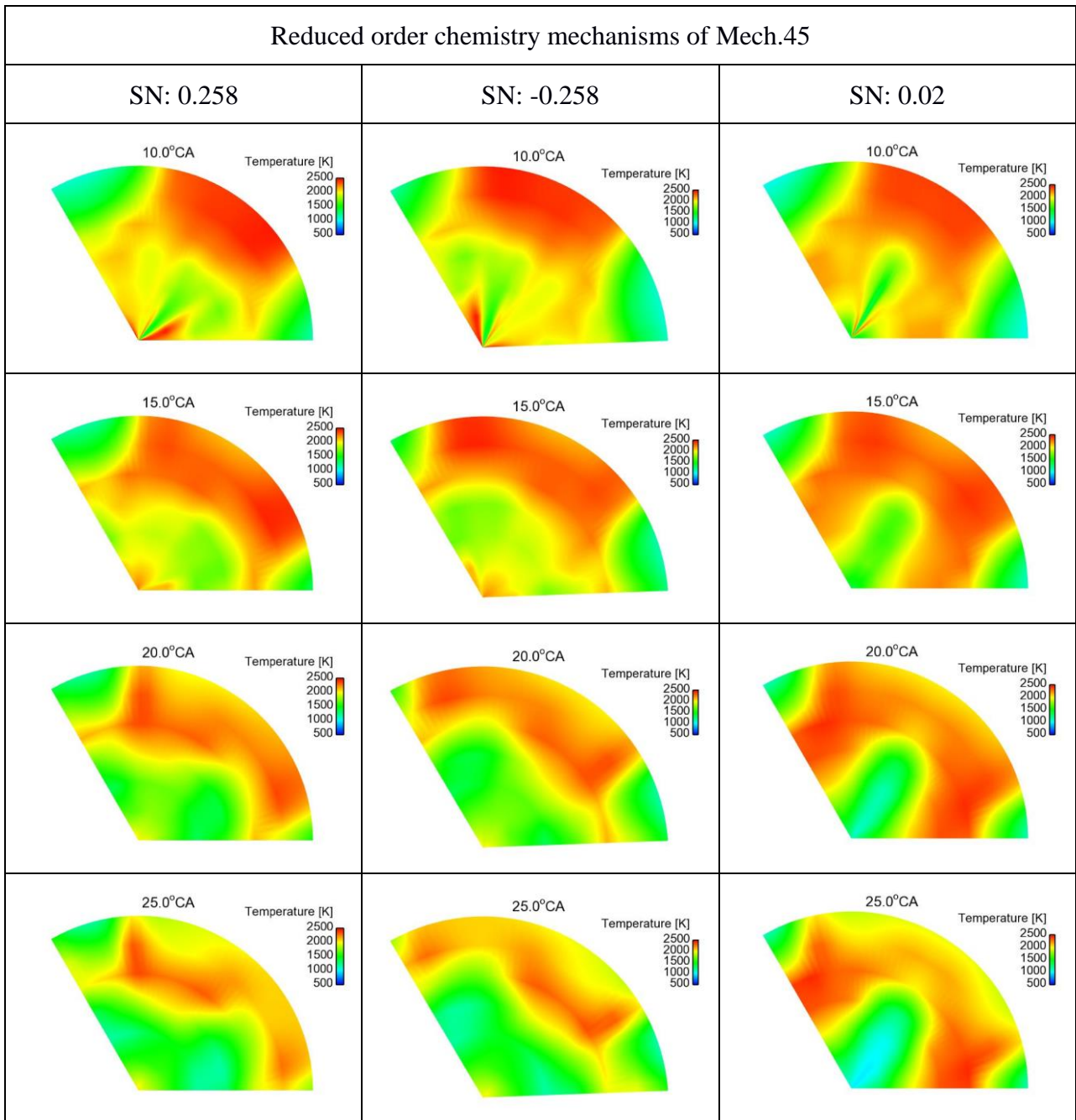


Figure A-2: Colour-coded contours of temperature using the reduced order chemistry mechanisms Mech.45 with cartesian mesh for three different values of SN (Swirl Number). A horizontal plane very close to the injector is considered, at selected time instants.